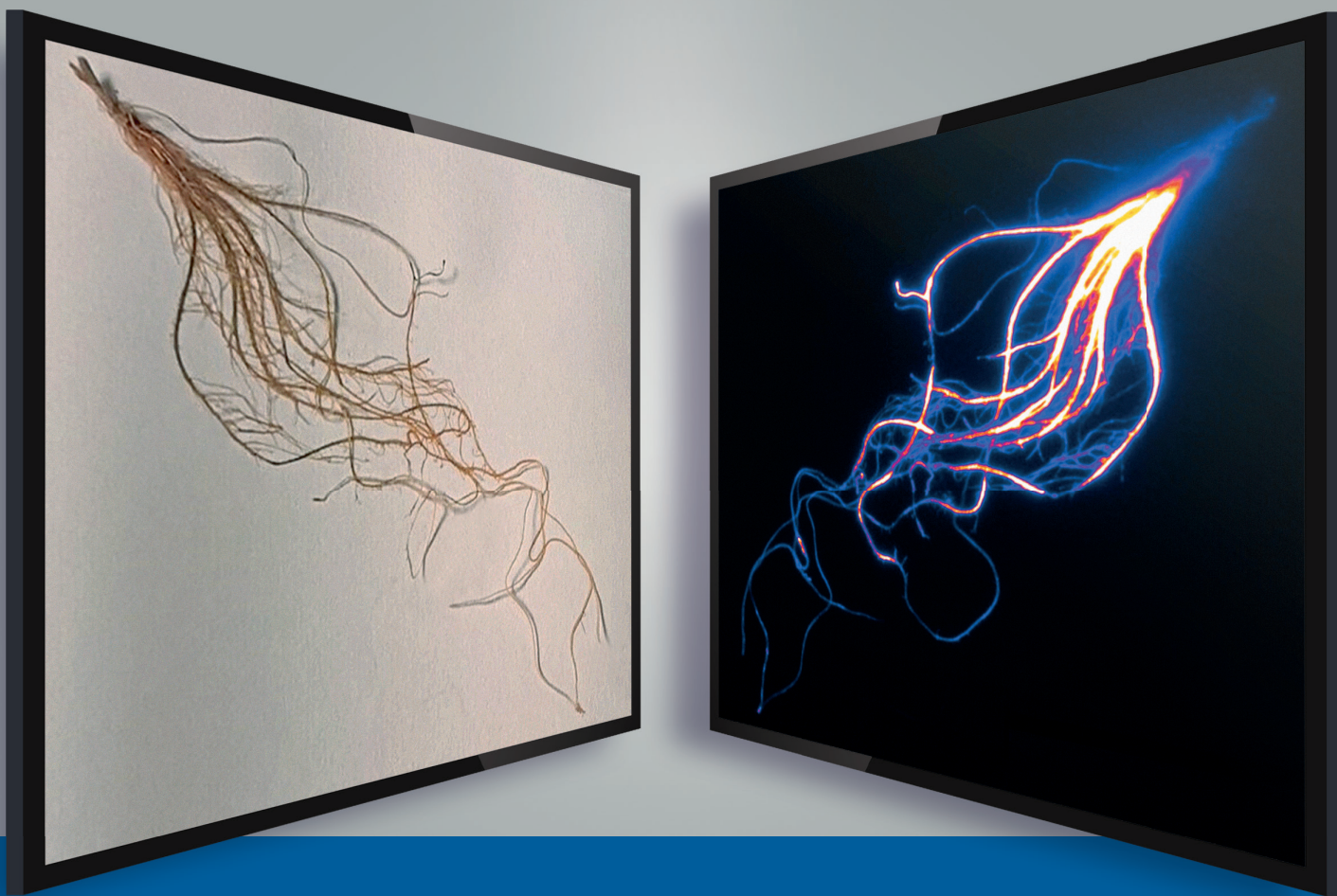


HZDR-128

ANNUAL REPORT 2023

Institute of Resource Ecology



Wissenschaftlich-Technische Berichte
HZDR-128 2024 . ISSN 2191-8708

HZDR
HELMHOLTZ ZENTRUM
DRESDEN ROSSENDORF

Wissenschaftlich-Technische Berichte
HZDR-128

Annual Report 2023

Institute of Resource Ecology

Editorial board:

Prof. Dr. Thorsten Stumpf
Dr. Harald Foerstendorf
Dr. Frank Bok
Dr. Anke Richter

Impressum

Print edition: ISSN 2191-8708

Electronic edition: ISSN 2191-8716

The electronic edition is published under Creative Commons License (CC BY-NC-ND):

<https://www.hzdr.de/publications/Publ-38795>

<https://nbn-resolving.org/urn:nbn:de:bsz:d120-qucosa2-902666>

Published by Helmholtz-Zentrum Dresden–Rossendorf e.V.

Contact

Helmholtz-Zentrum Dresden–Rossendorf e.V.

Institute of Resource Ecology

Bautzner Landstraße 400

D-01328 Dresden

Germany

Phone: +49 (0) 351 260 3210

Fax: +49 (0) 351 260 3553

e-mail: contact.resourceecology@hzdr.de

<https://www.hzdr.de/fwo>

This report is also available at <https://www.hzdr.de/fwo>

Cover picture

Environmental pollution with rare earth elements and radionuclides poses a risk for the human's food chain. Thus, knowledge about the fate of metal contaminations in plants is of utter importance for reliable risk assessments. We utilized autoradiography in order to visualize the bioassociation of ^{152}Eu , a β -emitter found in nuclear fission products and proxy for various other trivalent rare earth and transuranium elements, in the forage crop sand oat (*Avena strigosa*). Upon exposure of the radiating root to a phosphor imaging screen and subsequent photostimulated read-out a black-and-white autoradiogram was obtained. An internal calibration standard allowed to correlate signal intensity to the amount of ^{152}Eu per unit area, giving rise to the heat map where violet color represents low and white color high radioactivity. Supported by various other analytical methods we aim to follow the pathways of metal uptake, transport and distribution within plants on macroscopic and microscopic scale. Autoradiography helps us to resolve metal sinks and understand metal association to biological tissue.

Cover picture created by M. Klotzsche, HZDR–IRE.

Preface

DEAR INTERESTED READERS,
DEAR COLLEAGUES,

2023 was another turbulent year overall, marked by Russia's war of aggression against Ukraine, inflation and labor disputes. Even under these conditions, the Institute of Resource Ecology continued to develop well. An important strategic goal is the expansion of cooperation with universities. In this endeavor, we were able to strengthen our collaboration with the Université Grenoble Alpes and further emphasize this with the appointment of Kristina Kvashnina to a full professorship. Kristina Kvashnina also became head of the Department of Molecular Structures at our beamline at the ESRF in 2023. Furthermore, the cooperation with TU Dresden was intensified with the nomination of Natalia Mayordomo Herranz as a TUD Young Investigator. For 2024, we are hoping for further joint appointments with the universities in Leipzig and Cottbus-Senftenberg.

The IRE is one of the ten institutes of the Helmholtz-Zentrum Dresden-Rossendorf (HZDR). Our research activities are mainly integrated into the program "Nuclear Waste Management, Safety and Radiation Research (NUSAFE)" of the Helmholtz Association (HGF) and focus on the topics "Safety of Nuclear Waste Disposal" and "Safety Research for Nuclear Reactors". The program NUSAFE, and therefore all work which is done at IRE, belong to the research field "Energy" of the HGF.

IRE conducts applied basic research to protect humans and the environment from the effects of radioactivity. For this purpose, we develop molecular process understanding using state-of-the-art methods of microscopy, spectroscopy, diffraction, numerical simulation, theoretical chemistry, and systems biology. We implement this in a cross-institutional research environment at the HZDR. Our active interdisciplinarity combines radiochemistry, actinide chemistry, geo- and biosciences, as well as material science and reactor physics. We provide knowledge that is applied in particular to reactor and repository safety as well as in radioecology.

We achieve this goal with a unique infrastructure comprising chemical and biological laboratories as well as hot cells in corresponding radiation and biological safety laboratories in Dresden, Leipzig, and Grenoble. In Grenoble, at the European Synchrotron Radiation Facility (ESRF), the institute operates the only German beamline with four experimental stations for advanced X-ray spectroscopy and diffraction of radioactive samples, which is also made available to external users.

Although the Corona pandemic reached into 2023, 118 original papers were published in peer-reviewed international scientific journals with an average impact factor of 6.26. The extraordinary broadness of research topics and activities is illustrated by some selected highlights below:

The best-estimate HZDR reactor safety calculation chain Serpent/DYN3D/ATHLET was applied for the first time to a small modular reactor. This well-known coupled code system was used to analyze a main steam line break, in which the interaction of the reactor core with the components of the primary and secondary circuits plays an important role. This allowed demonstrating the ability of modeling small modular reactors (→ p. 72).

Radiation tolerance of crystalline materials – as the ability to withstand the accumulation of the radiation induced disorder – is a key feature not only for nuclear structural materials but also for selected semiconductors. We established Electron Backscatter Diffraction (EBSD) as a rapid tool to detect phase transformations in Ga₂O₃ after ion irradiation, based on high quality EBSD patterns. The high throughput of this method marks an important step towards efficient development of radiation resistant semiconductors (→ p. 65).

Over time, various biological functions have been demonstrated for many elements of the periodic table, most recently for the lanthanides. The latter have been described as necessary co-factors for methanol dehydrogenases (MDH), which enable bacteria to feed methylotrophically. But only recently we could show that these bacteria can alternatively use the trivalent actinides americium and curium instead of lanthanides to utilize reduced C1 compounds (→ p. 45). Furthermore, the addition of the actinides to the metal-free MDH leads to the formation of an active holoenzyme. This work shows for the first time that actinides can also act as co-factors in enzymes and thus enable microbial life.

DNA origami are rationally designed DNA structures with emerging applications in biotechnology, medicine, and physical chemistry. We have studied the yet unexplored factors that affect their stability, aiming at their use in nanoscopic evaluation of radionuclide-induced DNA damage. Atomic force microscopy and circular dichroism spectroscopy has been employed in these studies and revealed ion-dependent heat capacity changes as a key thermodynamic parameter in regulating DNA structural transitions (→ p. 56).

The highlights from the field of reactive transport range from experimental-analytical to numerical challenges and cover a wide range of length scales, from the nm to the cm range. First, we present a mechanistic explanation for the variable sorption efficiency on single crystal surfaces using muscovite as an example (→ p. 35). Another numerical study focuses on hydrogen transport between layers of transition metal dichalcogenides (→ p. 22). Material interfaces are critical for reactive transport, *e.g.*, between concrete and host rock in repository structures (→ p. 36). We have also investigated the influence of geometric heterogeneity in fractured granites on the variable residence time of advectively transported fluids (→ p. 34). Furthermore, we present an example of our work on radionuclide production at the cyclotron with a case study of its application in retention studies (→ p. 37).

Early in 2023, we installed and commissioned a new SQUID magnetometer in our labs, which is helping us to understand the magnetic (and thus electronic) properties of the actinides (→ p. 11). Recent investigations have revealed dynamics in metalorganic actinide complexes (→ p. 16), differences between U(VI) and Np(VI) reactivity (→ p. 14), and the reactivity of Np(IV) with different alkenolate ligands (→ p. 12). We have also discovered a novel coupling reaction catalyzed by the activation of a C–Cl bond by several actinides (→ p. 13) and a thorium MOF, which is remarkably stable against radiation (→ p. 18).

The Rossendorf beamline and all the available methods at ROBL have been employed to investigate the chemical complexity of Cr-doped UO₂ nuclear fuels. X-ray absorption spectroscopy measurements in both HERFD and

EXAFS modes of Cr-doped UO_2 single crystals have elucidated the Cr chemistry in UO_2 , and X-ray diffraction measurements were conducted for structural analysis. This investigation provides significant guidance for the safe application of Cr-doped UO_2 nuclear fuels in power generation and for their correct disposal when discharged from a reactor as spent nuclear fuel (→ p. 59).

The complexation of radionuclides with organic ligands plays a decisive role in many processes, *e.g.*, the final disposal of radioactive waste or the (unintentional) spread in nature up to the entry into the food chain for humans. Precise knowledge of the thermodynamic data of the compounds is essential in order to be able to accurately assess the binding of heavy metals to various complexing agents and to be able to use the best possible active substances for decontamination or decomposition. Using the example of the complexation of europium (Eu(III)) and curium (Cm(III)) with different aminocarboxylate ligands (NTA, EDTA, EGTA), it was shown that the combination of different spectroscopic ($^1\text{H-NMR}$, TRLFS), calorimetric and theoretical methods provides robust thermodynamic data that allow a reliable estimation of the strength of the complexation (→ p. 53 and p. 17).

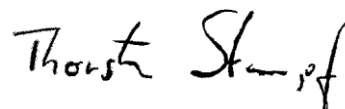
In addition to the impressive selection of scientific results presented in this annual report, also “meta-activities” are worth mentioning. One is the establishment of an internal knowledge management system where important first building blocks concerning guidelines for on- and off-boarding, access to qualification measures, recommendations for best practice in publishing as well as fund raising and project management are covered. Also, many administrative pitfalls and forms are discussed. This all shall help to preserve and foster expertise and knowledge on both individual and institutional level.

Beside these highlights, we obtained many other new scientific results in the past year, some of which are presented in this annual report.

In the last year, more than 150 scientists and technicians were employed at the Institute of Resource Ecology. Thereof, 39 Ph.D. students worked at the institute in 2023.

In addition, the young scientists at the Institute of Resource Ecology were once again very successful. Holger Lippold was habilitated at the University of Leipzig. Furthermore, Julia Neumann received the HZDR Doctoral Prize and Janis Wolf was honored with the Woman in Nuclear Award.

In retrospect of a very successful year 2023, I would like to thank the visitors, German and international ones, for their interest in our research and for their participation in the institute seminars. We will continue to strongly encourage collaborations and visits by scientists in the future. Special thanks are due to the board of directors and the executive board of the HZDR, the Ministry of Science and Arts of the Free State Saxony (SMWK), the Federal Ministry of Education and Research (BMBF), the German Federal Ministry for Economic Affairs and Climate Action (BMWK), the Federal Ministry for the Environment, Nature Conservation, Nuclear Safety and Consumer Protection (BMUV), the Deutsche Forschungsgemeinschaft (DFG), the European Commission, and other organizations for their support.



Prof. Dr. Thorsten Stumpf
Director of the
Institute of Resource Ecology

Contents

SCIENTIFIC CONTRIBUTIONS

Part I: The Chemistry of Long-Lived Radionuclides

SQUID magnetometry on actinide complexes.....	11
R. Gericke, D. Grödler, B. Hong, J. Balas, A. Näder, M. Patzschke, P. Kaden, M. Schmidt	
Synthesis and characterization of Neptunium(IV) heteroarylalkenolate complexes	12
D. Grödler, P. Kaden, B. Hong, J. M. Sperling, B. M. Rotermund, N. B. Beck, B. Scheibe, S. Mathur, T. E. Albrecht-Schönzart, R. Gericke	
C–Cl bond activation mediated by early actinides	13
J. Balas, C. Urbank, P. Kaden, J. März, R. Gericke	
Fate of oxidation states at actinide centers in redox-active ligand systems governed by energy levels of 5 <i>f</i> orbitals	14
T. Takeyama, S. Tsushima, R. Gericke, P. Kaden, J. März, K. Takao	
Identification of Pu redox species and tracking their formation: application of artificial neural networks on XAS.....	15
A. Rossberg, S. Reinhard	
Investigation of the flexibility of Ln(III) amidinate complexes using multiscale molecular dynamics simulations	16
A. Näder, B. Hong, M. Patzschke	
Spectroscopic and thermodynamic investigations of the NTA–Eu(III) and NTA–Cm(III) systems.....	17
C. Sieber, S. Friedrich, B. Drobot, S. Tsushima, A. Barkleit, K. Schmeide, T. Stumpf, J. Kretzschmar	
Radiation resistance of an ionicotinic acid-based actinide MOF	18
K. Lv, M. Patzschke, J. März, E. F. Bazarkina, K. O. Kvashnina, M. Schmidt	
Tc-99 reduction in carbonate environment: a spectroelectrochemical and NMR study	19
A. Bureika, J. Kretzschmar, K. Müller, N. Mayordomo	
Basis sets in density functional theory – An example of how heavy elements influence workflows.....	20
L. Waurick, M. Patzschke, B. Drobot	
Annihilation of proton transport in confined nanocompartments	21
H. Hao, E. M. Adams, S. Funke, G. Schwaab, M. Havenith, T. Head-Gordon	
Hydrogen transport between layers of transition metal-dichalcogenides.....	22
I. Eren, Y. An, A. Kuc	

Part II: Long-Lived Radionuclides & Transport Phenomena in Geological Systems

Eu(III), Am(III), Th(IV), Pu(IV), and U(VI) retention by C-S-H (C/S 0.8) – Effect of gluconate	25
K. Schmeide, S. Dettmann, N. Huittinen, N. Jahn, J. Kretzschmar, M. U. Kumke, T. Kutyma, J. Lohmann, T. Reich, S. Shams Aldin Azzam, L. Spittler, J. Stietz	
Uptake of Np(V) onto ZrO ₂ : a batch, spectroscopic, and modeling study.....	26
N. Jordan, I. Jessat, H. Foerstendorf, A. Rossberg, A. C. Scheinost, J. Lützenkirchen, K. Heim, T. Stumpf	
Monitoring the sorption of aged U(VI) solutions on zirconia by vibrational spectroscopy	27
H. Foerstendorf, I. Jessat, K. Heim, N. Jordan	

Sorption of Ba(II) onto gibbsite: a batch study	28
V. Dück, N. Jordan, F. Bok	
⁹⁹ Tc interaction with cast iron plates corroded in sterile or pristine Wyoming bentonite	29
K. Kirsch, N. Matschiavelli, N. Mayordomo, A. Cherkouk, D. Schild, T. Stumpf, A. Koerdt	
Sorption of cadmium on alumina nanoparticles and mixtures of alumina nanoparticles and FEBEX smectite	30
N. Mayordomo, T. Missana, U. Alonso	
Structural and spectroscopic characterization of Ca/Sr and Ce co-doped monazites	31
S. Richter, L. B. F. dos Santos, S. E. Gilson, N. Huittinen, T. Lender	
Synthesis and glancing incident XRD investigations of ion irradiated Ce(IV)-doped ZrO ₂ ceramics	32
L. B. F. dos Santos, J. Niessen, V. Svitlyk, S. E. Gilson, J. Marquardt, S. Richter, C. Hennig, N. Huittinen	
Oxidation state and structure of Fe in nontronite under various redox conditions	33
Y. Qian, A. C. Scheinost, S. Grangeon, J.-M. Greneche, A. Hoving, E. Bourhis, N. Maubec, S. V. Churakov, M. Marques Fernandes	
In-situ flow visualization with Geo-Positron-Emission-Tomography in a granite fracture from Soultz-sous-Forets, France.....	34
W. Zhou, J. Kulenkampff, C. Fischer	
Variability of radionuclide sorption efficiency on muscovite cleavage planes	35
J. Schabernack, A. Faria Oliveira, T. Heine, C. Fischer	
Characterization of the contact zone of an MgO-concrete dam with saline host rock	36
J. Kulenkampff	
Cyclotron production of ⁹⁵ Nb and its application for the quantitative description and mechanistic understanding of ⁹⁴ Nb retention in L/ILW repositories.....	37
K. Franke	
Quantitative consideration of heterogeneities in crystalline rocks within geochemical simulations: a modular workflow	38
A. Duckstein, S. Pospiech, V. Brendler	
Sorption Reference Database SOREDA – Sorption of neptunium(V) onto ferrihydrite.....	39
F. Bok, S. Zechel	
Sorption Reference Database SOREDA – A robust model for uranyl sorption onto quartz	40
S. Zechel, F. Bok	
Thermodynamic data of the double salt CsCl·2NaCl·2H ₂ O(cr)	42
F. Bok	

Part III: Long-Lived Radionuclides in Biological Systems

How the radioactive elements Am ³⁺ and Cm ³⁺ interact with Lanthanide-using bacteria.....	45
R. Steudtner, H. Singer, B. Drobot, L. Daumann	
Eu(III) as luminescence probe for microscopy and speciation analyses in <i>Brassica napus</i> plants	46
J. Jessat, H. Moll, W. A. John, M. Vogel, R. Steudtner, B. Drobot, R. Hübner, T. Stumpf, S. Sachs	
Tobacco (<i>Nicotiana tabacum</i>) BY-2 cells induce the intracellular precipitation of metal oxalate biominerals for detoxification of lanthanides	47
M. Klotzsche, M. Vogel, S. Sachs, J. Raff, T. Stumpf, B. Drobot, R. Steudtner	
Uranium toxicity on plant cells: Differentiation between chemotoxic and radiotoxic effects by isothermal microcalorimetry	48
S. Sachs, J. Oertel, K. Fahmy	

Microbial U(VI) reduction by a sulfate-reducing bacterium relevant to nuclear waste disposal	49
S. Hilpmann, A. Rossberg, R. Steudtner, B. Drobot, R. Hübner, F. Bok, D. Prieur, S. Bauters, K. O. Kvashnina, T. Stumpf, A. Cherkouk	
Effectiveness of glycerol for the bio-reduction of U in mine water	50
A. M. Newman-Portela, B. Drobot, R. Steudtner, A. Kassahun, M. L. Merroun, J. Raff, E. Krawczyk-Bärsch	
Dissimilatory iron reduction by <i>Desulfitobacterium</i> sp. G1-2 for ⁹⁹ Tc immobilization	51
I. Cardaio, S. Kluge, K. Müller, A. Cherkouk, N. Mayordomo	
Interaction of U(VI) with kidney cells – Speciation in cell culture medium and cell suspension	52
D. Butscher, C. Senwitz, R. Steudtner, A. Heller, A. Barkleit	
Thermodynamic investigations of a potential decorporation agent for Eu(III)/Cm(III)	53
S. Friedrich, C. Sieber, B. Drobot, S. Tsushima, A. Barkleit, K. Schmeide, T. Stumpf, J. Kretzschmar	
Multi-method coordination study of Eu(III)–HEDP complexation in aqueous solution.....	54
A. Heller, C. Senwitz, H. Foerstendorf, S. Tsushima, L. Holtmann, B. Drobot, J. Kretzschmar	
Macropa’s preference for various metal ions.....	55
B. Drobot, M. K. Blei, L. Waurick, F. Reissig, C. Mamat, J. Kretzschmar	
Superstructure-dependent stability of DNA origami nanostructures in the presence of chaotropic denaturants	56
D. Dornbusch, A. Keller, K. Fahmy	

Part IV: Nuclear Reactor Safety Research

Unraveling the chromium redox chemistry in advanced UO ₂ fuels.....	59
G. L. Murphy, R. Gericke, S. E. Gilson, E. F. Bazarkina, A. Rossberg, P. Kaden, R. Thümmeler, M. Klinkenberg, M. Henkes, P. Kegler, V. Svitlyk, J. Marquardt, T. Lender, C. Hennig, K. O. Kvashnina, N. Huittinen	
Speciation of fission products in oxide and metallic precipitates in nuclear fuel	60
R. Caprani, P. Martin, D. Prieur, J. Martinez, N. Clavier	
Quantum crystallographic study on π -hole interactions of quinoid rings with iodide anions	61
C. Hennig, V. Milašinović, V. Vuković, A. Krawczuk, K. Molčanov, M. Bodensteiner	
High-Energy Resolution Fluorescence Detection mode for EXAFS analysis	62
E. F. Bazarkina	
Molecular oxo-Hydroxo Ce clusters probed by HERFD-XAS at the Ce L ₃ edge	63
P. Estevenon, L. Amidani, T. Dumas, K. O. Kvashnina	
Fracture mechanics characterization of ferritic steels by means of miniaturized specimens	64
M. Sánchez, E. Altstadt, A. Das	
Electron backscatter diffraction (EBSD) applied to detect phase transformation in Ga ₂ O ₃	65
P. Chekhonin, U. Bektas, N. Klingner, G. Hlawacek	
Annealing behavior of a neutron-irradiated VVER-1000 reactor pressure vessel weld.....	66
A. Ulbricht, F. Bergner, E. Altstadt	
Microstructural characterization of reactor pressure vessel steels.....	67
L. Lai, P. Chekhonin, S. Akhmadaliev, J.-E. Brandenburg, F. Bergner	
A “safe-zone” approach to the bulk equivalent hardness of ion-irradiated layers.....	68
J.-E. Brandenburg, F. Bergner	
Comparison of experimental and calculated activities of monitors in near-reactor cavities.....	69
R. Rachamin, J. Konheiser, A. Barkleit	

Radiochemical analysis of activated concrete of Greifswald NPP	70
M. Zilbermann, E. Poenitz, A. Barkleit, J. Konheiser	
Simulation of transient behavior of Superphenix reactor with coupled neutronics/thermal hydraulics	71
A. Ponomarev, E. Nikitin, E. Fridman	
Analysis of boron dilution in the NuScale plant using the system code Athlet and CFD within the McSAFER project on small modular reactors.....	72
A. Grahn, E. Diaz-Pescador	

PUBLICATIONS

○ Articles (peer-reviewed).....	75
○ Further Contributions.....	83
○ Oral Presentations.....	83
○ Theses	89

SCIENTIFIC ACTIVITIES

○ AcE-Methods Workshop	93
○ Workshop of the ALLIANCE Topical Roadmap Working Group NORM.....	94
○ EBSA 2023 – Satellite Meeting 14 th European Biophysics Societies Association (EBSA) Congress 2023	94
○ STRUMAT-LTO – Workshop 2023	95
○ Awards	96
○ Seminars (Talks of Visitors)	96
○ Teaching Activities.....	97

PERSONNEL 99

ACKNOWLEDGEMENTS 105

INDEX OF AUTHORS 109

SCIENTIFIC CONTRIBUTIONS (PART I)

Chemistry

The Chemistry of
**LONG-LIVED
RADIONUCLIDES**

SQUID magnetometry on actinide complexes

R. Gericke, D. Grödler, B. Hong, J. Balas, A. Näder, M. Patzschke, P. Kaden, M. Schmidt

A Superconducting Quantum Interference Device (SQUID) was installed in the controlled area labs and commissioned for use with TRU elements. The device is able to measure temperature-dependent magnetic susceptibility data down to 1.9 K. For paramagnetic compounds, like most actinide complexes, the temperature-dependent magnetic susceptibility can be used to extract information about the over-all magnetism of the bulk, oxidation and spin state of the paramagnetic center, and therefrom ligand field parameters.

EXPERIMENTAL. SQUID measurements were performed in DC-scan mode on a MPMS3 from Quantum Design (San Diego, CA, U.S.A.) in the temperature range from 1.9–300 K at an applied field of 10,000 Oe. Background subtraction was performed with SQUID-Lab.^[1] EPR spectroscopy was carried out on an X-Band CW-EPR spectrometer of the ELEXSYS E500 series (Bruker Biospin, Rheinstetten, Germany) equipped with an Oxford Instruments Mercury iTC He cryostat.

RESULTS. Besides thorium, the fundamental properties of actinide complexes in their oxidation state +4 are influenced by unpaired electrons. In the series Th(IV), U(IV), Np(IV), and Pu(IV) the unpaired electrons are expected to be located in the 5f-shell leading to a configuration of 5f⁰, 5f², 5f³, and 5f⁴, respectively. In the vicinity of the paramagnetic An(IV) center, the influence is visible with Nuclear Magnetic Resonance (NMR) spectroscopy on the signal of the ligand's nuclei, whereby Th(IV) can be used as diamagnetic reference. The qualitative interpretation of the dipolar magnetic interactions can be used to investigate the structure in solution state.

However, quantification of the influence on NMR chemical shifts by the paramagnetism is a challenging task, which we are currently investigating by combining quantum chemical calculations with Electron Paramagnetic Resonance (EPR) spectroscopy and SQUID magnetometry. In general, the total magnetic moment (μ) of a complex is given by:^[2]

$$\mu^2 = g_J^2 J(J+1) \mu_B^2. \quad (1)$$

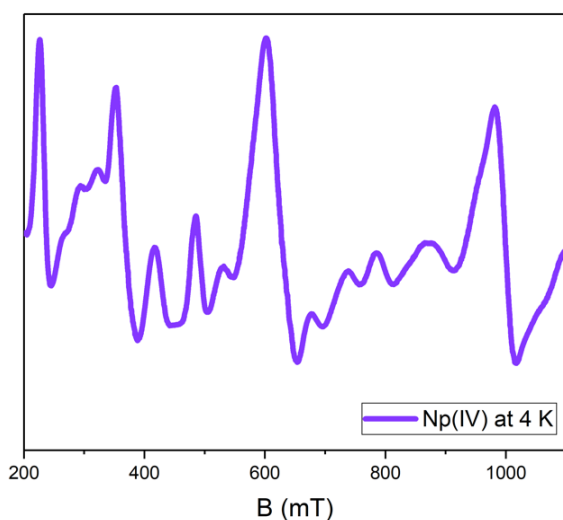


Figure 1. EPR spectrum of a Np(IV) complex in the solid state.

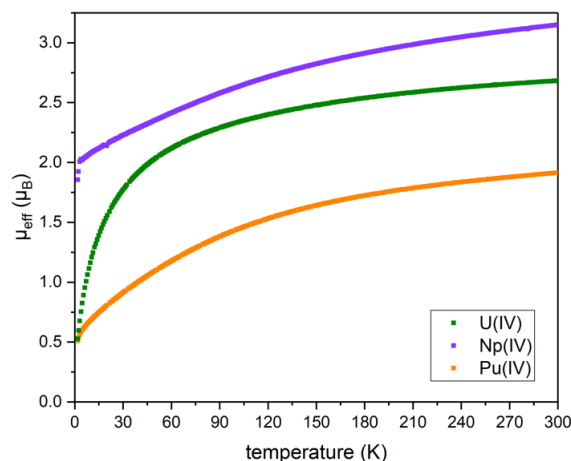


Figure 2. μ_{eff} -T-plot of actinide complexes in the oxidation state +4.

The Landé factor (g_J) can be extracted from EPR spectra measured of Kramer systems, *e. g.*, Np(IV) (Fig. 1).

High-level quantum chemical calculations shed light onto the effective spin at the ground state present in the respective An(IV) complex ($J(J+1)$, eq. 1). However, for description of the electronic situation in An(IV) complexes requires expensive and time-intensive calculations.

The temperature-dependent magnetic trendlines of the An(IV) complexes (Fig. 2) are consistent with those of the corresponding An(IV) oxides, confirming the +4 oxidation state.^[4–6] From these data, μ_{eff} for each complex can be extracted and subsequently used to guide EPR spectra fitting and NMR data interpretation. Ultimately, the combination of these methods will enable better structural characterization, especially in solution, and a deeper understanding of electronic and binding properties of the actinides.

In conclusion, the combination of analytic techniques to investigate magnetic properties of actinide complexes, especially transuranium elements, with SQUID (μ), EPR (g_J), and NMR in one laboratory is unique worldwide. The methods are non-destructive and in combination with quantum chemical calculations are ideally suited to describe the electronic configuration of actinide complexes. Therefrom, we are able to describe bonding trends on the atomic level along the actinide series and shed light into a non-observable: covalency in actinide bonding.

ACKNOWLEDGEMENTS. The MPMS3 was financed by the German Federal Ministry of Education and Research (BMBF) under the project number 02NUK059B (f-Char). This research was funded by the federal ministry for the environment, nature conservation, nuclear safety and consumer protection (BMUV) under the project number 1501667 (Am-BALL).

- [1] Coak, M. J. *et al.* (2020) *Rev. Sci. Instrum.* **91**, 023901.
- [2] Lueken, H. (1999) *Magnetochemie*, B.G. Teubner Verlag, Stuttgart.
- [3] Kögerler, P. (2018) *J. Comput. Chem.* **39**, 2133–2145.
- [4] Yoshimura, T. *et al.* (1974) *B. Chem. Soc. Jpn.* **47**, 515.
- [5] Amoretti, G. *et al.* (1992) *J. Phys. Condens. Matter* **4**, 3459.
- [6] Hudry, D. *et al.* (2014) *Chem. – Eur. J.* **20**, 10431.

Synthesis and characterization of Neptunium(IV) heteroarylalkenolate complexes

D. Grödler, P. Kaden, B. Hong, J. M. Sperling,¹ B. M. Rotermund,¹ N. B. Beck,¹ B. Scheibe,² S. Mathur,³ T. E. Albrecht-Schönzart,¹ R. Gericke

¹Department of Chemistry and Nuclear Science & Engineering Center, Golden, CO, U.S.A.; ²Pacific Northwest National Laboratory, Richland, WA, U.S.A.; ³Department of Chemistry, University of Cologne, Cologne, Germany

Homoleptic Np(IV) heteroarylalkenolate complexes [Np(PyTFP)₄] (1) and [Np(DMOTFP)₄] (2) have been investigated in this study. Both ligands contain a fluorinated alkenolate group attached to an aromatic system. One being a pyridine derivative 1-(pyridin-2-yl)-3,3,3-trifluoroprop-1-en-2-ol (PyTFP) and the other being a methylated oxazole ring 1-(4,5-dimethyloxazol-2-yl)-3,3,3-trifluoroprop-1-en-2-ol (DMOTFP). Systematic studies, such as NMR and SC-XRD analyses, were performed to investigate the influence of the aromatic substituent and differences to earlier tetravalent actinides.

Fluorinated heteroarylalkenolates have been proven to stabilize early actinides and lanthanides in the tetravalent oxidation state. U(IV) and Ce(IV) complexes showed marked air-stability and were used as precursor for chemical vapor deposition for the synthesis of catalytically active nanomaterials.^[1,2] In this contribution this chemistry was extended to Np(IV).

EXPERIMENTAL. Neptunium heteroarylalkenolates (**1**, **2**) were synthesized *via* salt metathesis reactions of one eq. [NpCl₄(DME)₂] and four eq. KPyTFP or KDMOTFP in THF solutions. After the reaction mixtures were stirred for 18h at room temperature, a colorless precipitate was removed *via* centrifugation. The complexes were obtained in good yields (> 80%) after evaporation of all volatiles in an inert glovebox. The crystals were characterized by SC-XRD analysis, mass spectrometry, and NMR spectroscopy after dissolution.

RESULTS. In both complexes (**1**, **2**), the Np(IV) center is coordinated in a square antiprismatic fashion by four of the bidentate ligands (Fig. 1). Complex **1** has mean Np–O and Np–N distances of 2.218(1) Å and 2.671(1) Å, respectively, which are slightly shorter than in the isostructural uranium complex. In solid-state the endogenous CF₃-groups arrange in separated layers along the crystallographic *a*- and *c*-axis due to *van der Waals* forces. The mean Np–O (2.240(2) Å) and Np–N (2.622(1) Å) distances of complex **2** are again slightly shorter than the isostructural uranium complex as expected for contraction along the actinide series.^[1] In general, both complexes show an eightfold coordination of four oxygen and four nitrogen atoms.

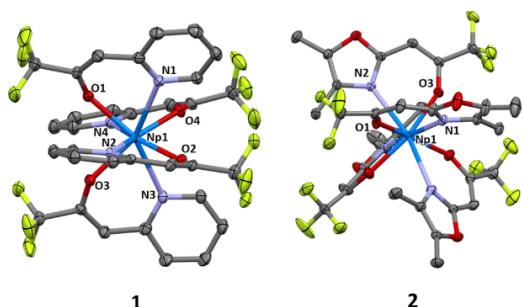


Figure 1. Solid-state molecular structure of [Np(PyTFP)₄] (**1**) and [Np(DMOTFP)₄] (**2**) with thermal ellipsoids drawn at the 50% probability level. Hydrogen atoms are omitted for clarity.

The paramagnetic influence of the 5f³ electrons of Np(IV) was investigated in solution with variable temperature (VT) NMR spectroscopy (Fig. 2). Despite the present paramagnetism, all expected ¹H, ¹³C and ¹⁹F NMR shifts could be found and assigned using 2D NMR experiments. Complex **1** shows one set of broad signals at 13.74 (H-1), 7.65 (H-3), 6.73 (H-2), 5.75 (H-4) and 2.10 ppm (H-6) in the ¹H NMR spectrum at 25 °C, suggesting a symmetric eightfold coordination in THF solutions. At –40 °C the signals sharpen and shift to 12.86 (H-1), 7.94 (H-3), 6.52 (H-2), 5.79 (H-4) and 0.96 ppm (H-6). From the SC-XRD structure and VT-NMR experiments (Fig. 2), the observed minimal changes in the chemical shifts of the pyridine protons across the temperature series indicate that their spatial orientation is close to the magic angle (54.74°) in relation to the magnetic axis. This observation leads to the speculation that the magnetic easy-axis of the complex is likely aligned very closely with its rotational symmetry axis present in solid state. Notably, the carbonyl carbon C-7 is drastically shifted to –10 ppm. Usually, carbonyls are expected to be found at 180–210 ppm, which shows the profound influence of the paramagnetic Np(IV) center. We suggest that this paramagnetic shift is mainly caused by a *Fermi-Contact-Shift* (FCS) contribution, since the carbonyl is directly coordinating to Np(IV).

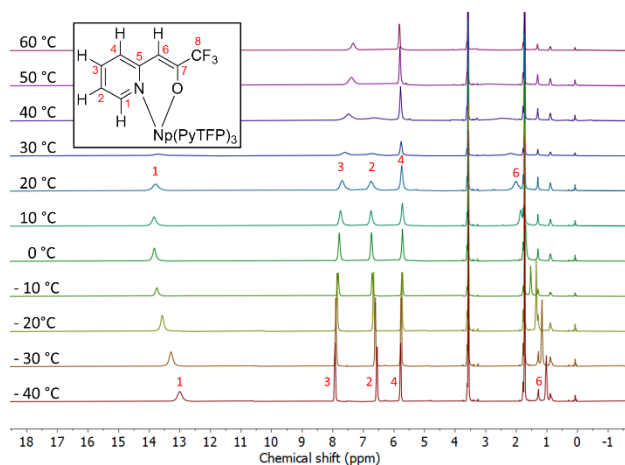


Figure 2. Variable temperature ¹H NMR spectra of complex **1**.

For complex **2** similar paramagnetic shifts have been observed. However, from first results it appears that the magnetic easy-axis aligns in two possible directions compared to complex **1**, probably caused by slight rearrangement of the ligands in solution.

Following work will target a more detailed qualitative discussion of this phenomenon with the help of quantum chemical calculations.

ACKNOWLEDGEMENTS. This research was funded in part by the Federal Ministry for the Environment, Nature Conservation, Nuclear Safety and Consumer Protection (BMUV) under the project number 1501667 (Am-BALL).

[1] Appel, L. *et al.* (2015) *Angew. Chem. Int. Ed.* **54**, 2209–2213.

[2] Leduc, J. *et al.* (2015) *New J. Chem.* **39**, 7571–7574.

C–Cl bond activation mediated by early actinides

J. Balas, C. Urbank,¹ P. Kaden, J. März, R. Gericke

¹Institute of Inorganic Chemistry, University of Göttingen, Germany

During complex syntheses of the tetravalent early actinides (An = Th, U, Np) with pyridine-2-thiolate (PyS[−]) in the non-coordinating solvent dichloromethane (DCM), bis(2-pyridylthio)methane (bptm) was found as an activation product of DCM. The by-product was characterized with single crystal X-ray diffraction (SC-XRD) and nuclear magnetic resonance spectroscopy (NMR). We propose a mechanism for the unusual actinide catalyzed coupling reaction.

In recent years, several examples of the activation of small molecules by actinides, as well as the use of An catalysts, have been published.^[1,2] This includes the coupling reaction between DCM and pyridine described by Baker *et al.* in 2010, which yielded a methylene-bridged bispyridinium cation in the presence of uranyl chloride and KOH.^[3] Of particular interest is the activation of the relatively stable C–Cl bond in DCM, where halide abstraction by the uranyl ion was postulated.^[3] The formation of a similar activation product of DCM has now been observed using PyS[−] ligands along the series of early actinides.

EXPERIMENTAL. All syntheses were carried out under N₂ atmosphere. 2-Mercaptopyridine (PySH) was deprotonated with KH in DCM at −30 °C. The tetravalent An complexes [An^{IV}(PyS)₄] were synthesized *via* salt metathesis reactions by adding a solution of 1 eq. [AnCl₄(dme)_x] (An: Th, Np {x = 2}, U {x = 0}) in DCM to 4 eq. of the potassium salt of PyS[−]. The reaction mixtures were stirred for 24 h at room temperature. After centrifugation, all volatiles were removed in vacuum and the dried solids were dissolved in DCM-d₂ for NMR spectroscopy. Crystals suitable for SC-XRD (colorless needles) were obtained by slow evaporation of DCM/*n*-pentane solutions in the glovebox at room temperature.

RESULTS. In an attempt to synthesize eightfold coordinated actinide complexes of the type [An^{IV}(PyS)₄], [AnCl₄(dme)_x] was reacted with KPyS in the non-coordinating solvent DCM. Each ¹H NMR spectra of the three reaction mixtures show eight signals. Using 2D NMR spectroscopy two respective signal sets could be identified, which corresponds to a putative [An^{IV}(PyS)₄] species and bptm (7.01, 7.16, 7.50, and 8.46 ppm in DCM-d₂).^[4] An estimation of the quantity ratios by evaluating the integral intensities shows that bptm is formed with increasing preference along the series of early An (Th: 0.2 eq, U: 2.5 eq, Np: 5 eq).

In order to determine their molecular structure, the colorless needle-shaped crystals were investigated by single crystal X-ray diffraction. The measurement reveals that these crystals indeed do not contain the desired An^{IV} complexes, but bptm. This by-product consists of two mercaptopyridyl groups, which are bridged to a methyl group *via* the corresponding sulfur atoms and crystallizes in the monoclinic space group *P*2₁/*c* (Fig. 1, top left). The mean bond lengths S–C_{py} (1.769(1) Å) and S–CH₂ (1.804(1) Å) indicate the character of S–C single bonds by comparison with literature data (S–C: 1.82 Å; S=C: 1.62 Å), with a slightly higher bond order for the S–C_{py} bond.^[4,5] The average C–N bond length (1.344(1) Å) in bptm corresponds

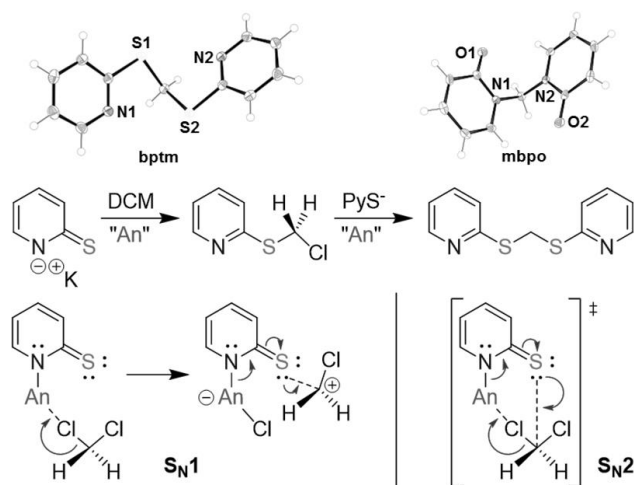


Figure 1. Molecular structures of bptm (top left) and mbpo (top right). Formation of bptm by An-mediated nucleophilic substitution from 2 eq. of KPyS and 1 eq. of DCM (middle). Proposed S_N1 and S_N2 mechanisms (bottom). Charge and ligands of the An, as well as K⁺ are not shown for clarity.

to the length known from the literature for aromatic C–N bonds in pyridine (1.34 Å).^[6] The structural parameters are in excellent agreement with previously published molecular structures of bptm.^[4,5]

A possible mechanism for the reaction is given in Fig. 1. We suggest a nucleophilic substitution mediated by the actinide centers. After coordination of PyS[−] to An to form *e.g.*, [An^{IV}(PyS)₄] leads to a coordinately unsaturated actinide center, An–Cl interactions are possible which could lead to a polarization of the C–Cl bond in DCM.^[3] The proximity of a nucleophilic sulfur atom and an electrophilic carbon atom from DCM are suitable for S–C bond formation. The softer sulfur atom is a good leaving group on the actinide side in favor of An–Cl bond formation. Further experimental data are required to distinguish between S_N1 (heterolytic halide abstraction and bond formation at the carbocation) and S_N2 (ring-shaped transition state) mechanisms (Fig. 1, bottom).^[7]

In previous work, we described the formation of 1,1'-methylenebis(pyridine-2-one) (mbpo, Fig. 1, top right) as an activation product of DCM in the complex syntheses of tetravalent An (Th, U) with pyridine-2-olate (PyO[−]). Here, the bond formation occurs at the N donor atom of the ligand.^[8] Thus, the softer donor atoms of the ambident ligands PyS[−] and PyO[−] are consistently the leaving group on the An side, underpinning the proposed mechanism. The examples of bptm and mbpo show the great potential of electron-rich An for C–Cl bond activation. The versatile reactivity could be used for catalysts for which there are no analogs in the transition metals.

[1] Pividori, D. *et al.* (2021) *Inorg. Chem.* **60**, 16455–16465.

[2] Liddle, S. T. (2015) *Angew. Chem. Int. Ed.* **54**, 8604–8641.

[3] Baker, R. J. *et al.* (2010) *Z. Anorg. Allg. Chem.* **636**, 443–445.

[4] de Castro, V. D. *et al.* (2002) *J. Mol. Struct.* **609**, 199–203.

[5] Amodo-Portela, A. *et al.* (2002) *Z. Anorg. Allg. Chem.* **628**, 939–950.

[6] Herzberg, G. (1966) in: *Electronic spectra and electronic structure of polyatomic molecules*, Van Nostrand, New York.

[7] Brückner, H. (2011) in: *Reaktionsmechanismen*, Spektrum, Berlin.

[8] Urbank, C. (2021) Master thesis, TU Dresden.

Fate of oxidation states at actinide centers in redox-active ligand systems governed by energy levels of 5f orbitals

T. Takeyama,^{1,2} S. Tsushima, R. Gericke, P. Kaden, J. März, K. Takao¹

¹Tokyo Institute of Technology, Tokyo, Japan; ²Sanyo-Onoda City University, Yamaguchi, Japan

While the interaction of Np(VI)O_2^{2+} with the redox-active ligand $\text{H}_2(\text{tBu-pdiop})$ (2,6-bis[*N*-(3,5-di-*tert*-butyl-2-hydroxyphenyl)iminomethyl]pyridine) leads to the direct reduction of Np(VI)O_2^{2+} to Np(IV) , the complexation of U(VI)O_2^{2+} with $\text{H}_2(\text{tBu-pdiop})$ does not induce a reduction. This difference can be explained by the decrease of the energy of the 5f orbitals in Np compared to those in U.

Both U and Np exist in a range of oxidation states ranging from I to VI for U and up to VII for Np. The higher oxidation states are most commonly present as the respective -yl ions. Ligand coordination has a significant impact on the redox chemistry of these elements. Multidentate ligands are known to promote the reduction from high valent actinide ions to the tetravalent state.^[1,2] In general, the coordination behavior of U(VI)O_2^{2+} and Np(VI)O_2^{2+} is considered to be similar.^[3,4] However, there are two critical differences: the complexes have different f^n configurations at the metal center (f^1 configuration for Np(VI)O_2^{2+} and f^0 configuration for U(VI)O_2^{2+}) and Np complexes have more contracted 5f orbitals with lower energy compared to the respective U complexes.

RESULTS. Reacting one equivalent of uranyl nitrate (An = U, Np) with $\text{H}_2(\text{tBu-pdiop})$ results in the formation of a 1:1 complex of uranyl with $(\text{tBu-pdiop})^{2-}$ acting as pentadentate chelating ligand. The same reaction using neptunyl nitrate, however, results in a reduction of neptunyl to form a complex of the type $[\text{Np(IV)}(\text{tBu-pdiop})(\text{NO}_3)_2(\text{Py})_x]$ in good yield (65%). Characterization of the resulting complexes have been conducted by SC-XRD in solid state and UV-vis, IR, and NMR spectroscopy in solution. Speculating about the identity of the reducing agent, the reaction was conducted both under ambient conditions as well as under an N_2 atmosphere. Even substituting ethanol or pyridine as solvents had no effect on the apparent reduction of the Np center. Sophisticated quantum chemical calculations involving CASSCF and NEVPT2 confirm the f^3 configuration at the Np center and allow attributing strong bands in the UV-vis spectra between 300–600 nm to ligand-to-metal charge transfer (LMCT), metal-to-ligand charge transfer (MLCT), and π - π^* transitions of $(\text{tBu-pdiop})^{2-}$. In addition, transitions between 700–1,000 nm could be identified as f - f transitions from the f^3 electron configuration of Np in these CASSCF/NEVPT2 calculations.

These findings are in sharp contrast to reactions of uranyl under similar conditions, where only uranyl complexes with the pentadentate chelating ligand could be isolated.^[5] Further studies concentrated on the electrochemistry of the ligand compared to the resulting Np(IV) complex. Both exhibited irreversible oxidation in the anodic scan, thus implying that the reaction occurs at $(\text{tBu-pdiop})^{2-}$. No electrochemical response was observed, that could be attributed to a potential $\text{Np}^{\text{IV/V}}$ couple that should occur at the higher end of the observed -2.0 to +2.0 V potential range. It is thus concluded, that $\text{H}_2(\text{tBu-pdiop})$ is reactive enough to reduce neptunyl and stabilize the resulting Np^{IV} complex.

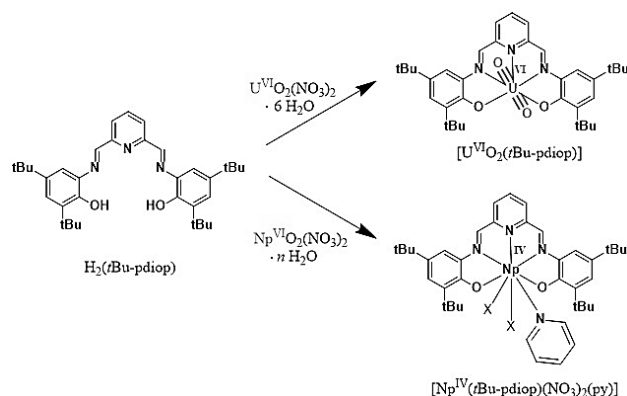


Figure 1. Reactions between $\text{An}^{\text{VI}}\text{O}_2(\text{NO}_3)_2 \cdot n\text{H}_2\text{O}$ (An = U, Np) and the redox active ligand $\text{H}_2(\text{tBu-pdiop})$ yield the respective complexes, however, with Np being reduced to Np(IV) .^[6]

CONCLUSION. Addition of $\text{H}_2(\text{tBu-pdiop})$ to a solution of $\text{Np}^{\text{VI}}\text{O}_2^{2+}$ is shown to lead to the reduction of $\text{Np}^{\text{VI}}\text{O}_2^{2+}$ to Np^{IV} , and to the formation of $[\text{Np}^{\text{IV}}(\text{tBu-pdiop})(\text{NO}_3)_2(\text{py})]$. This is in contrast to corresponding reactions of $\text{U}^{\text{VI}}\text{O}_2^{2+}$ where even after its electrochemical two-electron reduction no such respective species could be identified. The difference in redox behavior between the U and Np systems stems most probably from subtle changes in the energy levels of the 5f orbitals that lie close to the π or π^* orbitals of $(\text{tBu-pdiop})^{2-}$. The direct reduction of $\text{Np}^{\text{VI}}\text{O}_2^{2+}$ to Np^{IV} may thus be facilitated by an electron transfer from $(\text{tBu-pdiop})^{2-}$ to $\text{Np}^{\text{VI}}\text{O}_2^{2+}$.^[6] Studies of the mechanistic aspects of the observed reduction are currently under way while further exploring the redox chemistry of Np complexes with redox-active ligands.

[1] Carter, K. P. *et al.* (2021) *Inorg. Chem.* **60**, 973–981.

[2] Carter, K. P. *et al.* (2020) *Chem. Eur. J.* **26**, 2354–2359.

[3] Chiorescu, I. *et al.* (2023) *Inorg. Chem.* **62**, 830–840.

[4] Autillo, M. *et al.* (2019) *Inorg. Chem.* **58**, 3203–3210.

[5] Takeyama, T. *et al.* (2023) *Inorg. Chem. Front.* **10**, 4028–4044.

[6] Takeyama, T. *et al.* (2023) *Chem. Eur. J.* **29**, e2023027.

Identification of Pu redox species and tracking their formation: application of artificial neural networks on XAS

A. Rossberg, S. Reinhard¹

¹Institute of Radioecology and Radiation Protection, Gottfried Wilhelm Leibniz Universität, Hannover, Germany

As more physico-chemical parameters (Y) influence the fate of a chemical system, the functional dependencies become more complex, making predictions about the formation of possible chemical species challenging. However, given that the spectra of the species are different and when measuring a set of spectra (X) in dependence of Y , the functional relationship $X = F(Y)$ can be learned by using machine learning methods like counter propagation XY self-organizing maps (XY-SOM).^[1-3] SOMs are biological inspired artificial neural networks that enable the breakdown of the high dimensional input space, as given by X and Y , into a 2-dimensional (2D) space. This feature eases the interpretation of the relationships between the spectral shape of X and the parameters Y .^[4] Furthermore, after training, unknown X can be predicted from a set of Y , and *vice versa*.

EXPERIMENTAL. Ten aqueous Pu samples were prepared in dependence of six Y : [Pu] = 1.05–2.30 mmol L⁻¹ (1), HCl (2) or HNO₃ (3) or HClO₄ (4) with 0.66 or 1.00 mol L⁻¹, pH 1.9–12.4 (5) while some samples were prepared electrochemically (6). The Pu L₃-edge spectra of the samples were measured under cryogenic conditions (15K) by using an 18-element Ge detector at ROBL. By using ITFA, we were able to detect four coexisting Pu species.^[5] Ten prototype vectors (1–10), each containing the measured EXAFS spectrum, the corresponding six Y values and random numbers for the a-priori unknown fractions of the four Pu species, were constructed. Furthermore, four empty vectors (11–14) with the same dimensions as the prototypes were configured. X was trained in dependence of Y using an XY-SOM with 20 × 20 neurons, while each neuron contained a vector in the same dimension as the prototypes.

RESULTS. After training, four clusters emerged, which correspond to the fractions of the forming Pu species (Fig. 1, top right). The vectors 11–14, now filled with the SOM predicted X (Fig. 1, top left) and Y (Fig. 1, lower part) of the pure Pu species, match the neurons at the centers of the clusters at the corners of the map since they contain the most distinct X . Correspondingly, all other prototype vectors (1–10) match neurons within the area spanned by the cluster centers. Since the neurons in between contain non-linearly interpolated X , Y and species fractions, the relationships between X and Y can be inspected by comparing the 2D distributions of the Y with the fractional distribution of the Pu species (Fig. 1). EXAFS shell fit analysis revealed that Pu species contain aqueous Pu(IV)-hydrate (14), Pu(VI)-hydroxide (PuO₂(OH)₄²⁻) (12), and two Pu(IV)-colloids with different particle sizes (11, 13). For instance, Pu(IV)-hydrate is formed at low pH, low [Pu] and preferably in HCl medium, while Pu(VI)-hydroxide prevails at high pH, high [Pu] and preferably in HClO₄ medium. If the HClO₄ medium is exchanged by HNO₃, a Pu(IV)-colloid with large particle size is formed at high pH, moderate and high [Pu], while the small particle sized Pu(IV)-colloid exists at low pH, low and moderate [Pu] in HCl or HNO₃ medium, respectively.

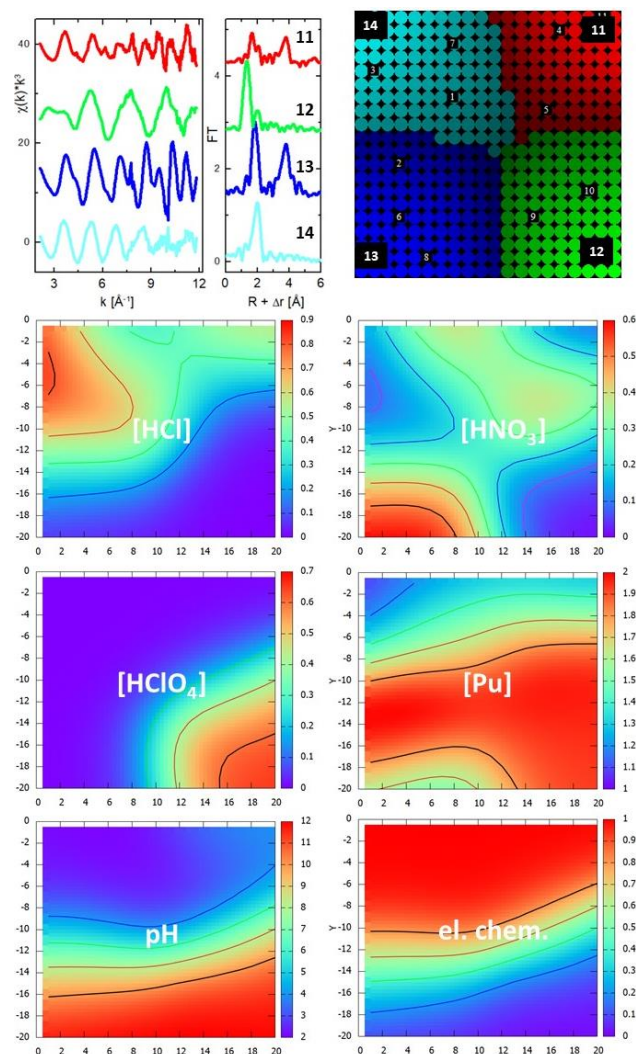


Figure 1. SOM isolated spectra (X) of Pu species (top left), colours correspond to their clustered fractional 2D distribution (top right) while each point represents one neuron (bright colours corresponds to high fractions). 2D Y -distributions of acid (mol L⁻¹) and Pu concentration (mmol L⁻¹), pH and electrochemical treatment (1–treatment, 0–no treatment).

The trained SOM can be used as a look up table. For a given set of physico-chemical parameters Y , a neuron can be found that best matches the Y . This neuron contains an X for which $X = F(Y)$, so that X represents an a-priori unknown spectrum predicted for the selected Y . *Vice versa*, from a measured spectrum X the corresponding a-priori unknown physico-chemical parameters Y can be predicted by finding the neuron that best matches the supplied X . This study demonstrate that SOMs can facilitate the analysis of high dimensional data spaces by breaking them down into a 2D visualization. Furthermore, SOMs reveal functional relationships between measured data and physicochemical parameters, enabling predictions.

- [1] Kuzmanovski, I. et al. (2008) *Chemometr. Intell. Lab. Systems* **90**, 84–91.
- [2] Domaschke, K. et al. (2014) *ESANN Proceedings*, 277–282.
- [3] Schmeide, K. et al. (2021) *Sci. Total Environ.* **770**, 145334.
- [4] Kohonen, T. (1982) *Biol. Cybern.* **43**, 59–69.
- [5] Rossberg, A. et al. (2003) *Anal. Bioanal. Chem.* **376**, 631–638.

Investigation of the flexibility of Ln(III) amidinate complexes using multiscale molecular dynamics simulations

A. Näder, B. Hong, M. Patzschke

Investigating coordination complexes with ligands of great sterical complexity and higher degrees of freedom, it is beneficial to look at the flexibility of the whole molecule in solution in order to understand dynamic properties usually not deducible from crystal structures or optimized geometries. Herein, the investigation of micro-solvated $[\text{Ln}^{\text{III}}(i\text{Pr}_2\text{BA})_3]$ (BA = benzene amidinate; Ln = Nd, Yb) complexes using multiscale molecular dynamics (MD) simulations is presented, offering insights into energetically low-lying and statistically significant conformations and linking their relevance to experimental (paramagnetic) NMR results.

COMPUTATIONAL METHODS. The Ln(III) complexes in solution were placed within a sphere of 80 toluene molecules fully surrounding the complex with two to three layers of the solvent. To prevent the molecules from escaping the aggregate due to high kinetic energy, an outer spherical potential (logfermi) was used. Having ensembles of this many compounds, molecular dynamics simulations can be very computationally demanding, even when using semi-empirical methods like GFN2-xTB.^[1] For this reason a hybrid quantum mechanics/molecular mechanics (QM/MM) approach was applied, combining different levels of theory: in this particular case semi-empirical (GFN2-xTB) and molecular mechanics (GFN-FF).^[2] The former was used for the more challenging lanthanide complex with partly covalent coordinative bonds, while the solvent molecules mainly defined by non-covalent interactions underwent force field treatment. Since, in the investigated amidinate complexes especially rotational processes of smaller subgroups of the ligands are of interest, the time range for the MD simulations had to be set to at least 100 ps to obtain representative statistics. Furthermore, within the setting of this micro-solvation environment, the program temperature does not reflect the real temperature missing macroscopic effects and usually tends to be much lower, justifying the usage of higher temperatures for most of the simulations.

RESULTS. Early evaluations of trajectories have shown significant rotational movement for the *i*Pr-groups (Fig. 1) and in combination with pNMR results – revealing the collapse of two distinct methyl ¹H peaks for each *i*Pr-group within one ligand at a characteristic coalescence temperature (T_c) – hinted at the T-dependence of this rota-

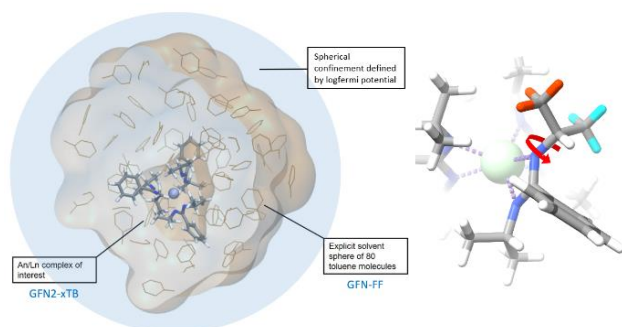


Figure 1. Setting for the multiscale MD simulation of the amidinate complexes in a solvent sphere (left) and a close up of the coordinated ligand with indicated rotation and distinct methyl groups (right).

tion. In case of a hindered rotation of the *i*Pr groups, the splitting of the ¹H-NMR signals is thought to be induced by a specific orientation of the ligand within the PCS (Pseudo Contact Shift) field of the paramagnetic metal center. Analyzing the rotation through dihedral angles over different temperatures, the characteristic temperature (although through a relative observation), which is needed to overcome the rotational barrier, could be demonstrated for Nd and Yb representatives using molecular dynamics (Fig. 2). The diagrams show an expanding and increasingly more diffuse distribution of states for rising temperatures beyond H–C–N–C-dihedral angles of 60° for both the Nd and Yb complexes. But only for Nd a flip to 180° is detected at a program temperature of 603 K. This agrees with the experimentally determined T_c value for Nd being significantly lower than for Yb (253 K vs. > 358 K).

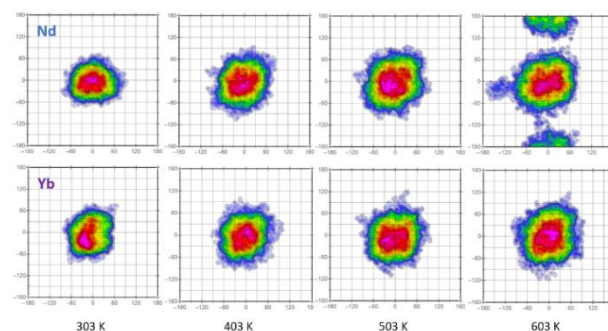


Figure 2. Temperature series of dihedral distribution functions of both *i*Pr-groups (each axis represents one group) from –180° to 180° within one ligand of the Nd and Yb complexes; analyzed with TRAVIS.^[3]

Furthermore, the obtained trajectory allowed for the evaluation of averaged, “true” Ln–N bond lengths of the complex in solution. Figure 3 shows the fluctuation of said bond over a time range of 100 ps (20,000 frames) for the Nd complex for 303 K and 403 K. The average value for the 303 K MD run was evaluated to be 0.82 % higher than the theoretical value and 0.74 % higher than the experimental crystallographic value. This discrepancy can be explained through the thermally induced movement of the ligands and the absence of packing effects.

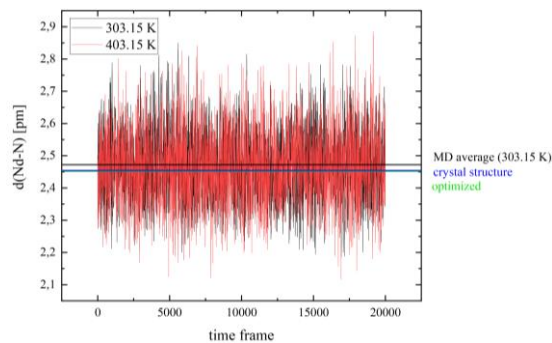


Figure 3. Varying Nd–N bond length over a time range of 100 ps for 303.15 K and 403.15 K. Average values and experimental as well as theoretical values for comparison are visualized as horizontal lines.

- [1] Bannwarth, C. et al. (2019) *J. Chem. Theory Comput.* **15**, 1652–1671.
- [2] Spicher, S. et al. (2020) *Angew. Chem. Int. Ed.* **59**, 5665–5673.
- [3] Brehm, M. et al. (2020) *J. Chem. Phys.* **152**, 164105.

Spectroscopic and thermodynamic investigations of the NTA-Eu(III) and NTA-Cm(III) systems

C. Sieber, S. Friedrich, B. Drobot, S. Tsushima, A. Barkleit, K. Schmeide, T. Stumpf, J. Kretzschmar

The complex formation of Eu(III) and Cm(III) with nitrilotriacetic acid (NTA) has been studied with the help of nuclear magnetic resonance (NMR) spectroscopy, time-resolved laser-induced fluorescence spectroscopy (TRLFS) and isothermal titration calorimetry (ITC), allowing for determination of molecular structures and thermodynamic data.^[1]

NTA is a commonly used complexone for various metal ions. Important applications include the use as a decontamination agent utilized during decommissioning of nuclear power plants. Consequently greater amounts of such complexones may be co-disposed with radioactive wastes. In a worst-case scenario, ground water may intrude into the repository and the complexones could alter radionuclide retention. Thus, a good understanding of their complexation behavior is required.

EXPERIMENTAL. Solutions containing Eu(III) or Cm(III) and NTA were measured with TRLFS, NMR spectroscopy and ITC. For Eu(III) TRLFS experiments, solutions contained 10 μM EuCl_3 and 0–112.5 mM NTA at pH 6. For Cm(III) TRLFS experiments, solutions contained 0.3 μM $\text{Cm}(\text{ClO}_4)_3$ and 0–450 μM NTA at pH 5. NMR spectroscopy measurements used 1 mM solutions of NTA in H_2O with 10% D_2O . For ITC, the syringe was loaded with 10 μM EuCl_3 and the cell with 90 μM NTA.

RESULTS. $\text{p}K_a$ values are easily obtained by NMR spectroscopy (see Fig. 1). The method also provides structural information from the ligand's perspective. $\log \beta$, ΔH , ΔS and ΔG were determined (cf. Tabs. 1 and 2).

Table 1. $\log \beta$ values of various NTA complexes of Eu(III) and Cm(III) determined in the present work^[1] in comparison to literature data.

Species	$\log \beta^{\text{a,b}}$	$\log \beta^{\text{a,c}}$	Lit.
$\text{Eu}^{3+} + \text{NTA}^{3-} \rightarrow \text{Eu}(\text{NTA})_{\text{aq}}^0$	13.4 ± 0.1	13.3 ± 0.1	13.23 ^{b[4]}
$\text{Eu}^{3+} + 2 \text{NTA}^{3-} \rightarrow \text{Eu}(\text{NTA})_2^{3-}$	22.4 ± 0.1	22.1 ± 0.2	20.42 ^[2]
$\text{Cm}^{3+} + \text{NTA}^{3-} \rightarrow \text{Cm}(\text{NTA})_{\text{aq}}^0$	12.90 ± 0.03	—	11.00 ^[2]
$\text{Cm}^{3+} + 2 \text{NTA}^{3-} \rightarrow \text{Cm}(\text{NTA})_2^{3-}$	21.40 ± 0.03	—	20.13 ^[2]

^aMeasured in 0.1 M NaCl, *I* extrapolated to zero ionic strength. Errors are standard deviation of at least three independent experiments. ^bTRLFS. ^cITC. SIT coefficients used for calculations were 0.26 ± 0.01 for Eu(III) in NaCl.^[5] For Cm(III) no data were available, hence Am(III) in NaCl (0.23 ± 0.02) was used as an analogue.^[6]

Table 2. Thermodynamic data for Eu(III) complexation by NTA, obtained from isothermal titration calorimetry at 25 °C in aqueous solutions containing 0.1 M NaCl, in comparison to literature data.^[1]

	$\text{Eu}(\text{NTA})_{\text{aq}}^0$	$\text{Eu}(\text{NTA})_{\text{aq}}^0$ ^[5]	$\text{Eu}(\text{NTA})_2^{3-}$
ΔH (kJ mol ⁻¹)	25.2 ± 1.9	7.5 ± 1.7	$-(36.6 \pm 3.6)$
ΔS (J mol ⁻¹ K ⁻¹)	304 ± 4	188 ± 6	44 ± 13
ΔG^{298} (kJ mol ⁻¹)	$-(65 \pm 0.3)$	63.6 ± 0.3	$-(50 \pm 0.5)$

Figure 1 shows the TRLFS single component spectra of Eu(III)- and Cm(III)-NTA solutions, extracted with PARAFAC, as previously described.^[7] Eu(III) and Cm(III) show similar complexation behavior with NTA. Both form a 1:1 and a 1:2 metal:NTA complex which show similar $\log \beta$ values. This makes Eu(III) an excellent analogue for

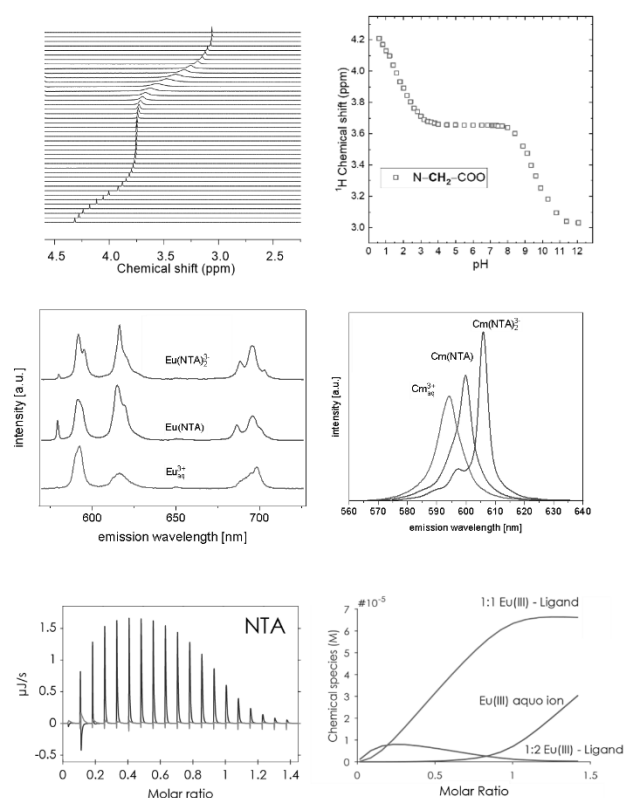


Figure 1. ¹H NMR pH-titration spectra of NTA (top left; pH increasing from bottom to top) and corresponding chemical shift data (top right). Single-component spectra extracted by PARAFAC from Eu and Cm TRLFS measurements (middle row). Eu(III) ITC thermogram (bottom left) and species distribution (bottom right).^[1]

Cm(III) in this system since it has nonradioactive isotopes and is thus easier to handle.

ITC observes reaction heat for both complex formations as well as the deprotonation of the ligand (NTA). The latter has been found to have little impact on the reaction heat and was not considered in our calculations. The results show entropy-driven formation of the $\text{Eu}(\text{NTA})_{\text{aq}}^0$ complex and enthalpy-driven formation of the $\text{Eu}(\text{NTA})_2^{3-}$ complex. The most probable explanation is the high impact of lanthanide (de-)hydration on the reaction for the first complex which is diminished for the second complex, since the hydration shell is already broken.

ACKNOWLEDGEMENTS. This research was supported by the German Federal Ministry for the Environment, Nature Conservation, Nuclear Safety and Consumer Protection (BMUV) under project number 02E11860B within the GRaZ II project.

- [1] Friedrich, S. *et al.* (2023) *Molecules* **28**, 4881.
- [2] Starý, J. (1966) *Talanta* **13**, 421–437.
- [3] Rizkalla, E. *et al.* (1989) *Inorg. Chem.* **28**, 909–911.
- [4] Choppin, G. *et al.* (1987) *Inorg. Chem.* **26**, 2318–2320.
- [5] Jordan, N. *et al.* (2022) *Coord. Chem. Rev.* **473**, 214608.
- [6] Grenthe, I. *et al.* (2020) OECD Publications: Boulogne-Billancourt, France, Volume 14.
- [7] Drobot, B. *et al.* (2015) *Chem. Sci.* **6**, 964–972.

Radiation resistance of an isonicotinic acid-based actinide MOF

K. Lv,¹ M. Patzschke, J. März, E. F. Bazarkina, K. O. Kvashnina, M. Schmidt

¹Institute of Nuclear Physics and Chemistry, China Academy of Engineering Physics, Mianyang, Sichuan, China

We have synthesized a metal-organic framework (MOF) based on isonicotinic acid (INA) and Th(IV) hexamers. The MOF selectively crystallizes from solutions containing a wide range of elements potentially found in spent nuclear fuel and remains intact upon irradiation with very high doses of up to 6 MGy β - and γ -radiation. These results indicate actinide MOFs may become viable waste forms in the future.^[1]

Actinide MOFs hold promise as future waste forms for specific nuclear wastes, because of multiple useful properties: they can be produced at low temperatures (< 200 °C), may contain large amounts of actinides (up to 60 wt.-%) and their 3D structure stabilizes them against radiation damage. Most importantly, their pore spaces can be tuned to accommodate a wide range of otherwise mobile fission products, such as Tc or I. Here, we assess the general feasibility of this approach by synthesizing a Th-based MOF Th-INA-1 from complex solution compositions and testing its radiation stability.

EXPERIMENTAL. Th(NO₃)₄·5H₂O (0.02841 g, 0.05 mmol), INA (0.01853 g, 0.15 mmol), and HCl (30–50 μ L) were dissolved in 2.0 mL DMF and 0.5 mL EtOH in a 15 mL capped vial, sonicated for five minutes and heated at 120 °C in DrySyn Parallel Synthesis Kit for three days. Single crystals emerged two days after the reaction started. It can be prepared by adopting alternative thorium precursors, or in the presence of co-existing ions using a specific amount of proton modulators. Syntheses were carried out in the presence of Cs⁺, Ba²⁺, Mn²⁺, Fe²⁺, Fe³⁺, Co²⁺, Ni²⁺, Cu²⁺, Pd²⁺, ReO₄⁻, La³⁺, Ce³⁺, Ce⁴⁺, and UO₂²⁺. In all cases Th-INA-1 was obtained, with the exception of Ni²⁺ and Co²⁺, which form bimetallic MOFs.

RESULTS. The 3D structure of Th-INA-1 was determined by SC-XRD and was found to contain two distinct hexanuclear Th moieties. Th₆^a contains 16 INA molecules [Th₆(μ_3 -O)₄(μ_3 -OH)₄(INA⁻)₂(INA)₄(HINA)₁₀(H₂O)(DMF)] and is linked to four other Th₆^a as well as two Th₆^b [Th₆(μ_3 -O)₈(INA⁻)₈(COO⁻)₄(H₂O)₆], which are themselves linked to eight Th₆^a (Fig. 1). The 6-/8-connectivity and the large number of coordination ligands yields a tightly-packed 3D framework with a solvent accessible void of only 6.9% and a BET surface area of 1.77 m².

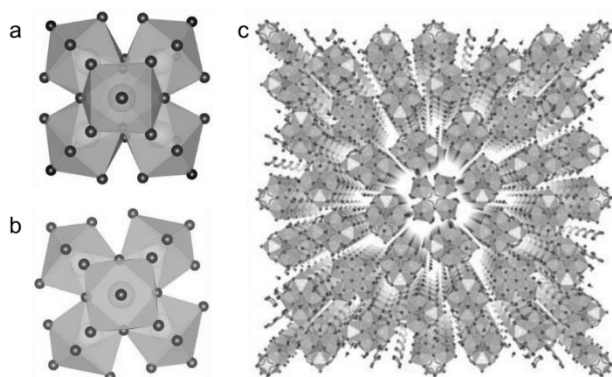


Figure 1. Th₆^a (a), Th₆^b (b), and 3D structure of Th-INA-1 (c).

The high number of 16 ligands binding to a single Th hexamer has not been previously observed and we speculated that this structural arrangement would lend itself to a high stability towards radiative and thermal damage. To test this hypothesis, Th-INA-1 was exposed to increasing doses of β - and γ -radiation from a ⁶⁰Co source while its stability was monitored by SEM, PXRD, and Raman spectroscopy (Fig. 2). We observe a decrease in the signal-to-noise ratio in PXRD, as well as the occurrence of an amorphous contribution starting at 3 MGy, which goes along with minor peak broadening in the Raman spectra. Nonetheless, the long and short range order of Th-INA-1 remain largely unchanged up to a dose of 6 MGy and even at 12 MGy a significant portion of the MOF remains stable. These are the highest doses reported so far that any MOF can tolerate.^[2]

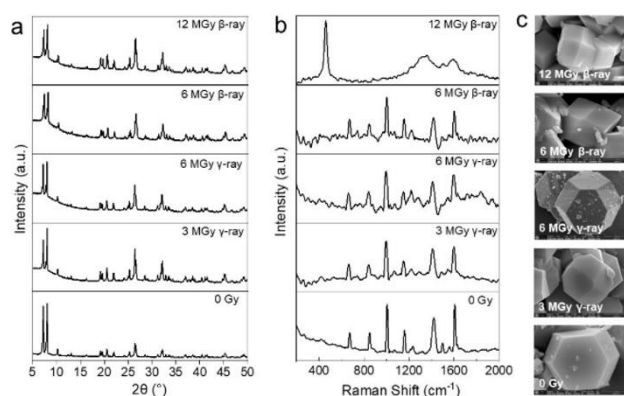


Figure 2. PXRD pattern (a), Raman spectra (b), and particle morphologies of the pristine sample and specimens that are irradiated with a total dosage of 0, 3, 6, and 12 MGy (c, from below to top).

The thermal stability of the material was evaluated by Thermogravimetric analysis with differential scanning calorimetry. The material loses some of its solvent content (DMF, H₂O) at temperatures below 200 °C, and the organic components begin to decompose at ~240 °C. Full transformation into crystalline ThO₂ is observed only at > 500 °C. In summary, we have expanded our yet limited knowledge of actinide MOF structures^[3] through the syntheses of Th-INA-1 (and Th-Ni-INA as well as Th-Co-INA). The straightforward synthesis of Th-INA-1 from complex media under benign conditions in combination with its remarkable radiation resistance demonstrates that actinide MOFs may become a viable option as tailor-made waste forms for problematic fission and activation products in the foreseeable future.

ACKNOWLEDGEMENTS. K.Lv acknowledges support from the President Fund of CAEP (Grant No. YZJLX2019003) and the National Natural Science Foundation of China (No. 21976166).

- [1] Lv, K. *et al.* (2023) *ACS Materials Lett.* **5**, 536–542.
- [2] Pei, J. *et al.* (2022) *J. Am. Chem. Soc.* **144**, 3200–3209.
- [3] Lv, K. *et al.* (2021) *Coord. Chem. Rev.* **446**, 214011.

Tc-99 reduction in carbonate environment: a spectroelectrochemical and NMR study

A. Bureika, J. Kretzschmar, K. Müller, N. Mayordomo

The reduction of technetium (Tc) from Tc^{VII} to Tc^{IV} in carbonate solutions at alkaline pH has been studied as a function of carbonate concentration by spectroelectrochemical methods, electrochemical analysis, and ⁹⁹Tc-NMR spectroscopy. The body of evidences suggests reduction of Tc^{VII} comprises formation of solid Tc^{IV} dioxide along with carbonate complexes of Tc^{IV} and Tc^{III} that are in equilibrium with Tc^V.

⁹⁹Tc is a high-yield long-lived ($\tau_{1/2} \sim 2.14 \times 10^5$ a) fission product of ²³⁵U and ²³⁹Pu. Tc migration in ground water is highly dependent on its oxidation state. Under oxidizing conditions it prevails as highly mobile, water soluble Tc^{VII}O₄⁻. Nevertheless, Tc mobility is limited when reduced to low soluble Tc^{IV}, forming Tc^{IV}O₂^[1] or Tc^{IV} immobilized on mineral surfaces.^[2–4] However, in carbonate medium and sufficiently reducing conditions, soluble carbonate complexes of Tc^{IV} and Tc^{III} are formed.^[5–6] Thus, the study of technetium speciation in carbonate medium has clear importance from a fundamental chemical point of view as well as environmental relevance, *e.g.*, for the long-term safety management of nuclear waste in deep geological repositories.

EXPERIMENTAL. Degassed solutions of 0.5 mM K₂TcO₄ in carbonate medium were analysed. Solutions pH is given by the carbonate/hydrogencarbonate ratio.

Tc^{VII} electrochemical reduction was monitored in parallel by UV-vis spectroscopy in a N₂-filled glovebox (Autolab PGSTAT 101 potentiostat, Metrohm; AvaLight-DH-S-BAL light source and AvaSpec-ULS2048 detector, Avantes).

A glassy carbon rod was the working electrode, a platinum coil in a glass frit-separated blank solution-filled compartment was the counter electrode, and a Ag/AgCl/(3M KCl) electrode was utilized as reference. Aliquots were taken at the beginning and the end of experiments to measure Tc total concentration by liquid scintillation counting (LSC) at HIDEX 600 SL. Solutions of electrochemically reduced Tc were also analyzed by ⁹⁹Tc-NMR (Agilent DD2-600 NMR system, 14.1 T) at 135.4 MHz operating frequency. Additionally, cyclic voltammetry was performed in a wide range of scan rates (5 to 200 mV s⁻¹) in stationary as well as in rotational (100 to 2,500 rpm) modes (884 Professional VA instrument, Metrohm) in [-1.0; +1.1] V potential window.

RESULTS. Figure 1 shows the electroreduction potential (top) through the course of the experiment applying -100 μA cathodic current as well as corresponding UV-vis absorption spectra (bottom). The charge transfer bands at 248 and 287 nm, characteristic of TcO₄⁻, are replaced by intense bands with maxima below 240 nm. The reduced species also display weaker bands in the visible light range which are responsible for the color of the solutions. These are located at 514 nm for Tc^{IV} and 630 nm for Tc^{III}. Electrochemical analysis indicates Tc^{VII} reduction to solid Tc^{IV} dioxide at -0.60 V followed by equilibrium conversion to soluble Tc^{IV} carbonate. Further reduction at -0.74 V eventually yields the formation of Tc^{III} carbonate complex. LSC measurements reveal that technetium solubility depends strongly on pH and on total carbonate concentration. NMR signals observed at 152 ppm (Tc^{III} carbonate) and 156 ppm can be assigned to Tc^{III}- and Tc^V-carbonate com-

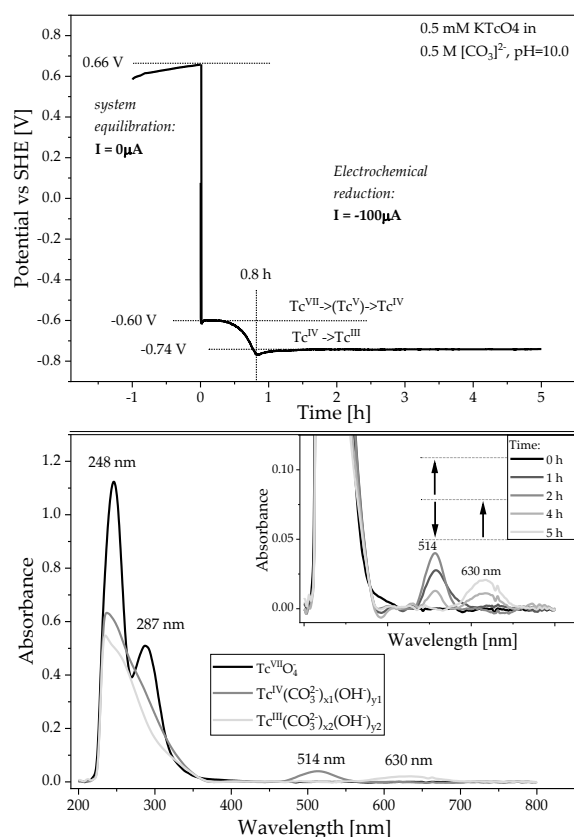


Figure 1. Chronopotentiometry (top) and UV-vis spectroscopy (bottom) of 0.5 mM K₂TcO₄ in 0.5 M carbonate medium at pH 10 upon electrochemical reduction.

plexes, respectively.^[7] Relatively to the signal of the pertechnetate anion (p.d. 0.0 ppm), they display drastic increase in linewidth (several kilohertz) as the result of symmetry reduction for Tc carbonate complexes since ⁹⁹Tc is a quadrupolar nucleus ($I = 5/2$). Reduced technetium species are very susceptible to re-oxidation in presence of oxygen. This makes *ex situ* NMR spectroscopy difficult to study reactive Tc species at low Tc concentration. We therefore attempt to develop and establish *in situ* electrochemistry coupled by ⁹⁹Tc-NMR spectroscopy as a powerful tool to probe Tc speciation and corresponding molecular structures as a function of the applied potential.

ACKNOWLEDGEMENTS. This research was funded by the German Federal Ministry of Education and research (002NUK072).

- [1] Yalçıntaş, E. *et al.* (2016) *Dalton. Trans.* **45**, 8916–8936.
- [2] Rodríguez, D. M. *et al.* (2021) *Chemosphere* **281**, 130904.
- [3] Mayordomo, N. *et al.* (2021) *Chem. Eng. J.* **408**, 127265 (2021).
- [4] Banerjee, D. *et al.* (2016) *Chem. Soc. Rev.* **45**, 2724–2739.
- [5] Alliot, I. *et al.* (2009) *Environ. Sci. Technol.* **43**, 9174–9182.
- [6] Paquette, J. and Lawrence, W. E. (1985) *Can. J. Chem.* **63**, 2369–2373.
- [7] Mikhalev, V. A. (2005) *Radiochemistry* **47**, 319–333.

Basis sets in density functional theory – An example of how heavy elements influence workflows

L. Waurick, M. Patzschke, B. Drobot

Before a density functional theory (DFT) calculation can be started, a few things are necessary and must be considered. Apart from a molecular structure to be optimized, the choice of a DFT functional and a corresponding basis set may be crucial for the success of the calculation. Experience has shown that the PBE0 hybrid functional performs well for heavy elements.^[1–3] However, the use of basis sets can be challenging for certain atom types, such as radium.^[4]

BASIS SETS IN GENERAL. A basis set in theoretical chemistry is a set of functions, representing the electronic wave function of atoms in the computational model. So far, a large number of different basis sets have been published for varying applications.^[5] For DFT operations, the def2-TZVPP basis as an adaptation of the Karlsruhe basis set with two additional polarization functions provides good accuracy.^[6] However, in the Karlsruhe basis sets, electrons close to the core are replaced by an effective core potential (ECP).^[7] When calculating certain electronic parameters of a molecule, all electrons should be explicitly included in the calculation. For geometry optimization, the use of an ECP provides similar accuracy paired with a significantly lower calculation time. In one calculation, it is also common to use different basis sets for small and large atoms, such as a transition metal complex with an organic ligand. If the size of the basis sets is similar enough, this does not lead to significant issues in the calculation.^[8]

MACROPA COMPLEXES. Complexes of different metal ions and the chelator molecule macropa (Fig. 1) were investigated for radiopharmaceutical purposes.^[4]

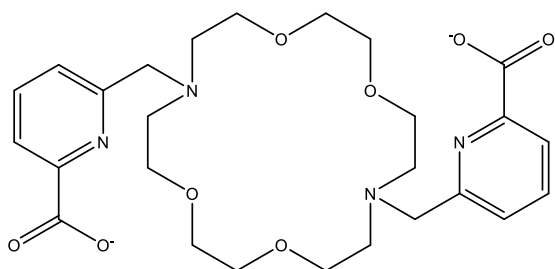


Figure 1. Structure of the macropa ligand with deprotonated carboxylic groups.

The combination of the PBE0 hybrid functional and the def2-TZVPP basis set therefore seemed suitable for geometry optimization. However, for radium, one of the metal centers, the def2-TZVPP was neither available in the used program package (Orca 5.0) nor in the basis set exchange database.^[9,10] Nevertheless, to ensure a high level of atom description, a combination of the aug-cc-pVTZ basis set for radium and the DKH-def2-TZVPP basis set for every other atom was used. Both basis sets explicitly describe near-core electrons, while the aug-cc-pVTZ basis set belongs to the correlation-consistent basis set family and was originally designed for post-Hartree-Fock methods.^[11] In contrast to lanthanide-macropa complexes, the DFT geometry optimization of the radium complex converged well, though slowly (Fig. 2).

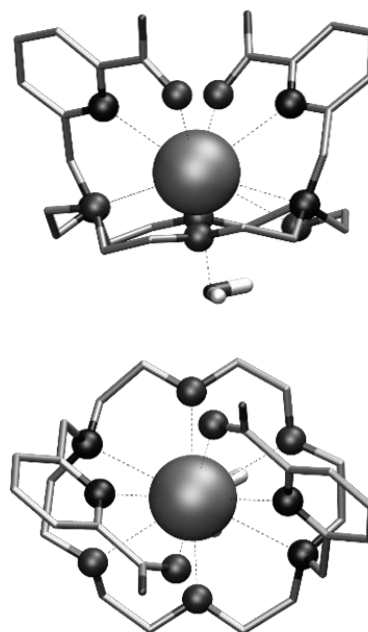


Figure 2. DFT optimized structures of the radium-macropa complex; side-view (top); top view (bottom).

After successful convergence of the geometry optimization, a frequency calculation was performed to ensure that each of the complexes has reached a local energy minimum. Since the aug-cc-pVTZ basis set is not implemented in the original Orca basis set library, an analytical frequency calculation for the radium-macropa complex failed. As a result, a time-consuming numerical frequency analysis had to be performed.

OUTLOOK. It has been shown that heavy elements can have a significant influence on workflows and computation time in theoretical chemistry. As a result, the setup for such a calculation can be challenging. Future calculations are planned for metal-macropa complexes in terms of electronic and NMR properties. In order to achieve comparable results in a reasonable time, the level of theory for geometry optimizations will be reduced to def-TZVP basis sets, followed by an all-electron single point calculation.

- [1] Perdew, J. P. *et al.* (1996) *J. Chem. Phys.* **105**, 9982–9985.
- [2] Adamo, C. *et al.* (1999) *J. Chem. Phys.* **110**, 6158–6170.
- [3] Vetere, V. *et al.* (2000) *Chem. Phys. Lett.* **325**, 99–105.
- [4] Blei, M. *et al.* (2023) *Inorg. Chem.* **62**, 20699–20709.
- [5] Jensen, F. (2013) *WIREs Comput. Mol. Sci.* **3**, 273–295.
- [6] Hellweg, A. *et al.* (2014) *Phys. Chem. Chem. Phys.* **17**, 1010–1017.
- [7] Hellmann, H. (1935) *J. Chem. Phys.* **3**, 61.
- [8] Yang, Y. *et al.* (2009) *J. Phys. Chem. A* **113**, 9843–9851.
- [9] Neese, F. (2012) *Wiley Interdiscip. Rev.: Comp. Mol. Sci.* **2**, 73–78.
- [10] Pritchard, B. P. *et al.* (2019) *J. Chem. Inf. Model.* **59**, 4814–4820.
- [11] Dunning, T. H. (1989) *J. Chem. Phys.* **90**, 1007–1023.

Annihilation of proton transport in confined nanocompartments

H. Hao,¹ E. M. Adams, S. Funke,² G. Schwaab,² M. Havenith,² T. Head-Gordon¹

¹University of California, Berkeley, United States, ²Ruhr University Bochum, Bochum, Germany

Nanoconfinement of solvated protons suppresses transport dynamics and alters their transport mechanism. The impact of surface charge on solvated protons confined in nanometer sized reverse micelles was explored with molecular dynamics simulations as well as spectroscopic characterization. The negatively charged surfactant sodium bis(2-ethylhexyl) sulfuccinate (AOT) suppresses proton transport to a greater extent than nonionic neutral headgroups, while the positively charged cetyltrimethylammonium bromide (CTAB) causes annihilation of proton transport. The slower dynamics in the presence of charged headgroups comes from the expulsion of hydronium and chloride ions from the interface due to the formation of an electric double layer, resulting in an interior waterpool with increased pH. The close proximity of the protons to chloride counterions reduces the available molecular configurations of the proton, closing the normal pathway of proton transport through hopping. Instead the proton is forced to localized oscillatory hopping with large residence times.^[1]

EXPERIMENTAL. Terahertz (THz) spectroscopy was used to investigate the solvated proton structure of a 1 M HCl solution confined within reverse micelles (RMs) composed of AOT or CTAB/hexanol. The conductivity of solutions, associated to the presence of proton transport, was obtained with dielectric relaxation spectroscopy. Reactive force field simulations and analysis were done with LAMMPS MD software utilizing the Amber force field GAFF and AM1-BCC charges obtained from ANTECHAMBER. To simulate the nano waterpools, the TIP3P water model was used for initial equilibration, and then replaced with the ReaxFF/CGeM water model.^[2] From the simulations, the average ion density distribution and proton hopping rates were extracted and compared to spectroscopic results.

RESULTS. Spectroscopic peaks corresponding to solvated protons and chloride ions were observed in AOT RMS for all sizes, but only for the larger sizes of CTAB RMS. Peaks corresponding to the surfactant counter ions, Na⁺ or Br⁻, were not observed, indicating these ions remain close to the surfactant headgroup in the RM. MD simulations, which reveal the distribution of ions in the RM, confirmed this observation. The distribution of the hydronium and chloride ions depended on RM charge and size. However, for the largest RMS measured, independent of charge, the proton and chloride resided in the interior water core. Dielectric spectra were modeled as a sum of Debye modes, from which the solution conductivity can be determined (Fig. 1). The conductivity represents the movement of protons in solution, and is interpreted here as corresponding to the number of forward hops. In the case of AOT RMS, conductivity is observed at a threshold RM size, and is significantly repressed compared to RMS composed of neutral surfactants. For CTAB RMS, however, solution conductivity is not observed for any size, suggesting a complete lack of proton transport via forward hopping. Extraction of the number of forward proton hops from MD simulations showed similar results, in which proton

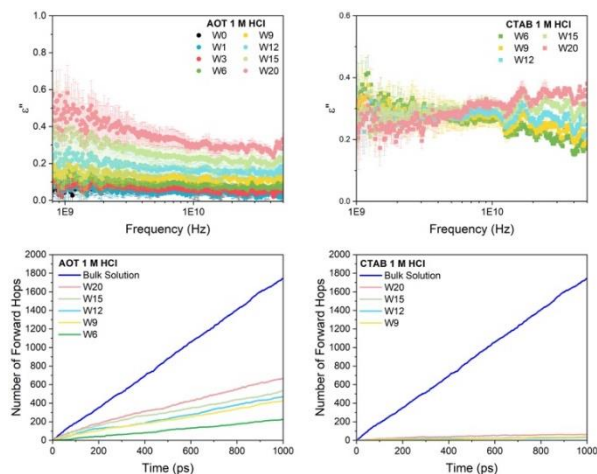


Figure 1. Imaginary part of the dielectric spectra of AOT (top left) and CTAB (top right) reverse micelles containing 1 M HCl. Number of forward hops of protons determined from MD simulations of 1 M HCl solution confined in AOT (bottom left) and CTAB (bottom right) reverse micelles.

hopping increases with increasing micelle size for AOT, but does not occur for CTAB.

Further tracking of the proton movements shows that in the AOT RMS, the proton transport switches from a forward hopping mechanism to an oscillatory hopping mechanism for water pools greater than 2 nm in radius. With the oscillatory mechanism, the proton hops from one water molecule to a second, but returns to the first. This results in a larger residence time per hop of the proton. In CTAB RMS, an oscillatory hopping mechanism dominates with increased residence times by a factor of 2 compared to AOT RMS. The proton is closely associated to the chloride counterion in the interior water pool, which ultimately limits the pathways that the proton may move. These results show that in nanoconfinement proton transport is significantly impacted by its environment. Relative to neutral interfaces, proton transport is suppressed by charged interfaces. The formation of an electric double layer at the micelles interface forces the proton and chloride ions to the micelle interior, where they compete for solvation water. The sharing of solvation water greatly reduces the amount of water available for efficient proton transfer, resulting in longer residence times and slower proton hopping events.

[1] Hao, H. et al. (2023) *J. Am. Chem. Soc.* **145**, 1826–1834.

[2] Adams, E. M. et al. (2021) *Angew. Chem.* **60**, 24419–25427.

Hydrogen transport between layers of transition metal-dichalcogenides

I. Eren, Y. An,¹ A. Kuc²

¹Peking University, Beijing, China; ²CASUS, HZDR, Görlitz, Germany

Hydrogen is a crucial source of green energy and has been extensively studied for its potential usage in fuel cells. The advent of two-dimensional crystals (2DCs) has taken hydrogen research to new heights, enabling it to tunnel through layers of 2DCs or be transported within voids between the layers, as demonstrated in recent experiments by Geim's group. In this study, we investigate how the composition and stacking of transition-metal dichalcogenide (TMDC) layers influence the transport and self-diffusion coefficients (D) of H atoms using well-tempered metadynamics (WTMetaD) simulations. Our findings show that modifying either the transition metal or the chalcogen atoms significantly affects the free energy barriers (ΔF) and, consequently, the self-diffusion of H atoms between the 2DC layers. In the H_h^h polytype, MoSe₂ exhibits the lowest ΔF (45 meV), while WS₂ has the highest (127 meV), resulting in the largest D for the former system. Additionally, H atoms inside the R_h^M polytype of MoS₂ encounter more than twice lower energy barriers (50 meV) and, thus, much higher diffusivity compared to those within the most stable H_h^h stacking (115 meV). These findings are particularly significant when investigating twisted layers or homo- or heterostructures, as different stacking areas may dominate over others, potentially leading to directional transport and interesting materials for ion or atom sieving.

EXPERIMENTAL. All systems were fully relaxed using density functional theory with Perdew–Burke–Ernzerhof exchange-correlation functional, Gaussian augmented plane wave basis sets, and Grimme's D3 dispersion correction, as implemented in the CP2K package. The Quickstep method was employed with Goedecker–Teter–Hutter pseudopotentials together with DZVP-MOLOPT-GTH-SR basis set for all elements except hydrogen, which was represented using the full potential.

We performed WTMetaD simulations, as implemented in the CP2K package, to obtain ΔF for H-atom diffusion between the layers of studied materials. Here, the canonical NVT ensemble was employed with the temperature set to 300 K and CSVR (canonical sampling velocity rescaling) thermostat with 0.5 fs timestep. Each trajectory was at least 45 ps long, to ensure convergence. Each WTMetaD simulation was preceded by standard Born-Oppenheimer molecular dynamics simulations (MD; NVT, 300 K, time step of 0.5 fs) with a duration of at least 5 ps to ensure thermal equilibrium. We defined two collective variables (CVs) to trigger the process of H-atom transfer between the layers: all chalcogen atoms in a given system were divided into three different kinds: X1 (inner layer with bound H atom), X2 (inner layer neighboring X1), and X (outermost layers). One of the collective variables, CV1, was defined as the coordination number (CN) of H to X1, CN_{H-X_1} , and the other, CV2, as CN of H to X2, CN_{H-X_2} .

RESULTS. In the present work, we extended our previous studies on the H atom transport between layers of hBN and MoS₂ to investigation of the self-diffusion of H atoms between layers of Group-6 TMDC bulk materials with different layer stackings.^[1] Our focus was on examining how the layer composition (metal atoms – Mo, W, Nb, or chal-

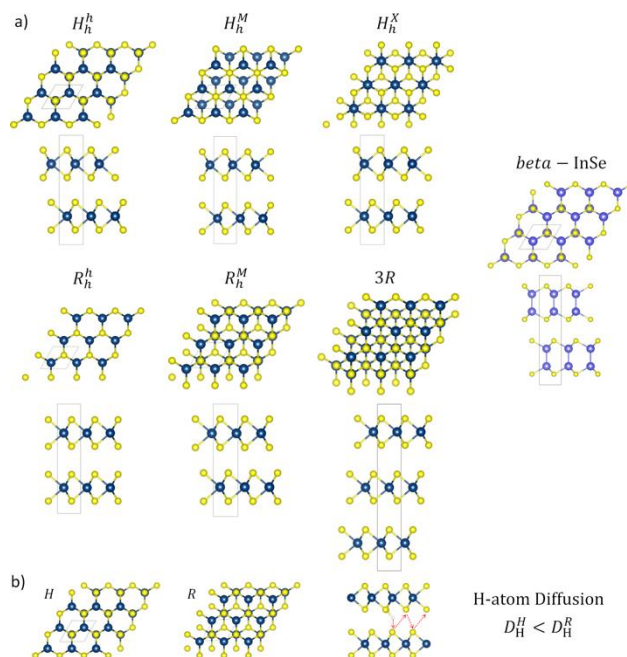


Figure 1. Top and side views of all considered structural high-symmetry stackings (a). Unit cells are marked with black lines. Metal atom (Mo, W, Nb) in blue, chalcogen atom (S or Se) in yellow, and In atom in violet. Inter-layer transport of H atoms by hopping between layers. R polytype shows larger diffusivity (b).

cogen atoms – S, Se) and the layer stacking in MoS₂ (H- or R-types of high-symmetry stackings) influence the free-energy barriers (ΔF) for H transport and the corresponding diffusivity (Fig. 1). To investigate the movement of H atoms between layers and construct the free-energy (F) landscape, we employed well-tempered metadynamics simulations. Our findings revealed that Se-based materials, as well as Mo-based materials, exhibit lower ΔF and higher self-diffusion coefficients (D) compared to their S- or W-based counterparts, making MoSe₂ systems ideal for H atom transport. Among different high-symmetry stackings, the R types have up to twice lower ΔF than the H types.

These discoveries hold significant importance for future studies concerning transport properties in materials with twisted layers, leading to Moiré structures and the formation of differently sized domains with various high-symmetry stackings. Such arrangements have the potential to form localized transport channels in these systems. Furthermore, our results demonstrate the potential for optimizing intriguing materials based on TMDC homo- or hetero-layers with different twist angles for applications involving ion- or atom-transport, such as in fuel cells.

ACKNOWLEDGEMENTS. This research was supported by the DFG (projects GRK 2721/1 and SFB 1415). The authors acknowledge ZIH Dresden, the Leipzig University Computing Centre, and the Paderborn Center for Parallel Computing for computational resources. The authors thank Prof. Thomas Heine for fruitful discussions.

[1] Eren, I. et al. (2024) *Adv. Mater. Interfaces* **11**, 202300798.

SCIENTIFIC CONTRIBUTIONS (PART II)

Geological Systems

Long-Lived Radionuclides & Transport Phenomena in

GEOLOGICAL SYSTEMS

Eu(III), Am(III), Th(IV), Pu(IV), and U(VI) retention by C-S-H (C/S 0.8) – Effect of gluconate

K. Schmeide, S. Dettmann,¹ N. Huittinen, N. Jahn,¹ J. Kretzschmar, M. U. Kumke,¹ T. Kutyma,² J. Lohmann,² T. Reich,² S. Shams Aldin Azzam, L. Spittler,² J. Stietz²

¹Universität Potsdam, Institute of Chemistry, Potsdam, Germany; ²Johannes Gutenberg-Universität Mainz, Department of Chemistry, Mainz, Germany

The effect of gluconate (GLU) on the retention of actinides in different oxidation states (An(X), ranging from tri- to hexavalent) was studied for a calcium-silicate-hydrate (C-S-H) phase with a C/S ratio of 0.8. In addition to the ternary systems An(X)/GLU/C-S-H, also binary systems An(X)/C-S-H, GLU/C-S-H, and An(X)/GLU were studied applying a range of analytic techniques. The results showed that GLU had little to no effect on the overall An(X) retention by C-S-H with C/S of 0.8, regardless of the oxidation state of the actinides.^[1]

In nuclear waste disposal concepts, cementitious materials serve as structural elements, liners and backfill material or as waste matrix. Nanocrystalline calcium-silicate-hydrates (C-S-H), as major constituents of hardened cement paste, are the most important cement phases for radionuclide retention. Organic ligands, being present in cement-based materials or in the waste itself, can influence radionuclide retention. For instance, GLU, applied as cement additive or decontamination agent, forms stable chelate complexes with various radionuclides. Its influence on actinide retention was examined for a C-S-H phase with a C/S ratio of 0.8, which represents aged cement of degradation stage III.

EXPERIMENTAL. Amorphous C-S-H (C/S 0.8) was prepared under inert gas atmosphere. During batch sorption experiments, the order of An(X) and GLU additions to C-S-H suspensions was varied. Further experimental details are compiled in Dettmann *et al.*^[1]

RESULTS. At the cement degradation stage III (pH ~10), no blocking of sorption sites by GLU is expected due to the low sorption of GLU on C-S-H. For the An(X) sorption onto C-S-H in absence and presence of GLU, distribution coefficients (R_d) were determined (Fig. 1). For all actinides studied, the $\log R_d$ values were in the range of 4.5 to 7, indicating a quantitative uptake of An(X) by the C-S-H phase, independent of the presence of GLU and the order of the reactant addition. These values also confirm the $\log R_d$ data reported in the literature for An(X) sorption in

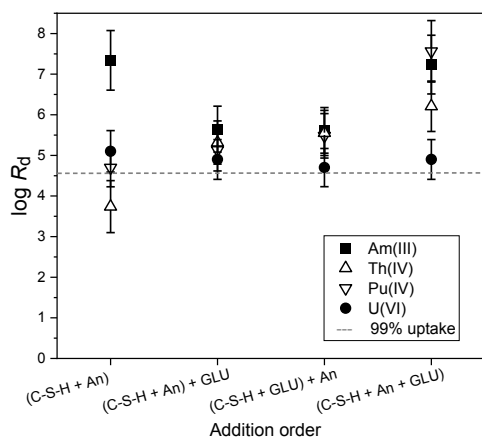


Figure 1. Distribution coefficients (R_d , 1 σ error) determined for Am(III), Th(IV), Pu(IV) and U(VI) uptake at C-S-H in absence and presence of GLU (for detailed experimental conditions, cf. [1]). The order of adding An(X) and GLU to the C-S-H suspensions is indicated at the abscissa.

the absence of GLU. That means, the organic ligand GLU has only a very small influence on the An(X) retention by C-S-H under these conditions.

XRD (not shown) and ²⁹Si SP MAS NMR (Fig. 2) investigations showed that no alteration of the C-S-H short- and long-range orders, microcrystallinity, and degree of condensation occurred due to sorption of GLU, of An(X), or both. The respective ¹³C CP MAS NMR spectra of the GLU containing samples (Fig. 2) confirmed that only a small fraction of GLU was sorbed to C-S-H. Thereby, the GLU was strictly associated with the surface Ca(II) but not incorporated confirming results from molecular dynamics simulations.^[1,2]

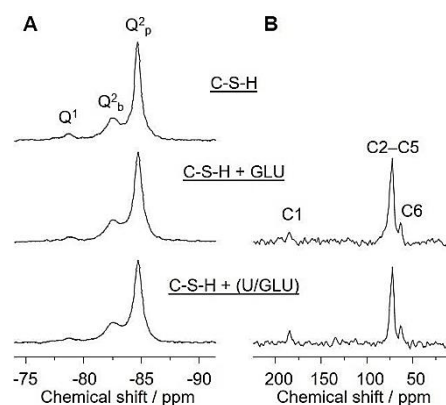


Figure 2. ²⁹Si SP MAS NMR (A) and ¹³C CP MAS NMR spectra (B) of C-S-H as well as after sorption of GLU or sorption of U(VI)/GLU on C-S-H; ([U(VI)]₀ = 5 × 10⁻⁶ M, [GLU]₀ = 1 × 10⁻² M, S/L = 10 g/L).

Leaching experiments showed no remobilization of sorbed Eu(III) (used as chemical analogue for trivalent actinides) or U(VI) upon the addition of GLU, and no aqueous GLU complexes were found for the ternary Eu(III) or U(VI)/GLU/C-S-H systems. In case of Eu(III), a strong influence of GLU on the Eu(III) coordination environment in the precipitate was observed by luminescence spectroscopy. It can be assumed that coprecipitation of Eu(III) with pore water constituents Ca(II) and Si(IV) occurred. The effect of GLU on the Eu(III) speciation might be explained by the formation of Ca(II)-GLU complexes, leading to a change in the stoichiometry and structure of the formed coprecipitate. The influence of GLU on the proportion of the three U(VI) sorption complexes on C-S-H is small, as shown by luminescence spectroscopy.

The observed trend of the electrophoretic mobilities of Th(IV), determined by CE-ICP-MS measurements of the Th(IV)/GLU system, indicates the formation of Th-OH-GLU complexes. In presence of Ca(II), Ca is associated to these ternary species.

ACKNOWLEDGEMENTS. This work has received funding from the European Union's Horizon 2020 Research and Innovation Programme (Work Package CORI, no. 847593) and from the Federal Ministry for the Environment, Nature Conservation, Nuclear Safety and Consumer Protection (GRaZ II project, no. 02E11860A, 02E11860B, 02E11860F).

[1] Dettmann, S. *et al.* (2023) *Front. Nucl. Eng.* **2**, 1124856.

[2] Androniuk, I. *et al.* (2017) *Phys. Chem. Earth* **99**, 194–203.

Uptake of Np(V) onto ZrO₂: a batch, spectroscopic, and modeling study

N. Jordan, I. Jessat, H. Foerstendorf, A. Rossberg, A. C. Scheinost, J. Lützenkirchen,¹ K. Heim, T. Stumpf

¹Institute for Nuclear Waste Disposal, Karlsruhe Institute of Technology, Eggenstein-Leopoldshafen, Germany

Batch sorption experiments showed an increased sorption of Np(V) onto zirconia (ZrO₂) upon raising pH. The impact of ionic strength, Np(V) concentration, and the solid-to-liquid ratio of ZrO₂ on the Np(V) sorption was investigated. Results suggested the predominant formation of inner-sphere Np(V) surface complexes. However, the sorption isotherm obtained at pH 4.5 and 6.0 indicated the presence of different sorption sites on the zirconia surface. The derived information at the macroscopic and molecular levels were used to parameterize a surface complexation model.

The interactions of actinides such as neptunium, a long-lived transuranium element, with corrosion products in the near-field of a geological repository are of concern regarding its safety assessment. The main corrosion product of the zircaloy cladding material is ZrO₂, which represents one of the first barriers for interactions with radionuclides.^[1] In the present work, we developed an uptake model for Np(V) onto ZrO₂.

EXPERIMENTAL. All experiments were conducted at room temperature under N₂(g) atmosphere to exclude carbonate and in 0.1 or 0.01 mol L⁻¹ NaCl. The equilibration times for the samples of the pH dependent and the isotherm series were 3 days and 2–9 days, respectively. After pH measurements, samples containing 0.5 g L⁻¹ monoclinic ZrO₂ (US Research Nanomaterials, Inc.) were centrifuged (1 h, 4,020 × g), whereas those containing 4 g L⁻¹ ZrO₂ were ultracentrifuged (45 min, 174,900 × g). All concentrations of Np-237 in the supernatants were determined by liquid scintillation counting or ICP-MS.^[2]

RESULTS. The sorption of the positively charged neptunyl-ion (NpO₂⁺) generally started around pH 3 and reached its maximum above pH 7 (Fig. 1), which is ascribed to the increasingly negatively charged zirconia surface upon raising pH.^[2] Np(V) hydroxo and chloro species can be neglected under the investigated conditions.^[3,4] The change of the ionic strength from 0.01 to 0.1 mol L⁻¹ did not impact the Np(V) sorption (Fig. 1), indicating the formation of inner-sphere Np(V) surface complexes.

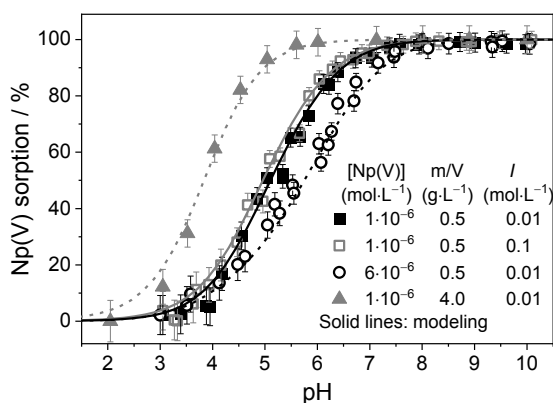


Figure 1. Sorption pH edges of Np(V) onto ZrO₂ at different conditions: [Np(V)] = 10⁻⁶ or 6 × 10⁻⁶ mol L⁻¹, m/V = 0.5 or 4 g L⁻¹ ZrO₂, I = 0.1 or 0.01 mol L⁻¹ (NaCl). Solid lines represent the fit curves derived from the surface complexation model.

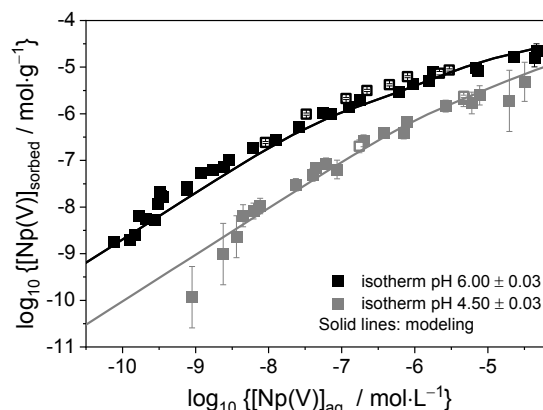


Figure 2. Sorption isotherms with m/V = 0.5 g L⁻¹ ZrO₂, 0.01 mol L⁻¹ NaCl and 10⁻⁹–6 × 10⁻⁵ mol L⁻¹ Np(V) at pH 4.5 and 6.0. Empty symbols: batch (from Fig. 1) and EXAFS samples. Solid lines represent the fit curves derived from the surface complexation model.

At a higher Np(V) concentration (6 × 10⁻⁶ mol L⁻¹), the sorption edge was slightly shifted towards higher pH as a result of increased competition of Np(V) for sorption sites (Fig. 1).

At increased solid-to-liquid ratio a considerable shift of the sorption edge towards lower pH values was observed (Fig. 1), which might indicate the presence of different kinds of sorption sites. This can also be inferred from sorption isotherms (Fig. 2) showing a linear slope (on log₁₀-log₁₀ plots) over a broad concentration range and a steeper slope at very low Np(V) concentrations. The lower slope observed at increased Np concentrations (> 10⁻⁶ mol L⁻¹) is assigned to the saturation of the binding sites on the zirconia surface.

Spectroscopic investigations, namely X-ray absorption spectroscopy and *in situ* ATR FT-IR experiments, both confirmed the formation of Np(V) inner-sphere complexes. EXAFS experiments revealed the formation of a bidentate inner-sphere surface complex in the weak sorption site regime.^[2]

Inverse modelling was then used to derive thermodynamic surface complexation constants. The formation of a Np(V) bidentate edge-sharing inner-sphere surface species {(≡Zr_wOH)(≡Zr_wOH₂)NpO₂}⁺ onto weak sites was adopted in the adsorption model. The same stoichiometry was assumed for the strong sites.^[2] Overall, a satisfactory description of the pH edges, isotherms, and zeta potential data was obtained for the different experimental conditions.^[2] The results derived in this work from a combined batch sorption, spectroscopy and modeling approach significantly contribute to more reliable predictions of the environmental fate of neptunium(V) and its analogs. Furthermore, we provide the first SCM data set for the sorption of a pentavalent actinide onto zirconia, improving the overall thermodynamic data situation.

[1] Motta, A. T. et al. (2015) *Annu. Rev. Mater. Res.* **45**, 311–343.

[2] Jessat, I. et al. (2024) *J. Hazard. Mater.* **461**, 132168.

[3] Neck, V. et al. (1992) *Radiochim. Acta* **56**, 25–30.

[4] Müller, K. et al. (2015) *Environ. Sci. Technol.* **49**, 2560–2567.

Monitoring the sorption of aged U(VI) solutions on zirconia by vibrational spectroscopy

H. Foerstendorf, I. Jessat, K. Heim, N. Jordan

***In situ* vibrational spectroscopic experiments of the sorption processes of metastable U(VI) solutions on zirconia revealed an increased contribution of surface precipitation in dependence of the age of the solution used. The spectra provided information on the solid U(VI) phase formed on the zirconia surface and on the coordination of the atmospherically derived carbonate as well.**

The exploration of molecular surface processes representing the transition from adsorption of aqueous U(VI) species to surface precipitation is still a challenging task for spectroscopic techniques. In particular at a circumneutral pH level, spectroscopic investigations are often hampered by the instability of aqueous U(VI) solutions at a concentration level required for an accurate signal-to-noise ratio. Here, we conducted a series of *in situ* IR sorption experiments on zirconia to demonstrate the growing contribution of solid formation beneath ongoing sorption processes using metastable U(VI) solutions.

EXPERIMENTAL. For the studies of the time-dependent sorption of U(VI) on ZrO₂, *in situ* ATR FT-IR spectroscopy experiments were performed at room temperature according to a procedure described in detail elsewhere.^[1] In a flow through experiment a stationary phase (*i.e.*, ZrO₂) is exposed to a 10 μM U(VI) solution (0.1 M NaCl, pH 7.0) after extensive equilibration with a solution containing only 0.1 M NaCl electrolyte at a flow rate of 100 μL·min⁻¹. All solutions were kept in ambient atmosphere.

RESULTS. The spectra recorded at distinct U(VI) exposure times evolving during the *in situ* experiment conducted with the freshly prepared solution (Fig. 1, top) revealed characteristic bands at 907, 1,385, and 1,525 cm⁻¹ representing the antisymmetric stretching mode of the uranyl moiety (ν_{as}(UO₂)), the symmetric and antisymmetric stretching modes of the carbonate molecules (ν_s(COO) and ν_{as}(COO)), respectively. The frequencies and the splitting of the bands demonstrated the formation of a ternary uranylcarbonato surface species where the uranyl moiety serves as a bridging unit between the zirconia surface and the carbonate ligands.^[2]

The performance of the homologous sorption experiment using aged U(VI) solutions revealed distinct spectral changes. A shoulder around 940 cm⁻¹ with increasing intensity was observed with the ageing of the U(VI) solution applied (Fig. 1, middle and bottom). This spectral feature is attributed to the formation of a solid U(VI) phase at the surface of the zirconia, most likely due to the sorption of colloids present in the aged solutions. Similar spectral features were observed recently during sorption reactions where surface-mediated precipitation occurred or from reference spectra of colloidal U(VI) solutions.^[3,4] From the frequency of the band around 940 cm⁻¹ the formation of a U(VI) hydroxo phase is suggested.

Simultaneously with the appearance of the surface precipitate, the shapes of the bands above 1,200 cm⁻¹, representing the modes of the atmospherically derived carbonate molecules, changed. The bands became broader indicating the abundance of further carbonate species now contributing to the spectra. These additional carbonate species most likely represent surface species coordinated to the

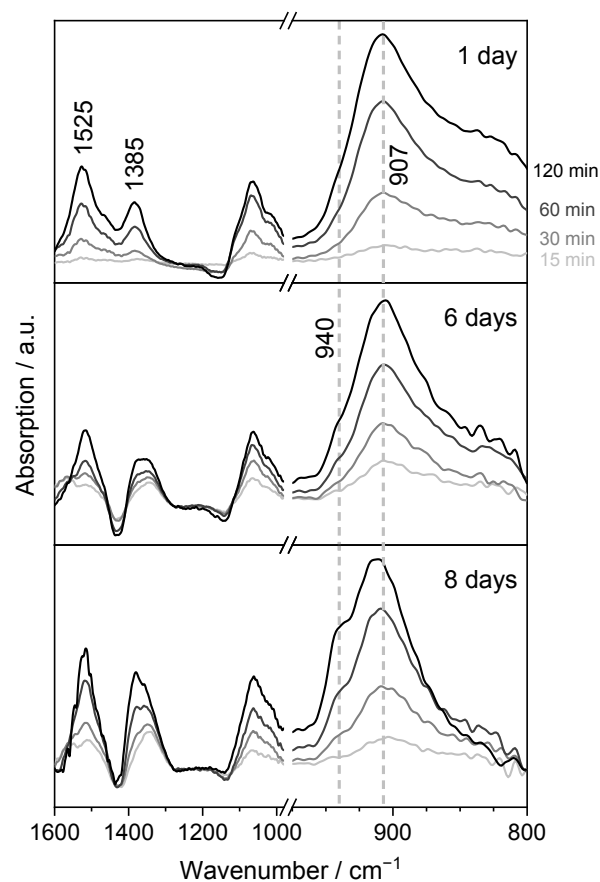


Figure 1. Difference spectra derived from *in situ* IR experiments of U(VI) sorption on zirconia at pH 7 ([U]_{init} = 10 μM; I = 0.1 M NaCl). The experiments were performed with a U(VI) solution, which was freshly prepared (top), and were repeated with the same solution after 6 (middle) and 8 days (bottom). Spectra were recorded at different times of U(VI) exposure (15, 30, 60, and 120 min) as shown for each experiment.

precipitate formed or they are even intrinsic parts of the precipitate.

The series of experiments demonstrates the utility of the *in situ* IR experimental setup for monitoring the formation of solid or colloidal phases simultaneously to ongoing sorption processes. In general, vibrational bands of solid compounds are intrinsically characterized by much smaller bandwidths and higher intensities in comparison to sorbed species. Hence, the detection of the formation of such phases already at relatively low abundancies is feasible. In turn, the *in situ* setup can be considered as a figure of merit for the presence of colloids in solution and at the solid/water interface.

- [1] Jessat, I. et al. (2024) *J. Hazard. Mater.* **461**, 132168.
- [2] Jessat, I. (2024) Ph.D. Thesis, Technische Universität Dresden, Dresden, Germany.
- [3] Müller, K. et al. (2008) *Inorg. Chem.* **47**, 10127–10134.
- [4] Müller, K. et al. (2013) *Chem. Geol.* **357**, 75–84.

Sorption of Ba(II) onto gibbsite: a batch study

V. Dück, N. Jordan, F. Bok

The sorption of Ba(II) onto gibbsite ($\text{Al}(\text{OH})_3$, Gbs) was investigated by means of batch experiments. The interaction was shown to be fast and pH-dependent. At 0.01 mol L^{-1} NaCl, the sorption increased with pH and the sorption maximum was reached at pH 11.5. However, an increased ionic strength (0.1 mol L^{-1} NaCl) significantly decreased the uptake of Ba(II) onto Gbs.

Exposure to radium (Ra) as a prominent example for NORM (Naturally Occurring Radioactive Material) must be avoided to protect people and the environment. For respective prognostic modelling of Ra reactive transport, sorption is an essential process. Here, mechanistic Surface Complexation Models (SCM) can take into account various site-specific geochemical parameters. Currently, SCM data on the sorption of Ra onto naturally occurring aluminosilicates (especially feldspar) is sparse and often derived from the chemical analogues barium or strontium.^[1-3] However, there is evidence in the literature that the sorption behavior within the series of alkaline earth metal cations is not as similar as expected^[4], which renders the application of such chemical analogies questionable. To improve the situation, sorption experiments of Ba onto gibbsite were performed as representatives of a mineral with aluminol binding sites.

EXPERIMENTAL. The zeta potential of Gbs (0.5 g L^{-1}) were measured to determine the pH_{IEP} of the mineral. Samples were prepared with background electrolyte concentrations of 0.005 and 0.01 mol L^{-1} NaCl and equilibrated for three days under $\text{N}_2(\text{g})$ atmosphere.

All batch experiments (Tab.1) (sample preparation and measurements) were also performed under inert gas (N_2) with a Gbs solid-to-liquid ratio of 0.5 g L^{-1} . The series were prepared with a background electrolyte concentration of 0.1 and 0.01 mol L^{-1} NaCl. To minimize the dissolution of gibbsite, samples were at first equilibrated during three days. After centrifugation (1.5 h at $6,800 \times g$), the supernatants were contacted with fresh gibbsite. After addition of Ba(II), the samples were equilibrated 3 days (except for the time-dependent study). After pH measurements, the phase separation was performed as already mentioned. Ba(II) concentrations in the supernatants were determined by inductively coupled plasma-mass spectrometry.

Table 1. Experimental conditions of the Ba(II) batch experiments.

Variable	Time dependent	pH-dependent
pH	11	7–12.3
NaCl [mol L^{-1}]	0.01	0.01/0.1
Ba(II) [mol L^{-1}]	10^{-6}	10^{-6}
Equilibration time [h]	1–168	72

RESULTS. The time dependent batch experiments (Fig. 1) showed a rapid uptake of Ba(II) with maximum sorption of 80% reached after about 24h. But to add a safety margin, an equilibration time of 72h for the experiments was used.

The pH series at 0.01 mol L^{-1} NaCl showed a sorption edge starting at pH 8.8 and reaching a maximum at pH 11.5 (Fig. 2). Increasing the ionic strength affects the onset of sorption by starting sorption at higher pH. At an ionic

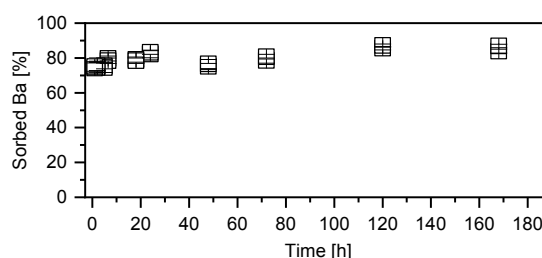


Figure 2. Time dependent experiments for the sorption of Ba(II) onto gibbsite ($m/v = 0.5 \text{ g L}^{-1}$, $\text{pH} = 11$, $[\text{Ba}(\text{II})]_{\text{initial}} = 10^{-6} \text{ mol L}^{-1}$, $I = 0.01 \text{ mol L}^{-1}$ NaCl, $\text{N}_2(\text{g})$) (error bars represent standard deviations at each point).

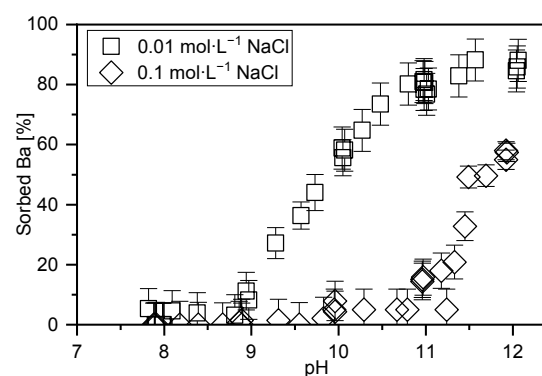


Figure 1. Sorption curve of Ba(II) onto gibbsite at $I = 0.01 \text{ mol L}^{-1}$ (\diamond) and 0.1 mol L^{-1} (\square) NaCl ($m/v = 0.5 \text{ g L}^{-1}$, $[\text{Ba}(\text{II})]_{\text{initial}} = 10^{-6} \text{ mol L}^{-1}$, of equilibration, $\text{N}_2(\text{g})$) (error bars represent standard deviations at each point).

strength of 0.1 mol L^{-1} NaCl, the sorption of Ba(II) was significantly decreased. Zeta potential measurements (at 0.005 and 0.01 mol L^{-1} NaCl) showed that the pH_{IEP} of pure Gbs is located at pH 8.1, which is in the range of literature values.^[5,6] The sorption of Ba(II) therefore started at pH values above the pH_{IEP} of Gbs.

According to Katz *et al.*,^[4] the sorption of Ba(II) on Gbs should not be influenced by the ionic strength and at least one inner-spherical complex should form. Figure 2 shows a clear ionic strength effect, which is more indicative of an outer-sphere complex.

Further evidence through extended X-ray absorption fine structure spectroscopic measurements and surface complexation modeling is needed to support this observation.

The derived surface complexation parameters will then be used to develop an SCM for Ba(II) sorption onto natural occurring minerals with both aluminol and silanol (here utilizing quartz data) binding site types, namely feldspar. This bottom-up approach will be extended to Sr and Ra as well to evaluate the limitations of the alkaline earth metals chemical analogy in the context of sorption. The models obtained will help to better predict the spread of NORM and reduce conservatism.

ACKNOWLEDGEMENTS. The RadoNORM project received funding from the EURATOM research and training programme 2019-2020 under grant agreement No. 900009.^[7]

- [1] Fabritius, O. *et al.* (2022) *Appl. Geochem.* **140**, 105289.
- [2] Rahnemaie, R. *et al.* (2006) *J. Colloid Interf. Sci.* **297**, 379–388.
- [3] Sverjensky, D. A. (2006) *Geochim. Cosmochim. Acta* **70**, 2427–2453.
- [4] Katz, L. E. *et al.* (2013) *J. Colloid Interf. Sci.* **399**, 68–76.
- [5] Su, C and Suarez, D. L. (1997) *Clays Clay Miner.* **45**, 814–825.
- [6] Kozmina *et al.* (1963) *Kolloid. Zh.* **25**, 169–173.
- [7] <https://www.radonorm.eu>.

^{99}Tc interaction with cast iron plates corroded in sterile or pristine Wyoming bentonite

K. Kirsch,¹ N. Matschiavelli, N. Mayordomo, A. Cherkouk, D. Schild,² T. Stumpf, A. Koerdt¹

¹Federal Institute for Materials Research and Testing (BAM), Berlin, Germany, ²Karlsruhe Institute of Technology, Institute for Nuclear Disposal, Karlsruhe, Germany

The effects of corroded cast iron plates on the reduction of technetium-99 (^{99}Tc) from $^{99}\text{Tc(VII)}$ to $^{99}\text{Tc(IV)}$ in Opalinus Clay pore water (OPA) were studied.^[1] The results show that a reduction of $^{99}\text{Tc(VII)}$ to $^{99}\text{Tc(IV)}$ occurs facilitated by the presence of iron. Higher degrees of degradation of the metal appear to delay the reduction, but do not influence the total amount of ^{99}Tc removed. $^{99}\text{Tc(IV)}$ is the dominant species on the cast iron plate surface, indicating that the removal of ^{99}Tc is a reduction-driven process.

Microbiological processes have been shown to affect deep geological repository systems on various levels, e.g., impacting mineral transformation in bentonite, gas production, or facilitating corrosion of nuclear waste storage containers.^[2] Consequently, microbiologically influenced corrosion (MIC) is one of the potential risk factors affecting the safety of deep geological repository systems. However, the impact of MIC on the lifetime and integrity of disposal containers for nuclear waste is not yet clear.^[2] In case of a container failure, radionuclides, such as technetium, are expected to be released and interact with the corrosion phases. ^{99}Tc poses a high environmental risk mainly due to its long half-life (2.15×10^5 years) in combination with the high mobility of the $^{99}\text{Tc(VII)}$ species.^[3]

In this work, we have explored the interaction of $^{99}\text{Tc(VII)}$ with corroded and uncorroded cast iron by scanning electron microscopy coupled with energy dispersive X-ray spectroscopy (SEM-EDX), X-ray photoelectron spectroscopy (XPS), and liquid scintillation counting (LSC). For these preliminary experiments, no replicate experiments were conducted.

EXPERIMENTAL. Cast iron (EN-GJS-400) plates were corroded in oxygen-free microcosms (containing 4 g Wyoming bentonite (B27)^[4] and 40 mL OPA^[1]) by incubation at 25 °C for 50 days. The bentonite used was either sterilized by autoclaving or left in pristine condition, i.e., leaving microorganisms intact. The plates were analyzed with SEM-EDX and showed varying degrees of surface degradation. However, these could not be clearly linked to MIC, but a higher degree of surface degradation was found on plates from microcosms with pristine bentonite.

Subsequently, the corroded cast iron plates were brought into contact with ^{99}Tc . ^{99}Tc sorption experiments were carried out using 40 mL OPA containing 5 μL $^{99}\text{Tc(VII)}$ in an oxygen-free N_2 glove box. A cast iron coupon (corroded in pristine or sterile bentonite, or an uncorroded control) was placed in the solution (pH 8.38) and shaken for 48 h to react. Solution samples were taken between 0–72 h. pH and Eh of the solution were measured and ^{99}Tc removal was determined by LSC. After 72 h of interaction with ^{99}Tc , the cast iron plates were recovered and stored in the glove box until analysis with SEM-EDX and XPS.

RESULTS. The corroded cast iron plates showed a higher degree of surface degradation when incubated in pristine bentonite compared to sterilized bentonite. SEM-EDX analysis after sorption showed the formation of solid

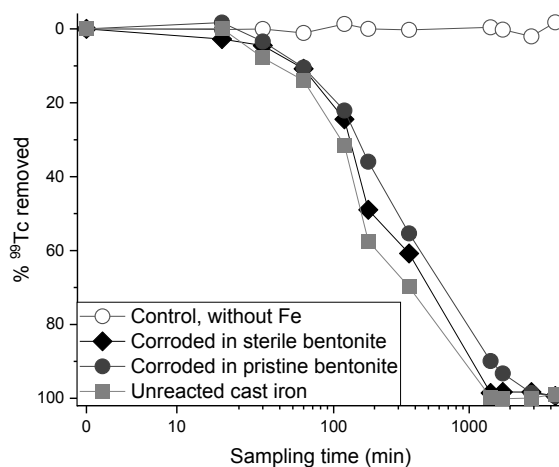


Figure 1. ^{99}Tc immobilization (in % ^{99}Tc removed) by different cast iron plates as a function of time.

phases in which ^{99}Tc is associated with Ca, S, and O, Mg and Ca, Cl, or S.

A Pourbaix diagram of ^{99}Tc was plotted based on NEA (2020).^[5] According to the diagram, the solution is in the stability range of $^{99}\text{Tc(VII)}$ at starting conditions but shifts to $^{99}\text{Tc(IV)}$ upon cast iron plate addition, where it stays for the remainder of the experiment.

The onset of ^{99}Tc removal from the solution is near instantaneous (Fig. 1). After 24 h of interaction, the yield of ^{99}Tc removal was the highest (>99%) for uncorroded cast iron plates. In contrast, ^{99}Tc removal is slightly lower for cast iron plates corroded in sterile or pristine bentonite (98% and 90%, respectively). Thus, the higher degree of degradation may have a retarding effect on immobilization. It is noteworthy that the ^{99}Tc removal was complete after 48 h in all cases.

XPS analyses show that $^{99}\text{Tc(IV)}$ is present mainly on the metal plate surfaces regardless of the degree of corrosion (data not shown). This indicates that ^{99}Tc removal by cast iron is a reduction-driven process.

These results indicate a possible correlation between the potential of cast iron to reduce $^{99}\text{Tc(VII)}$ and the degree of corrosion. Corroded cast iron from pristine bentonite may have formed a passivation layer that limits the transfer of electrons to less corroded areas, thus delaying the reduction. These preliminary and initial findings must be expanded upon in future experiments with iron plates corroded with MIC bacteria and more extensive XPS analyses.

ACKNOWLEDGEMENTS. For the financial support, we thank the Federal Ministry for Economic Affairs and Energy, Grant Number 02E11870B. Bentonite was provided by S. Kaufhold (BGR, Hannover, Germany).

[1] Joseph, C. et al. (2011) *Chem. Geol.* **284**, 240–250.

[2] Ruiz-Fresneda, M.A. et al. (2023) *Front. Microbiol.* **14**, 1134078.

[3] Pearce, C.I. et al. (2020) *Sci. Total Environ.* **716**, 132849.

[4] Kaufhold, S. and Dohrmann, R. (2008) *Appl. Clay Sci.* **39**, 50–59.

[5] NEA (2020) *Second Update on the Chemical Thermodynamics of U, Np, Pu, Am and Tc*, OECD Publishing, Paris.

Sorption of cadmium on alumina nanoparticles and mixtures of alumina nanoparticles and FEBEX smectite

N. Mayordomo, T. Missana,¹ U. Alonso¹

¹Centro de Investigaciones Energéticas Medioambientales y Tecnológicas (Ciemat), Madrid, Spain.

The immobilization of cadmium (Cd) by alumina nanoparticles and mixtures of alumina nanoparticles and smectite was studied experimentally and theoretically by batch sorption experiments and sorption modelling, respectively. Cd sorption on alumina was maximum for pH > 7.5 regardless on the ionic strength. However, Cd uptake by alumina/smectite mixtures was dependent on pH, ionic strength and mixture composition. Thus, the alumina/smectite ratio of components must be optimized to ensure an efficient Cd removal according to the environmental conditions.

Cd stands among the most toxic substances worldwide.^[1] Thus, Cd scavenging methods play a crucial role in decreasing its mobility in water and availability to living organisms. This work studies the Cd sorption by alumina nanoparticles (A), and mixtures of alumina nanoparticles and FEBEX smectite (A/S mixtures) as a function of pH, ionic strength, Cd concentration, and A/S mixture composition. A two-site non-electrostatic surface complexation model was developed to describe Cd sorption on A. Cd sorption on A/S mixtures was described using an additive approach of pure A and S sorption models, and taking into account the chemistry in solution (*i.e.*, A dissolution and ion competition for Cd sorption).^[2,3]

EXPERIMENTAL. All experiments were performed under ambient atmosphere. A and S used in this work were previously characterized.^[4,5] Batch sorption experiments were carried out using 0.5 g L⁻¹ A or A/S mixture suspensions in presence of ¹⁰⁹CdCl₂ at given concentrations. The pH of the suspension was established by the use of buffers.^[4] The samples were shaken for seven days. Afterwards, they were centrifuged at 14,000 rpm for one hour and the supernatant was analyzed for pH and Cd concentration using gamma counting with a NaI detector (Packard Autogamma COBRA2). The sorption models were developed by using the geochemical code CHESS 2.4 and the Cd thermodynamic database collected described elsewhere.^[2,6]

RESULTS. Figure 1 shows Cd removal by A and A/S mixtures at different pH values and ionic strengths. The sorption of Cd on A increases with increasing pH, being maximum at pH > 7.5, regardless on the ionic strengths (Fig. 1 top). It is remarkable that at pH < 5.0 Cd uptake by A reaches 10–20% of Cd sorption. This behavior is unexpected for sorption of cations on metal oxides, since at low pH cation sorption should be electrostatically hindered. Most likely this behavior is due to the formation of a ternary complex favored by anions in solution. However, due to the lack of spectroscopic evidences, this contribution of Cd sorption was represented as an empirical Cd sorption in the sorption model. A two-site non-electrostatic sorption model was able to predict the Cd uptake by A.^[2] Cd uptake by A/S mixtures shows a strong dependency on ionic strength, increasing with a decrease in the ionic strength at pH > 4.5 (Fig. 1, bottom), which is related to the cationic exchange mechanism in S. The experimental data were simulated by an additive approach of the individual Cd sorption models of A, and S (solid lines in Fig. 1, bot-

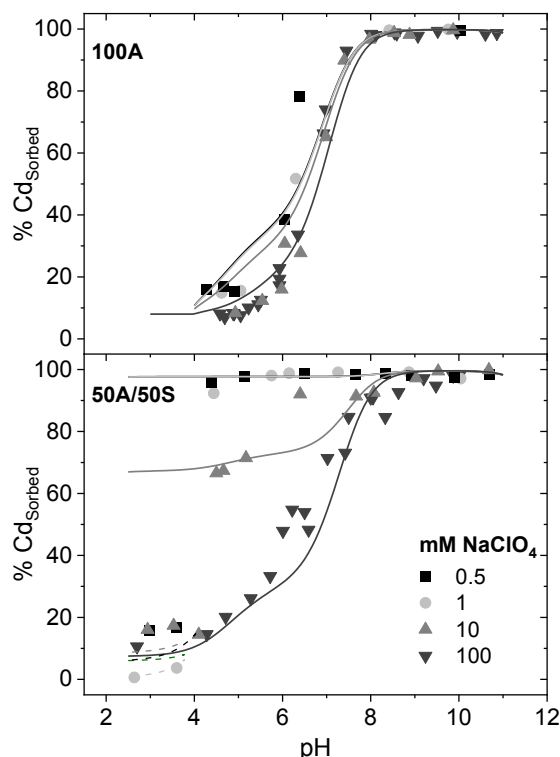


Figure 1. Cd sorption (%Cd_{sorbed}) on alumina (A) (top) and alumina/smectite mixtures at 50 wt.-% (50A/50S) (bottom) as a function of pH and different NaClO₄ ionic strengths (defined in the figure legend). Lines represent the Cd sorption models according to their respective thermodynamic data,^[2,3] in absence (solid line) and presence (dashed line) of 1 µg L⁻¹ of Al³⁺. [Cd]₀ = 50 nM, 0.5 g L⁻¹ of A or A/S suspension.

tom).^[2,3] The additivity of the models could only predict the decrease of Cd sorption by A/S mixtures at pH < 4.0 when the dissolution of A, and thus the competition of Al³⁺ for sorption on S was included in the model (dashed lines in Fig. 1., bottom).

In conclusion, the chemical conditions of Cd-polluted scenarios should be assessed prior to the use of A and A/S mixtures as scavengers since the presence of ions might strongly influence Cd immobilization.

ACKNOWLEDGEMENTS. This research was partially funded by the NukSiFutur TecRad young investigator group, funded by the German Federal Ministry of Education and research, (ref number 002NUK072), the European Union's Horizon 2020 Research and Innovation Programme under Grant Agreement no. 847593 (EURAD, WP FUTURE), and the Spanish Ministry of Science and Innovation (PID2022-138402NB-C22, ACOMER Project).

- [1] WHO (2011) *Cadmium in drinking-water*. WHO, Geneva, Switzerland.
- [2] Mayordomo, N. *et al.* (2023) *Minerals*, **13**, 1534.
- [3] Missana, T. *et al.* (2023) *Toxics*, **11**, 130.
- [4] Missana, T. *et al.* (2014) *Appl. Geochem.* **49**, 68–79.
- [5] Missana, T. *et al.* (2007) *Phys. Chem. Earth* **32**, 55–67.
- [6] Van der Lee, J. *et al.* (1999) *Chess tutorial and cookbook*. Technical report LHM/RD/99/5; École des Mines de Paris, Paris, France.

Structural and spectroscopic characterization of Ca/Sr and Ce co-doped monazites

S. Richter, L. B. F. dos Santos, S. E. Gilson, N. Huittinen, T. Lender¹

¹RWTH Aachen, Aachen, Germany

Doped monazites of the series $\text{La}_{1-x}(\text{Ca} + \text{Ce})_x\text{PO}_4:\text{Eu}^{3+}$ and $\text{Gd}_{1-x}(\text{Sr} + \text{Ce})_x\text{PO}_4:\text{Eu}^{3+}$ obtained by solid-state synthesis and co-precipitation were characterized with Raman and luminescence spectroscopy. Analyses of the Raman shifts and the full width half maxima of the phosphate vibrational bands showed that homogenous monazite solid solutions were not obtained regardless of synthesis method. Luminescence spectroscopy revealed the presence of several monazite phases, likely differing in their Ce^{3+} and Ce^{4+} ratio. Samples with high Ca content showed a very broad emission signal, indicative for an amorphous calcium pyrophosphate-type environment.

Monazites are naturally occurring orthophosphate minerals that have been suggested as host matrices for the immobilization of radionuclides from high-level nuclear waste streams.^[1] Natural monazite is known to incorporate significant amounts of thorium and uranium into its crystal structure.^[2] However, even very old monazites rarely show any metamictization due to alpha-decay and daughter recoil of incorporated actinides suggesting high radiation resistance.^[3] In this study, Raman and luminescence spectroscopy was used to investigate the incorporation of Ca(II) and Ce(III,IV) in LaPO_4 as well as Sr(II) and Ce(III,IV) in GdPO_4 monazites. 500 ppm Eu^{3+} was used as luminescent probe in the samples.

EXPERIMENTAL. Doped monazites of the series $\text{La}_{1-x}(\text{Ca} + \text{Ce})_x\text{PO}_4:\text{Eu}^{3+}$ and $\text{Gd}_{1-x}(\text{Sr} + \text{Ce})_x\text{PO}_4:\text{Eu}^{3+}$ were synthesized *via* solid-state synthesis and co-precipitation. For solid-state synthesis, adequate amounts of the respective metal oxides and $(\text{NH}_4)(\text{H}_2\text{PO}_4)$ in 10 wt.-% excess were mixed together with mortar and pestle, pelletized, and calcined at 1,250 °C for 24 h. For co-precipitation, the respective amounts of metal nitrates were mixed with citric acid and dissolved in water followed by addition of H_3PO_4 . For precipitation, NH_4OH was added until a pH of 10 was reached. The precipitate was washed 4–5 times, dried at 50 °C, and calcined at 800 °C for 24 h. Initial XRD analyses of the samples indicated the presence of several monazite phases, especially in the $\text{Gd}_{1-x}(\text{Sr} + \text{Ce})_x\text{PO}_4:\text{Eu}^{3+}$ series, and generally more homogenous samples following co-precipitation than solid-state synthesis. In Ca-containing samples, different calcium phosphate phases could be identified. Furthermore, previous XANES studies revealed mixed cerium oxidation states ($\text{Ce}^{3+} > 70\%$, $\text{Ce}^{4+} < 30\%$) in the samples, implying incomplete incorporation of M^{2+} ($\text{M} = \text{Sr}, \text{Ca}$) via coupled $\text{M}^{2+} + \text{Ce}^{4+}$ substitution into the monazite matrix. To shed light on the presence of minor impurity phases in the samples or X-ray amorphous phases, selected samples were subjected to Raman and luminescence spectroscopic investigations.

RESULTS. Band assignment of the PO_4 internal modes was carried out according to Silva *et al.*^[4] Although some samples showed very broad Raman spectra, no clear bands belonging to non-monazite (impurity) phases could be detected. Using Lorentzian fits, the Raman peak positions and the full width half maxima (FWHM) were determined and plotted as a function of the dopant concentration. In a homogenous solid solution, the Raman shift

changes linearly with composition.^[1] In the present series, no such trends are apparent, corroborating the previous XRD studies. The FWHM, particularly of the ν_1 and ν_3 Raman bands, serves as an indicator for assessing short-range order within crystal structures.^[1] Band broadening occurs in solid solutions when going from the pure end-members to mixed compositions. However, no such trends are evident for any of the analyzed series. While the variations of the FWHM are rather small for the La-monazite series, they are particularly large for the Gd-monazite series, indicative of a higher degree of disorder in these samples.

The Eu^{3+} luminescence investigations showed narrow excitation spectra of the pure monazite end-members while spectra of the doped monazites featured either broader or several excitation peaks, indicative of multiple Eu^{3+} environments in the sample. For the samples with one or several narrow excitation spectra, typical monazite-like emission spectra with 3-fold and 5-fold splitting of the ${}^7\text{F}_1$ and ${}^7\text{F}_2$ bands, respectively, were obtained. In the $\text{Gd}_{0.8}(\text{Sr} + \text{Ce})_{0.2}\text{PO}_4:\text{Eu}^{3+}$ sample, the two Eu^{3+} -monazite environments are slightly shifted from the excitation peak position of the pure GdPO_4 end-member (17,268 cm^{-1}). The excitation energy of the blue-shifted species (17,276 cm^{-1}) implies a slightly larger Eu-O bond length in comparison to pure GdPO_4 , while the opposite is true for the red shifted species (17,264 cm^{-1}). A larger lattice volume and, consequently, a larger Eu-O bond length, is obtained following incorporation of the larger Ce^{3+} cation into the GdPO_4 structure. Ce^{4+} on the other hand is smaller than Gd^{3+} , which could explain the presence of the red-shifted species in the sample. This observation would exclude coupled $\text{Sr}^{2+} + \text{Ce}^{4+}$ substitution, as the large Sr^{2+} cation would rather increase the monazite lattice volume in comparison to GdPO_4 than decrease it. Finally, the broad excitation spectrum of the $\text{La}_{0.2}(\text{Ca} + \text{Ce})_{0.8}\text{PO}_4:\text{Eu}^{3+}$ with a large excess of Ca+Ce, resulted in a very broad, non-monazite-like emission spectrum, implying that Eu^{3+} is incorporated into a disordered, likely amorphous, calcium pyrophosphates-type environment in this sample.

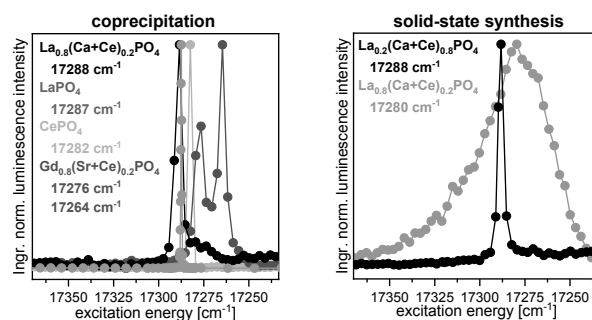


Figure 1. Integrated excitation spectra of Eu^{3+} luminescence in samples obtained by co-precipitation and solid-state synthesis.

ACKNOWLEDGEMENTS. This work was funded by BMBF as part of the AcE project (02NUK060A).

[1] Huittinen, N. *et al.* (2017) *J. Nucl. Mater.* **486**, 148–157.

[2] Förster, H.-J. (1998) *Am. Mineral.* **83**, 259–272.

[3] Gramaccioli, C. M. *et al.* (1978) *Am. Mineral.* **63**, 757–761.

[4] Silva, E. N. *et al.* (2006) *Opt. Mater.* **29**, 224–230.

Synthesis and glancing incident XRD investigations of ion irradiated Ce(IV)-doped ZrO₂ ceramics

L. B. F. dos Santos, J. Niessen,¹ V. Svitlyk, S. E. Gilson, J. Marquardt,² S. Richter, C. Hennig, N. Huitinen

¹RWTH Aachen University, Aachen, Germany; ²Goethe-Universität Frankfurt am Main, Frankfurt am Main, Germany

In the present work, one selected composition of cubic cerium doped zirconia (ZrO₂) co-doped with gadolinium was synthesized via a co-precipitation route to produce a dense ceramic. To investigate the radiation tolerance of the ceramic, ion irradiation experiments were conducted. In preparation for these experiments, the ceramic surface was polished and partly masked with Al-foil. The non-masked part of the pellet was irradiated with 14 MeV Au⁴⁺ ions using two different ion fluences. Post-irradiation analyses were conducted with scanning electron microscopy (SEM) and synchrotron X-ray diffraction in glancing incidence mode (GI-XRD), to capture irradiation-induced changes at the ceramic surface. The results showed that the Zr_{0.77}Ce_{0.18}Gd_{0.15}O_{1.925} ceramic is extremely radiation tolerant, with no visible radiation damage and a preserved main crystallinity, even after irradiation at the highest fluence of 1 × 10¹⁵ ions/cm².

Zirconia (ZrO₂) is the primary corrosion product of zircaloy cladding on nuclear fuel rods. Hence, it is considered as the first technical barrier to immobilize the radionuclides from the spent nuclear fuel.^[1] Zirconia exhibits interesting properties, such as high radiation tolerance, mainly when the crystal structure is cubic, high chemical durability, and the ability to incorporate a large amount of cations into its crystalline structures.^[2] All these properties make zirconia a potential material to be used as a waste form to immobilize radionuclides.^[3] As an analog to plutonium, cerium was used in this study. Previously, it was shown that codoping zirconia with trivalent cations is crucial for the stabilization of the pure cubic structure for Ce(IV) concentrations lower than 70 mol-%. Hence, two identical parallel pellets of cerium-doped zirconia co-doped with gadolinium were prepared and irradiated with two different fluences to determine the stability against irradiation and to elucidate if this composition has a potential to be used as a waste form for high-level actinide-bearing waste.

EXPERIMENTAL. To investigate the stability of ceramics after the irradiation, a cubic ZrO₂ solid solution with 18 mol-% Ce and 15 mol-% Gd was synthesized. The synthesis methodology until the drying step was the same as described by dos Santos.^[4] The dry precursor sample was diluted in isopropyl alcohol by adding 5 wt-% polyethylene glycol (PEG) followed by mortar in a ball mill two times for two minutes. The sample was placed in a fume hood for 48 hours to evaporate all the isopropyl alcohol. Two pellets were pressed from the dry powder using an uniaxial pressure of 200 kN for one minute. The calcination of the pellets was done at 1,500 °C for two hours. Prior to the ion irradiation, the pellets were polished with 1 μm diamond paste until they achieved a smooth surface. After polishing, half of the pellet was covered with aluminum foil to retain a pristine (non-irradiated) part of the pellet, and the other half was irradiated with 14 MeV Au⁴⁺ ions at two fluences: 1 × 10¹⁴ ions/cm² (A1), and 1 × 10¹⁵ ions/cm² (A2) at the Ion Beam Center (HZDR). The pellet's microstructures were analyzed by scanning electron microscopy using acceleration voltages from 1–15 kV. The XRD was

performed at the ROBL beamline at the European Synchrotron Radiation Facility (ESRF) in Grenoble, on the XRD2 diffractometer using 11.1 keV X-rays. Both sides of the pellet were measured at glancing incidence angles from 1 to 14 degrees. At very low glancing angles, close to the critical one, the incident X-ray photons interact only with the surface.^[5]

RESULTS. Dense ceramics were obtained with small cracks, likely because the samples were not pre-calcined, and hence all the intrinsic water was removed only during the calcination process. However, the cracks did not hamper the irradiation and pellets remained intact both during polishing and the ion irradiation. Figure 1 (left) shows that the irradiated part is much darker than the pristine. SEM images (Fig. 1, middle) did not show any differences between the pristine and irradiated sides, *i.e.*, no visible damage has occurred to the samples independent of the applied fluences. The diffractograms of the pristine sides show Bragg peaks which are more intense and narrower than on the irradiated side (Fig. 1, right). This implies that irradiation has promoted slight microstructural changes such as a reduction of the crystallite size or an increase in strain. A small, non-systematic shift of the Bragg peaks towards lower angles is noticed on the irradiated side, which is more pronounced for fluence A2. This phenomenon has been associated with induced internal strain.^[6] With the very minor microstructural changes, the doped zirconia phases exhibited high stability towards radiation.

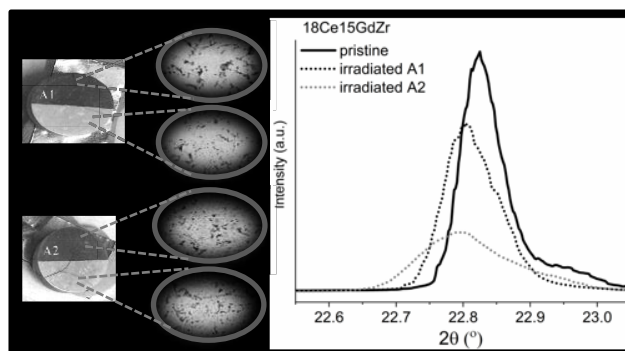


Figure 1. Photo of the pellets after the irradiation experiments (left). The dark discoloring originates from the irradiation. SEM images of the pristine and irradiated pellets (middle). GI-XRD diffractogram (right).

ACKNOWLEDGEMENTS. This work was supported by the German Federal Ministry of Education and Research (BMBF) under the ACE project (02NUK060A). As well as for the support from the Ion Beam Center and ESRF.

- [1] Katoh, Y. (2014) *CMCs*, p. 495–523.
- [2] Debelle, A. *et al.* (2010) *J. Nucl. Mater.* **396**, p. 240–244.
- [3] Singh, B. K. B. *et al.* (2021) *ACS ES&T Eng.* **1**, 1149–1170.
- [4] dos Santos, L. B. F. *et al.* (2022) *Report HZDR-119*, p. 52.
- [5] Hoogenhof, V. D. *et al.* (1993) *Spectrochim. Acta B* **48**, 277–284.
- [6] Phillips, R. *et al.* (2021) *Carbon Trends* **5**, 100124.

Oxidation state and structure of Fe in nontronite under various redox conditions

Y. Qian,^{1,2} A. C. Scheinost, S. Grangeon,³ J.-M. Greneche,⁴ A. Hoving,⁵ E. Bourhis,⁶ N. Maubec,³ S. V. Churakov,^{1,2} M. Marques Fernandes¹

¹LES PSI, Villigen, Switzerland; ²Institute of Geological Sciences, University of Bern, Bern, Switzerland; ³BRGM, Orléans, France; ⁴IMMM UMR CNRS, Le Mans, France; ⁵TNO, Utrecht, The Netherlands; ⁶ICMN CRS, Orléans, France

Structural Fe in natural clay minerals may play a pivotal role in controlling the mobility of redox-sensitive radionuclides under anoxic and reducing conditions, but surprisingly little is known about its oxidation state and structure. Here, we investigated the structure of a ferruginous natural clay smectite, nontronite, under different redox conditions, and compare several methods for the determination of iron redox states.^[1]

EXPERIMENTAL. The nontronite clay NAu-2 was obtained from the Clay Source Repository of the Clay Minerals Society (Purdue University, West Lafayette, IN). Iron was gradually reduced chemically with the Citrate-Bicarbonate-Dithionite (CBD) method.^[1] Transmission electron microscopy (TEM) was performed using a Philips CM 20 operated at 200 kV. Fe K-edge XANES and EXAFS spectra were measured at 15 K using an 18-element Ge detector.^[2]

Table 1. Comparison of Fe^{II} fractions in three increasingly reduced nontronite (Nau-2) samples by different methods.

Method	Native Nau-2	Low-red Nau-2	High-red Nau-2
Moessbauer 77 K	0.00	0.19	0.44
XPS	0.07	0.24	0.46
XANES pre-edge (centroid)	0.00	0.16	0.50
XANES edge (ITFA)	0.00	0.15	0.51
EXAFS (R _{Fe-O})	0.00	0.11	0.44
MEO/MER	0.00	0.19	0.58

RESULTS. ⁵⁷Fe Mössbauer spectrometry, X-ray Photoelectron Spectroscopy (XPS), X-ray Absorption Near Edge Structure (XANES) spectroscopy including its pre-edge, Extended X-ray Absorption Fine Structure (EXAFS) spectroscopy, and Mediated Electrochemical Oxidation and Reduction (MEO/MER), resulted in similar Fe^{II} fractions (Tab. 1, Fig. 1a and b). Therefore, all methods deliver reliable Fe^{II} estimates, provided that utmost care is taken to conserve the Fe^{II} state during sample storage, transportation and measurements. By combining X-Ray Diffraction (XRD) and Transmission Electron Microscopy (TEM), we show that the long-range structure of nontronite at the highest obtained reduction degree of 44% Fe^{II} is not different from that of fully oxidized nontronite except for a slight basal plane dissolution on the external surfaces (Fig. 2). The short-range order probed by EXAFS spectroscopy suggests, however, an increasing structural disorder and Fe clustering with increasing reduction of structural Fe (Fig. 1c and d).

This suggests that structural Fe in nontronite can act like a battery and may go through several redox cycles without significant structural changes, which is very different from Fe oxides, which are commonly dissolved when being reduced, and after re-oxidation may precipitate at a different location and as a different type of mineral.

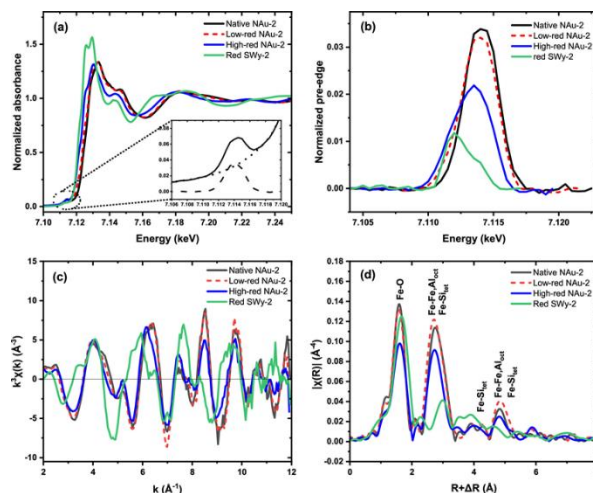


Figure 1. Fe K-edge XAFS spectra of native NAu-2, low-red NAu-2, high-red NAu-2, and red SWy-2. XANES (a); the insert shows the pre-edge peak (solid line) of native NAu-2 with background (dotted line) and the separated pre-edge peak (dashed line). Normalized Fe K pre-edge peaks (b). k³-weighted EXAFS chi function (c). k³-weighted EXAFS Fourier transform magnitude (d).

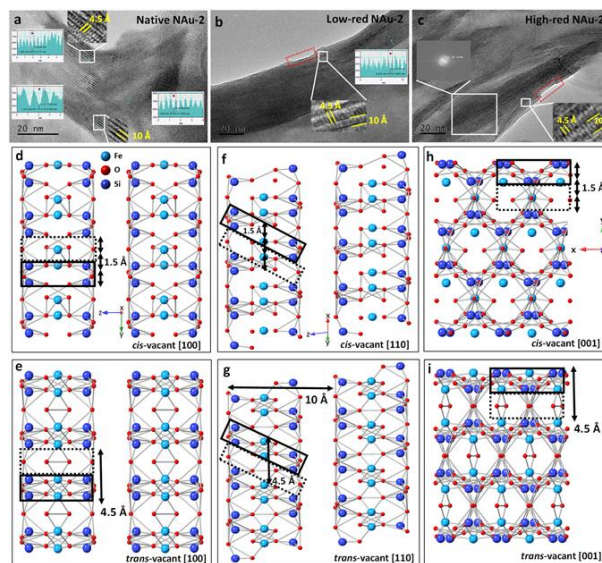


Figure 2. TEM image of native NAu-2 (a), low-red NAu-2 (b), high-red NAu-2 (c). Nontronite structure of cis-vacant octahedra [100] (d), trans-vacant octahedra [100] (e), cis-vacant octahedra [110] (f), trans-vacant octahedra [110] (g), cis-vacant octahedra [001] (h), trans-vacant octahedra [001] (i).

[1] Qian, Y. et al. (2023) *ACS Earth Space Chem.* **7**, 1868–1881.

[2] Scheinost, A. C. et al. (2021) *J. Synchr. Rad.* **28**, 333–349.

In-situ flow visualization with Geo-Positron-Emission-Tomography in a granite fracture from Soultz-sous-Forets, France

W. Zhou, J. Kulenkampff, C. Fischer

We studied the fluid flow field in a fractured granite core sample using sequential imaging with Positron-Emission-Tomography (PET).^[1] This technique enables direct reconstruction of flow streamlines, providing a unique insight into the fluid dynamics of complex fractured crystalline materials. Pulse migration tracer tests using the positron-emitting radionuclide ^{18}F were conducted in a fractured granitic drill core from a depth of 1,958 m at the Enhanced Geothermal System (EGS) reference site in Soultz-sous-Forets, France. The flow field was analyzed based on the inlet and outlet positions across the fracture, as well as the applied flow rates. The tests identified various flow path characteristics. Both the variation in fracture aperture and topography of the fracture surface have an impact on the flow field, which can lead to flow channeling and preferential flow paths. The experiments with higher flow rates showed wider and more dispersed flow paths, while lower velocity resulted in more localized flow and channeling behavior. This study provides enhanced experimental insights into the hydrodynamics of fracture flow and its relation to the rough structure of a single fracture, compared to input-output experiments. It can help validate model simulations and experimentally determine hydrodynamic parameters needed for reactive transport modeling, which are otherwise estimated with a high degree of uncertainty.

EXPERIMENTAL. The spatial distribution of multiple fluid inlets and outlets provides different combinations of input-output dipoles. The injection fluid was adjusted to pH 5.6, $\text{NaCl } 3.04 \times 10^{-4} \text{ mol L}^{-1}$, $\text{KCl } 5.43 \times 10^{-4} \text{ mol L}^{-1}$, and $\text{NaF } 1.3 \times 10^{-4} \text{ mol L}^{-1}$ (i.e., total dissolved salt: 0.0638 g L^{-1}). A pulse of 1 mL was labeled with concentrations between 62 and 89 MBq $^{18}\text{F}^-$ and was injected into the fracture. Continuous flow rates of 6 mL h^{-1} and 12 mL h^{-1} were used. The activity at the outlet was continuously monitored with a gamma flow counter.

The $\mu\text{-CT}$ images (resolution: $72.6 \mu\text{m}$) were post-processed using Avizo software, which included co-registration with PET, fracture segmentation, calculation of the thickness map (aperture), and fracture topography. In addition, the $\mu\text{-CT}$ image was downsampled to PET resolution and used as a geometry database for attenuation and scatter correction. The PET images were calculated from the coincidence data with a final time frame of 1 min and calibrated with respect to the injected activity.

RESULTS. The series of PET images represents a tomogram of the tracer fluid propagation. These tomograms can be directly compared with the fluid propagation from $\mu\text{-CT}$ -based model simulations and thus serve as a validation of the transport simulation calculations. However, they also provide direct insight into flow variables such as local effective porosity, flow path geometry, and local flow rates or velocities.

We investigated potential correlations between flow rate (velocity) and fracture aperture heights. From the orthographic projections of the flow velocities onto the fracture width, we were able to compute a correlation histogram of the flow velocities with respect to its fracture distribution.

As shown in Fig. 1, there is no clear linear increasing or decreasing correlation between the aperture width and a corresponding increase or decrease in the flow rate values. However, there is a clear clustering trend of flow rate values for all experiments. Although with slight variations, the bulk of the data is in the $0.02\text{--}0.05 \text{ mm}^2$ aperture range. This leads to the conclusions that the configuration of the flow path is influenced by other parameters such as geometry of the fracture and topography of the fracture walls.

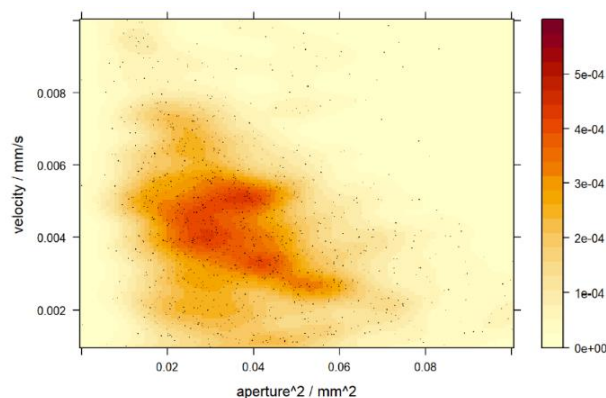


Figure 1. Example of quantitative correlation histograms of Poiseuille-law derived flow velocity values with respect to their spatial aperture distribution of a granite fracture, shown as a point cloud denoting the velocity [mm/s] and the quadratic relationship with the aperture width [mm^2]. The color bar represents the normalized frequency density.

Ongoing research is therefore aimed at gaining a better understanding of the conditions under which flow velocity variability occurs in fractures in crystalline rocks. How sensitive are changes in fracture surface curvature and differences in fracture wall roughness to the variability of flow velocity in fractures? Answering this question is complex because the described variability in geometric boundary conditions operates over a wide range of length scales, i.e. the spatial frequencies to be considered are affected by roughness in the μm range as well as waviness in the mm to cm range. However, an improved understanding of this is essential for applications in the field of nuclear waste disposal and contaminant transport, where the residence time of fluids in fractured rocks controls the effective fluid-solid interaction, e.g., in dissolution, precipitation or sorption reactions.

[1] Pingel, J. et al. (2023) *Geothermics* **111**, 102705.

Variability of radionuclide sorption efficiency on muscovite cleavage planes

J. Schabernack, A. Faria Oliveira, T. Heine, C. Fischer

In geological repositories for nuclear waste, the surrounding rock formation serves as an important barrier against radionuclide migration. Multiple potential host rocks contain phyllosilicates, which have shown high efficiency in radionuclide sorption. Recent experimental studies report a heterogeneous distribution of adsorbed radionuclides on nanotopographic mineral surfaces. In this study, the energetic differences of surface sorption sites available at nanotopographic structures such as steps, pits, and terraces are investigated.^[1] Eleven important surface sites are selected and the energies of adsorption and desorption reactions are obtained from density functional theory (DFT) calculations. The adsorption energies are then used for the parametrization of a kinetic Monte Carlo (kMC) model simulating the distribution of adsorbed europium on a typical nanotopographic muscovite surface. On muscovite, silicon step sites are favorable for europium sorption and lead to an increased adsorption in regions with high step concentrations. Under identical chemical conditions, sorption on typical nanotopographic surfaces is increased by a factor of three compared to atomically flat surfaces. Desorption occurs preferentially at terrace sites, leading to an overall 2.5 times increased retention at nanotopographic structures. This study provides a mechanistic explanation for heterogeneous sorption on nanotopographic mineral surfaces due to the availability of energetically favorable sorption sites.

EXPERIMENTAL. A kMC simulation of europium adsorption on a muscovite (001) surface has been performed by using $400 \times 100 \times 8$ unit cells in the *a*, *b*, and *c* directions. In the dissolution simulation, five defects are placed initially and 2 million atoms are dissolved. In the following adsorption part, 15 thousand $\text{Eu}(\text{OH})_3$ molecules are adsorbed to the generated surface. The number of $\text{Eu}(\text{OH})_3$ atoms is chosen to yield a surface coverage of 0.33 $\text{Eu}(\text{OH})_3$ per unit cell area. This value is selected as the limit since it results in charge compensation of the negative muscovite surface charge which drives the adsorption reaction. Therefore, the number of $\text{Eu}(\text{OH})_3$ on the surface can be considered representative.

RESULTS. The kinetic Monte Carlo (kMC) model is applied to conditions that are far from equilibrium, where the number of available sites greatly exceeds the number of adsorbing europium atoms. As a result, the model demonstrates the initial response of the system to adsorption. Complete coverage, where any local contrast would be lost, is never achieved. To identify any local increase in sorption, an adsorption density is calculated using the kernel density estimation method (Fig. 1). An increased density of adsorbed atoms is visible at etch pit centers and surface steps (as shown by the boxes in Fig. 1, lower part) compared to atomically flat surface areas. Surface steps cause a moderate increase in density of approximately 1.5 times compared to the atomically flat surface. The concentration of surface steps is remarkably high close to the center of all etch pits. The observed adsorption density is the highest, with an increase in density of more than three times compared to the atomically flat surface. This observation enables the identification of topographical structures such as etch pits or steps. Heterogeneous adsorption

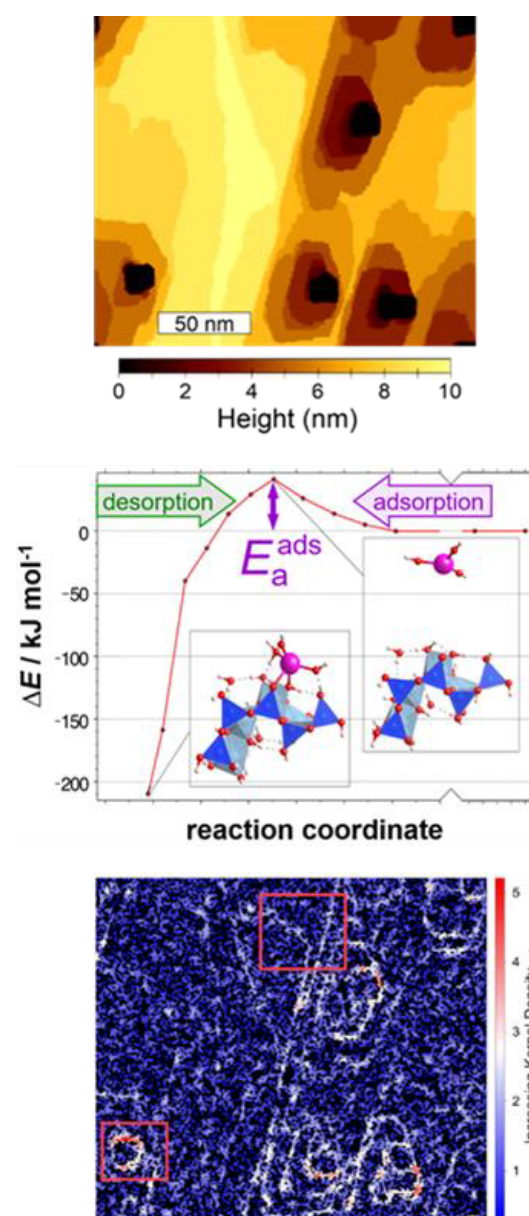


Figure 1. This scheme illustrates our strategy for analyzing the variability of sorption efficiency. The upper section shows a typical nanotopography of muscovite resulting from kinetic Monte Carlo (kMC) simulation of crystal dissolution, which provides the substrate topography for studying heterogeneous sorption. The middle section shows an example of a surface site for the energy of adsorption and desorption reactions obtained from Density Functional Theory (DFT) calculations. The results of the kMC sorption/desorption simulation show the spatial distribution of Eu retention. The observed heterogeneity is mechanistically explained by favorable adsorption at Si step sites and desorption preferentially at terrace sites.

can be explained by site-specific differences in adsorption probability and the distribution of those sites on the mineral surface. The preferential silicon step site can be found in high concentrations on surface steps originating at crystal defects in the muscovite structure. Here an increase in the concentration of adsorbed atoms can be observed. The highest concentration of steps, which is often found at surface etch pits, leads to the most significant increase in surface sorption.

[1] Schabernack, J. et al. (2023) *Adv. Theory Simul.*, 2300406.

Characterization of the contact zone of an MgO-concrete dam with saline host rock

J. Kulenkampff

The contact zone between engineered sealing structures and the host rock, together with the excavation damaged zone, are critical parts of underground barriers that are required for safe disposal of nuclear waste. Construction of an MgO-concrete test dam in salt rock as a prerequisite for in-depth investigation of the properties of the contact zone and for improvement of sealing methods was the focus of the STROEFUN III project.

The contribution of our subproject was non-destructive characterization of drill cores from the contact zone using μ CT in order to detect and quantify possible transport pathways and to support the identification of potential improvements in material and construction technology. Our results are required for improved dam constructions that are key components of the safety concept and currently developed by project partners.

EXPERIMENTAL. An MgO-concrete half-dam (cross section: 6.5m², length: 15.7m) was cast over three days in a drift that had been cut with a well-characterized surface roughness in the GTS mine in Teutschenthal.^[1] Six months later, boreholes were drilled for permeability measurements and drill core investigations. Selected drill cores, in particular from the contact zone, were examined with X-ray micro-computed tomography (μ CT), cf. Fig. 1, upper part. Tomograms of the drill cores (\varnothing : 100mm) were acquired with our μ CT-scanner Nikon XTH 250 (generator power: 190kV and 200 μ A, filter: 2.5mm Cu). The voxel size is 45 μ m.

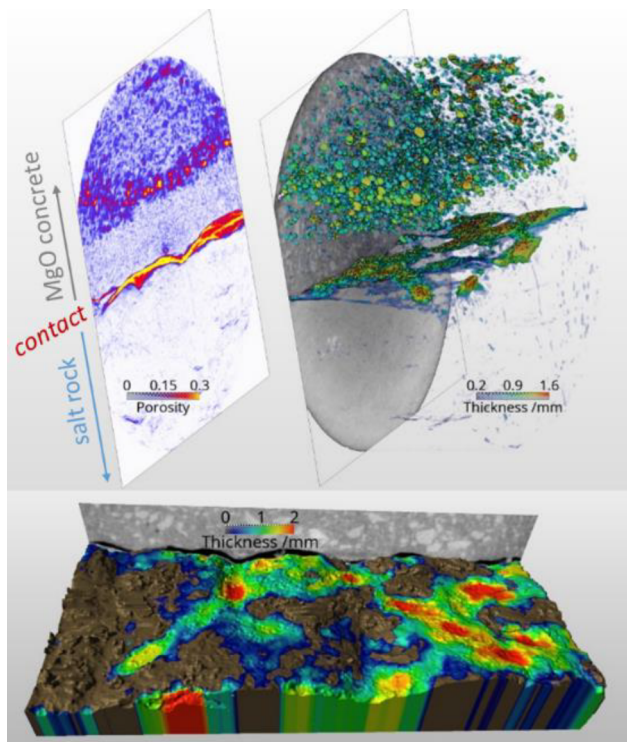


Figure 1. Analysis of voids of a drill core section from the contact zone between MgO-concrete and salt rock at the base. Thickness map of voids and porosity, computed as a projection along the core axis (top). Thickness of the joint merged with the basement surface structure (bottom). Sample diameter: 90 mm, length: 50 mm.

RESULTS. In general, the contact between concrete and host rock appeared tight. However, open joints were observed in the central zone of the floor. Analysis of the μ CT images shows that the maximum width of these voids is about 2 mm, and appears to be associated with centimeter-sized grooves in the floor (Fig. 1, upper right and detailed visualization in the lower part of the figure). The overall extent of this debonding structure is around 10–20 cm, as judged from a combination of four drill core sections (Fig. 2). The open joint is adjoined by a solid zone of concrete with indistinguishable porosity, followed by a thin porous zone with noticeable air bubbles transitioning to the porous structure of the bulk material (Fig. 1, upper part “MgO concrete”).

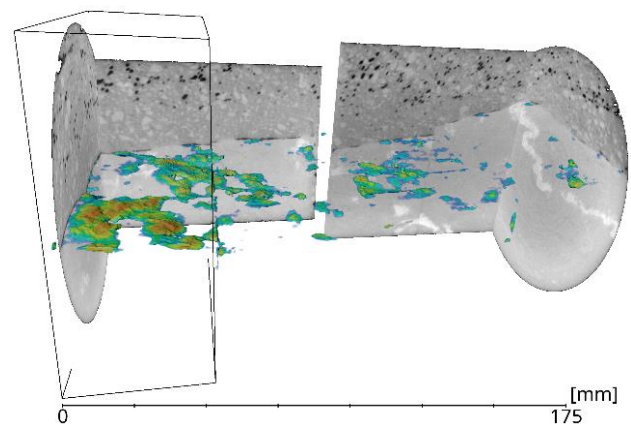


Figure 2. Void structure of four joined drill core sections. The labeled front section is shown in detail in Fig. 1. The other three core sections follow the first section to the right. The large-scale pore pattern was reconstructed by merging the four data sets (color coding as in Fig. 1). Note high density internal salt rock structures (white color).

The causes of these open structures are not yet understood. Possible reasons include the fluid dynamics of the slurry, the surface structure of the host rock floor, and the loss of moisture into the salt rock during concrete molding.

ACKNOWLEDGEMENTS. The project STROEFUN III was supported by the Federal Ministry for Economic Affairs and Climate Action (BMWK) (02E11748A/B). Project coordination by TU Clausthal under challenging conditions, the excellent cooperation with project partners (IBeWa, BGE Tec, and K-UTEC) as well as project management by PTKA are highly appreciated.

[1] Bauermeister, J. et al. (2023) Report: Strömungstechnischer Funktionsnachweis für Verschlussbauwerke und flüssigkeitsgestützte Abdichtung des Kontaktbereiches. TU Clausthal / TIB Hannover.

Cyclotron production of ^{95}Nb and its application for the quantitative description and mechanistic understanding of ^{94}Nb retention in L/ILW repositories

K. Franke

Niobium isotopes were produced at the cyclotron Cyclone 18/9 and supplied for the quantitative analysis of the uptake of niobium by hardened cement paste HCP in the degradation stage I (CEM III/C and CEM III/C + CaCO_3) and calcium silicate hydrate (C-S-H) phases.^[1] This considers cement-based repositories for low- and intermediate-level radioactive waste as deposits for ^{94}Nb as an activation product of ^{93}Nb in nuclear reactors. The strong uptake of Nb in cement with C-S-H as the main sink was decreased by the presence of isosaccharinic acid (ISA). No significant effect was observed for chloride (2M).^[1] Here, we report the details of the production of Nb isotopes now routinely available for subsequent and similar experimental approaches.

EXPERIMENTAL. The (d,x) nuclear reaction on a zirconium target was used to produce active Nb isotopes. A Zr foil (0.12 mm thick, 99.5% purity, Alfa Aesar) with the natural isotopic abundance was bombarded by 9 MeV deuterons with 700 μAh for 73 h using the COSTIS target station (IBA RadioPharma Solutions, Belgium) placed at a beam line at port 3 of the cyclotron Cyclone 18/9® (IBA RadioPharma Solutions, Belgium). The target was cooled at the front with helium (60 L min^{-1}) and at the back with water (16 L min^{-1}). A 12.5 μm titanium foil was used as the vacuum window of the target station. Four days after EOB (end of bombardment), the target was opened and transferred to γ -spectrometry (Fig. 1). The sample was placed 575 cm in front of an HPGe detector GEM C5060 (ORTEC) equipped with a DSPEC 50 system (ORTEC).



Figure 1. Opened target capsule after end of bombardment with the irradiated zirconium foil on top of the aluminum backing.

The irradiated Zr foil was dissolved in 48% HF, and the separation of the Nb isotopes from the bulk Zr was performed using a combination of ion-exchange resins (DOWEX® 50X8 and UTEVA). The separation process was developed on the basis of previously reported methods.^[2–4]

RESULTS. Yttrium and zirconium nuclides together with several niobium isotopes were detected in the zirconium foil after irradiation (Tab. 1). After target processing, the concentration and activities of the Nb and Zr isotopes in the stock solution were determined as follows:

- $[^{91\text{m}}\text{Nb}] = (3.1 \pm 0.1) \times 10^{-9} \text{ M}$ ($0.23 \pm 0.01 \text{ MBq mL}^{-1}$),
- $[^{92\text{m}}\text{Nb}] = (9.9 \pm 0.1) \times 10^{-10} \text{ M}$ ($0.47 \pm 0.02 \text{ MBq mL}^{-1}$),
- $[^{95}\text{Nb}] = (1.4 \pm 0.1) \times 10^{-9} \text{ M}$ ($0.20 \pm 0.01 \text{ MBq mL}^{-1}$), and

Table 1. Identified nuclides within the irradiated zirconium foil 4 d after EOB.^[1]

Nuclide	Activity [Bq]	Uncertainty [%]
^{88}Y	4.78E+05	1.11E-01
$^{90\text{m}}\text{Y}$	7.33E+05	3.84E-01
^{95}Zr	2.17E+07	1.85E-02
^{90}Nb	4.89E+04	1.04E+00
$^{91\text{m}}\text{Nb}$	7.45E+07	4.04E-01
$^{92\text{m}}\text{Nb}$	9.43E+07	6.55E-03
^{95}Nb	2.74E+07	1.10E-02
$^{95\text{m}}\text{Nb}$	2.46E+07	4.85E-02
^{96}Nb	5.72E+06	6.65E-02
^{97}Nb	1.16E+06	1.32E-01
$^{97\text{m}}\text{Nb}$	1.03E+06	3.38E-01

- $[^{95}\text{Zr}] < 6.6 \times 10^{-12} \text{ M}$ ($< 0.5 \text{ kBq mL}^{-1}$, detection limit of γ -spectrometry in the stock state with high activity of Nb isotopes).^[1]

In the sorption experiments with C-S-H phases linear sorption isotherms are obtained over almost eight orders of magnitude in terms of niobium concentration ($10^{-14} \text{ M} \leq C_{\text{aq}} \leq 10^{-5} \text{ M}$). For HCP and C-S-H phases a strong uptake was found, with $\log R_d = (5.5 \pm 0.6)$ and (6.5 ± 0.3) , respectively.^[1] A feasible retention mechanism of niobium in repositories for L/ILW is the isotopic exchange of ^{94}Nb with ^{93}Nb in cement.

The uptake of Nb(V) by HCP is significantly decreased in the presence of ISA in cement pore water, although a moderate sorption ($\log R_d \approx 3.5$) is maintained even at the highest ligand concentration investigated in this work ($[\text{ISA}]_{\text{tot}} = 0.1 \text{ M}$). Most likely ternary complexes (Ca-) Nb-ISA are formed.^[1] Additionally, no significant influence of chloride on the retention of Nb(V) by HCP sorption was observed in the ternary HCP-Nb/Cl and quaternary HCP-Nb/ISA/Cl systems.^[1]

[1] Jo, Y. *et al.* (2023) *Cement Concrete Res.* **172**, 107233.

[2] Çevirim-Papaioannou, N. *et al.* (2022) *Cement Concrete Res.* **153**, 106690.

[3] Busse, S. *et al.* (2002) *Radiochim. Acta* **90**, 411–415.

[4] Radchenko, V. *et al.* (2014) *Radiochim. Acta* **102**, 433–442.

Quantitative consideration of heterogeneities in crystalline rocks within geochemical simulations: a modular workflow

A. Duckstein, S. Pospiech, V. Brendler

The understanding and numerical modelling of hydro-geochemical processes is essential for the assessment of contaminant migration in groundwater systems, including applications in hazardous waste disposal. The SANGUR project deals with the question, which methods and parameters are relevant for the reactive transport with special focus on heterogeneities in crystalline rocks. Here, we are developing a workflow that combines data acquisition with geostatistical approaches and model reduction based on sensitivity analysis. Finally, this shall improve forecasting radionuclide retention in the far field of a nuclear waste repository.

THE SANGUR PROJECT. The SANGUR (Systematic sensitivity analysis for mechanistic geochemical models using field data from crystalline rock) project aims to improve the understanding and inclusion of the uncertainty of geological parameters associated with nuclear waste repositories in deep geological formations. The focus is on crystalline rock formations as host rocks (here: granites). Modelling heterogeneities of crystalline rock should address that the composition of mineral surfaces along fluid migration paths can differ considerably from the average composition of the rock as a whole. Therefore, geostatistical approaches will be applied that can describe not only the average composition of the rock, but also the average composition of the mineral surface and its variability along migration paths in terms of uncertainties. This is a prerequisite for the selection of realistic surface complexation models and parameters, which in turn allow the calculation of smart K_d matrices describing radionuclide migration patterns.^[1] This is followed by a sensitivity analysis to identify the most critical parameters.

To achieve all this, the expertise of three institutes will be integrated: Geochemical modelling and (radio)analytical work (HZDR, Institute for Resource Ecology), development and application of sensitivity analysis methods (Institute for Waste Management Research, TU Clausthal) and data acquisition and interpretation in crystalline rocks (ÚJV Řež, Czech Republic, as subcontractor of HZDR).

MODULAR WORKFLOW. The idea behind a modular, program-independent workflow is that individual steps can be adapted and exchanged separately, *e.g.*, depending on the host rock, data availability, or computer capacities. The workflow developed in SANGUR is illustrated in Fig. 1. The first step is to parameterize the site-specific environmental conditions (groundwater composition, radionuclides, rock composition) according to the scientific question. Using geostatistical approaches, not only field data gaps can be closed, but also a large number of realizations of the mineral composition along the migration path can be calculated to allow a good quantification of the variances and the investigation of the uncertainties. A subsequent consistency check will ensure that the simulated conditions are realistic.

In addition, site-independent data from thermodynamic databases are necessary. For this purpose, the HZDR provides a sorption database called RES³T with the focus on surface complexation.^[2] This is supported with data describing aqueous systems and mineral solubilities.^[3] A

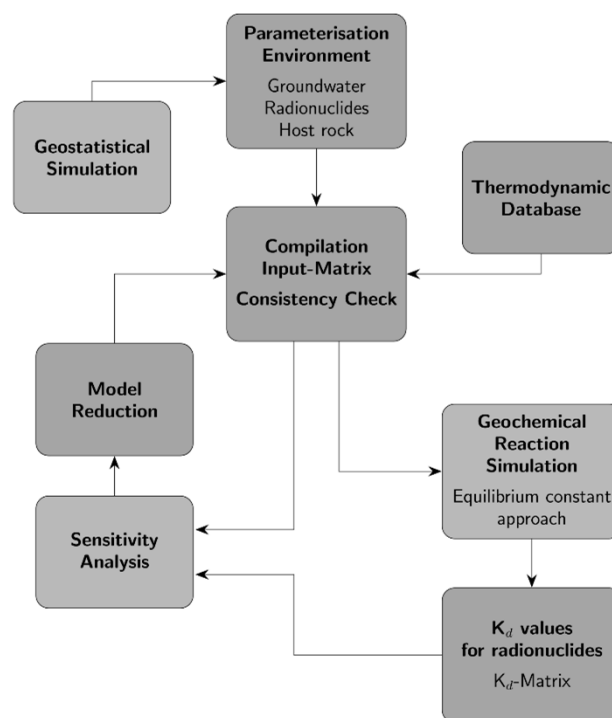


Figure 1. Modular Workflow for SANGUR.

combined mechanistic model then can provide distribution coefficients (K_d values) based on the principle of the equilibrium constant approach. Such smart K_d values are calculated for a variation of input parameters, resulting in K_d matrices.

Both the input matrix and the K_d matrix are included in the subsequent sensitivity analysis to identify how relevant certain parameters are for the simulation of radionuclide retention. This allows, on the one hand, a greater effort to be put into the determination of the most relevant parameter and its uncertainties and, on the other hand, parameters with less influence can be set as constants, leading to less complex and computational-time demanding models.

OUTLOOK. At present, work is being carried out on the simulation of heterogeneities in the rock. We are using the Multinary Random Fields approach, which allows a high number of realizations and thus a good estimation of the parameter uncertainties.^[4] In a first study, it will be determined on which order of scale heterogeneities have to be described or which size a representative volume element has to have in order to achieve optimum simulation results of the radionuclide retention in the crystalline rocks.

[1] Stockmann, M. *et al.* (2017) *Chemosphere* **187**, 277 – 285.

[2] RES³T-Rosendorf Expert System for Surface and Sorption Thermodynamics, www.hzdr.de/res3t.

[3] Hummel, W. *et al.* (2023) *The PSI Chemical Thermodynamic Database 2020*, nagra Technical Report 21–03, Wettingen Switzerland.

[4] Menzel, P. *et al.* (2020) *Math. Geosci.* **52**, 731–757.

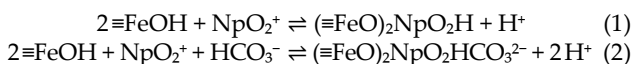
Sorption Reference Database SOREDA – Sorption of neptunium(V) onto ferrihydrite

F. Bok, S. Zechel

In the SOREDA project, literature sorption data is processed to create a consistent sorption database.^[1] Occasionally, the experimental data is insufficient for a direct derivation of reaction constants ($\log K^\circ$). This contribution describes how to proceed with unknown surface species stoichiometry and the application of estimation methods like Linear Free Energy Relationship (LFER) using the example of the sorption of mobile Np(V) on ferrihydrite (Fh) surface.

PROCEDURE. Spectroscopic investigations by Müller *et al.* revealed a bidentate binding of neptunyl(V) ions to hematite which was applied to Fh here.^[2] For the CO₂-free system, the experimental sorption data from Girvin *et al.* were used to derive the $\log K^\circ$.^[3] For the best possible description, the yet missing number of H⁺ released per sorbed NpO₂⁺ is also important. This was determined by slope analysis of the linearized expression of the law of mass action ("Kurbatov plot") and resulted in an NpO₂⁺/H⁺ ratio of 1:1 (Fig. 1).

The $\log K^\circ$ value for the formation reaction (1) was fitted using the geochemical speciation software "PhreePlot" with the PSI/Nagra Chemical Thermodynamic Database/TDB 2020 (Fig. 2).^[4,5]



No experimental literature data are available for the sorption of NpO₂⁺ onto Fh in the presence of carbonate. Since sorption on Fh showed almost identical behavior to that on goethite (Goe) for all sorptives investigated so far, the $\log K^\circ$ values of all surface complexes were correlated for U(VI), Np(V) and Th. From this linear free energy relation (LFER), the $\log K^\circ$ for the ternary neptunyl carbonate surface complex formation (2) could be estimated (Fig. 3). The obtained SCM data are given in Tab. 1.

Table 1. SCM parameters for the Np(V) sorption onto Fh.

Surface species	$\log K^\circ$
($\equiv\text{FeO}$) ₂ NpO ₂ H	-2.65 ± 0.03
($\equiv\text{FeO}$) ₂ NpO ₂ HCO ₃ ²⁻	-6.71 ± 0.08

The stated uncertainty refers to two standard deviation (2σ).

RESULTS. Unlike many available SCM datasets on Np(V) sorption in Fh in the absence of CO₂, the present one requires only one species – the spectroscopically evident one – and thus describes the available sorption data very well. This approach allows robust modeling with potential for extrapolation. Experimental data gaps in the CO₂ containing system could be closed by the LFER application.

ACKNOWLEDGEMENTS. SOREDA is funded by the Federal Company for Radioactive Waste Disposal (BGE; contract no. EKFuE-21-03-js).

[1] Zechel, S. *et al.* (2023) this report, p. 40.

[2] Müller, K. *et al.* (2015) *Environ. Sci. Technol.* **49**, 2560–2567.

[3] Girvin D. C. *et al.* (1991) *J. Colloid Interface Sci.* **141**, 67–78.

[4] Kinniburgh, D. *et al.* (2011) *PhreePlot: Creating graphical output with PHREEQC.*, <https://www.phreeplot.org>, 648 p.

[5] Hummel, W. *et al.* (2023) *The PSI Chemical Thermodynamic Database 2020*, nagra Technical Report 21–03, Wettingen, Switzerland.

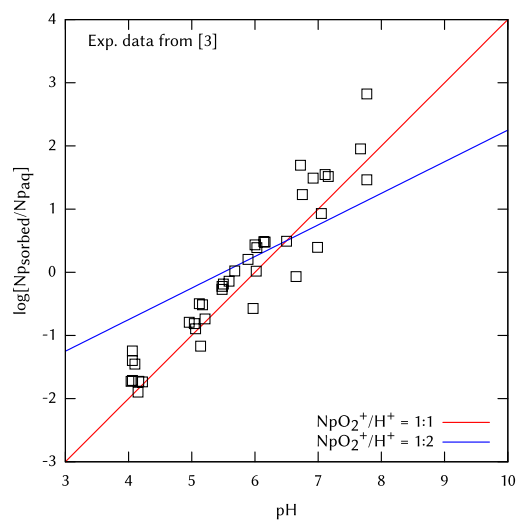


Figure 1. Kurbatov plot for determining the number of H⁺ released during the sorption of NpO₂⁺ on ferrihydrite. Symbols: experimental data.^[3] Lines: calculation with a NpO₂⁺/H⁺ ratio of 1:1 (red) or 1:2 (blue).

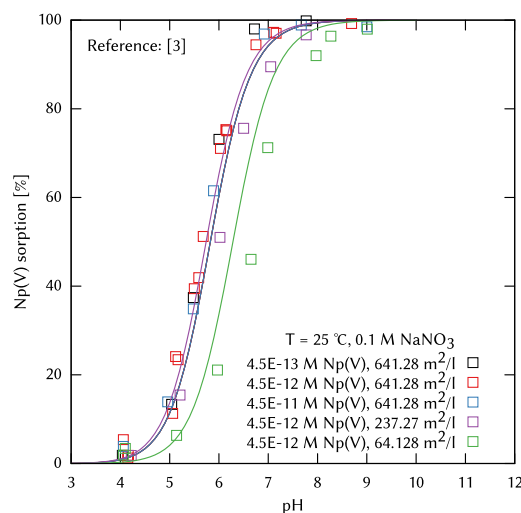


Figure 2. Sorption of Np(V) onto ferrihydrite in absence of carbonate. Symbols: experimental data.^[3] Lines: Calculations (this work).

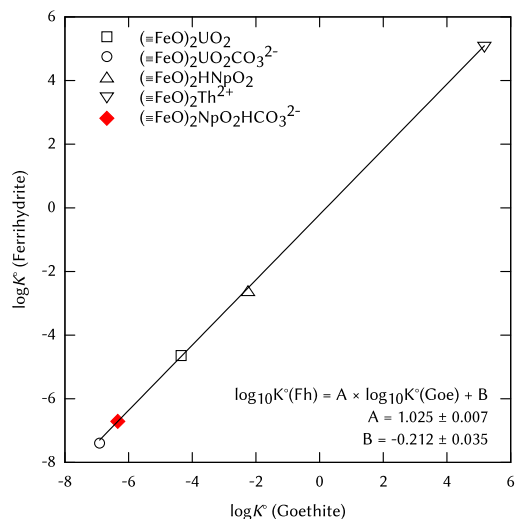


Figure 3. Determination of the ($\equiv\text{FeO}$)₂NpO₂HCO₃²⁻ formation constant using LFER between ferrihydrite (Fh) and goethite (Goe) surface complexation constants of U, Np and Th.

Sorption Reference Database SOREDA – A robust model for uranyl sorption onto quartz

S. Zechel, F. Bok

The SOREDA project addresses the creation of quality-assured surface complexation modeling (SCM) data sets for the sorption of radionuclides on common mineral phases. For this purpose, experimental data from literature are critically reviewed to derive reaction constants ($\log K^\circ$) for the formation of spectroscopically evident surface species. The procedure for data generation is explained here using the sorption of uranium(VI) on quartz as an example. This is a sorbate of particular interest due to the high mobility of hexavalent uranium and the ubiquitous occurrence of the mineral phase.

DATA SELECTION. Based on the calculation of the surface site density of quartz using crystallographic data, it became possible to determine the constants of the protolysis and sorption reactions in order to create a consistent SCM dataset.^[1] Therefore, potentiometric titration as well as batch sorption data were collected from the literature. These were critically evaluated with regard to completeness of given experimental conditions: proper mineral characterization, ionic strength and background electrolyte, sorptive and carbonate concentration, sorption of > 1%, experimental temperature of 25 °C, and in potentiometric titrations a specific surface area (SSA) > 10 m²/L as well as plausibility of the given points of zero charge. Matching datasets were then re-digitized using “Engauge Digitizer”, duplicates removed and converted to the target quantities intended for the fits (surface charge [C/m²] for protolysis data, sorbed fraction [%] for sorption data).^[2]

FITTING PROCEDURE. For the fitting of the reaction constants with the Diffuse Double Layer model (DDL), the software “PHREEQC” coupled with “UCODE_2014” were used. The PSI/Nagra Chemical Thermodynamic Database/TDB 2020 served as a quality-assured thermodynamic data collection for aquatic chemistry and mineral solubility.^[3–5] **Protolysis:** Due to the very low PZC of quartz, only the $\log K^\circ$ value of the second protolysis reaction (1) was required. Fig. 1 shows a part of the protolysis model demonstrating a very good agreement between the experimental titration data and the modeling.^[6–10] **Sorption:** The determination of the sorption reaction’s $\log K^\circ$ was carried out using spectroscopically evident surface species.^[11] Due to the lack of sorption data under CO₂-free conditions in the literature, only experimental data in the presence of carbonate could be used in the fitting procedure. However, it turned out that the best description of the data is possible using the bidentate surface complex (2) only (Fig. 2). The model parameters are given in Tab. 1.

RESULTS. In contrast to many SCM datasets from the literature here only one surface species was necessary to give a very good description of the uranyl sorption on quartz. The model was derived using 221 batch sorption experiments with a broad variety of experimental conditions like uranium concentration, ionic strength with different background electrolytes, solid-liquid ratio, pH range and so on. The resulting surface complexation model is characterized by robustness and the potential for extrapolation to other chemical conditions.

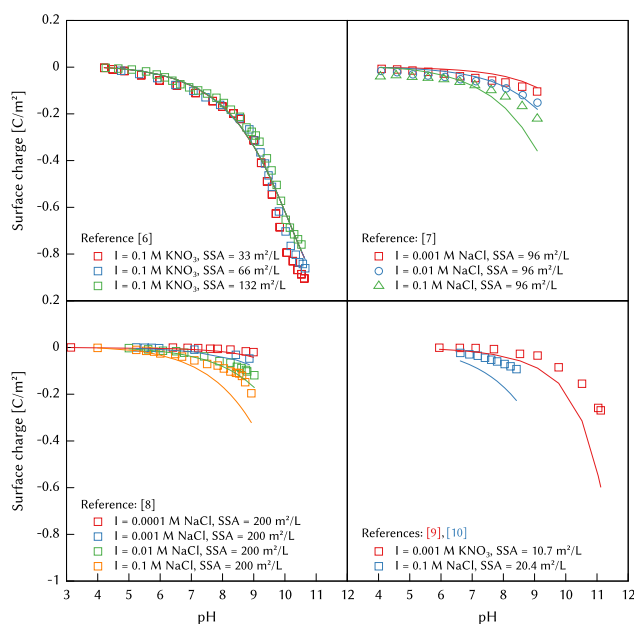


Figure 1. Potentiometric titration of quartz surface. Symbols: experimental data.^[6–10] Lines: calculations (this work).

Table 1. SCM parameters for the U(VI) sorption onto Quartz.

No.	Surface reaction	$\log K^\circ$
(1)	$\equiv\text{SiOH} \rightleftharpoons \equiv\text{SiO}^- + \text{H}^+$	-7.18 ± 0.04
(2)	$2\equiv\text{SiOH} + \text{UO}_2^{2+} \rightleftharpoons (\equiv\text{SiO})_2\text{UO}_2 + 2\text{H}^+$	-5.37 ± 0.02

The stated uncertainty refers to two standard deviations (2σ).

ACKNOWLEDGEMENTS. SOREDA is funded by the Federal Company for Radioactive Waste Disposal (BGE) with the contract number EKFuE-21-03-js.

- [1] Zechel, S. et al. (2023) *HZDR-Report-122*, p. 47.
- [2] Mitchell, M. et al. (2020) Engauge Digitizer, <https://github.com/markumitchell/engauge-digitizer> (2023-01-09).
- [3] Parkhurst, D.L. and Appelo, C.A.J. (2013) *Description of input and examples for PHREEQC version 3 – A computer program for speciation, batch-reaction, one-dimensional transport, and inverse geochemical calculations.*, U.S. Geological Survey Techniques and Methods, book 6, chap. A43, 497 p.
- [4] Lu, D. et al. (2014) *Environ. Model. Softw.* **25**, 457–462.
- [5] Hummel, W. et al. (2023) *The PSI Chemical Thermodynamic Database 2020*, nagra Technical Report 21-03, Wettingen Switzerland.
- [6] Tao, Z. et al. (2002) *J. Coll. Int. Sci.* **252**, 15–20.
- [7] Michael, H.L. et al. (1984) *J. Electroanal. Chem.*, **179**, 131–139.
- [8] Riese, A.C. (1982) *Adsorption of radium and thorium onto quartz and kaolinite: A comparison of solution/surface equilibria models*, Ph.D. thesis, 292 p.
- [9] Ahmed, S.M. (1966) *Canad. J. Chem.* **44**, 1663–1670.
- [10] Kitamura, A. et al. (1996) *J. Nucl. Sci. Technol.* **33**, 840–845.
- [11] Reich, T. et al. (1998) *J. Elec. Spec. Rel. Phe.* **96**, 237–243.
- [12] Davis, J.A. (2001) *Surface Complexation Modelling of Uranium(VI) Adsorption on Natural Mineral Assemblages*, NUREG/CR-6708.
- [13] Dong, W. et al. (2001) *Environ. Sci. Technol.* **48**, 6569–6577.
- [14] Fox, P.M. et al. (2006) *Geochim. Cosmochim. Acta.* **70**, 1379–1387.
- [15] Pabalan, R.T. et al. (1998) *Adsorption of metals by geomeedia. Variables, mechanisms, and model applications*, Academic Press, 99–130.
- [16] Arnold, T. et al. (2001) *J. Cont. Hydrol.* **47**, 219–231.

See next page for Fig. 2.

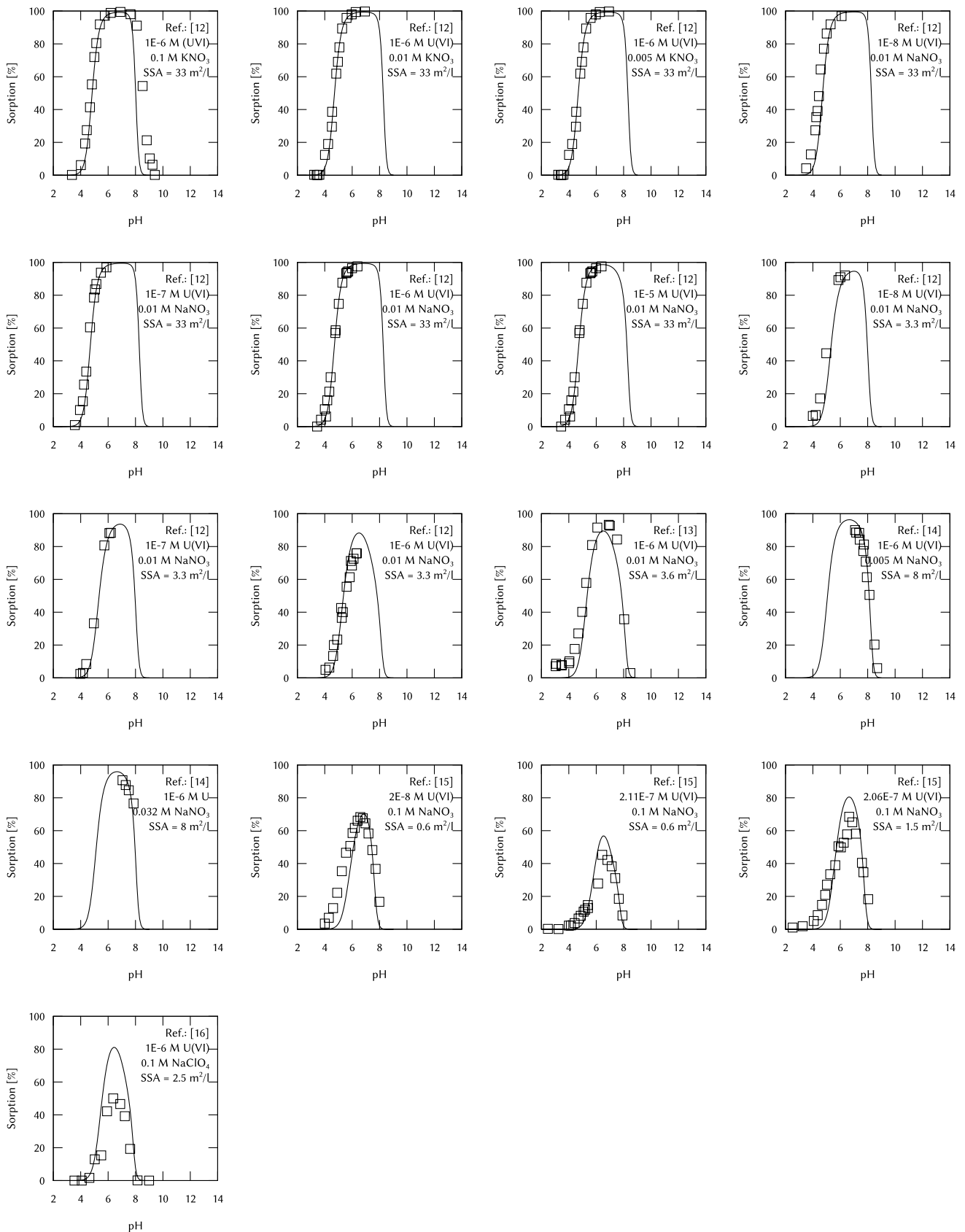


Figure 2. Sorption of uranium(V) onto quartz surface with air atmosphere at $\vartheta \cong 25^\circ\text{C}$. Symbols: experimental data.^[11–16] Lines: calculations (this work).

Thermodynamic data of the double salt $\text{CsCl} \cdot 2\text{NaCl} \cdot 2\text{H}_2\text{O}(\text{cr})$

F. Bok

In the ternary salt system $\text{CsCl}-\text{NaCl}-\text{H}_2\text{O}(\text{l})$, a double salt is known to be formed having the stoichiometric formula $\text{CsCl} \cdot 2\text{NaCl} \cdot 2\text{H}_2\text{O}(\text{cr})$.^[1] This double salt as well as $\text{CsCl}(\text{cr})$ are the end-members of a solid solution. For the pure double salt, the solubility product was determined. The obtained data were applied to calculate higher systems like the solubility diagram of the quaternary system $\text{CsCl}-\text{NaCl}-\text{KCl}-\text{H}_2\text{O}(\text{l})$.

Knowledge of the behavior of fission products such as cesium is crucial for safety calculations in the context of a repository for radioactive waste. If rock salt (NaCl) is selected as the host rock, the $\text{CsCl}-\text{NaCl}-\text{H}_2\text{O}(\text{l})$ system is of particular interest for cesium. Solubility studies have been carried out for the system,^[1–6] but no thermodynamic values have been determined so far for the occurring double salt with the formula ($\text{CsCl} \cdot 2\text{NaCl} \cdot 2\text{H}_2\text{O}$), which is also an end-member of a solid solution with CsCl .

PROCEDURE AND RESULTS. For the solubility product determination of the double salt, the compositions of the invariant point $\text{NaCl}(\text{cr}) + \text{CsCl} \cdot 2\text{NaCl} \cdot 2\text{H}_2\text{O}(\text{cr})$ available in the literature were recalculated to molal scale and fitted using the geochemical speciation code PHREEQC couples with the numerical parameter estimation software Ucode_2014.^[7,8] The THEREDA Pitzer dataset was used as corresponding thermodynamic database to ensure consistency.^[9,10] The Gibbs free energy of reaction ($\Delta_r G^\circ$) (Eq. 1) as well as the Gibbs free energy of formation ($\Delta_f G^\circ$) were calculated from the formation constant ($\log K^\circ$) obtained. Results are given in Tab. 1.

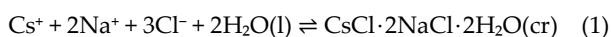


Table 1. Thermodynamic parameters for $\text{CsCl} \cdot 2\text{NaCl} \cdot 2\text{H}_2\text{O}(\text{cr})$.

Data Type	Value ± Uncertainty
$\log K^\circ$ (Eq. 1)	$-4.288 \pm 0.014^\dagger$
$\Delta_r G^\circ$ [J/mol]	$24,476 \pm 79^\ddagger$
$\Delta_f G^\circ$ [J/mol]	$-1,658,820 \pm 1,416^\ddagger$

[†]The stated uncertainty refers to two standard deviation (2σ).

[‡]Uncertainty calculated from $\log K^\circ$'s uncertainty.

APPLICATION. With the obtained thermodynamic dataset for the double salt in combination with an ideal solid solution model, it is now possible to fully describe the solubility in the ternary system $\text{CsCl}-\text{NaCl}-\text{H}_2\text{O}(\text{l})$ (Fig. 1). The dataset is consistent to the THEREDA Pitzer dataset.^[10] No further adjustment of the Pitzer interaction coefficients or other solubility products of the solid phases in this system were necessary.

The result shows a very good agreement between the calculation and the experimental values. Testing the effects of the introduction of the new double salt, the solubility data for the quaternary system $\text{CsCl}-\text{NaCl}-\text{KCl}-\text{H}_2\text{O}(\text{l})$ were successfully recalculated (Fig. 2), all dominant phases are correctly depicted. Test calculations in the even more complex reciprocal-quaternary system $\text{Cs}^+, \text{Na}^+ \parallel \text{Cl}^-, \text{SO}_4^{2-}-\text{H}_2\text{O}(\text{l})$ are shown elsewhere.^[11]

ACKNOWLEDGEMENTS. Many thanks to Wolfgang Voigt and Julia Sohr (TU Bergakademie Freiberg) for fruitful discussions. THEREDA is funded by the Federal Company for Radioactive Waste Disposal (BGE; contract no. 45181017).

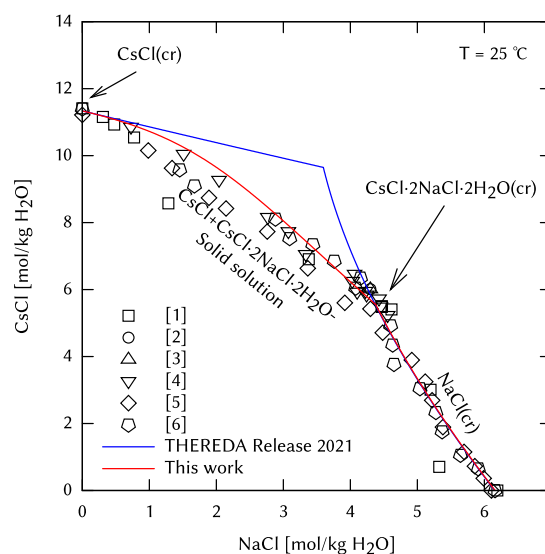


Figure 1. Solubility diagram of the ternary system $\text{CsCl}-\text{NaCl}-\text{H}_2\text{O}(\text{l})$. Points: experimental solubility data.^[1–6] Lines: Calculations using THEREDA without (blue) and with (red) double salt and a solid solution.

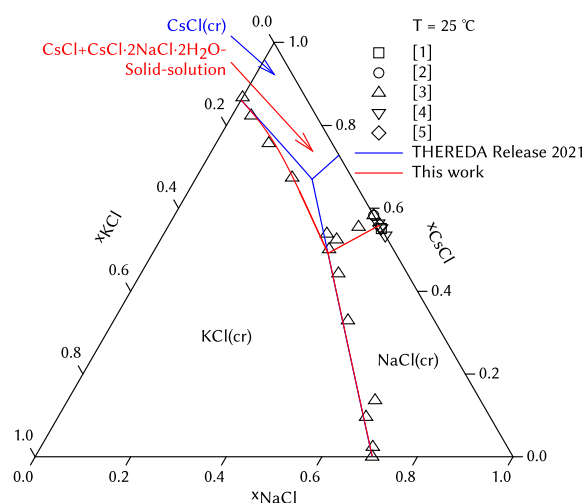


Figure 2. Solubility diagram of the quaternary system $\text{CsCl}-\text{NaCl}-\text{KCl}-\text{H}_2\text{O}(\text{l})$. Points: experimental solubility data.^[1–5] Lines: Calculations using THEREDA without (blue) and with (red) double salt and a solid solution.

- [1] Plyushchev, V. E. *et al.* (1957) *Zh. Neorg. Khim.* **2**, 2655–2660.
- [2] Arkhipov, S. M. *et al.* (1970) *Zh. Neorg. Khim.* **15**, 1086–1089.
- [3] Arkhipov, S. M. *et al.* (1984) *Zh. Neorg. Khim.* **29**, 2704–2705.
- [4] Chou, I-M. *et al.* (1983) *J. Chem. Eng. Data* **28**, 393–396.
- [5] Gao, Y. *et al.* (2017) *J. Chem. Eng. Data* **62**, 2533–2540.
- [6] Balarew, C. *et al.* (1975) *C. R. Acad. Bulg. Sci.* **28**, 221–223.
- [7] Parkhurst, D. L. *et al.* (2013) *Description of input and examples for PHREEQC version 3—a computer program for speciation, batch-reaction, onedimensional transport, and inverse geo-chemical calculations*. U.S. Geological Survey, Book 6, Chapter 43, Section A of Techniques and Methods, 497 p.
- [8] Lu, D. *et al.* (2014) *Environ. Model. Softw.* **25**, 457–462.
- [9] Scharge, T. *et al.* (2012) *J. Chem. Eng. Data* **57**, 1637–1647.
- [10] THEREDA Thermodynamic Reference Database: www.thereda.de.
- [11] Bok, F. (2023) *THEREDA J.* **3**, 1–6.

SCIENTIFIC CONTRIBUTIONS (PART III)

Biological Systems

Long-Lived Radionuclides in

**BIOLOGICAL
SYSTEMS**

How the radioactive elements Am³⁺ and Cm³⁺ interact with Lanthanide-using bacteria

R. Steudtner, H. Singer,¹ B. Drobot, L. Daumann²

¹Ludwig-Maximilians-University, Department of Chemistry, Munich, Germany; ²Heinrich-Heine-University, Bioinorganic Chemistry, Düsseldorf, Germany

The biological relevance of early lanthanides (Lns), such as neodymium, remained undiscovered until methylotrophic bacteria with lanthanide-dependent metabolism were identified. The respective strains incorporate these Lewis acids into the active site of their key metabolic enzyme methanol dehydrogenase. Here, we investigate how the ionic radii of the f-block elements affect these biological systems by replacing the lanthanides with actinides (Ans). Growth studies with two strains, the extremophilic bacterium *Methylobacterium furmariolicum* SolV and the mesophilic *Methylobacterium extorquens* AM1 ΔmxA mutant, demonstrate that the trivalent actinides americium and curium easily complement the essential lanthanides in bacterial metabolism. In fact, the bacteria make no distinction between Lns and Ans if they have the right size and oxidation state.

Here, we investigate the effect of the radioactive Ans Am³⁺ and Cm³⁺ on the activity of Ln-dependent methanol dehydrogenases as well as on the growth of Ln-using and -dependent bacteria. These two Ans were chosen because they have similar properties to the early Lns: Am and Cm are stable in +III oxidation state, and their size matches Nd³⁺ (98.3 pm, with Am³⁺ 98.0 pm and Cm³⁺ 97.0 pm). Replacing the Lns by the described Ans, conclusions can be drawn about the influence of size in combination with oxidation state of metal ions in Ln-dependent biological systems.

EXPERIMENTAL. To evaluate which Ans could be used instead of Lns by *M. furmariolicum* SolV and *M. extorquens* AM1, we set up different growth experiments screening for (i) ability to grow on actinides and (ii) evaluating concentration dependence. The methanotrophic strain SolV requires an atmosphere of air supplemented with CH₄ and CO₂, 55 °C and a pH of 2–3 for life. All experimental details are summarized in our publication.^[1]

RESULTS. Using the bacterial strains *M. furmariolicum* SolV and *M. extorquens* AM1 and their respective lanthanide-dependent methanol dehydrogenases, we investigated the effect of the size of the f-element Lewis acid on bacteria and their enzymes. We demonstrate that trivalent Ans Am³⁺ and Cm³⁺ with a similar ionic radius as the early Lns such as neodymium elicit a similar growth response as well as comparable enzymatic activity. The growth of SolV and AM1 was monitored with different Ln and An, and with different concentration of selected Ln and An. The depletion of metals from the growth medium was investigated with LSC and ICP-MS and shows an inverted course – while the biomass increases with ongoing time, the concentration of metals in the medium decreases. Time-resolved laser-induced fluorescence spectra clearly confirm the uptake of Ln and An by the Ln-dependent bacterial strains. Studying the enzymatic activity of the Ln-dependent MDH with a dye-coupled assay revealed similar substrate conversion rates of An and early Ln. Due to the moderate growth conditions in contrast to SolV, the strain AM1 might be a potential candidate for cleaning

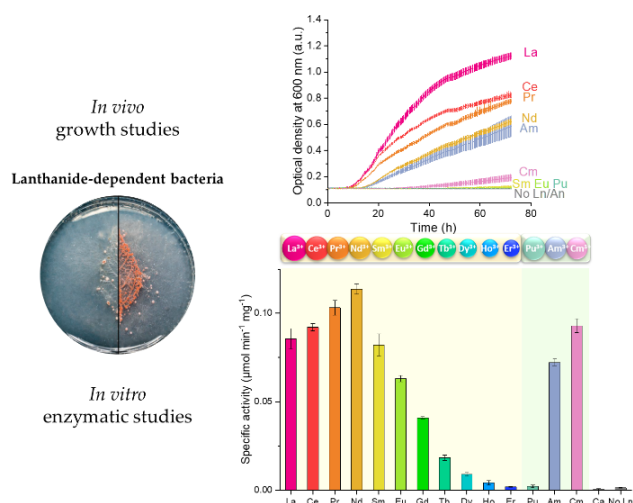


Figure 1. Methylotrophic bacteria utilize Ans instead of Lns to sustain their metabolism: Studies with two bacterial Ln-using strains demonstrate that the trivalent radioactive 5f elements Am³⁺ and Cm³⁺ can support growth. Also, catalytic activity of the Ln-dependent methanol dehydrogenases with Ans is shown. For the first time it is established that Ans can play a beneficial role in biological metabolism.^[1]

spilled radioactive material, e.g., for the decontamination of radioactive contaminated soils. For AM1, it has previously been demonstrated that one of its Ln-dependent proteins also functions with An. More specifically, it has been shown that Lanmodulin can bind Ans very well, in some cases even with higher affinities than Lns. Further, methylotrophic bacteria such as AM1 possess dedicated uptake mechanisms for the poorly bioavailable Lns. One such cluster, the Ln-chelating cluster has recently been characterized and suggests the production of chelator similar to siderophores. It is well documented that Ans can bind to siderophores and siderophore-like molecules and that these are recognized by binding partners such as siderocalin. The isolation of such chelators from Ln-dependent bacteria could thus advance An-chelation therapies. Extremophilic organisms, thriving at low pH such as SolV can be used in recycling of Lns and Ans from e.g., end of lifetime resources, industrial feedstocks or metal leachates. For the latter, mostly harsh chemical conditions, e.g., low pH values in combination with high temperatures, are required for a good solubility of the metals that is tolerable for the extremophilic bacteria. The results presented here pave the way to use extremophilic bacteria for the recycling and/or separation of Lns and Ans. In addition, our work paves the way for the future use of Ln-dependent strains in bioremediation and provides insight into possible pathways of microbial driven mobility of actinides in the environment.

ACKNOWLEDGEMENTS. This work is licensed under Angewandte Chemie International Edition – <https://doi.org/10.1002/anie.202303669>^[1]

[1] Singer, H. et al. (2023) *Angew. Chem. Int. Ed.* **62**, e20230366.

Eu(III) as luminescence probe for microscopy and speciation analyses in *Brassica napus* plants

J. Jessat, H. Moll, W. A. John,¹ M. Vogel, R. Steudtner, B. Drobot,² R. Hübner, T. Stumpf, S. Sachs

¹VKTA – Strahlenschutz, Analytik Entsorgung Rossendorf e.V., Germany; ²HZDR, Institute of Ion Beam Physics and Materials Research, Dresden, Germany

Eu(III) as an analogue for trivalent actinides was used as a luminescence probe for combined microscopic and chemical speciation analyses of Eu(III) in *Brassica napus* plants. As a result, three Eu(III) species were identified in root tissue. We could show that different Eu(III) species occur simultaneously within root tissue and in hydroponic solution.

The assessment of the radionuclide transfer in the environment up to the food chain requires a deeper process understanding at the molecular level. The focus of this study was to characterize the uptake of Eu(III) as an analogue for trivalent actinides in *Brassica napus* plants by microscopic and in particular by chemical speciation mapping.^[1] The Eu(III) speciation in solution and in plants was further studied by ultraviolet (UV) excitation and site selective time-resolved laser-induced fluorescence spectroscopy (TRLFS) as well as scanning transmission electron microscopy combined with energy-dispersive X-ray spectroscopy ((S)TEM-EDXS).

EXPERIMENTAL. After germination and root formation, young *B. napus* plants were cultivated in half-strength modified Hoagland medium with a pH of 5.5. For Eu(III) exposure, plants were spiked with 30 or 200 μM Eu(III) in an HR_{red} nutrient solution. After 1, 4, 24, 48, and 72 h of exposure, nutrient media samples were taken and their Eu content was analyzed by inductively coupled plasma mass spectrometry. After 72 h of exposure, the plants were removed from the nutrient solutions and processed as described in Jessat *et al.*^[1] Fluorescence mapping of Eu(III)-loaded plant parts after 72 h of exposure (200 μM Eu(III)) was performed with a Raman microscope (LabRAM system, HORIBA Yvon, Lyon, France). HR_{red} nutrient solutions and plant parts were analyzed for Eu(III) speciation by TRLFS with UV excitation at 394 nm and site-selective TRLFS. Root tissue was also analyzed by (S)TEM-EDXS. All experimental details are summarized in literature.^[1]

RESULTS. Upon plant exposure to 30 μM Eu(III), a strong increase in the amount of bioassociated Eu(III) was observed within the first 4 h followed by a gradual increase up to 24 h. Finally, an equilibrium was reached where about 87 % of Eu was immobilized by interaction with the plant. In the presence of 200 μM Eu(III), again a rapid increase of bioassociated Eu was initially detected up to 4 h after exposure. After 24 h, a further, slower increase in bioassociation took place, reaching the maximum of 62 % immobilized Eu after 72 h. An equilibrium state was not reached. Most of the Eu was immobilized at the roots, while only traces were found in the shoot and leaves. Luminescence spectroscopy of Eu(III) demonstrated the occurrence of two Eu(III) species with clearly different spectral characteristics for Eu(III) in HR_{red} solutions over the entire duration of the experiment. Eu(III) species 1 could be assigned to the free Eu³⁺ aquo ion. The spectral characteristics of Eu(III) species 2 led to the conclusion that a Eu(III)-EDTA complex is formed. NaFeEDTA is part of the used HR_{red} solutions. From the time dependent course of both species, it can be concluded that the EDTA

is made available for complex formation with Eu(III) when Fe from the Fe-EDTA complex is taken up by the plant. Luminescence data of a whole *B. napus* plant showed the occurrence of only one Eu(III) species in the plant. Based on the spectral characteristics (F_1/F_2 peak ratio), we conclude that this species is not the Eu³⁺ aquo ion. The Eu(III)-species distribution in thin roots and cross sections of thick roots was analyzed by fluorescence spectroscopic mapping for exposure to 200 μM Eu(III). Three Eu(III) species could be localized. Two species (green and magenta in Fig. 1) are located in the vascular bundle of the root. The third species (blue in Fig. 1) is mainly located in the cortex and on the epidermis. The magenta species shows similar spectroscopic parameters with Eu(III) complexed with organic acids like citric acid or malic acid.^[2,3] The spectral shape of the green species leads to an assignment of Eu(III) complexed with organic phosphate. In the blue species, Eu(III) is most likely complexed to root tissue (cell walls, proteins). Site-selective TRLFS of Eu(III) exposed root tissue indicated the formation of low symmetry Eu(III) species with a strong inner-sphere character. The site-selective luminescence spectra represent sum data composed of the three Eu(III) species identified by chemical microscopy. (S)TEM-EDXS experiments showed that Eu signals were detected throughout the root cross-section from the periphery to the xylem vessels. Eu was immobilized within the cell walls as very dense phosphate precipitates, demonstrating that the cell wall acts as a sink for metals. Moreover, Eu was also found immobilized to lipid bilayers at the plasma membrane and in certain organelles or vesicles of cortical cells.

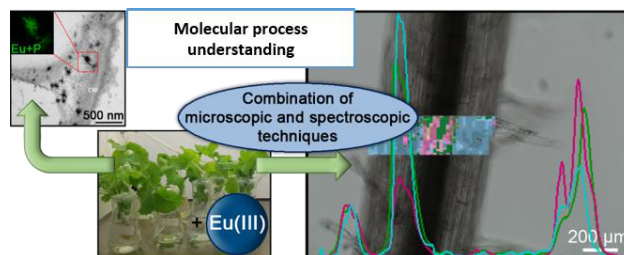


Figure 1. The use of Eu(III) as molecular probe for heavy metal interactions of potentially toxic metals with *Brassica napus* plants.^[1]

For the first time, the interaction of Eu(III) with *B. napus* plants was studied and the individual processes of Eu accumulation, sorption, complexation, and precipitation were described in more detail.

MISCELLANEOUS. This work is licensed under Ecotoxicology and Environmental Safety <https://doi.org/10.1016/j.ecoenv.2023.114741>.^[1]

ACKNOWLEDGEMENTS. This work was partly funded by the German Federal Ministry of Education and Research under contract number 02NUK051B.

- [1] Jessat, J. *et al.* (2023) *Ecotox. Environ. Safe.* **254**, 114741.
- [2] Heller, A. *et al.* (2012) *Dalton Trans.* **41**, 13969–13983.
- [3] Taube, F. *et al.* (2019) *Inorg. Chem.* **58**, 368–381.

Tobacco (*Nicotiana tabacum*) BY-2 cells induce the intracellular precipitation of metal oxalate biominerals for detoxification of lanthanides

M. Klotzsche, M. Vogel,¹ S. Sachs, J. Raff, T. Stumpf, B. Drobot, R. Steudtner

¹VKTA – Strahlenschutz, Analytik & Entsorgung Rossendorf e.V., Dresden, Germany

Suspension cells of tobacco BY-2 were exposed to Eu(III) to elucidate molecular interactions of lanthanides (Ln) with plant cells. The applied analytical approach revealed the presence of four distinct Eu(III) species located in different cellular compartments to which binding motifs could be assigned. BY-2 cells were found to induce the precipitation of Eu(III)-containing oxalate biominerals to mitigate an excess of free Ln ions. Oxalate crystals were obtained in analogous experiments with Gd and Sm as well.

Lanthanides have become indispensable for science, industry and many high-technology products. Their widespread use leads to anthropogenic input of these metals into the environment. Knowledge of their environmental fate is crucial for appropriate risk assessments and for developing remediation strategies. In order to understand metal–plant interactions at a molecular level, a suspension cell culture of tobacco BY-2 was exposed to 100 μ M Eu(III) as strong luminescent probe and representative of other trivalent Ln. A combination of biochemical methods, luminescence spectroscopy and chemical microscopy was applied to elucidate the bioassociation behavior and spatial distribution of the metal.

EXPERIMENTAL. Tobacco (*Nicotiana tabacum*) Bright Yellow 2 (BY-2) cells were cultivated as described by Rajabi *et al.*^[1] 1 mL of a 96-h BY-2 culture was transferred into 30 mL of MS_{red} medium with a reduced phosphate content and corresponding amount of Eu(III). Cells were separated from the culture medium and washed. For TRLFS analysis, cell pellets were readily analyzed at $\lambda_{exc} = 394$ nm and subsequent PARAFAC data analysis. Cells for chemical microscopy were fixed with paraformaldehyde, washed with TRIS-mannitol buffer and analyzed with a Raman microscope at $\lambda_{exc} = 532$ and 633 nm. The datasets were deconvoluted by Non-negative Iterative Factor Analysis (NIFA).

RESULTS. Immediately after the first contact of Eu(III) and BY-2 cells, a Eu(III) species with a luminescence lifetime of $\tau_1 = 190$ μ s was detected in the cell pellet indicating an instantaneous coordination to functional groups on the cell wall, *e.g.*, carboxylate or hydroxyl groups. According to the results of PARAFAC analysis, a formation of another species occurred between 24 h and 48 h exposure time, showing a change of the peak intensity ratios, peak shapes and a luminescence lifetime of $\tau_2 = 219$ μ s.

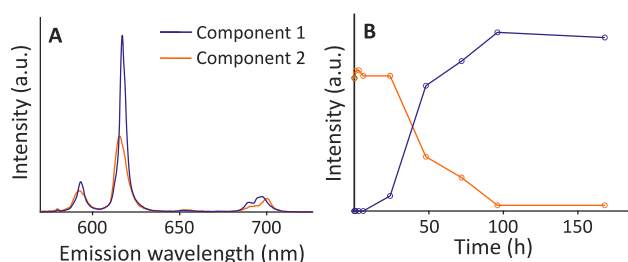


Figure 1. PARAFAC deconvolution results from TRLFS data of cell pellets. Single component spectra (A), species distribution with exposure time (B).^[2]

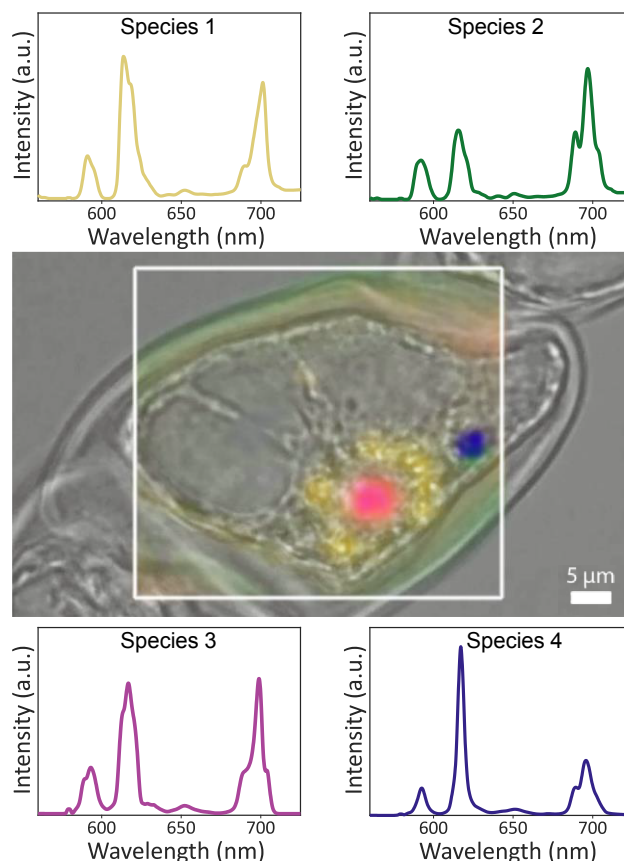


Figure 2. Single component luminescence spectra and microscopic image with local distribution of respective Eu(III) species, derived from NIFA.^[2]

In order to unravel the location and distribution of these Eu(III) components, microspectroscopic mappings were conducted. In fact, four distinct Eu(III) species were detected in the cells, which we assigned to species coordinating with (i) organic phosphate groups of DNA or RNA (species 1, yellow), with (ii) carboxylate and hydroxyl groups of *e.g.*, polysaccharides (species 2, green), (iii) protein-bound Eu(III) (species 3, magenta), and (iv) a species which matched component 2 from TRLFS measurements. Upon light microscopic examination of species 4 and subsequent Raman measurements, we discovered a Eu(III)-containing crystal-like structure exhibiting unambiguous signals of oxalate minerals. In analogous experiments with the lanthanides Gd and Sm, we observed similar biominerals. Hence, we hypothesized that biomineralization of Ln(III)-containing oxalates is a detoxification pathway to mitigate an excess of Ln ions in tobacco BY-2 cells.

MISCELLANEOUS. This work is licensed under RSC Analyst <https://doi.org/10.1039/D3AN00741C>.^[2]

ACKNOWLEDGEMENTS. The authors thank Prof. P. Nick (Botanical Institute, KIT) for providing the first batch of BY-2 cells, J. Seibt and S. Beutner for experimental support. The research was funded by the BMBF as a part of the joint project RENA (contract no. 02NUK066A).

[1] Rajabi, F. *et al.* (2021) *Ecotoxicol. Environ. Saf.* **211**, 111883.

[2] Klotzsche, M. *et al.* (2023) *Analyst* **19**, 4561–4908.

Uranium toxicity on plant cells: Differentiation between chemotoxic and radiotoxic effects by isothermal microcalorimetry

S. Sachs, J. Oertel, K. Fahmy

Applying “isotope-editing”, *i.e.*, the use of different U isotopes in isothermal microcalorimetric measurements, it was possible to detect the radiotoxic effect of ^{233}U as α -emitter on *Brassica napus* plant cells.

The uptake of radionuclides (RNs) into the food chain is a central concern in radioecology. It is speciation dependent and may induce several stress response reactions that change the plant metabolism. In a previous work, we applied isothermal microcalorimetry (IMC) as a sensitive real-time monitoring to study the chemical toxicity of uranium (U) with canola (*Brassica napus*) cells.^[1] We were able to monitor the metabolic activity of the cells in the presence of U and to correlate this with the oxidoreductase activity of the cells and the U speciation in solution. Due to the ionizing radiation, RNs can have not only chemotoxic but also radiotoxic effects, which are difficult to distinguish and to evaluate at low doses in a realistic environment. In our recent IMC study, we investigated the possibilities of “isotope-editing”, *i.e.*, the use of different isotopes of an element, to distinguish chemotoxic and radiotoxic effects on the heat metabolism of cultured cells. In this context, the toxicity of U on *B. napus* cells was studied in the presence of natural U (U_{nat}) and ^{233}U as α -emitter.^[2]

EXPERIMENTAL. *B. napus* suspension cells were cultivated in liquid modified Linsmaier and Skoog medium (medium R).^[1] For microcalorimetric experiments, cells were suspended in medium R with a reduced phosphate concentration (R_{red}) to limit the precipitation of poorly soluble U(VI) phosphate complexes. To differentiate between the radiotoxic and chemotoxic effects of U, *B. napus* cells were simultaneously exposed to U_{nat} as well as ^{233}U , with the concentration of U_{nat} in medium R_{red} varied between $50\ \mu\text{M}$ and $35\ \mu\text{M}$ and that of ^{233}U between 0 and $15\ \mu\text{M}$. The total U concentration of $50\ \mu\text{M}$ ($\text{U}_{\text{nat}} + ^{233}\text{U}$) was always kept constant. Control samples of medium R_{red} containing *B. napus* cells without U were prepared for each experiment. IMC measurements were performed with a TAM III instrument (Waters GmbH). Experimental details can be found in our publication.^[2] After the microcalorimetric measurements, the bioassociated amount of U was determined by inductively coupled plasma mass spectrometry for selected samples containing only U_{nat} or by liquid scintillation counting for samples containing ^{233}U .

RESULTS. The U exposure concentration of $50\ \mu\text{M}$ is below the half-maximal inhibitory concentration of U for *B. napus* cells, which was estimated to be about $160\ \mu\text{M}$ under similar conditions.^[1] The dominant U(VI) species under the applied conditions in solution is the $(\text{UO}_2)_3(\text{OH})_5^+$ complex. After the microcalorimetric measurement, about $19\ \mu\text{g U}/0.3\ \text{g cells}$ were bioassociated to the *B. napus* cells. This value was independent of the ^{233}U concentration and corresponds to about 80% of the initial U concentration. Figure 1A shows the recorded thermograms of *B. napus* cells exposed to U_{nat} ($50\text{--}35\ \mu\text{M}$) and ^{233}U ($0\text{--}15\ \mu\text{M}$). These data were transformed into enthalpy plots that are depicted in Fig. 1B. The raw data of the samples with different ^{233}U concentrations are very similar. The same applies for the scaled en-

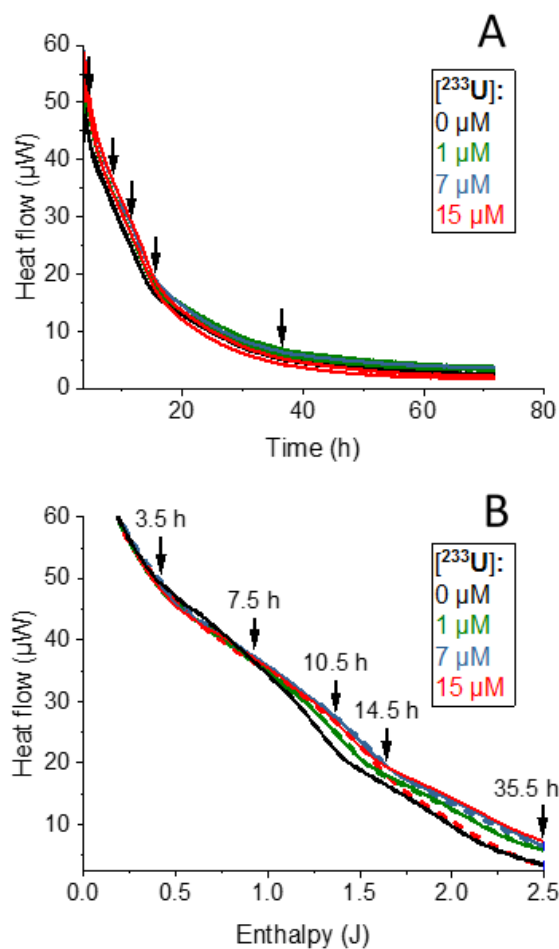


Figure 1. Thermograms of *B. napus* cells exposed to U_{nat} and ^{233}U with a total concentration of $50\ \mu\text{M}$ U (A). Enthalpy plots of the same data (B, dashed lines). Solid lines represent the enthalpy plot of the control (without ^{233}U) after rescaling it along the x and y-axis to best match the data of the ^{233}U containing samples. This was done to adjust for small changes in cell quantity when weighing and transferring the cells in the measuring ampules. Arrows indicate corresponding time points in the two plots.^[2]

thalpy plots, which exhibit characteristic features at the indicated times. Only at the highest ^{233}U concentration of $15\ \mu\text{M}$ (red dashed line), a clear deviation from the control was observed. Here, the thermal power was reduced below that of the control, indicating a radiotoxic effect of the α -emitter. The late occurrence of this deviation after about 14 h of exposure suggests that radiation damage accumulates over time rather than causing cell death for a certain fraction of cells already at the very beginning of the exposure to the RN, as observed for *Lysinibacillus sphaericus*.^[2] These experiments reveal the great potential of “isotope-editing” in IMC measurements to monitor metabolic responses of cells and to distinguish between radiotoxic and chemotoxic effects of RNs *in situ* on the low-dose level.

ACKNOWLEDGEMENTS. We acknowledge the technical assistance from J. Seibt, S. Beutner, and J. Philipp.

[1] Sachs, S. *et al.* (2017) *Environ. Sci. Technol.* **51**, 10843–10849.
[2] Oertel, J. *et al.* (2023) *Microorganisms* **11**, 584.

Microbial U(VI) reduction by a sulfate-reducing bacterium relevant to nuclear waste disposal

S. Hilpmann, A. Rossberg, R. Steudtner, B. Drobot, R. Hübner,¹ F. Bok, D. Prieur, S. Bauters, K. O. Kvashnina, T. Stumpf, A. Cherkouk

¹HZDR, Institute of Ion Beam Physics and Materials Research, Dresden, Germany

Microbial reduction of U(VI) significantly affects uranium mobility in contaminated subsurface areas and may impact high-level radioactive waste management by converting water-soluble U(VI) to less mobile U(IV). This study investigated the reduction of U(VI) by the sulfate-reducing bacterium *Desulfosporosinus hippei* DSM 8344^T, which is phylogenetically closely related to naturally occurring microorganisms in clay rock and bentonite. Different microscopic and spectroscopic techniques were used to gain a deeper insight into the ongoing processes on a molecular level.^[1]

EXPERIMENTAL. *Cultivation:* *D. hippei* DSM 8344^T was cultivated under shaking using DSMZ 641 medium at 30°C in the dark. All cells were harvested in the late exponential growth phase by centrifugation and washed in artificial Opalinus Clay pore water (OPA).^[2]

U(VI) reduction: For the U(VI) reduction experiments, cells were suspended in artificial OPA containing 10 mM lactate and 100 µM U(VI). The suspensions were incubated at room temperature, and samples were collected at intervals from 0 hours to one week. Subsequently, these samples were centrifuged, and the remaining U concentrations in the supernatants were determined using ICP-MS.

UV-vis spectroscopy: For UV-vis spectroscopy measurements, the cell pellets were dissolved for 1 h in 5 M HCl on a shaking plate. Following centrifugation, the supernatants were analyzed using a Cary 5G UV-Vis-NIR spectrophotometer.

Transmission Electron Microscopy (TEM): Samples for TEM imaging were incubated for 4 and 24 h. TEM specimen preparation followed the method outlined by Völkner *et al.*^[3] with the exception that *en-bloc* staining using uranyl acetate was excluded in this study. TEM images were captured using an image-C_s-corrected Titan 80-300 microscope operating at 300 kV. Additionally, spectrum imaging analysis in scanning TEM (STEM) mode based on energy-dispersive X-ray spectroscopy (EDXS) was conducted on a Talos F200X microscope equipped with a high-brightness X-FEG electron source and a Super-X EDX detector system, operating at an accelerating voltage of 200 kV (FEI).

RESULTS. In the experiments conducted in artificial OPA, the U concentration in the supernatants decreased by approximately 80% within 48 h and reached 90% removal after one week. In experiments using heat-killed cells, a lower removal of U (30%) was observed. This suggests that a metabolically active process is responsible for the increased U removal by living cells.

To ascertain the reduction of U(VI) in the samples and the consequent formation of U(IV), UV-vis measurements of the dissolved cell pellets were performed. Figure 1 illustrates the resulting spectra at various incubation times, alongside reference spectra of U(VI) and U(IV). A comparison of band positions distinctly confirmed the formation of U(IV). In the spectral region between 400 and 500 nm, also bands of the U(VI) were still detectable, suggesting a concurrent sorption-reduction process in the ongoing interaction mechanism. Calculations based on the molar ex-

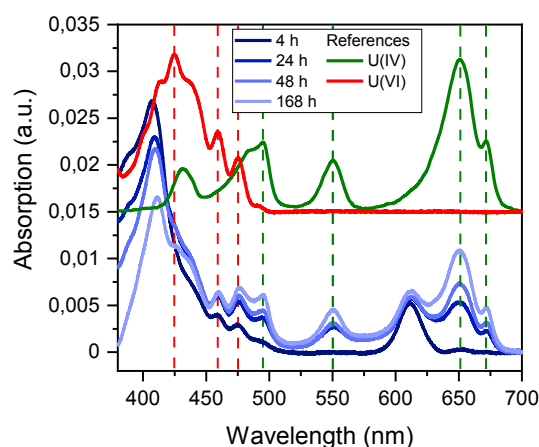


Figure 1. UV-vis spectra of the dissolved cell pellets after different incubation times in comparison with reference spectra of U(IV) and U(VI).

inction coefficients for both oxidation states showed a fraction of up to 40% of U(IV) in the samples after one week. Further insights into the different oxidation states of U in the samples were obtained *via* HERFD-XANES measurements, which will be published in the ESRF Highlights 2023.^[4]

Spectrum imaging analysis in STEM mode was performed to localize U in the cell pellets (Fig. 2). The element distributions showed the formation of U-aggregates on the cell surface and indicated the potential release of membrane vesicles, suggesting a possible defense mechanism against cell encrustation.

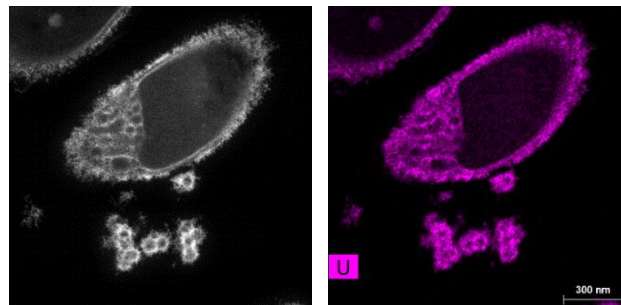


Figure 2. Representative TEM images (left) and corresponding U element distribution (right) of thin-sectioned samples of *D. hippei* DSM8344^T cells.

The results of this study offer novel insights into microbial U(VI) reduction processes and significantly contribute to a comprehensive safeguard concept for the long-term storage of high-level radioactive waste.

ACKNOWLEDGEMENTS. The authors gratefully acknowledge the funding provided by the German Federal Ministry of Education and Research (BMBF) (Grant 02NUK053E) and the Helmholtz Association (Grant SO-093), as well as a partial funding by the Helmholtz Association, grant PIE-0007 (CROSSING) and the European Union's Horizon 2020 research and innovation program under the Grant Agreement No. 95237 (SurfBio). Additionally, we thank Dr. T. Kurth and S. Kretzschmar (Center for Regenerative Therapies Dresden) for preparing the TEM specimens.

[1] Hilpmann, S. *et al.* (2023) *Sci. Total. Environ.* **875**, 162593.

[2] Wersin, P. *et al.* (2011) *Appl. Geochem.* **26**, 931–953.

[3] Völkner, M. *et al.* (2021) *Front. Cell Dev. Biol.* **9**, 645704.

[4] Hilpmann, S. *et al.* (2024) ESRF Highlights 2023 (in preparation).

Effectiveness of glycerol for the bio-reduction of U in mine water

A. M. Newman-Portela,¹ B. Drobot, R. Steudtner, A. Kassahun,² M. L. Merroun,¹ J. Raff, E. Krawczyk-Bärsch

¹Department of Microbiology, University of Granada, Spain; ²WISMUT GmbH, Germany

The metabolic activity of microorganisms is able to alter the solubility of radionuclides (e.g., uranium) through different biochemical interactions. Additionally, these interactions can be stimulated to accelerate environmental detoxification, thus improving the bioremediation process.^[1] The aim of this study is to assess, through a spectroscopic approach, the effectiveness of glycerol as an electron donor for the biostimulation of the indigenous microbial community involved in the removal of U in the mine water of the Schlema-Alberoda. The results demonstrated a high efficacy of glycerol as a stimulant for the native microbial community of the Schlema-Alberoda mine water, almost entirely removing soluble U(VI) and forming U(IV).

EXPERIMENTAL. A set of biostimulated anaerobic microcosms (2L serum bottles) was established using glycerol (10 mM) (ROTIPURAN, Germany) in mine water from Schlema-Alberoda with a U(VI) concentration of 1 mg/L. The microcosms were incubated for 4 months at $28 \pm 2^\circ\text{C}$ in darkness. The concentration of U was monitored throughout the experiment using inductively coupled plasma mass spectrometry (ICP-MS). A microcosm was sacrificed when the concentration of soluble U(VI) decreased by 20%, 60%, and 90%. The U(VI) in the aqueous phase of the microcosm was investigated using cryo-time-resolved laser fluorescence spectroscopy (cryo-TRLFS). Samples for cryo-TRLFS were collected in single-use 2 mL plastic cuvettes (Rotilabo, Carl Roth, Germany), and measurements were performed under cryogenic conditions using a Nd:YAG pulsed laser system (Continuum Inlite series, Continuum, U.S.A.), and luminescence spectra in the wavelength range of 350 to 650 nm were recorded with an iHR550 spectrograph and an amplified CCD-camera system (HORIBA Jobin Yvon, Edison, USA). Ultraviolet-visible (UV-vis) spectroscopy was used to detect the formation of U(IV) in the black precipitate formed at the bottom of the microcosms during the experiment. Samples were prepared by dissolving the black precipitate in 5 M HCl, and the spectral range between 500 and 750 nm was captured by the Cary 5G UV/Vis-NIR spectrophotometer (Varian, U.S.). A 100 μM U(IV) solution in 5 M HCl was used as the reference spectrum.

RESULTS. The ICP-MS results indicated an approximately reduction of 99% in U(VI) concentration at the end of the experiment using glycerol as the electron donor. The cryo-TRLFS results revealed distinct fluorescence band maxima at 480, 501, 519, 542, and 566 nm (Fig. 1A). These bands correspond to those for $\text{Ca}_2\text{UO}_2(\text{CO}_3)_3(\text{aq})$ reported previously.^[2] The UV-vis results (Fig. 1B) displayed a peak at 650 nm, coinciding with the formation of U(IV) when compared to the reference. Additionally, a peak at 560 nm was observed, which is consistent with the previously reported formation of U(IV).^[3] A distinct peak appeared between 675 nm and 700 nm, possibly due to the binding of U(IV)-chloride species, which is likely due to the high concentration of HCl used during sample preparation.^[4] In summary, the formation of U(IV) became evident from the increasing bands with decreasing concentration of soluble U(VI) in the UV-vis spectra (Fig. 1B). Conversely, the

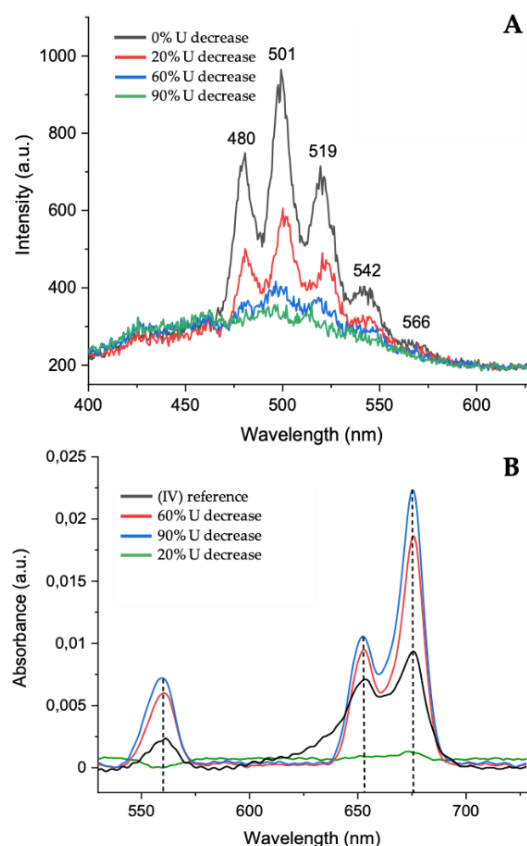


Figure 1. Cryo-TRLFS of the supernatant (A) and UV-vis spectra of the dissolved black precipitate in HCl (B) obtained at different U(VI) concentration decrease in the microcosms.

peaks in the cryo-TRLFS spectra become less pronounced as the concentration of soluble U(VI) decreases (Fig. 1A).

CONCLUSIONS. Stimulating the indigenous microbial community with glycerol seems to be a promising alternative to conventional remediation technologies. Our studies highlighted the effectiveness of glycerol as a biostimulant for the native microbial community, achieving 99% removal of U(VI) and the formation of U(IV). Nevertheless, further studies are needed to understand the stability and speciation of the formed U(IV) in the microcosm.

ACKNOWLEDGEMENTS. The authors are grateful to S. Beutner and S. Schöne (all HZDR, Germany) for ICP-MS and IC analyses.

- [1] Merroun, M. L. and Selenska-Pobell, S. (2008) *J. Contam. Hydrol.* **102**, 285–95.
- [2] Newman-Portela, A. M. et al. (2023) *Environ. Sci. Pollut. Res.* **31**, 7227–7245.
- [3] Gao, W. and Francis, A. J. (2008) *Appl. Environ. Microbiol.* **74**, 4580–4584.
- [4] Tutschku, J. et al. (2004) *Report FZR-400*, p. 13.

Dissimilatory iron reduction by *Desulfitobacterium* sp. G1-2 for ^{99}Tc immobilization

I. Cardaio, S. Kluge, K. Müller, A. Cherkouk, N. Mayordomo

The iron reducer *Desulfitobacterium* sp. G1-2 was isolated from samples of the FEBEX-DP bentonite and cultivated by providing ferric citrate as electron acceptor.^[1,2] During the microbial growth, the precipitation of mineral phases was observed. Both Raman analysis and X-ray diffraction indicated the formation of vivianite ($\text{Fe}^{\text{II}}_3(\text{PO}_4)_2 \cdot 8\text{H}_2\text{O}$).^[3] The aforementioned mineral is currently further studied regarding the removal of TcO_4^- from the aqueous phase.

^{99}Tc is a β^- emitter and a high yield fission product of ^{235}U and ^{239}Pu . It is a long-lived ($\tau_{1/2} \sim 2.13 \times 10^5 \text{ a}$) isotope that can be found in the environment as $\text{Tc}^{\text{VII}}\text{O}_4^-$ or $\text{Tc}^{\text{IV}}\text{O}_2$ depending on oxidizing or reducing conditions, respectively. As pertechnetate ($\text{Tc}^{\text{VII}}\text{O}_4^-$), ^{99}Tc has an increased mobility in aqueous solutions, whereas Tc^{IV} is immobilized by means of its precipitation as solid.^[4] In multi-barrier deep geological repositories for the long-term storage of nuclear waste, the use of bentonite clays as buffer material would prevent water corrosion of the nuclear waste container and thus, radionuclide migration in the biosphere. Nevertheless, geotechnical barriers harbor microorganisms, whose metabolic activities can influence radionuclides migration. The isolate *Desulfitobacterium* sp. G1-2 is an indigenous anaerobe in bentonite, which can use Fe^{III} as electron acceptor during dissimilatory iron reduction.^[1] The release of Fe^{II} in solution can lead to the formation of ferrous solid phases, which in turn can promote Tc^{VII} reduction to Tc^{IV} and prevent ^{99}Tc mobility in groundwater.

EXPERIMENTAL. The bacterium *Desulfitobacterium* sp. G1-2 was cultivated in anaerobic serum flasks at pH 6.8 in order to promote dissimilatory iron reduction by providing Fe^{III} citrate as electron acceptor and Na-pyruvate as electron donor, according to the medium DSMZ 579.^[5] The atmosphere in the anaerobic serum flasks was set up to a ratio of 80%/20% N_2/CO_2 by gas/vacuum cycles. An inoculum of 3 mL was provided and the cultures were incubated at 30 °C for 7 days. Growth curves for the bacterial growth during anaerobic respiration of Fe^{III} were obtained by cell counting using a Neubauer cell chamber (Fig. 1, a). During cultivation, the precipitation of solids was observed in the form of black particles and white solid layers

(Fig. 1, b). Samples of the solids were observed by optical microscopy and mounted under inert conditions in an N_2 -glovebox ($\text{O}_2 < 0.1 \text{ ppm}$) on Raman cells and XRD sample holders to perform Raman microscopy (Aramis, Horiba) and X-ray diffraction (MiniFlex 600 powder XRD, Rigaku) by maintaining the anaerobic conditions.

RESULTS. The optimal growth for *Desulfitobacterium* sp. G1-2 in DSMZ 579 showed the start of the exponential phase between the first and the second day of cultivation, followed by the stationary phase and the death phase between the third and the fourth day (Fig. 1, a). The bacterial anaerobic reduction of Fe^{III} could be confirmed both by Ferrozine assay and the formation of solid precipitates at the bottom of the flasks during the exponential growth (Fig. 1, b).^[6] Raman spectra of the white solids showed most of the shifts corresponding to the OH-bending ($\delta\text{H}_2\text{O}$) and OH-stretching (νOH) of water, as well as the ν_2 bending, ν_1 symmetric stretching and ν_3 antisymmetric vibrations of PO_4^{3-} (Fig. 1, c).^[7,8] Therefore, the spectra could be overall associated with mineral phases belonging to the group of vivianite, $\text{Fe}^{\text{II}}_3(\text{PO}_4)_2 \cdot 8\text{H}_2\text{O}$ which was confirmed also by X-ray diffractograms.^[3,9] Furthermore, Raman shifts resulting from the analysis of black precipitates hint at the formation of pyrite, magnetite, hematite, ferrihydrite and siderite.^[10]

The production of Fe^{II} phosphate minerals by *Desulfitobacterium* sp. G1-2 through the anaerobic respiration of ferric iron can be a promising strategy for ^{99}Tc immobilization through iron secondary mineral phases. Hence, the ferrous biogenic minerals are currently investigated for $\text{Tc}^{\text{VII}}\text{O}_4^-$ removal from aqueous solutions.

ACKNOWLEDGEMENTS. This work has received funding from the German Federal Ministry of Education and Research (BMBF) in the frame of the NukSiFutur TecRad young investigator group (02NUK072).

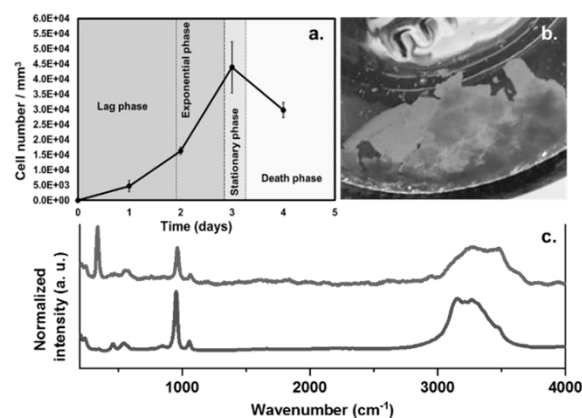


Figure 1. Growth curve for *Desulfitobacterium* sp. G1-2 in culture medium DSMZ 579 (a). Solid precipitates observed during cultivation at the bottom of the culture flasks (b). Raman spectra of the iron phosphate mineral vivianite; lower trace: reference spectrum R050076; upper trace: results obtained after one day from the collection of the precipitates.^[3]

- [1] Drozdowski, J. (2019) *Report HZDR-096*, p. 40.
- [2] Villemur, R. et al. (2006) *FEMS Microbiol. Rev.* **30**, 706–733.
- [3] RRUFF™ Project, <https://rruff.info/Vivianite/R050076>.
- [4] Schmeide, K. et al. (2021) *Sci. Total Environ.* **770**, 145334.
- [5] DSMZ: https://www.dsmz.de/microorganisms/medium/pdf/DSMZ_Medium579.pdf, accessed on Dec. 19, 2023.
- [6] Viollier, E. et al. (2000) *Appl. Geochem.* **15**, 785–790.
- [7] Wang, Z. et al. (2004) *J. Phys. Chem. A* **108**, 9054–9063.
- [8] Litasov, K. D. et al. (2017) *J. Raman Spectrosc.* **48**, 1528–1527.
- [9] International Centre for Diffraction Data, <https://www.icdd.com/>.
- [10] Rodríguez, D. M. et al. (2020) *Environ. Sci. Technol.* **54**, 2678–2687.

Interaction of U(VI) with kidney cells – Speciation in cell culture medium and cell suspension

D. Butscher, C. Senwitz,^{1,2} R. Steudtner, A. Heller,^{1,2} A. Barkleit

¹Chair for Radiochemistry and Radioecology, Technische Universität Dresden, Dresden, Germany; ²Central Radionuclide Laboratory, Technische Universität Dresden, Dresden, Germany

Speciation experiments with U(VI) in cell culture medium before and after contact with HEK-293 cells showed the same species. Therefore, the speciation of U(VI) in the cell culture medium is not influenced by cell-related compounds. In contrast, the cellular species differs from that in the cell culture medium.^[1]

The increasing use of radionuclides (RN), for example in medicine as radiopharmaceuticals, raises the risk that they will be released into the environment and taken up by humans.^[2] Once incorporated, they pose a potential health risk due to their radio- and chemotoxicity.^[3] As the kidneys are mainly responsible for excreting toxic substances from the bloodstream, they are particularly exposed to incorporated RNs.^[4] Therefore, the effect of uranium(VI) on the human kidney cell line HEK-293 was investigated using a combination of *in vitro* cell culture techniques and spectroscopic methods to get a better understanding on cellular and molecular level. This study is part of our investigations on the interaction of Ba(II), Eu(III), and U(VI) on kidney cells *in vitro*.^[1]

EXPERIMENTAL. The human kidney cells HEK-293 were cultivated in Dulbecco's Modified Eagle's Medium (DMEM; high glucose with sodium pyruvate) supplemented with fetal bovine serum (10 vol.-%) and glutamine (4 mM) at 37°C, 95% relative humidity (rH), and 5% CO₂. Time-resolved laser-induced fluorescence spectroscopy (TRLFS) was applied to investigate the speciation of U(VI) in cell culture medium, in medium after contact with the cells, and in cell suspension. The cells were incubated for 7, 24 and 48 h in medium containing 1 mM U(VI). After the exposure time, the medium was removed and frozen in liquid nitrogen for the TRLFS measurement. The cells were washed 3 times with a NaCl solution (0.9%, pH 7) and also frozen for TRLFS measurements. The same conditions were used for the cell culture medium without cells. The TRLFS measurements were conducted at low temperatures (~120°C). Parallel Factor Analysis (PARAFAC) was used to extract single component spectra from the emission spectra.^[5] More details on the cell cultivation and experimental approach can be found elsewhere.^[1]

RESULTS. TRLFS measurements of U(VI) in the cell culture medium before and after contact with HEK-293 cells exhibit very similar luminescence spectra (Fig. 1). Furthermore, the emission spectra show no time-dependent alterations within 48 h, indicating no change in U(VI)-speciation. PARAFAC reveals that only one species is formed in the medium before and after contact with HEK-293 cells. This species can be assigned as a U(VI)-carbonate species, as the band positions, the intensity ratios and the luminescence lifetime correspond very well with the reference spectrum of UO₂(CO₃)₃⁴⁻. This is also supported by the high carbonate concentration in the medium of 44.05 mM and the pH of 7.4–8.0. Therefore, the speciation of U(VI) in the cell culture medium is not influenced by the cells. Possible metabolites excreted by contact with U(VI) are therefore either weakly complexed with U(VI) or the excreted fraction is too low.

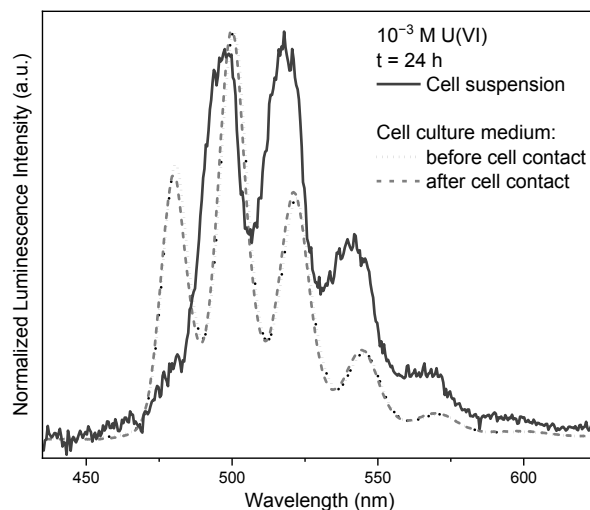


Figure 1. Luminescence spectra of 10⁻³ M U(VI) in cell culture medium, in supernatant of cell culture medium after contact with HEK-293 cells and in HEK-293 cell suspension after 24 h exposure. All luminescence spectra were normalized to the band of highest intensity.

The emission spectrum of U(VI) in HEK-293 cell suspension shows clear differences to the spectra of U(VI) in cell culture medium. On the one hand, there is a shift and broadening of the bands. On the other hand, the signal-to-noise ratio is significantly lower, as only a small proportion of U(VI) is cellularly complexed. Using PARAFAC, two single component spectra could be extracted. The minor species is the same soluble U(VI)-carbonate species formed in the cell culture medium. The dominant species, however, is an inorganic or organic U(VI) phosphate complex. Since U(VI)-phosphate precipitates have already been detected in kidney cells, our spectroscopic results indicate that U(VI) is taken up into the cells as a soluble U(VI)-carbonate species and then precipitates in the cells mostly as U(VI)-phosphate.^[6,7] These speciation results thus provide information on the behavior of U(VI) after intracellular uptake, which is important for risk assessment.

ACKNOWLEDGEMENTS. The authors thank Steffen Taut and Margret Acker from the Central Radionuclide Laboratory of the Technische Universität Dresden for the opportunity to carry out most of the work in their laboratories. This work was funded by the German Federal Ministry of Education and Research under contract number 02NUK057A and B.

- [1] Senwitz, C., Butscher, D. *et al.* (2024) *Sci. Total Environ.*, submitted.
- [2] Akbar, M. U. *et al.* (2016) *J. Radioanal. Nucl. Chem.* **310**, 477–493.
- [3] Rump, A. *et al.* (2019) *Toxicol. Lett.* **313**, 159–168.
- [4] Ansoborlo, E. *et al.* (2006) *Biochimie* **88**, 1605–1618.
- [5] Drobot, B. *et al.* (2015) *Chem. Sci.* **6**, 964–972.
- [6] Rouas, C. *et al.* (2010) *Chem. Res. Toxicol.* **23**, 1883–1889.
- [7] Carrière, M. *et al.* (2008) *J. Biol. Inorg. Chem.* **13**, 655–662.

Thermodynamic investigations of a potential decorporation agent for Eu(III)/Cm(III)

S. Friedrich, C. Sieber, B. Drobot, S. Tsushima, A. Barkleit, K. Schmeide, T. Stumpf, J. Kretschmar

The complex formation reactions of the potential decorporation agent ethylene glycol-bis(2-aminoethyl ether)-*N,N,N',N'*-tetraacetic acid (EGTA) with Eu(III) and Cm(III) have been analyzed using nuclear magnetic resonance (NMR) spectroscopy, time resolved laser fluorescence spectroscopy (TRLFS) and isothermal titration calorimetry (ITC).

If radionuclides and heavy metals are accidentally released into the environment and enter the human body by oral intake, they can pose a serious health risk. Until today, suitable decorporation agents are still scarce. Therefore, within this project new potential substances are investigated to displace or complete current decorporation strategies. To characterize the complexation reactions of EGTA with Eu(III)/Cm(III) and to decide on its suitability as decorporation agent, time-resolved laser-induced fluorescence spectroscopy (TRLFS) and isothermal titration calorimetry (ITC) was applied and compared to the reactions investigating EDTA.

EXPERIMENTAL. For Eu(III), TRLFS experiments solutions contained 10 μM Eu(III) and 0–112.5 μM EGTA at pH 3. For Cm(III), TRLFS experiments solutions contained 0.3 μM Cm(III) and 0–450 μM EGTA at pH 3. For ITC, the syringe was loaded with 450 μM Eu(III) and the cell with 30 μM EGTA. All solutions contained 0.1 M NaCl. Furthermore, NMR spectroscopy was used to determine the pK_a values of EGTA. Experimental details are given elsewhere.^[1]

RESULTS. Concentration-dependent TRLFS titrations series at pH 3 achieved stepwise complexation of Eu(III) and Cm(III) with EGTA. Using PARAFAC analysis, the single-component spectra (Fig. 1) were determined. Based on the resulting speciation as well as the well-determined pK_a values of EGTA (Tab. 1), the complex formation constants of EGTA complexes with Eu(III) and Cm(III) were determined (Tab. 2). For the Eu(III) complexation, additional thermodynamic parameters (ΔH , ΔS and ΔG , see Tab. 3) were achieved using ITC (Fig. 2).

Thermodynamic values showed a high affinity of octadentate EGTA-ligand towards hard acid ions Eu(III) and Cm(III). Cm(III) showed higher complex stability compared to Eu(III), most probably based on the more covalent binding character of Cm(III) bonding. Furthermore, the high entropy value for the formation of $[\text{Eu}(\text{EGTA})]^-$ is an excellent evidence for the large amount of water molecules (approx. eight) displaced by EGTA from the 1st coordination sphere of the europium aquo ion.

These results will improve further decorporation strategies to ensure a safe handling of radiotoxic metals. The effectiveness of ligands like EGTA for the decorporation of Eu(III) and Cm(III) under physiological conditions is subject of experiments in progress.

ACKNOWLEDGEMENTS. This work was funded by the German Federal Ministry of Education and Research (BMBF) under contract number 02NUK057A.

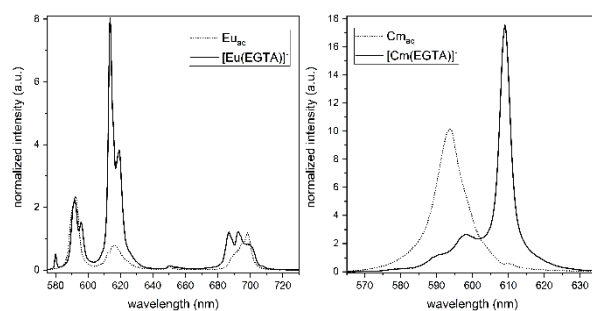


Figure 1. Single-component spectra for the EGTA complexes with Eu(III) (left) and Cm(III) (right), extracted using PARAFAC analysis.

Table 1. pK_a values of EGTA determined in the present work.^[1]

	pK_{a1}	pK_{a2}	pK_{a3}	pK_{a4}
$\text{H}_4\text{EGTA}^0 \rightarrow \text{H}_3\text{EGTA}^- \rightarrow \text{H}_2\text{EGTA}^{2-} \rightarrow \text{HEGTA}^{3-} \rightarrow \text{EGTA}^{4-}$				
$I = 0.1\text{M}$	1.45 ± 0.04	2.28 ± 0.08	9.25 ± 0.01	9.25 ± 0.01
$I \rightarrow 0^a$	1.69 ± 0.04	2.74 ± 0.08	9.89 ± 0.01	10.05 ± 0.01

^a I (NaCl) extrapolated to zero ionic strength. The SIT interaction coefficients for EDTA_4^- (H_3EDTA^- : -0.33 ± 0.14 , $\text{H}_2\text{EDTA}^{2-}$: -0.37 ± 0.14 , HEDTA^{3-} : -0.10 ± 0.14 , EDTA^{4-} : 0.32 ± 0.14 , all in NaCl^[2]) were used, since no values for EGTA_4^- were available.

Table 2. Complex formation constants ($\log \beta$) of EGTA–Eu(III) and –Cm(III) complexes determined by means of TRLFS and ITC.^[1]

	$\log \beta^a$ (TRLFS)	$\log \beta^{0,b}$ (TRLFS)	$\log \beta^a$ (ITC)	$\log \beta^{0,b}$ (ITC)	Ref. ^{[4]c}
$[\text{Eu}(\text{EGTA})]^-_{\text{aq}}$	17.9 ± 0.2	20.5 ± 0.2	18.0 ± 0.1	20.5 ± 0.1	17.65 ± 0.08
$[\text{Cm}(\text{EGTA})]^-_{\text{aq}}$	18.6 ± 0.01	21.2 ± 0.01			17.94 ± 0.09

^a $I = 0.1\text{M}$ (NaCl). ^b I extrapolated to zero ionic strength. The SIT interaction coefficients used for the calculations were 0.26 ± 0.01 for Eu(III) in NaCl.^[9] For Cm(III) no data were available and Am(III) coefficients (Am(III) in NaCl: 0.23 ± 0.02 ^[2]) have been used as substitute. ^c $I = 0.1\text{M}$ (NaClO₄).

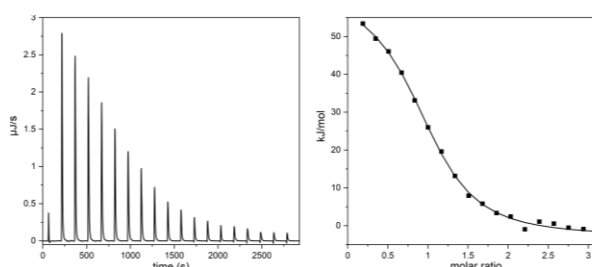


Figure 2. Thermogram (left) and corresponding integrated heat and best fit (right) of an ITC titration of Eu(III) against EGTA.

Table 3. Thermodynamic data for Eu(III) complexation by EGTA, obtained from ITC at 25 °C in aqueous solutions containing 0.1 M NaCl.^[1]

	ΔH (kJ/mol)	ΔS (J/mol K)	ΔG (kJ/mol)
$[\text{Eu}(\text{EGTA})]^-$	66.7 ± 6.4	568 ± 18	-103 ± 1

- [1] Friedrich, S.; Sieber, C. *et al.* (2023) *Molecules* **28**, 4881.
- [2] Grenthe, I. *et al.* (2020) Chemical thermodynamics Volume 14; NEA of the OECD, Boulogne-Billancourt, France.
- [3] Jordan, N. *et al.* (2022) *Coord. Chem. Rev.* **473**, 214608.
- [4] Thakur, P. *et al.* (2011) *J. Coord. Chem.* **64**, 3215–3237.

Multi-method coordination study of Eu(III)–HEDP complexation in aqueous solution

A. Heller,^{1,2} C. Senwitz,^{1,2} H. Foerstendorf, S. Tsushima, L. Holtmann,³ B. Drobot, J. Kretzschmar

¹Technische Universität Dresden, Professorship of Radiochemistry/-ecology, Dresden, Germany; ²Technische Universität Dresden, Central Radionuclide Laboratory, Dresden, Germany; ³Leibniz-Universität Hannover, Institute of Radioecology and Radiation Protection, Hannover, Germany

Bisphosphonates like 1-Hydroxyethylidene-1,1-diphosphonate, HEDP, are widely used in industry, technology, and medicine and, therefore, can enter the biogeosphere. Furthermore, HEDP is a proposed decorporation agent for U(VI).^[1] However, since incorporation of only one radionuclide is rather unlikely, investigations addressing the suitability of HEDP to sequester other radionuclides, *i.e.*, trivalent actinides, are crucial.

EXPERIMENTAL. Eu(III) was used as a non-radioactive chemical analog of trivalent actinides. Experiments covered aqueous sample series at varying pH, Eu(III) total concentration, and metal-to-ligand ratio (M:L) that were studied by TRLFS, IR and NMR spectroscopy, ESI-MS, and ICP-MS.^[2] All experiments were performed under ambient atmosphere at (25 ± 1) °C, and complemented by quantum chemical calculations at DFT level.

RESULTS. Five HEDP ligand species with stepwise deprotonation of the phosphonate groups were characterized and reliable pK_a values determined (Tab.1). The hydroxyl group was shown to remain protonated up to pH 14.

Table 1. Acid dissociation constants of H₄HEDP obtained from NMR pH-titration data (0.1M NaCl). Values represent means from ¹H and ³¹P spectra.^[2]

Site	pK _a ± 2σ (I = 0.1 M)	pK _a ± 2σ (I → 0) ¹
PO ₃ H ₂ (1)	1.36 ± 0.35	1.57 ± 0.35
PO ₃ H(2)	2.46 ± 0.19	2.89 ± 0.19
PO ₃ H ⁻ (1)	6.93 ± 0.14	7.57 ± 0.14
PO ₃ H ⁻ (2)	11.12 ± 0.09	11.98 ± 0.09
–OH	> 14	> 15

¹Values are extrapolated to I = 0 using the Davies Equation.

In the Eu(III)–HEDP system, solubility depends on both pH and concentration. In the acidic and alkaline pH range, Eu(III) is highly soluble indicating the formation of charged Eu(III)–HEDP complex species. In contrast, in the near-neutral pH range, hardly soluble complex species form and precipitate. Increasing the Eu(III) concentration causes faster precipitation over a wider pH range.

The stoichiometry of the complexes at acidic pH was found to be 1:1 for nearly equimolar M:L and 1:2 at ligand excess. Furthermore, we demonstrated a deprotonation of the HEDP ligand upon Eu(III) binding and complexation with the H₂L²⁻ ligand. At alkaline pH, the stoichiometry of the Eu(III)–HEDP complex was found to be 1:1 at ligand excess and the binding ligand species is L⁴⁻. Deprotonation of the OH upon complexation of Eu(III) was ruled out. However, at equimolar Eu(III) and HEDP concentrations, there the formation of a polynuclear species was suggested.

Thermodynamic studies in the Eu(III)–HEDP system revealed six complex species in dependence on the pH and the M:L, which are distinct by their luminescence spectroscopic parameters. Out of these, the following four species were identified: EuH₂L⁺ and Eu(H₂L)₂⁻ at acidic pH, EuHL⁰_(s) at near neutral pH, and EuL⁻ at alkaline pH. Two more Eu(III)–HEDP species occurred at near neutral pH and ligand excess as well as at alkaline pH and equimolar

M:L, respectively. However, their structure remains unsolved at the moment.

For all Eu(III)–HEDP species identified, the energetically most stable solution structure is a chelate involving, at least, one six-membered ring (see Fig.1). Furthermore, in all four complexes, both phosphonate groups participate in Eu(III) binding. Comparable solution structures are reported for HEDP complexes of other (heavy) metals. Noteworthy, the coordination number of Eu(III) is decreased from nine to eight in all four complexes.

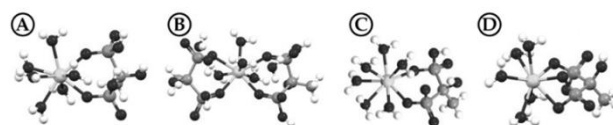


Figure 1. DFT calculated solution structures of the EuH₂L⁺ (A), Eu(H₂L)₂⁻ (B), EuHL⁰_(s) (C), and EuL⁻ (D) complexes.

Corresponding formation constants determined with PARAFAC are given in Tab.2. Details on formation conditions and reaction equations can be found elsewhere.^[2]

Table 2. Formation constants of Eu(III)–HEDP complexes at I = 0.^[2]

Species	log K ± 2σ (I → 0) ¹	log β ± 2σ (I → 0) ¹
EuH ₂ L ⁺	5.6 ± 0.4	25.2 ± 0.4
Eu(H ₂ L) ₂ ⁻	10.5 ± 0.2	49.6 ± 0.2
EuHL ⁰	15.2 ± 0.2	27.2 ± 0.2
EuL ⁻	13.8 ± 0.2	13.8 ± 0.2

¹Values are extrapolated to I = 0 using the Davies Equation.

In cell culture medium, there is a competition between HEDP and biological ligands for the complexation of Eu(III). Mixing Eu(III) and HEDP before adding the medium leads to nearly quantitative precipitation of the hardly soluble EuHL⁰ complex. In contrast, mixing Eu(III) or HEDP with medium before adding the other component leads to a soluble fraction of Eu(III) complexed by ligands from the medium. With prolonged incubation time, however, HEDP is able to outcompete the biological ligands, resulting in decreasing Eu(III) solubility.

In conclusion, HEDP is a very complex ligand system. With regard to environmental scenarios, HEDP can lead to both mobilization (acidic and alkaline pH) and immobilization (near neutral pH) of trivalent lanthanides and actinides. Regarding its potential use as a decorporation agent, we demonstrated that side reactions with trivalent lanthanides and actinides have to be taken into account and need to be considered in risk assessment as hardly soluble species will form under physiological conditions.

ACKNOWLEDGEMENTS. This work is funded by BMBF under grant number 02NUK057B and is part of the joint project RADEKOR. L.H. acknowledges funding received from BMBF, grant number 02NUK057D. The authors kindly thank the staff from TUD, Central Radionuclide Laboratory for their valuable support and lab space.

[1] Fattal, E. *et al.* (2015) *Adv. Drug Deliv. Rev.* **90**, 40–54.

[2] Heller, A. *et al.* (2023) *Molecules*. **28**, 4469.

Macropa's preference for various metal ions

B. Drobot, M. K. Blei,¹ L. Waurick, F. Reissig,¹ C. Mamat,¹ J. Kretzschmar

¹HZDR, Institute of Radiopharmaceutical Cancer Research, Dresden, Germany

The macropa ligand (H2bp18c6) is a promising candidate for radiopharmaceutical applications.^[1] In addition, this chelating agent offers great potential for studies on the binding behavior of metal ions. Different metal ions (La³⁺, Eu³⁺, Lu³⁺, Pb²⁺, Ra²⁺, and Ba²⁺) were investigated for their interaction with macropa using a calorimetric, spectroscopic, radioanalytical, and theoretical approach.

EXPERIMENTAL. The general experimental workflow including pK_a determination of the ligand and spectroscopy is described elsewhere.^[1] Further details can be found in the underlying publication.^[2]

RESULTS. After a precise determination of the pK_a values (Tab.1) of all involved functional groups, the individual complex formation constants for the different metal ions have been determined directly. Therefore, the respective pH values were chosen so that the individual affinities correspond to a concentration range suitable for calorimetry. While the pH for low-affinity metals is close to neutral (pH 5 for Lu³⁺), more acidic conditions were used for high-affinity metals (pH 3.5 for Pb²⁺). The identity and predominance of the formed metal-macropa complex is supported by Eu-TRLFS and NMR.

Table 1. Acid dissociation constants of macropa (H₄L²⁺) obtained from ¹H NMR pH-titration data.

H ₄ L ²⁺ → H ₃ L ⁺	H ₃ L ⁺ → H ₂ L ⁰	H ₂ L ⁰ → HL ⁻	HL ⁻ → L ²⁻
2.40	3.13	6.80	7.73

The none-radioactive metals were investigated by ITC. For data analysis, an in-house developed algorithm was used taking into account changes in the pH value while titration. Complex formation constants are given in Tab. 2.

Table 2. Formation constants of macropa (L²⁻) complexes with selected metal ions.

Complex	This work	Literature
[Pb(mcp)] ⁰ _{aq}	18.5 ± 0.01	16.23 ^[3]
[La(mcp)] ⁺	13.9 ± 0.19	14.99 ^[4]
[Eu(mcp)] ⁺	13.0 ± 0.05	13.01 ^[4]
[Ba(mcp)] ⁰ _{aq}	11.0 ± 0.10	11.11 ^[5]
[Lu(mcp)] ⁺	7.3 ± 0.19	8.25 ^[4]

This study provides revised constants with higher accuracy due to the direct measurement of the constants. Although the difference can be up to one logarithmic unit, the overall trends remain, with divalent lead forming the strongest complex and trivalent lutetium the weakest.

The difference of six orders of magnitude within the lanthanide series is particularly impressive. The theoretical investigations of the interaction demonstrate that the lanthanide contraction is responsible for this difference. Lanthanum, the ion with the largest ionic radius, is essentially centered on macropa's macrocycle while the smaller lutetium is dynamically decentered.

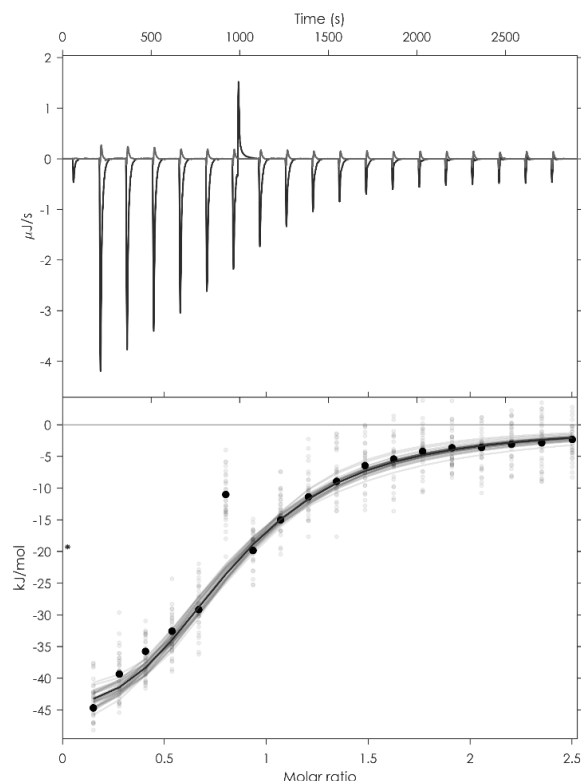


Figure 2. Exemplary ITC thermogram showing the titration of 600 μM macropa to 50 μM Ba²⁺ at pH 5.

OUTLOOK. Complex stability is an important thermodynamic parameter. Dynamic behavior such as dissociation rates are crucial parameters, especially for metal-ligand complexes in medical applications. These parameters will be investigated in future studies.

- [1] Roca-Sabio, A. *et al.* (2009) *J. Am. Chem. Soc.* **131**, 3331–3341.
- [2] Friedrich, S.; Sieber, C. *et al.* (2023) *Molecules* **28**, 4881.
- [3] Blei, M. K.; Waurick, L. *et al.* (2023) *Inorg. Chem.* **62**, 20699–20709.
- [4] Brühlmann, S. A. *et al.* (2022) *Pharmaceuticals* **15**, 1167.
- [5] Schneider, H.-J.; Dürr, H. (1991) *Frontiers in Supramolecular Organic Chemistry and Photochemistry*, VCH, Weinheim, Germany.
- [6] Reissig, F. *et al.* (2020) *Pharmaceuticals* **13**, 272.

Superstructure-dependent stability of DNA origami nanostructures in the presence of chaotropic denaturants

D. Dornbusch, A. Keller,¹ K. Fahmy

¹Technical and Macromolecular Chemistry, Paderborn University, Paderborn, Germany

The stability of DNA origami nanostructures in various chemical environments is critical in applications in biomedicine and analytical chemistry and for studying DNA radiation damage at the nanoscale. The stability of six different 2D and 3D DNA origami nanostructures was assessed in the presence of the chaotropic salts, guanidinium sulfate (Gdm_2SO_4), guanidinium chloride (GdmCl), and tetrapropylammonium chloride (TPACl). Using atomic force microscopy (AFM), Gdm_2SO_4 was found to be the weakest and TPACl the strongest denaturant. Despite different mechanisms of actions of the selected salts, DNA origami stability in each environment depends on DNA origami superstructure. This is especially pronounced for 3D DNA origami nanostructures, where mechanically more flexible designs show higher stability in both GdmCl and TPACl than more rigid ones.^[1]

DNA origami, *i.e.*, the art of folding DNA with molecular precision into almost arbitrary nanoscale shapes, has emerged as a powerful tool with the potential to transform numerous research fields.^[2] Aiming at applications in quantitative studies of DNA radiation damage at the nanoscale, the factors that govern the stability of DNA origami nanostructures need to be known to be tailored deliberately. Therefore, we have performed systematic studies of the stability of 2D and 3D nanostructures using statistical evaluations of AFM images recorded after treatment of DNA origami nanostructures with denaturants previously used in research on protein stability. The employed denaturants interact through hydrophobic, ionic or both types of forces with the DNA origami nanostructure. In a previous study we showed that these interactions are surprisingly complex, leading to non-monotonic temperature sensitivity of DNA origami nanostructures and to unexpected indirect effects of cations on stability, despite their electrostatic repulsion from the DNA surface.^[3]

EXPERIMENTAL. The assembly of the Rothemund triangle,¹ the “tall” rectangle,¹ the Z shape,⁴¹ the 6HB 42-bpCS,¹⁹ the 6HB 21-bpCS,¹⁹ and the 24HB,⁴² was performed as previously described.^[4] A 10:1 molar ratio of staples (Eurofins) to scaffold (Tilibit) was employed in 10 mM Tris buffer (Sigma-Aldrich) containing 10 mM MgAc_2 (Sigma-Aldrich). The pH of the buffer was adjusted to 8.0 with acetic acid. In the assembly of the DNA origami rectangles, all edge staples were omitted to avoid aggregation in liquid due to blunt-end stacking.^[1] The DNA origami nanostructures were either purified by spin filtering using Amicon Ultra-0.5 mL spin filters with 100 kDa molecular weight cut-off (Merck) or by PEG precipitation based on a previous protocol. The concentrations of the purified DNA origami nanostructures were determined using an Implen Nanophotometer P330 and afterwards adjusted to 100 nM.

RESULTS. Figure 1a shows the histograms of the projected area for the DNA origami triangle. At 1 M GdmCl , prominent monomer and dimer peaks can be observed with the corresponding AFM images revealing intact tri-

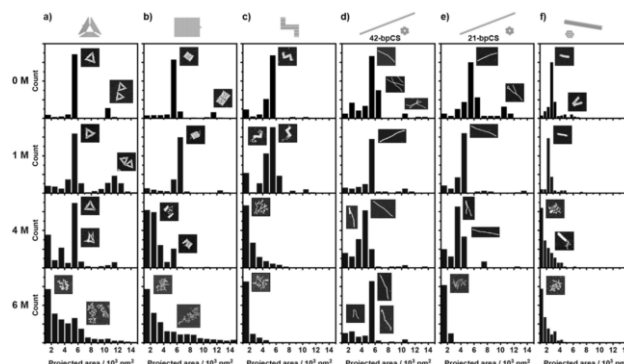
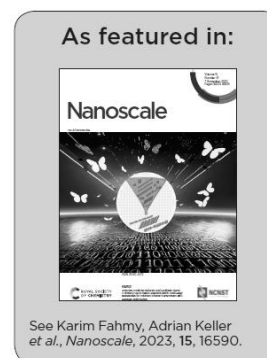


Figure 1. Histograms of the projected surface areas of DNA origami triangles (a), rectangles (b), Z shapes (c), 6HBs 42-bpCS (d), 6HBs 21-bpCS (e), and 24HBs (f) after 1 h incubation at 42 °C in buffer containing 0 M, 1 M, 4 M and 6 M GdmCl . Upper and lower limits of the projected area of 1×10^3 and $15 \times 10^3 \text{ nm}^2$ were applied. Insets show representative AFM images of individual or aggregated DNA origami nanostructures that correspond to the peaks in the histograms. For each condition, between 43 and 1,239 individual particles have been evaluated.

angles. At 4 M GdmCl , however, the histogram shows an increase in the counts of projected surface area values below $4 \times 10^3 \text{ nm}^2$ and AFM images show heavily damaged DNA origami triangles, *i.e.*, under conditions where damage at the same concentration of Gdm (2 M Gdm_2SO_4) was marginal. At an even higher GdmCl concentration of 6 M, the DNA origami triangles were fully denatured. In the histogram, this complete denaturation results in a broad projected area distribution with a maximum at low area values and a slope toward higher values, because the native scaffold may still carry different numbers of staples, adopt a large variety of conformations at the mica surface, and form large aggregates. The stronger denaturant activity of GdmCl compared to Gdm_2SO_4 is reflected accurately in the histograms of the projected surface area. All six DNA origami nanostructures showed a similar dependence on the salt type. In particular, TPACl caused complete DNA origami already at a concentration of 1.5 M. The rod shaped 6HB 42-bpCS exhibited the highest stability which we tentatively assign a lower amount of strain accumulating upon intercalation of Gdm as compare to the same superstructure constructed with less shorter staple strands.



ACKNOWLEDGEMENTS. We acknowledge the technical assistance from J. Philipp.

- [1] Hanke, M. *et al.* (2023) *Nanoscale* **15**, 16590.
- [2] Rothemund, P. W. K. *et al.* (2006) *Nature* **440**, 297.
- [3] Hanke, M. *et al.* (2022) *Comput. Struct. Biotechnol. J.* **20**, 2611.
- [4] Hanke, M. *et al.* (2022) *Nanoscale* **14**, 11552.

SCIENTIFIC CONTRIBUTIONS (PART IV)

Safety

Nuclear Reactor

**SAFETY
RESEARCH**

Research

Unraveling the chromium redox chemistry in advanced UO_2 fuels

G. L. Murphy,¹ R. Gericke, S. E. Gilson, E. F. Bazarkina, A. Rossberg, P. Kaden, R. Thümmeler,¹ M. Klinkenberg,¹ M. Henkes,¹ P. Kegler,¹ V. Svitlyk, J. Marquardt,² T. Lender,³ C. Hennig, K. O. Kvashnina, N. Huittinen

¹Forschungszentrum Jülich, Jülich, Germany; ²Goethe-Universität Frankfurt am Main, Frankfurt am Main, Germany; ³RWTH Aachen University, Aachen, Germany

The redox chemistry of chromium in Cr-doped UO_2 powder samples and single crystal (SC) grains has been investigated using a combination of structural, microscopic and spectroscopic methods.^[1] SEM EDS measurements revealed the presence of Cr-rich precipitates in the powder samples, while SC grains were absent from similar Cr clusters. When examining the two sample types using HERFD-XAS, only Cr^{3+} could be detected in the SCs, attributed to incorporated Cr in the UO_2 matrix, while powder samples showed significant contributions of Cr^0 and Cr^{2+} in addition to Cr^{3+} , arising from metallic Cr and oxide related $\text{Cr}^{2+}/\text{Cr}^{3+}$ precipitates. Finally, EPR measurements of SC grains confirmed the presence of Cr^{3+} , while excluding U^{5+} for charge compensation in the samples. Thereby, the Cr cation incorporates into the UO_2 lattice with the formation of oxygen vacancies.

Transition metal doped UO_2 fuels or so called advanced nuclear fuel blends are used by the nuclear power industry due to their increased in-reactor efficiencies, improved safety performance and reduced waste accumulation. A prominent example of an advanced fuel blend is Cr-doped UO_2 , where the mixing of Cr_2O_3 with UO_2 during fuel fabrication results in a product containing ≈ 700 – $1,000$ ppm Cr.^[2] Some of the initial chromate volatilizes during the fuel sintering process, while the remaining Cr becomes incorporated into the UO_2 matrix, or forms metallic (Cr^0), oxide ($\text{Cr}^{3+}_2\text{O}_3$) and eutectic (Cr^{2+} , $\text{Cr}^{3+}_2\text{O}_3$, $\text{Cr}^{2+,3+}_3\text{O}_4$) precipitates in the ceramic. These precipitates hamper the accurate description of the oxidation state of incorporated Cr, which has been suggested to be Cr^{1+} , Cr^{2+} , or Cr^{3+} .^[3–5] To unambiguously resolve the redox chemistry of Cr in the UO_2 matrix, both Cr-doped UO_2 powder samples as well as SC grains extracted from the polycrystalline material have been examined with scanning electron microscopy energy dispersive X-ray spectroscopy (SEM EDS), electron paramagnetic resonance (EPR) spectroscopy and high-energy resolution fluorescence detection X-ray spectroscopy (HERFD-XAS).

EXPERIMENTAL. Cr-doped UO_2 was produced by dissolving $\text{UO}_2(\text{NO}_3)_2$ and $\text{Cr}(\text{NO}_3)_3$ in MilliQ water followed by precipitation of ammonium diuranate (ADU) with NH_3 . The ADU samples were calcined under air at 800°C for 5 h and thereafter at 600°C under 4% H_2 –96% Ar atmosphere for additional five hours. Finally, the powders were pelletized and sintered at $1,700^\circ\text{C}$ for 10 h in 4% H_2 –96% Ar atmosphere. The extraction of the SC grains from sintered pellets was achieved directly via mechanical separation. Powder samples and each SC grain were analyzed with XRD prior to microscopic and spectroscopic investigations to confirm the bulk structure to be pure cubic fluorite UO_2 ($Fm\bar{3}m$).

RESULTS. SEM EDS measurements of U-L, O-K, and Cr-K edges revealed a homogenous U distribution in the powder samples, while clear Cr-O clusters were found particularly in grain boundary regions. Similar Cr-O precipitates were absent in the SC grains. The collected

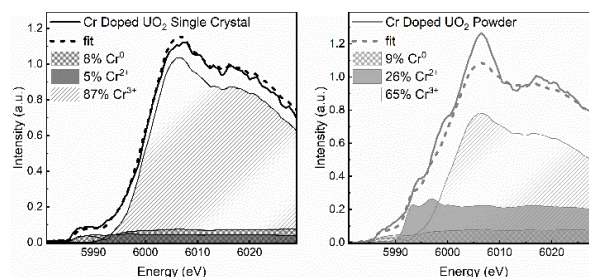


Figure 1. HERFD-XAS spectra and simulated iterative transformation factor analysis components of a Cr-doped UO_2 SC grain (left) and powder (right).

HERFD-XAS spectra between the single crystal and bulk material displayed significant differences, which could be attributed to a different Cr-redox chemistry in the samples. While the SC grain showed predominantly the presence of Cr^{3+} in the sample (Fig. 1, left), the powder sample additionally displayed significant contributions from Cr^0 and Cr^{2+} (Fig. 1, right).

Combining the microscopic and spectroscopic findings, the redox chemistry of Cr in the two sample types can be attributed to Cr incorporation into the UO_2 matrix as Cr^{3+} , and the formation of metallic Cr (Cr^0), oxide related Cr^{2+} and $\text{Cr}^{3+}_2\text{O}_3$, attributed to grain boundary species and precipitates in the bulk material. To shed light on the charge compensation mechanism in the UO_2 matrix following incorporation of the subvalent Cr^{3+} ion, EPR investigations of five SC grains were conducted. The obtained EPR spectrum along with the fitted model of Cr-doped UO_2 are consistent with Cr^{3+} in a distorted octahedral environment. From EPR analysis, and overall spin of $S = \frac{3}{2}$ could be fitted, pointing toward a high-spin Cr^{3+} together with oxygen vacancies to balance the charge. Cr^{3+} coupled with oxidized U^{5+} for charge compensation, would result in an $S = 2$ spin-state (or $S = 1$, due to spin pairing) and can be excluded, as this would lead to a silent EPR spectrum.

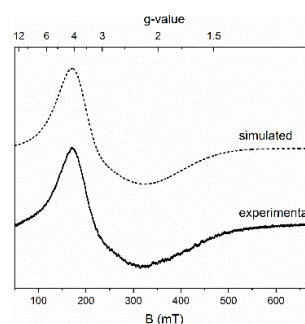


Figure 2. Measured and modelled EPR spectra of Cr-doped UO_2 single crystal grains at room temperature.

ACKNOWLEDGEMENTS. This work was funded by the German Federal Ministry of Education and Research as part of the AcE project (02NUK060).

- [1] Murphy, G. L. *et al.* (2023) *Nat. Commun.* **14**, 2455.
- [2] Riglet-Martial, C. *et al.* (2014) *J. Nucl. Mater.* **447**, 63–72.
- [3] Cooper, M. W. D. *et al.* (2018) *Acta Mater.* **150**, 403–413.
- [4] Sun, M. *et al.* (2020) *Commun. Mater.* **1**, 1–8.
- [5] Smith, H. *et al.* (2022) *Commun. Chem.* **5**, 163–170.

Speciation of fission products in oxide and metallic precipitates in nuclear fuel

R. Caprani,¹ P. Martin,¹ D. Prieur, J. Martinez,¹ N. Clavier²

¹CEA, Bagnols-sur-Cèze, France; ²ICSM, Bagnols-sur-Cèze, France

Through the coupling of multi-scales techniques, we were able to achieve a thorough picture of the fission products (FP) speciation inside irradiated MOx fuel. First, we observed the effects of soluble FP (Ce, La, Nd, Y, Sr, Zr) on the (U, Pu, FP)O₂ solid solution, and then, we focused on the speciation of the metallic and oxide precipitates (white and grey phases).

Model Uranium-based materials called SIMfuel have been developed in the last decades to overcome the high radio-toxicity of spent fuel, and to enable separation-of-effect studies on its otherwise overwhelmingly complicated chemistry. Doping UO₂ with selected stable FP isotopes reduces significantly the radiological risk, but the complex interaction between Pu and FP cannot be addressed. Therefore, we developed a fabrication route for U_{1-y}Pu_yO_{2-x} SIMfuel (SIMMOx), in order to synthesize materials representative of real irradiated fuel and to study the speciation of FP inside the MOx fuel.

EXPERIMENTAL. Three (U, Pu, FP)O₂ batches were synthesized through an optimized powder metallurgy routes. Batch S contains only soluble FPs while batch SM contains the precursors for the metallic inclusions Mo, Pd, Rh and Ru. Batch SMB has the same composition as SM, with the addition of Ba.

RESULTS. Metallography of all the three SIMMOx batches highlight the presence of white phases in batch SM, and, of white and grey phases in batch SMB.

As expected, the three SIMMOx batches are characterized by the same crystallographic structure (fluorite – SG 225) and have similar structural parameters (Fig. 1), suggesting that the introduction of metallic and oxide inclusions does not drastically change the speciation of the actinide matrix. Small differences in the O/M have been observed among the three batches, which could be due to the interaction between the different families of FP and the MOx matrix.

Through microstructural analysis, we were able to identify the size and distribution of the metallic secondary phases, which are mostly nanometric inclusions precipitating at the matrix grain boundary. Some larger (ECD > 10 μm) white phases are visible, which are probably due to the melting and transport of some of the alloys component, such as Pd. This size distribution, dominated by nanometric grain boundary inclusions, with a few larger (ECD > 10 μm) precipitates, is typical in irradiated MOx, where the high temperatures reached in the material cause part of the alloys to melt and migrate towards the centre of the pellet.

In batch SM, all the three possible crystallographic phases of white phases are observed: FCC or α-phases (SG 225), BCC or β-phases (SG 229), and HCP or ε-phases (SG 194). On the other hand, in batch SMB analysis though, no FCC could be detected (Fig. 1). The speciation of the individual elements also changed in batch SMB, with Mo showing clear signs of partial oxidation, which could have caused a shift in average composition of the alloys, and therefore of their crystallographic structure. Also Pd XANES evi-

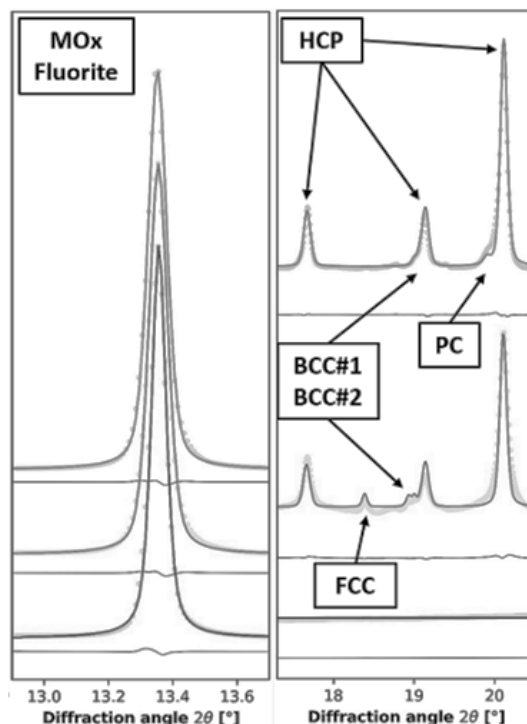


Figure 1. Experimental and fitted SP-XRD pattern collect at 17 keV of the samples S, SM and SMB. Magnification of first MOx peak (left) and of region in which FP-based minor phases are identified (right).

denced a significant change in structure, which unfortunately, we were not able to quantify.

The ensemble of these effects are due to the interaction between Ba and the other FP. The formation of grey phases, induces a partial oxidation of the Mo inventory, which we hypothesize would precipitate in some kind of perovskite-type phase, as expected from studies on irradiated MOx fuel. All characterization techniques – structural, microstructural, and atomic-scale – agree that the structure of Ba-based precipitates is a Primitive Cubic (SG 221) perovskite structure. We were able to estimate that these inclusions have a very complex chemical composition, the main components being Ba and Zr, but hosting relatively large quantities of Sr and RE, especially Ce. The precipitation of these elements from the solid solution, which we found quantitatively consistent with the slight change in the lattice parameter of the (U, Pu, FP)O₂ solid solution from batch S to batch SMB.

Arriving at such a complete description of the speciation of FP and of their respective FP-based precipitates, was only possible through the multi-scale coupling of several techniques, some of which are not easily available to irradiated fuel studies. Furthermore, the ability to design sample batches with different compositions, allows to determine the effect of – potentially – individual FP on the entire system, performing real separation-of-effect studies, which is impossible to do on irradiated MOx.

[1] Caprani, R. et al. (2023) *J. Nucl. Mater.* **585**, 154607.

Quantum crystallographic study on π -hole interactions of quinoid rings with iodide anions

C. Hennig, V. Milašinović,¹ V. Vuković,² A. Krawczuk,³ K. Molčanov,¹ M. Bodensteiner²

¹Department of Physical Chemistry, Rudjer Bošković Institute, Zagreb, Croatia; ²Röntgenstrukturanalytik, Universität Regensburg, Germany; ³Institut für Anorganische Chemie, Universität Göttingen, Germany; ³Röntgenstrukturanalytik, Universität Regensburg, Germany

Quantum crystallographic studies require very high resolution and excellent signal-to-noise ratio. These experimental conditions are available to the crystallographic community at the XRD-2 diffractometer of the Rossendorf Beamline.^[1] An example of such investigations is demonstrated by a combined experimental and theoretical charge density study using multipole modelling on a co-crystal of 3-chloro-N-methylpyridinium iodide and tetrabromoquinone.^[2]

The experimental setup for single crystal diffraction at the XRD-2 diffractometer comprises a Huber Kappa goniometer on which the samples are mounted and a Pilatus3 X2M detector for data collection (Fig. 1). The detector has typically a distance of 170 mm to the sample and remains constantly tilted by 45 degrees during the measurement.



Figure 1. Experimental setup for electron density measurements at the XRD-2 diffractometer of the Rossendorf Beamline.^[1] The Pilatus3X2M detector is tilted by 45 degrees.

The required resolution is achieved *via* the selected excitation energy (Fig. 2). Such measurements can be performed using the highly reflective Rh mirror below the Rh K absorption edge at 23.22 keV. An excitation energy of 22 keV is usually sufficient, which corresponds to a resolution of

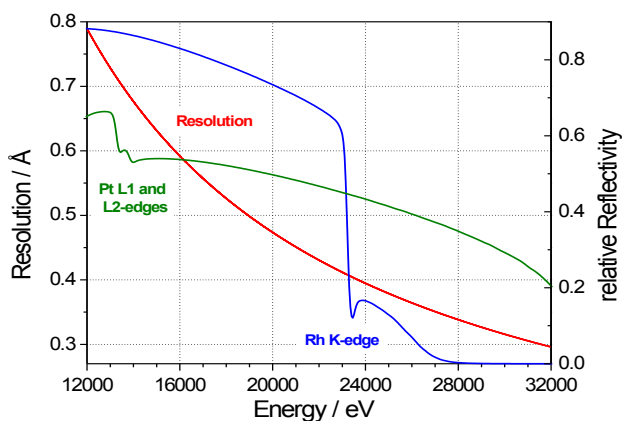


Figure 2. Resolution as function of excitation energy for the experimental setup shown in Fig. 1 and relative reflectivity of the Rh and Pt mirrors.^[1] Most experiments are performed at 22 keV excitation energy, which is a good combination of high flux and high resolution.

approximately 0.43 Å. Higher resolutions can be achieved with the Pt mirrors.

The co-crystal of 3-chloro-N-methylpyridinium iodide with tetrabromoquinone (Br4Q) was prepared using an excess of solid 3-chloro-N-methylpyridinium iodide added to a 5 °C cold saturated solution of tetrabromoquinone in acetone. The single-crystal diffraction was performed using the Si(111) monochromator, a sample temperature of 100 K and 0.1 s illumination time per frame. An appropriate crystal was measured to a resolution of 0.475 Å with a high data redundancy. A total of 131,167 reflections were merged to 12,766 symmetry-independent reflections. The obtained crystal structure reveals a π -hole interaction between the iodide anion and a quinoid ring involving an $n \rightarrow \pi^*$ charge transfer. The deformation density maps in the mean planes of Br4Q is shown in Fig. 3.

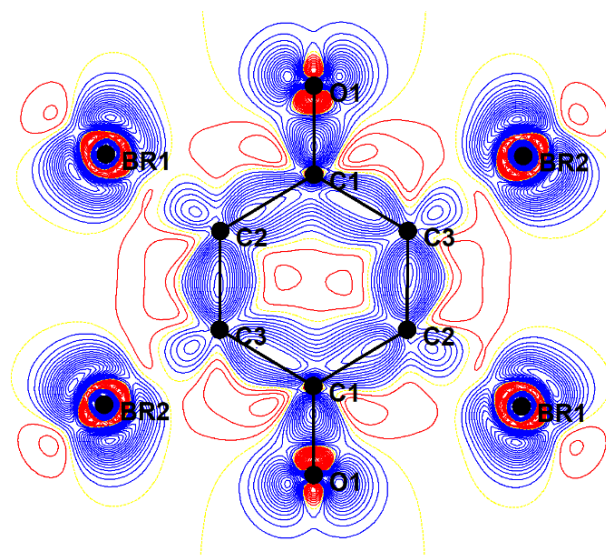


Figure 3. Deformation density maps in the mean planes of Br4Q. The spacing between contours is of 0.05 $e\text{Å}^{-3}$; the positive density is blue, the negative is red and the zero contour is drawn as a yellow dotted line.^[2]

Crystals of neutral tetrabromoquinone are yellow, whereas the investigated crystals are black. The investigation revealed that the quinoid ring has a partial negative charge (estimated to be in the range 0.08–0.11 e) and a partial radical character, which is related to the black color of the crystals.^[2] A detailed X-ray charge density study showed two symmetry-independent bond critical points between the iodide anions and carbon atoms of the ring. Their maximum electron density of 0.065 $e\text{Å}^{-3}$ was reproduced by quantum chemical modelling. The energy of the interaction is estimated to be $-11.16\text{ kcal mol}^{-1}$, which is comparable to the strength of moderate hydrogen bonding (about -10 kcal mol^{-1}); it is dominantly electrostatic, with a considerable dispersion component. The interaction is an $n \rightarrow \pi^*$ type and donates electrons into an empty π^* (*i.e.*, LUMO) orbital of quinone.^[2]

[1] Scheinost, A. C. *et al.* (2021) *J. Synchr. Rad.* **28**, 333–349.

[2] Milašinović, V. *et al.* (2023) *IUCrJ* **10**, 156–163.

High-Energy Resolution Fluorescence Detection mode for EXAFS analysis

E. F. Bazarkina

High-Energy Resolution Fluorescence Detection (HERFD) spectroscopy is widely used for XANES analyses, however, EXAFS analysis can also benefit from it. This report addresses the particularities of HERFD-EXAFS in comparison to TFY-EXAFS, emphasizing its particular relevance to actinide science.

The Extended X-ray Absorption Fine Structure (EXAFS) is a powerful technique for determining the local atomic structure of an element of interest within the matrix of other elements. EXAFS is a function of multiple parameters, including the coordination number in shell, the backscattering amplitude, the interatomic distance, a phase shift, the Debye–Waller factor, and the amplitude reduction factor.

EXAFS is indispensable for studying the local structure in poor crystalline and amorphous solids, as well as at the ppm-level impurities/dopants. It is valuable for investigation of dissolved complexes in liquids, where other techniques such as X-ray diffraction are silent. Initially, EXAFS technique was developed for the measurements in transmission mode (TR-EXAFS); later it was extended to the total fluorescence (TFY-EXAFS) that has become the most favorable because it generally provides a very high signal-to-noise ratio and a low detection limit. However, HERFD-EXAFS offers distinct advantages: (i) when the background of the X-ray absorption spectrum is too high compared to the edge jump, for example due to the other elements or from the low-energy tail of the Compton peak; (ii) when the emission lines of elements present in the samples overlaps with those of analyzed element; (iii) in cases where the electronic structure of the element (multi-electron excitations) affects the EXAFS signal; (iv) when the emission line is sensitive to the state of the element (valence, spin, site) thus the HERFD-EXAFS can be state-selective and explored for mixed-state compounds (as reported for Mn^{2+} and Mn^{3+} , Fe^{2+} and Fe^{3+} compounds).

EXPERIMENTAL. The X-ray emission (XES) spectrometer is indispensable for HERFD measurements.^[1,2] The main optical elements of the XES spectrometer include crystal analyzers and the detector, mounted together with the sample in Rowland circle geometry. The spectrometer configuration is individual for each element and each emission line.

RESULTS. HERFD offers enhanced sensitivity and selectivity, especially for dilute samples. As all actinides are heavy atoms, the analysis of the elements present in actinide compounds as dopants/impurities by EXAFS is more difficult comparing to other matrixes (typically dominated by such atoms as O, C, H, N, Si, Al). Thus, in the case of Cr-doped UO_2 , the TFY-XAS spectra of Cr at the K-edge suffers from the extremely strong absorption from UO_2 matrix (*i.e.*, the X-ray attenuation is 1.5 microns for incident X-rays at 5,989 eV and 0.95 for emitted $K\alpha_1$ fluorescence of Cr, Fig. 1A). This makes the EXAFS measurements very challenging.^[3] The TFY-XAS spectra obtained in the Cr-doped UO_2 powder is noisy and difficult to explore for EXAFS despite rather high Cr concentration (thousands of ppm), neither in TR mode, but only in the HERFD mode (Fig. 1B).^[3] The potential applications of HERFD-EXAFS in actinide studies are diverse. For exam-

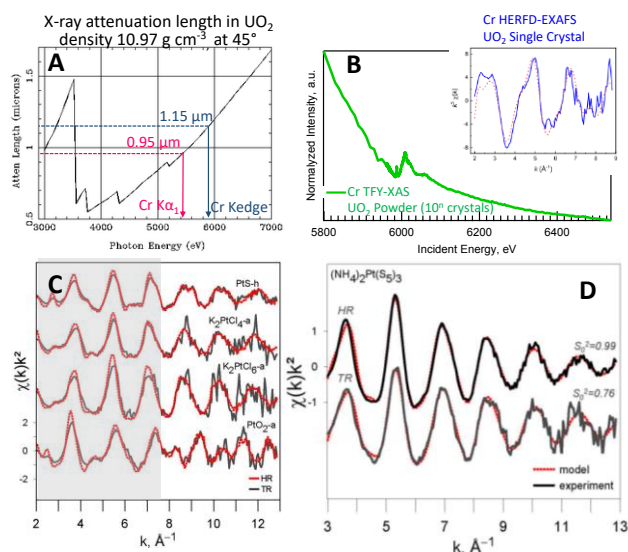


Figure 1. The X-ray attenuation length (the depth where the intensity of X-rays falls to 1/e of its value at the surface) in the UO_2 crystal between 3,000 and 7,000 eV (A). Non-normalized TFY XAS spectra at Cr K-edge of the Cr-doped UO_2 powder and the HERFD-EXAFS of the single crystal UO_2 (B). EXAFS spectra of Pt compounds in TR and HERFD (HR) modes (C); the grey area indicates the k-range when HERFD-EXAFS has systematic increase of the amplitudes. Experimental and modelled EXAFS of $(NH_4)_2Pt(S_5)_3$ compound in TR and HERFD (HR) modes with S_0^2 parameter found to be different between two modes (D).

ple, Y-bearing matrix with low U concentration would require HERFD modes due to strong absorption of Y-rich matrix at the $U L_3$ edge.

The HERFD-EXAFS is out of main-stream techniques and thus should be applied carefully. The recent systematic study of Pt compounds has shown that EXAFS spectra in TR, TFY and HERFD modes requires distinct amplitude reduction factor (S_0^2) values, 0.76 ± 0.04 (for TFY and TR) and 0.99 ± 0.07 (for HERFD).^[4] The amplitude reduction factor is an important parameter in EXAFS models because it is strongly correlated with coordination number. The S_0^2 value is usually found from a spectra of well-known structures and applied to a set of unknowns as a scale factor. Thus the value of S_0^2 value is constant for every absorbing atom due to the relaxation of all the other electrons in the absorbing atom to the core hole in the ground state, but it can be different when HERFD-EXAFS is applied as it is a case for Pt. This example demonstrates that HERFD-XANES and TFY-EXAFS may require different S_0^2 values.

To conclude, comparing to the TFY-EXAFS, HERFD-EXAFS is far from the main-stream techniques and requires more systematic studies. However, despite the fact that HERFD-EXAFS is less explored and remains more time-consuming (additional time is required for the alignment of the spectrometer and the EXAFS acquisition time per sample is longer due to relatively low signal to noise ratio in the EXAFS region), it is perspective and sometimes indispensable for the specific case studies including actinide science field.

[1] Scheinost, A. C. *et al.* (2021) *J. Synchrotron Rad.* **28**, 333–349.

[2] Bazarkina, E. F. and Kvashnina, K. O. (2022) *Report HZDR-119*, p. 24.

[3] Murphy, G. *et al.* (2023) *Nature Comm.* **14**, 2455.

[4] Laskar, C. *et al.* (2022) *Minerals* **12**, 1602.

Molecular oxo-Hydroxo Ce clusters probed by HERFD-XAS at the Ce L₃ edge

P. Estevenon,¹ L. Amidani, T. Dumas,¹ K. O. Kvashnina

¹CEA, DES, ISEC, DMRC, Université Montpellier, Marcoule, France

We recently employed Ce L₃ HERFD-XAS in combination with electronic structure calculations to investigate Ce oxo-hydroxo polynuclear complexes. These clusters have the potential to act as fundamental building blocks in nanoscale architectures, where multiple clusters together can exhibit highly active properties similar to small particles.

To explore this, a series of Ce clusters with increasing size (ranging from 0.6 nm to 1.2 nm) and nuclearity (comprising 6 to 38 Ce atoms) were synthesized and characterized using high-energy X-ray Scattering (HEXS), X-ray Pair Distribution Function (PDF) and High Energy Resolution Fluorescence Detected X-ray Absorption Spectroscopy (HERFD-XAS) methods.^[1] The obtained results were compared to larger CeO₂ nanoparticles and bulk CeO₂. The employed methods consistently revealed trends as the system size progressed from molecular Ce-*n* clusters (2, 6, 24, 38, and 40) to bulk CeO₂.

EXPERIMENTAL. HERFD-XAS at the Ce L₃-edge (Fig. 1) was employed to characterize the cerium (IV) clusters. The cerium oxidation state in the samples was determined by examining the cerium pre-edge region (around 5,718 eV), denoted as peak A in Fig. 1. This peak arises from the electronic transition between the 2p and 4f valence orbitals. In the aqueous solution, Ce(IV) exhibited a spectrum with two primary peaks centered around 5,726.6 eV and 5,737.0 eV, labeled as peaks B and C in Fig. 1 (top). These peaks correspond to dipole-allowed electron transitions from the 2p_{3/2} to 5d_{5/2} states and can be attributed to the screened (B) and unscreened (C) excited states.

RESULTS. A splitting of these peaks was observed in the CeO₂ spectrum, resulting in peaks B₁ and B₂ as well as peaks C₁ and C₂ in Fig. 1. This splitting is a consequence of the crystal field present in the CeO₂ fluorite structure, where each Ce atom is surrounded by eight oxygen atoms with Oh point symmetry. Consequently, two groups of peaks are observed: the first group has peaks located around 5,724.5 eV (B₁) and 5,728.4 eV (B₂), while the second group is located around 5,735.9 eV (C₁) and 5,738.5 eV (C₂). In the cubic crystal field, the Ce 5d density of states is split into e_g and t_{2g} bands, corresponding to B₁ and B₂, respectively. Based on this analysis, it was observed that the Ce-*n* cluster (Fig. 1) closely resembled the shape of Ce(IV) in aqueous solution, with a slight broadening observed in peaks B and C. In contrast, the larger cerium clusters, Ce-*n* (24 and 38), exhibited broader HERFD-XAS spectra that fell between the spectra observed for aqueous Ce(IV) and CeO₂. Notably, a significant broadening of the two characteristic Ce(IV) peaks (B and C) was observed in these spectra, indicating a peak splitting analogous to the crystal field splitting observed in CeO₂.

Overall, the trend observed was a progressive splitting of both B and C peaks, bringing the spectra closer to the CeO₂ spectral shape as the cluster size increased. In order to elucidate the spectral shape of the clusters, authors took advantage of the cluster structure from XRD and PDF and used it to simulate Ce L₃ HERFD-XAS spectra. The simulation depicted in Fig. 1 (bottom) clearly reproduces the

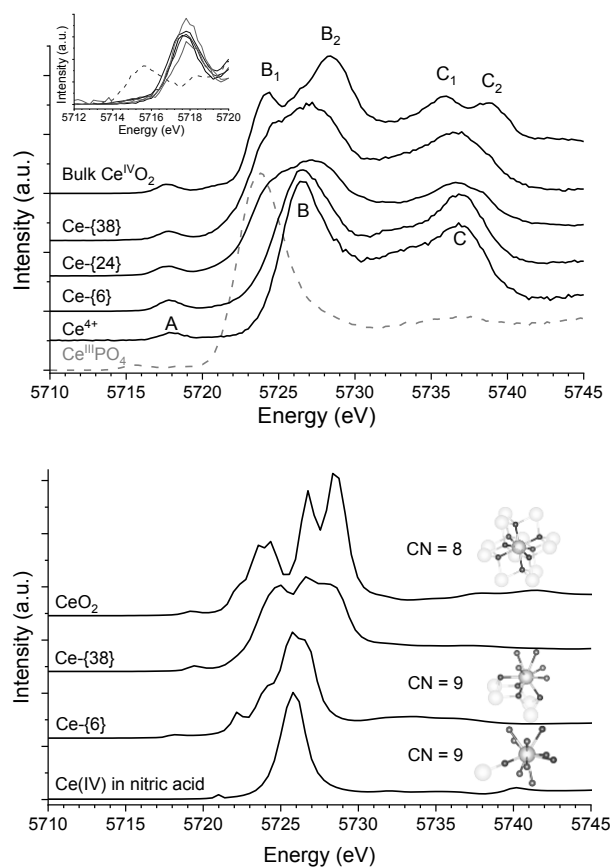


Figure 1. HERFD-XAS experimental spectra at Ce L₃-edge for the Ce⁴⁺, Ce-*n* (6, 24 and 38) clusters compared to CeO₂ and CePO₄ references (top). The magnification of the pre-edge was reported in the inserts and compared to monazite as Ce(III) oxidation state reference (grey dashed line). Simulated spectra at Ce L₃-edge for aqueous Ce⁴⁺, Ce-*n* (24, 38) and bulk CeO₂ (bottom).

splitting of the 5d states in CeO₂, resulting in two distinct groups of transitions. The first group corresponds to less intense transitions to e_g orbitals (B₁), while the second group represents more intense transitions to t_{2g} orbitals (B₂). In contrast, Ce(IV) ions in nitric acid solution resulting in a single peak for the 5d orbitals. This single-peak spectrum corresponds well to the experimental B peak in the respective experiment.

HERFD-XAS performed at the Ce L₃ edge demonstrated a gradual splitting of the Ce 5d states, indicating a transition towards more CeO₂-like characteristics as the core of the complexes developed. These experimental findings were supported by electronic structure calculations based on the crystallographic determination of the cluster structures. Theoretical simulations enabled the isolation of structural and electronic properties of individual Ce sites within the clusters, emphasizing the significant distinction between surface and core Ce atoms. This example demonstrates how the local and electronic characteristics of Cerium oxo-hydroxo nanoparticles can be examined through the synergistic utilization of HEXS, PDF and HERFD-XAS methods.

[1] Estevenon, P. *et al.* (2023) *Chem. Mater.* **35**, 1723–1734.

Fracture mechanics characterization of ferritic steels by means of miniaturized specimens

M. Sánchez,¹ E. Altstadt, A. Das

¹University of Cantabria, Santander, Spain

The use of mini-CT (CT – compact tension) specimens for the fracture characterization of structural steels is currently a topic of great interest from both scientific and technical points of view. In this work, we reviewed the challenges and benefits associated with this method and demonstrated its robustness.

Long-term operation of nuclear plants requires accurate characterization of the reactor pressure vessel materials and evaluation of the neutron irradiation induced embrittlement without excessive conservatism. However, the available surveillance materials used to characterize the resulting degradation is generally small. Consequently, in order to increase the reliability of fracture toughness measurements and reduce the volume of material needed for the tests, innovative characterization techniques are being developed, among which the use of mini-CT specimens is one of the most promising options. Those mini-CTs can be manufactured from already tested larger specimens, *e.g.*, from Charpy sized single edged bending (SEB) specimens (10×10×55 mm). In the frame of the Master curve concept, fracture toughness data, measured with mini-CT specimens, are used to evaluate the reference temperature T_0 as a measure for the transition from ductile to brittle behavior with decreasing temperature. The miniaturization of CT specimens entails a number of challenges that are discussed below.

EXPERIMENTAL. CT specimens are one of the most common types of standardized specimens used in fracture mechanics testing. The geometry provides an efficient use of the tested material, with the majority of the sample volume used to establish a controlled stress state at the crack tip during loading. Here, we focus on 4 mm-thick CT specimens. Two different mini-CT geometries have been proposed in the literature. Figure 1 shows both geometries, also illustrating a comparison between mini-CT specimens and larger CT specimens (Fig. 1b). The first one is the proportionally reduced standard geometry for the CT specimen given by the ASTM E1921 (10×9.6×4 mm). The second geometry (10×10×4.2 mm) is designed to capture directly the size of the parent SEB specimen. The latter has the advantage of simplified machining, which may be especially important with irradiated materials.^[1]

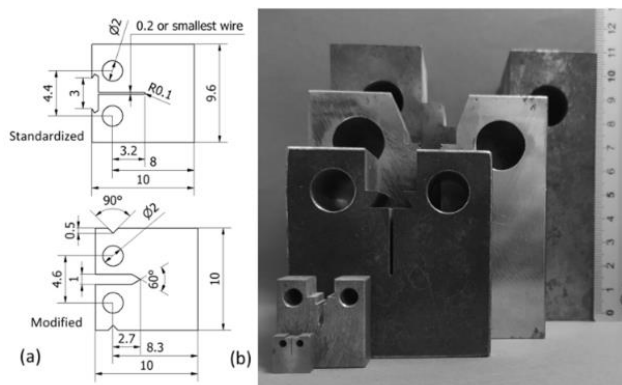


Figure 1. Standardized mini-CT vs. modified mini-CT (a, dimensions in mm); image showing the scales of different CT specimens and a standardized mini-CT (b).^[1]

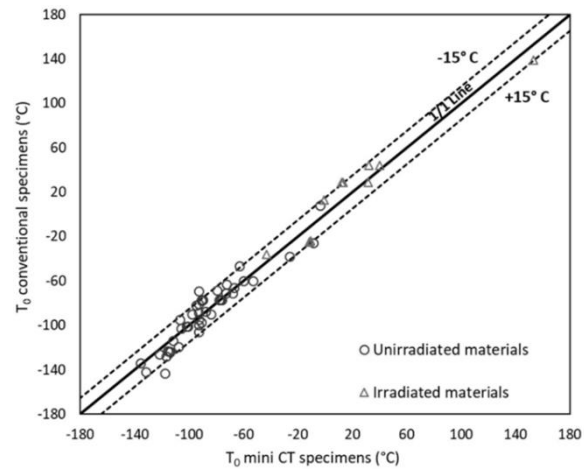


Figure 2. Comparison between T_0 values of unirradiated materials determined from conventional specimens and T_0 values obtained using mini-CT specimen.

RESULTS. A generic issue with the use of mini-CT specimens is associated with the small size itself. The stress intensity factor is a function of the far-field load and the absolute crack size (*i.e.*, $K_I \sim \sigma_0 \cdot \sqrt{a}$). Therefore, at a given fracture mechanic load K_I , the relative size of the plastic zone (plastic volume/specimen volume) is larger in mini-CTs as compared to larger specimens. Consequently, the violation of the small-scale yielding criterion (and thereby the loss of constraint) starts at lower K -values in mini-CTs, reducing the measuring capacity of mini-CT specimens compared to larger specimens. This implies, that mini-CTs have to be tested at lower temperatures to avoid censoring and to get a valid T_0 (as the material's fracture toughness K_{Jc} is increasing with temperature). Test temperatures $T > T_0 - 20^\circ\text{C}$ are associated with a significant censoring probability.^[2] On the other hand, the ASTM standard E1921 limits the window of valid test temperatures to $|T - T_0| < 50\text{K}$. Therefore, the proper choice of test temperatures is tricky, as T_0 is unknown at the beginning of the test series. In conclusion, the Master curve procedure requires a higher number of mini-CT tests for a valid T_0 (at least 14) as compared to larger specimens (6–8 tests). Nevertheless, once the mini-CT tests yield a valid T_0 , the results can be trusted. Figure 2 shows a comparison between the T_0 values obtained with large conventional specimens and those obtained using mini-CT specimens.^[1] The majority of the values gathered from the literature, including unirradiated and irradiated materials, are located between the bands of $\pm 15^\circ\text{C}$, as shown in the graph. Moreover, it is important to note, that there is no systematic bias for the mini-CT based T_0 . Thus, in general, the values of T_0 obtained with mini-CT specimens are in good agreement with those obtained with larger specimens, demonstrating the robustness of mini-CT Master curve characterization.

ACKNOWLEDGEMENTS. This work received financial support from the EU-Euratom project "Fractesus" (contract no. 900014).

[1] Sanchez, M. *et al.* (2023) *Metals* **13**, 176.

[2] Das, A. *et al.* (2023) *Nucl. Mater. Energy* **34**, 101395.

Electron backscatter diffraction (EBSD) applied to detect phase transformation in Ga₂O₃

P. Chekhonin, U. Bektas,¹ N. Klingner,¹ G. Hlawacek¹

¹HZDR, Institute of Ion Beam Physics and Materials Research, Dresden, Germany

EBSD was used to facilitate a very quick and practical way to detect phase transformation after ion irradiation of Ga₂O₃.

Automated EBSD facilitates local crystal orientation measurements in a scanning electron microscope (SEM). This method creates surface mappings, in which each point is characterized by three Euler angles.^[1] In most applications, this data is used to reveal features such as grains, grain boundaries and other microstructural details. Moreover, different phases can be distinguished and under certain conditions, texture measurements are possible. EBSD permits the analysis of large surfaces (of order mm²) thus capable of providing a statistically reliable amount of data for a general microstructural description. Furthermore, EBSD is a very surface sensitive method, only a surface layer of order 10 nm contributes to the information contained within an EBSD pattern (EBSP).

EXPERIMENTAL. Single crystals of Ga₂O₃, which is a promising candidate material for power electronics, have been locally ion irradiated in the ion beam center (IBC) of the HZDR in order to investigate their radiation hardness. A part of the sample has been masked, and thus remained unirradiated. The irradiation was done with neon ions accelerated to 140 keV to a fluence of 3.5 × 10¹⁶ cm⁻² at room temperature. EBSD was carried out on the unirradiated as well as ion-irradiated area of the crystal using a Zeiss NVision 40 SEM equipped with a Bruker EBSD system. High quality EBSPs were recorded using a detector resolution of 800 × 570 pixels and 8 × 122 ms exposure time per frame.

RESULTS. The EBSP recorded on the unirradiated pristine β-Ga₂O₃ crystal with a monoclinic structure is shown in Fig. 1a. The irradiated sample area shows a different EBSP (Fig. 1b), which was matched to the γ-Ga₂O₃ crystal with a cubic lattice.^[2]

The unirradiated β-Ga₂O₃ crystal results in a high quality EBSP, where many high indexed Kikuchi bands and details inside those are discernible. The EBSP quality in the γ-Ga₂O₃ area exhibits much less contrast, only low indexed strong intensity Kikuchi bands are clearly distinguishable. A lower EBSP quality may be explained by the intrinsic defective spinel structure of γ-Ga₂O₃ and not necessarily by additional defects introduced as a consequence of irradiation. This interpretation is supported by still ongoing Doppler broadening variable energy positron annihilation spectroscopy (DBVEPAS) measurements at pELBE. However, a quantification from this pattern is not possible. The orientation relationship between the two phases was determined by EBSD as:

$$\begin{aligned} \beta\text{-Ga}_2\text{O}_3 [100] // \gamma\text{-Ga}_2\text{O}_3 [1 \quad -5.6 \quad -1] \\ \beta\text{-Ga}_2\text{O}_3 [010] // \gamma\text{-Ga}_2\text{O}_3 [1 \quad 0 \quad 1] \\ \beta\text{-Ga}_2\text{O}_3 [001] // \gamma\text{-Ga}_2\text{O}_3 [-1 \quad 0 \quad 1] \end{aligned}$$

and

$$\begin{aligned} \gamma\text{-Ga}_2\text{O}_3 [100] // \beta\text{-Ga}_2\text{O}_3 [0 \quad 1.9 \quad -1] \\ \gamma\text{-Ga}_2\text{O}_3 [010] // \beta\text{-Ga}_2\text{O}_3 [-1.9 \quad -0.1 \quad -1] \\ \gamma\text{-Ga}_2\text{O}_3 [001] // \beta\text{-Ga}_2\text{O}_3 [0 \quad 2 \quad 1] \end{aligned}$$

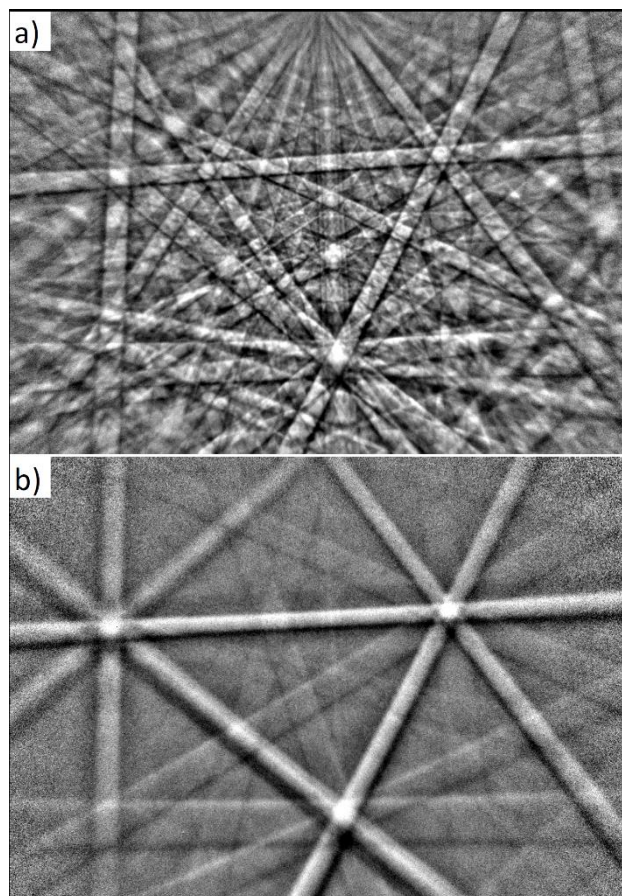


Figure 1. EBSD patterns of the unirradiated pristine Ga₂O₃ crystal (a, β-Ga₂O₃) and after neon ion irradiation (b, γ-Ga₂O₃).

The fractional numbers indicate that there is misalignment between some low indexed directions of the β-Ga₂O₃ and the γ-Ga₂O₃ polymorphs.

EBSD proved to be a very efficient method to locally determine the phase transformation and the orientation relationship between the pristine crystal and a phase formed after ion irradiation. Thus, it facilitates the possibility to conduct a large array of experiments (for example done by means of focused ion beams) with different ions, ion energies and fluences. While an alternative approach by means of transmission electron microscopy (TEM) is attractive to analyze the irradiated layers in cross section and to study the interface between the phases, particularly the TEM sample preparation is not feasible for a large number of experiments.

ACKNOWLEDGEMENTS. M-ERA.NET Program is acknowledged for financial support via GOFIB project (administrated by the Research Council of Norway project number 337627 in Norway, the Academy of Finland project number 352518 in Finland, and the tax funds on the basis of the budget passed by the Saxon state parliament in Germany). Support by the Structural Characterization Facilities Rossendorf at IBC is gratefully acknowledged, too.

[1] Dingley, D. (2004) *J. Microsc.* **213**, 214–224.

[2] Azarov A. et al. (2023) *Nature Comm.* **14**, 4855.

Annealing behavior of a neutron-irradiated VVER-1000 reactor pressure vessel weld

A. Ulbricht, F. Bergner, E. Altstadt

Post-irradiation annealing of neutron-irradiated reactor pressure vessel steels is a measure, both used in the past and potentially to be used in future, to extend the lifetime of running nuclear power plants. In order to better understand how and to which degree neutron damage is reversed upon annealing, we have applied small-angle neutron scattering (SANS) and Vickers hardness testing to a VVER-1000 reactor pressure vessel weld. We have found partial to almost full recovery towards the unirradiated reference depending of the temperature of post-irradiation annealing.

EXPERIMENTAL. The material is a SV10KhGNMAA-type submerged arc weld (1.14 % Mn, 0.38 % Si, 1.66 % Cr, 1.71 % Ni, 0.63 % Mo, 0.04 % Cu, rest Fe) used in VVER-1000 reactors. Unirradiated samples representative of unit 1 of the South-Ukrainian Nuclear Power Plant were provided in the 1980s by VNIIAES. Yield stress $R_{p0.2}$ and Vickers hardness HV10 of the weld are 595 MPa and 206, respectively. Specimens of size $10 \times 10 \times 55$ mm were irradiated in the near-core high-flux channels of the VVER-2 prototype reactor at Rheinsberg. The irradiation temperature was $(255 \pm 5)^\circ\text{C}$. The neutron flux was $2.8\text{--}5.4 \times 10^{12} \text{ cm}^{-2} \text{ s}^{-1}$ ($E > 0.5 \text{ MeV}$). The mean neutron fluence received by the studied samples was estimated to be $65.1 \times 10^{18} \text{ cm}^{-2}$, which corresponds to a neutron exposure of 0.065 dpa (displacements per atom). A number of small samples of size $10 \times 10 \times 1$ mm were cut from broken halves of the notched bars tested before. Part of the as-irradiated samples was exposed to annealing treatments in Argon atmosphere followed by furnace cooling. The annealing temperatures were chosen to be 350, 400, 425, 450, and 475°C , one sample per temperature. The annealing time was 10 h.

The SANS experiment was conducted at the beamline D11 of ILL Grenoble using a neutron wavelength of 0.5 nm, a beam diameter of 7 mm and sample–detector distances of 1.1 m and 5 m.^[1] During the measurements a saturation magnetic field of 1.4 T oriented perpendicular to the neutron beam was applied to the samples. The ILL software routine was used to separate magnetic and nuclear scattering cross sections from the total cross sections as functions of the scattering vector Q . The size distribution of scatterers was calculated by solving the inverse problem for the measured magnetic difference scattering curves (the scattering curve of the unirradiated condition taken as reference) using the indirect Fourier-transform method. Spherical nonmagnetic scatterers randomly dispersed in the ferromagnetic matrix were assumed as an approximation to estimate mean size, number density and volume fraction c of scatterers. After completion of the SANS experiment, the Vickers hardness HV10 (load 98.1 N) was measured using the same samples.

RESULTS. The calibrated magnetic scattering cross sections measured for the unirradiated, as-irradiated and post-irradiation annealed conditions of the weld are plotted in Fig. 1. The increase of the cross sections at large values of Q indicates the irradiation-induced formation of nm-scale Mn-Ni-Si-P-enriched solute atom clusters. The mean diameter was estimated to be 1.1 nm. Post-irradiation annealing gives rise to a reduction of the cross sections as compared to the as-irradiated condition indi-

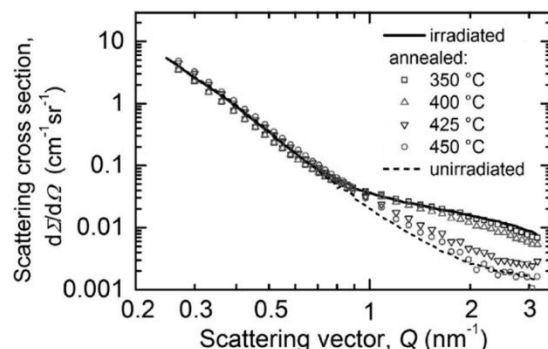


Figure 1. Measured magnetic scattering curves for the as-irradiated weld, the post-irradiation annealed conditions and the unirradiated reference.

ating partial dissolution of clusters combined with limited coarsening of the remaining ones. The total volume fraction expressed in percent of the volume fraction c_{irr} of clusters in the as-irradiated condition is plotted in Fig. 2 as function of the annealing temperature. The percentage of the excess Vickers hardness increase over the unirradiated reference is included for comparison. Both quantities decrease gradually to approximately reach the unirradiated level at $475^\circ\text{C}/10 \text{ h}$.

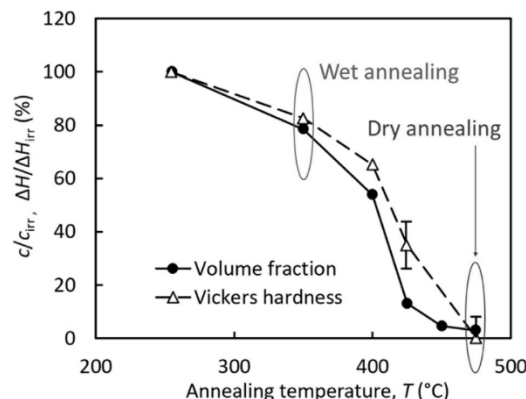


Figure 2. Volume fraction c and excess Vickers hardness $\Delta\text{HV}10$ in percent of the as-irradiated condition as functions of the annealing temperature.^[1]

The annealing curves of the volume fraction of clusters and the excess Vickers hardness exhibit similar shapes. This confirms that the dominant reason for the gradual hardness recovery is the reduction of the volume fraction of irradiation-induced clusters upon annealing. Two regions of the annealing temperature of particular technical interest for large-scale annealing are marked in Fig. 2. Dry annealing requires the removal of the reactor internals in order for the inner near-core region of the pressure vessel to be exposed to a heating system. Dry annealing at 475°C for 10 h gives rise to almost complete recovery of the unirradiated condition in the present case. The less expensive, but also less efficient, process of wet annealing is based on the exposure of the pressure vessel to the temperature of the pressurized water, the maximum achievable temperature being 343°C . Figure 2 indicates a small but significant partial recovery by way of annealing at 350°C for 10 h in the present case.

[1] Ulbricht, A. et al. (2023) *Front. Nucl. Eng.* **2**, 1176288.

Microstructural characterization of reactor pressure vessel steels

L. Lai, P. Chekhonin, S. Akhmadaliev,¹ J.-E. Brandenburg, F. Bergner

¹HZDR, Institute of Ion Beam Physics and Materials Research, Dresden, Germany

Two reactor pressure vessel (RPV) steels have been ion irradiated and studied by means of transmission electron microscopy (TEM).

The RPV is a safety relevant component of a nuclear power plant which determines its maximal potential operation time span. An obstacle to study the RPV steels embrittlement after neutron irradiation is the scarcity of neutron irradiation facilities as well as the handling of activated material. Ion irradiation is a promising tool to emulate neutron-irradiation effects on RPV steels. This approach requires the consideration of ion-neutron transferability issues, which are addressed in the present study by comparing the effect of ions with neutron-irradiation effects reported for the same materials.

EXPERIMENTAL. Two commercial RPV steels with body-centered cubic (bcc) structure, here referred to as ANP-6 (western second-generation RPV weld) and ANP-10 (2nd/3rd generation RPV steel forging) have been investigated.^[1] Ion irradiations on polished samples were done in the Ion Beam Center (IBC) at HZDR using Fe²⁺ ions with an energy of 5 MeV. Using the same flux, two different fluences of $2.67 \times 10^{14} \text{ cm}^{-2}$ (low dose) and $2.67 \times 10^{15} \text{ cm}^{-2}$ (high dose) were chosen. At the depth of 500 nm the resulting exposures are 0.1 dpa and 1.0 dpa, respectively. After ion irradiation, cross-sectional samples of irradiated materials were lifted out by focused ion beam (FIB) technique and studied in a Talos 200 transmission electron microscope in scanning operation mode (STEM). Subsequently, segments with a width of $0.1 \mu\text{m}$ were defined from the surface of the cross-sectional samples and analyzed along the perpendicular direction. This way the depth profiles of the number density and size of loops were acquired.

RESULTS. After both materials were ion irradiated, dislocation loops can be observed as small dots or loops in the STEM bright field images. Figure 1 shows an example STEM image of ion-irradiated cross sections in ANP-10. On the left-hand side of the STEM images, the depth profiles of calculated displacement damage and injected interstitials are attached. The most prominent feature is the damage band with a high density of dislocation loops located in the range from $1.2 \mu\text{m}$ to $1.6 \mu\text{m}$ below the surface, which overlaps with the depth range of maximum injected interstitials. At lower depth, the dislocation loops are not distributed homogeneously and located preferentially in the vicinity of sinks (initial line dislocations and grain boundaries). The number density and average diameter of loops were measured segment by segment and are presented in Figs. 2a, b as a function of depth. Both, the number density and size of irradiation-induced loops increase as functions of dose in such a way that the number density of point defects constituting the loops is linearly related to dose. The number density and size of loops representative of the zone between the surface and the band (safe zone) were compared with results reported for the same materials irradiated with neutrons. Within the safe zone the amount of injected interstitials is close to zero, thus making this zone more comparable to neutron irradiation.

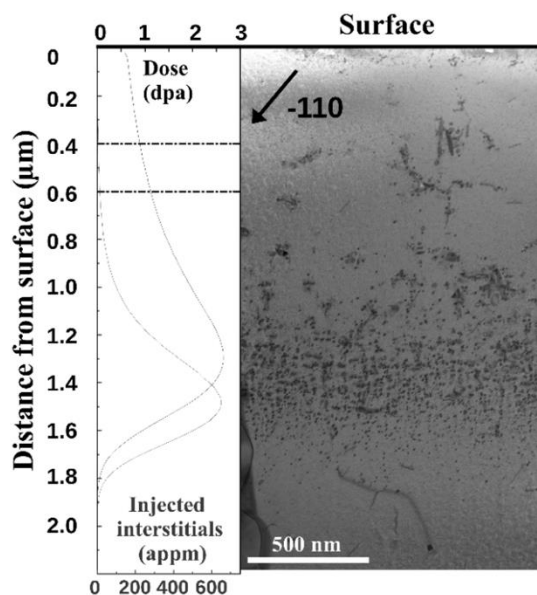


Figure 1. Cross section micrograph of ion-irradiated RPV steel ANP-10 recorded by STEM. Left side shows the depth profiles of calculated displacement damage and injected interstitials.

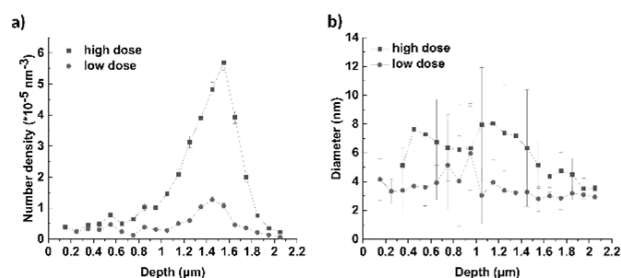


Figure 2. Number density (a) and average loop diameter (b) in ANP-10 as a function of depth.

At comparable dose levels, the size of dislocation loops is almost the same for ion and neutron irradiation. The number density of loops for the ion-irradiated samples is significantly higher (by at least one order of magnitude) than for the neutron-irradiated samples. This is related to the higher dose rate of ion irradiation as compared to neutron irradiation.

ACKNOWLEDGEMENTS. This research was funded by project ENTENTE, Euratom research and training programme 2019/2020 under grant agreement No. 900018. The authors are grateful to Vanessa Dykas for the preparation of traditional TEM samples; Wolfgang Webersinke for annealing treatment; Hans-Jürgen Engelmann for the preparation of FIB samples; and Cornelia Kaden, Karin Vogel, and René Hübner for discussion related to TEM/STEM. Support by the Structural Characterization Facilities Rossendorf at IBC is gratefully acknowledged.

[1] Lai, L. *et al.* (2023) *Metals* **13**, 1339.

A “safe-zone” approach to the bulk equivalent hardness of ion-irradiated layers

J.-E. Brandenburg, F. Bergner

A method to directly calculate the bulk-equivalent hardness of a thin ion-irradiated layer from individual data points of its indentation hardness, as measured by nanoindentation, was developed. This allows restricting the evaluation to a “safe-zone” free from the influence of both surface effects and embedded ions, which would otherwise pose a transferability issue towards neutron irradiated materials.

SAFE-ZONE APPROACH. Using ion irradiation can be a cost-effective alternative for the investigation of irradiation induced embrittlement in nuclear construction materials. The limited penetration depth of ions into the material, however, poses several challenges as the properties of the affected layer are usually only accessible by micro- or nanoindentation. This necessitates the calculation of a bulk-equivalent hardness from the usually depth dependent indentation hardness. The sensitivity of the measured data to surface effects and the presence of embedded ions at higher depths, which limit transferability towards the effects of neutron irradiation, make this a complicated process. Any evaluation should ideally be restricted to a depth range free from the influence of these effects. Under typical conditions only a handful of data points fulfill this condition, so using evaluation methods based on a direct-fit approach would lead to a high uncertainty of the obtained bulk-equivalent hardness.

METHOD. Our approach is based on a generalized Nix-Gao equation introduced by Hähner.^[1] The increase of the indentation hardness H_{IT} at smaller depths due to the indentation size effect is modeled as

$$H_{IT} = H_0 \sqrt{1 + \frac{h^*}{h_c} \exp\left(-\frac{\bar{h}}{h_c}\right)} \quad (1)$$

Bulk-equivalent hardness H_0 and the two characteristic lengths h^* and \bar{h} are usually determined by fitting Eq. (1) to the experimentally measured indentation hardness. Doing so only for the safe-zone of an ion-irradiated layer, however, would lead to unreliable results due to the low amount of data points.

The aim is therefore to replace the characteristic lengths for the irradiated layer with parameters of the material in the unirradiated condition, which can easily be acquired by fitting the measured indentation hardness of a reference sample over a broad range of indentation depths.

The quantity \bar{h} represents a material dependent upper threshold for the dislocation density and should not change due to irradiation ($\bar{h}_i = \bar{h}_u$). For the second characteristic length, we employ a linear relation between h^* and $1/H_0$ first proposed by Nix and Gao.^[2] Evaluation of various results available in the literature confirmed this correlation to be valid over a broad range of materials and the coefficient of proportionality being independent from irradiation. This leads to

$$h_i^* = h_u^* \cdot \frac{H_{0,u}^2}{H_{0,i}^2} \quad (2)$$

Substituting these two assumptions into Eq. (1) leads to an expression for the bulk-equivalent hardness of the irradiated layer

$$H_{0,i}(h) = \sqrt{H_i^2(h) - H_{0,u}^2 \frac{h_u^*}{h} \exp\left(-\frac{\bar{h}_u}{h}\right)} \quad (3)$$

which allows direct calculation of $H_{0,i}$ from individual data points of the measured indentation hardness.

APPLICATION. The method was tested on selected Fe-9Cr alloys, for which the indentation hardness after ion irradiation and the Vickers hardness in various neutron irradiated conditions had been obtained in a previous project.^[3] A depth range between 100nm and 144nm was identified as the safe-zone free from the influence of surface effects or embedded ions. The bulk-equivalent hardness for all (typically three to five) data points in this range was calculated according to Eq. (3) and the average is compared to the converted Vickers hardness after neutron irradiation in Fig. 1.

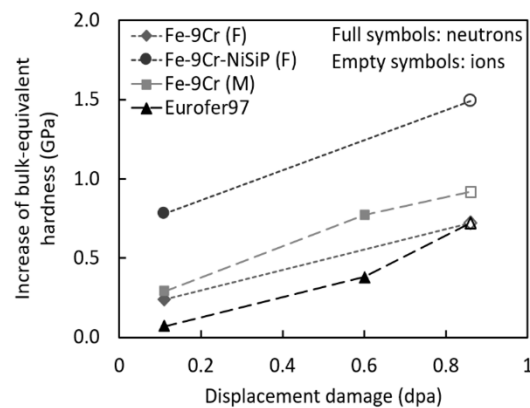


Figure 1. Irradiation induced increase of the bulk-equivalent hardness for selected Fe-9Cr alloys in neutron- and ion-irradiated condition.

It should be noted that the displacement damage (dpa), which is generally accepted to be the main reason for the changes in microstructure leading to irradiation induced hardening, differs significantly between the ion- and neutron-irradiated samples.

Taking this into account, the obtained values for the bulk-equivalent hardness after ion irradiation fall into the range expected from extrapolation of the hardness after neutron irradiation towards the respective radiation damage of 0.86 dpa. They also agree with hardness values obtained from the same data sets using a layered model to represent the microstructure of the samples after ion-irradiation.^[3]

In summary, these results proof that the suggested safe-zone approach yields reasonable values for the bulk-equivalent hardness of an ion-irradiated layer while minimizing the influence of surface effects and implanted ions.

ACKNOWLEDGEMENTS. The model was tested on data collected within the European Commission funded project M4F (Grant No. 755039).

- [1] Bergner, F. et al. (2022) *J. Appl. Phys.* **132**, 045101.
- [2] Nix, W.D. and Gao, H. (1998) *J. Mech. Phys. Solids* **46**, 411–425.
- [3] Malerba, L. et al. (2021) *Nucl. Mat. Energy* **29**, 101051.

Comparison of experimental and calculated activities of monitors in near-reactor cavities

R. Rachamin, J. Konheiser, A. Barkleit

In Germany, the last NPPs have been shut down and the decommissioning of these plants is scheduled. In order to decommission the NPPs safely, economically and on time, it is necessary to estimate the different waste quantities, *e.g.*, between active and inactive material. This requires knowledge of neutron activation and the contamination of surfaces that occurred during operation. This information can significantly minimize radioactive waste and contribute to the safety of operating personnel and the public. Contamination can be minimized by cleaning the surface, but neutron activation cannot. The level of activation in a NPP depends on its power history, neutron diffusion in the rooms and neutron fluence distribution within the components. Therefore, the neutron fluence is the fundamental and important parameter in the assessment of possible activations of materials in the decommissioning and it should be accurately calculated.

A detailed 3D Monte Carlo (MC) model of a German pressurised water reactor (PWR) was developed to calculate the neutron fluence characteristics within components of the reactor. The developed model was validated using metal foil activation measurements. Such metal foils, also known as neutron fluence monitors, have been successfully used in reactor dosimetry for many years and are an ideal and simple method for measuring neutron fluence on an active reactor. The activation increases proportionally to the neutron flux and can, in most cases, be determined by gamma spectrometry after irradiation. Therefore, the measurement of the foil activation can provide sufficient information about the neutron fluence needed for the validation, tuning and optimization of the Monte Carlo model.

CALCULATION. The Monte Carlo code MCNP (version 6.2) was used for the simulation.^[1] The reactor and the surrounding rooms were modelled in detail on the basis of technical drawings. The material densities and compositions used in the model were based on the available plant documentation and literature data. A schematic representation of the model is shown in Fig. 1. Volumes were defined at the positions of the monitors in order to be able to estimate corresponding values. The neutron source was defined as a fixed source in the model. This was specified

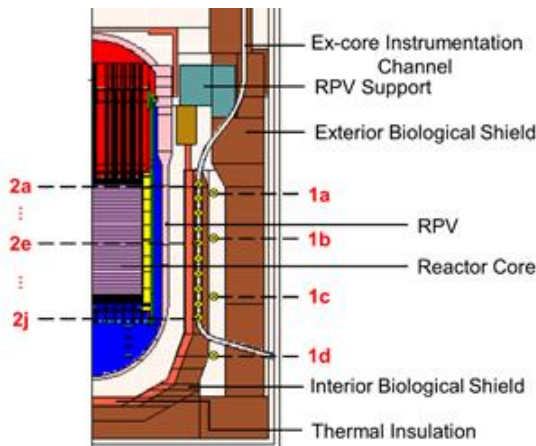


Figure 1. 3D MCNP model of a German PWR and respective sample positions.

as a pin-by-pin distribution and 32 axial layers. The neutron source used is based on burn-up calculations provided by the plant operator.

EXPERIMENTAL. Different metal foils (Ti, Cu, Ni, Fe, In, Sn, Zn) were available in various formats (\varnothing : 8mm or 10×10 mm), were fixed in Kapton tape and packed in an aluminum box. These were secured in the planned positions using steel cables. This was done during the annual revision of the NPP. At the end of the cycle, these were collected again and then analyzed using gamma spectroscopy.

RESULTS. Figure 2 shows the calculated and measured activities of the $^{113}\text{In} (n,\gamma) ^{114\text{m}}\text{In}$ reaction. Other analyzed reactions provide equally good agreement. This demonstrates that the model reproduces the neutron fluence correctly and can be used for the calculation of activations in the surrounding areas of the reactor. A comparison with calculations from other suppliers also shows that these calculations set new quality standards.

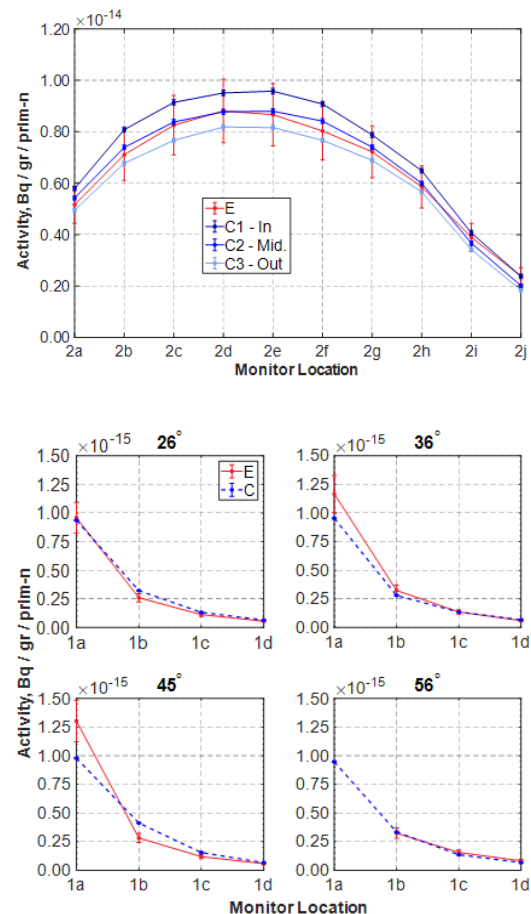


Figure 2. Activation of calculations (blue) and measurements (red) for $^{113}\text{In} (n,\gamma) ^{114\text{m}}\text{In}$.

ACKNOWLEDGEMENTS. This work is funded by the German Federal Ministry of Education and Research (BMBF) under contract number 15S9409A and supported by PreussenElektra GmbH.

[1] Goorley, T. et al. (2012) Nucl. Technol. **180**, 298–315.

Radiochemical analysis of activated concrete of Greifswald NPP

M. Zilbermann, E. Poenitz, A. Barkleit, J. Konheiser

Precise knowledge of activation is essential for effective decommissioning planning of shutdown NPPs. For the Greifswald NPP, which is already being dismantled, the activities of the most important radionuclides in the concrete of the bioshield (^{60}Co , ^{152}Eu , and ^{154}Eu) were determined experimentally using original materials and compared with corresponding activation calculations. The experimental and calculated results agree very well.

In order to reduce time-consuming and cost-intensive measurement campaigns, calculation models should replace or at least support the determination of the activation of components in NPPs. Such models help to plan decommissioning safely and economically and to reduce the amount of waste to be stored in a nuclear waste repository. However, experimental results of radioanalytical characterization are necessary to validate the calculation models. The specific activities of the radionuclides ^{60}Co , ^{152}Eu , and ^{154}Eu in the concrete shielding below the reactor pressure vessel (RPV) of Greifswald NPP were determined by gamma spectrometry and depth profiles of the activity distribution were determined on selected concrete drill cores. For the calculation of the activation, the elemental compositions were determined by mass spectrometry.^[1]

EXPERIMENTAL. Concrete drill cores (diameter: ~10 cm, length: ~50–120 cm) from different positions within the biological shield and reactor basement of the Greifswald NPP were provided by EWN GmbH. The drill cores from the floor below the RPV consist of an 11 cm thick screed layer that was applied on top of the normal-density concrete (see Fig. 1, photograph at the bottom). Smaller samples (diameter: ~2 cm, length: ~3–4 cm) of the drill cores were taken by drilling perpendicular to the core axis at different depths and milled to homogenize.

Gamma spectrometry was performed on the powdered samples for radioanalytical analyses using an HPGe gamma spectrometer from EG&G Ortec. The elemental compositions were analyzed by inductively coupled plasma mass spectrometry (ICP-MS) after micro-wave digestion of the powders in aqua regia.

CALCULATION. For activation calculation, a geometry model was built using plans of the NPP. The ICP-MS results were used as input for the concrete composition. Activation calculation was carried out using the Monte Carlo code MCNP 6.2.^[2]

RESULTS. Figure 1 shows a comparison of the experimentally determined and calculated results for ^{60}Co , ^{152}Eu , and ^{154}Eu . The highest activation was observed in a depth of around 5 cm within the screed layer. A sudden increase in activation could be observed at the boundary between the screed and the concrete layer. This was due to the different elemental composition of the materials. The amount of both Co and Eu was higher in the concrete than in the screed (see insets in the diagrams in Fig. 1). Thereafter, the activation decreased continuously with greater depth. The experimentally determined and calculated activities agreed very well and reflected all effects described. Even if some experimental data are still missing for more precise calculations, e.g., the content of nitrogen, carbon or water, which could not be determined by ICP-MS, the

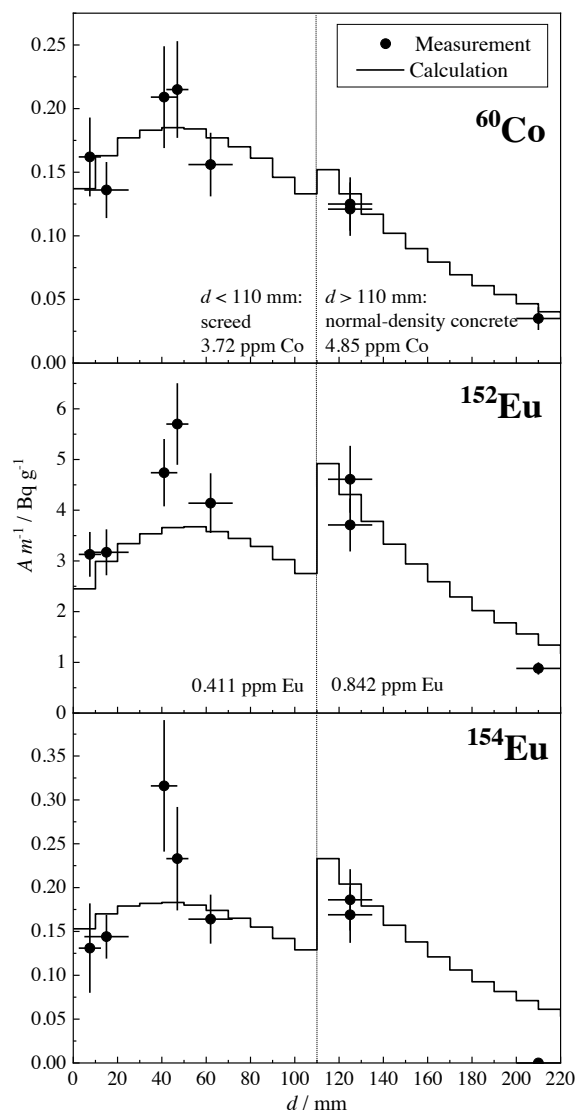


Figure 1. Measured and calculated activities of ^{60}Co , ^{152}Eu , and ^{154}Eu of a drill core from the floor below the RPV consisting of an 11 cm screed-layer on top of normal-density concrete. Bottom: Photograph of the analyzed drill core.

comparison already showed that the model provided very good predictions of the activation of the concrete in the biological shield.

ACKNOWLEDGEMENTS. This project was funded by the German Federal Ministry of Education and Research (BMBF) under contract number 1559412 and supported by EWN GmbH.

[1] Zilbermann, M. (2023) Master thesis, TU Dresden.
[2] Goorley, T. et al. (2012) *Nucl. Technol.* **180**, 298–315.

Simulation of transient behavior of Superphenix reactor with coupled neutronics/thermal hydraulics

A. Ponomarev, E. Nikitin, E. Fridman

The coupled code system DYN3D/ATHLET has been recently extended enabling application for sodium-cooled fast reactors (SFRs). In particular, it allows treatment of all major reactivity effects specific to SFRs. This study benefits from these latest developments focusing on the analysis of the neutronics/thermal hydraulics benchmark on French Superphenix reactor. The benchmark contains a detailed description of the reactor core and its characteristics necessary to model its transient behavior investigated during the start-up tests of the reactor. Application of the coupled code system demonstrated consistency of the coupled approach and results in good agreement with the benchmark solution and measured data.

SUPERPHENIX REACTOR BENCHMARK. Neutronics and transient benchmark analysis of the Superphenix (SPX) French Sodium-cooled Fast reactor (SFR) core was performed within the framework of the ESFR-SMART EU project. The benchmark on this commercial-size reactor with power of 3,600 MWth was formulated based on the data, measured during commissioning start-up tests initiated with fresh loaded core. Peculiarity of this exercise is necessity to include into consideration the reactivity feedbacks related to thermal expansion of the out-of-core primary system components, *i.e.*, core support structure (strongback), primary vessel wall and control rod drive lines (CRDL).

MODELS. The capabilities of stand-alone DYN3D and ATHLET were demonstrated in former studies using neutronic and transient phases of the benchmark, respectively. This study used the developed models to establish the coupled simulations. It also required interpretation of the benchmark for the spatial kinetics solution of DYN3D whereas the benchmark considered a point kinetics approach.

For transient simulations with the nodal diffusion solver of DYN3D so called few-group homogenized cross sections (XS) library was generated using the Monte Carlo code Serpent. In order to account for all reactivity effects of interest, the XS were parameterized in terms of (i) fuel temperature, (ii) coolant temperature, (iii) axial fuel rod expansion, and (iv) radial diagrid expansion. The selected parameters range allows to cover reactor states of the six SPX start-up tests which differ by power and primary cooling flow conditions.

Thermal hydraulics model of the core includes set of one-dimensional channels (one channel for each subassembly) connected via inlet and outlet plenums. Additional heat structures model the out-of-core primary system components: vessel, strongback and CRDL. Variation of their temperatures and correspondingly axial dimensions influences the control rods (CRs) position in the core. In the benchmark definition, the corresponding reactivity effect is calculated using predefined differential CRs worth value. In the current study, in contrast, the position of CRs was explicitly traced in the DYN3D model, while the initial position was adjusted individually for few groups of transients in accord with the reactor power level.

SELECTED RESULTS. Six transients in power range from zero to 50% of nominal have been analyzed applying identical XS library, core- and system models of SPX.

Figure 1 depicts the evolution of the selected parameters – power and reactivity – for the transient initiated at about 23% of nominal power by a control rod insertion introducing the reactivity of -50 pcm. The measured power after initial power drop due to the CR insertion can be reproduced only by including the feedback effect of the CRs position in the core which is the cumulative reactivity effect resulting from thermal expansions of the primary system components: vessel wall, strongback and CRDL. These are, acting on different time scales, result in CRs position variation during the transient. More specifically, a contraction of CRDL during first ~ 500 s of the transient, due to the decrease of the core outlet temperature, is the major contributor to the initial CRs withdrawal, while later in transient the contraction of the vessel wall, due to a decrease of the cold pool and the core inlet temperature, results in the CRs insertion.

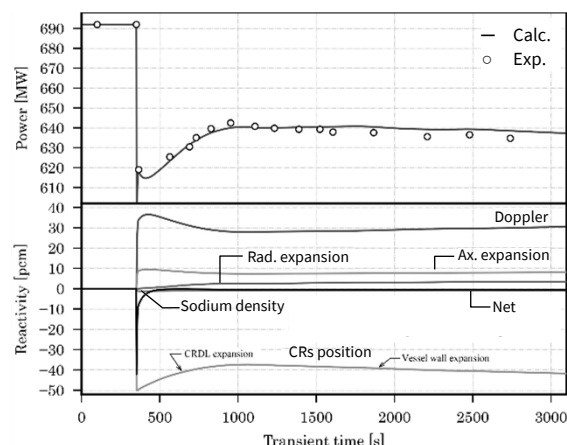


Figure 1. Evolution of the power, net reactivity and its components in transient initiated by introducing of -50 pcm due to control rod insertion.

The phenomenology of all six simulated transients was reproduced by the coupled solution at reasonable level of agreement with the measured data, reflecting adequacy of the developed models and correct interpretation of the benchmark with the coupled solution. Particular limitations of the benchmark, *e.g.*, lack of the information on core conditions and quality of the available measured data, were also indicated.

ACKNOWLEDGEMENTS. The work has been prepared within EU Project ESFR-SMART which has received funding from the EURATOM Research and Training Program 2014-2018 under the Grant Agreement No. 754501.

- [1] Fridman, E. et al. (2023) *Ann. Nucl. Energy* **182**, 109619.
- [2] Ponomarev A. et al. (2022) *J. Nucl. Eng. Radiat. Sci.* **8**, 011320.
- [3] Ponomarev, A. et al. (2022) *J. Nucl. Eng. Radiat. Sci.* **8**, 011321.

Analysis of boron dilution in the NuScale plant using the system code Athlet and CFD within the McSAFER project on small modular reactors

A. Grahn, E. Diaz-Pescador

The aim of the H2020 McSAFER project is to advance the safety research for Small Modular Reactors (SMR) by combining experimental investigations and numerical simulations for different SMR concepts. One of the concepts under investigation is the NuScale Power Module™ (NPM) from the U.S.A. It is an integral concept of a pressurized water reactor which relies on natural circulation to establish the primary coolant flow. The reactor coolant system (RCS) and the pressurizer are integrated within the cylindrical reactor pressure vessel (RPV) and no pumps are needed in the primary side (Fig. 1). The RCS is composed of a small-sized core (37 fuel assemblies, 2m of active height, 160MW thermal power), a riser above the core, a steam generator (SG) made of two independent sets of 345 intertwined heat exchanger tubes that are helically coiled around the upper riser, a downcomer and a lower plenum. The present study combines a whole-plant analysis using the system code ATHLET, using point kinetics for simulating core neutronics, with a CFD analysis of the coolant mixing in the downcomer and in the lower plenum using the software package TrioCFD. Boron dilution was chosen as a standard scenario for testing multi-physics code systems in reactor safety analyses.

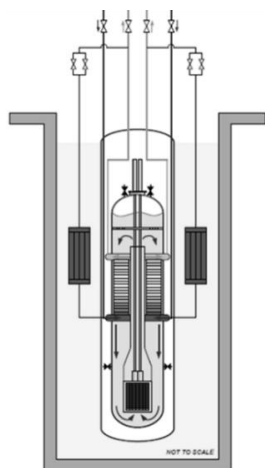


Figure 1. Schematic view of the NuScale Power Module.

BORON DILUTION TRANSIENT. To compensate the excess reactivity over the fuel cycle in light water reactors without saturated boiling in the primary circuit, boric acid is added to the reactor coolant. The coolant circulation during normal operation ensures that this boric acid is homogeneously distributed in the primary circuit. An operator error or a malfunction in the chemical volume and control system (CVCS) could result in an unintended decrease in boron concentration which increases the reactivity of the core and decreases the shutdown margin.

NuScale MODEL. Besides the RPV with the reactor core, pressurizer (PZR) and the embedded SGs, the ATHLET model developed at HZDR incorporates an extended secondary side piping and the decay heat removal system (DHRS). The 3-D RPV is built upon multidimensional cylindrical and rectangular grids based on the massive representation of vertical (1-D) parallel channels. The computational mesh used in the TrioCFD simulation part is based on a CAD model provided by the project partner UJV. It reproduces the downcomer and lower plenum of the NuScale geometry in great detail. It extends from the SG lower end down to the core inlet plane where it connects to the fuel assembly feet and the core reflector. The computational mesh consists of 5.7M tetrahedral cells. Coolant flow in the downcomer and lower plenum regions is expected to be turbulent and non-isothermal, and

it features the transport of a dissolved species (boron). Turbulence is modeled using the k-ε RANS model.

RESULTS. During the transient’s simulation, ATHLET monitors the temporal evolution of key thermal-hydraulic parameters characterizing the plant’s operational state and implements the engineered safety features actuation system (ESFAS) of a real reactor that counteracts critical states according to prescribed threshold values. Computed events are listed in Tab.1 und compare well with results found by project partner organizations. Time-dependent boundary conditions at the CFD inlets (plane below the SG) and at the CFD outlets (fuel assembly inlets) were extracted from the ATHLET solution and served as input for the TrioCFD calculation. The computed boron concentration at the reactor core inlet is symmetrically distributed around the vessel axis and displays little oscillations (Fig. 2). It reflects the good mixing of the coolant as it travels through the downcomer and the lower plenum. This is in accordance with the findings of the previous system-code simulation. Both system-code and CFD analyses have shown that the NuScale design effectively prevents asymmetric distributions of feedback parameters in the reactor core and prevents larger perturbations of core reactivity and reactor power during a boron dilution event.

Table 1. Timing of ESFAS events simulated by ATHLET.

Event	Time [s]	Comment
Initial event	0.0	CVCS injection of unborated water
Control rod insertion start	131.6	2s signal delay
CVCS isolation	138.6	7s delay after shutdown
Low PZR level	231.0	PZR level < 35 %
PZR heaters trip	233.0	3s signal delay
Low PZR Pressure	228.0	PZR pressure < 11,032 MPa
Secondary loop isolation	230.0	2s signal delay
High Main Steam Pressure	1,575.0	SG outlet pressure > 5,516 MPa
DHRS activated	1,577.0	2s signal delay

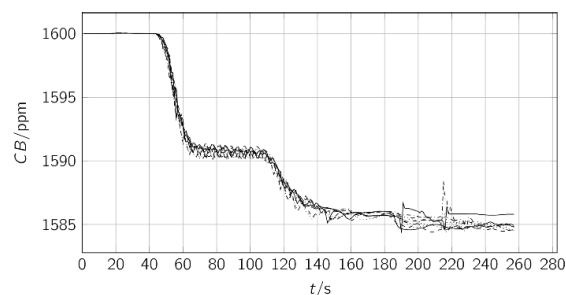
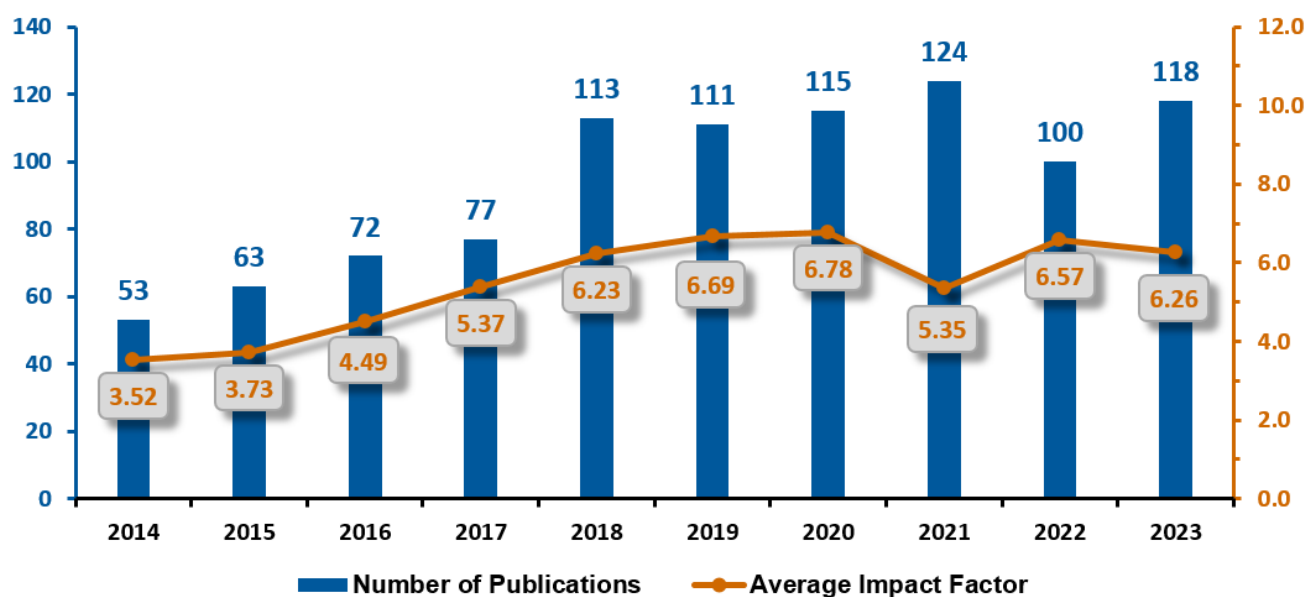


Figure 2. Boron concentration at the core inlet, selected fuel assemblies; TrioCFD simulation based on ATHLET-provided boundary conditions.

ACKNOWLEDGEMENTS. This project has received funding from the European Union’s Horizon 2020 research and innovation program under grant agreement No. 945063.

- ARTICLES (PEER-REVIEWED)
- FURTHER CONTRIBUTIONS
 - ORAL PRESENTATIONS
 - THESES

ARTICLES (PEER-REVIEWED)



Statistics on the publication activity of the Institute of Resource Ecology (IRE) within the last 10 years. The diagram considers peer-reviewed articles that were published under primary responsibility of the institute. Note that the given impact factors are based on data from 2023. The annual update might change the statistics retrospectively.

The following compilation provides peer-reviewed articles and further publications published in 2023 (online first) representing any contribution of members of the Institute of Resource Ecology.

Altstadt, E.

An improved correlation for the estimation of the yield strength from small punch testing

Metals 13, Article No. 1716 (2023).

Doi: 10.3390/met13101716.

Amidani, L.; Dumas, T.; Shuh, D. K.; Butorin, S. M.;

Sahle, C. J.; Longo, A.; Kvashnina, K. O.

Oxygen K-edge X-ray Absorption Spectra of ThO₂ and CeO₂: experiment, interpretation and structural effects.

Journal of Physical Chemistry C 127, 3077–3084 (2023).

Doi: 10.1021/acs.jpcc.2c07771.

Arnold, F. M.; Ghasemifard, A.; Kuc, A. B.; Kunstmann, J.; Heine, T.

Relaxation effects in twisted bilayer molybdenum disulfide: structure, stability, and electronic properties

2D Materials 10, Article No. 045010 (2023).

Doi: 10.1088/2053-1583/aceb75.

Bag, S.; Sasmal, H. S.; Chaudhary, S. P.; Dey, K.; Blätte, D.; Guntermann, R.; Zhang, Y.; Položij, M.; Kuc, A. B.; Shelke, A.; Vijayaraghavan, R. K.; Ajithkumar, T. G.; Bhattacharyya, S.; Heine, T.; Bein, T.; Banerjee, R.

Covalent Organic Framework Thin-film Photodetectors from Solution Processable Porous Nanospheres

Journal of the American Chemical Society 145, 1649–1659 (2023).

Doi: 10.1021/jacs.2c09838.

Bianchetti, E.; Oliveira, A. F.; Scheinost, A. C.;

Valentin, C. D.; Seifert, G.

Chemistry of the interaction and retention of Tc^{VII} and Tc^{IV} species at the Fe₃O₄(001) surface

Journal of Physical Chemistry C 127, 7674–7682 (2023).

Doi: 10.1021/acs.jpcc.3c00688.

Bilodid, Y.; Fischer, M.; Zilly, M.; Aures, A.; Henry, R.;

Kilger, R.; Kliem, S.

Extension of the X2 VVER-1000 benchmark by a control rod cluster ejection exercise

Annals of Nuclear Energy 192, Article No. 110007 (2023).

Doi: 10.1016/j.anucene.2023.110007.

Blei, M. K.; Drobot, B.; Kretzschmar, J.; Pietzsch, H. J.;

Kopka, K.; Mamat, C.

Bestimmung von log K-Werten macropa-basierter Chelatoren für die stabile Komplexbildung von ¹³¹Ba, ^{223/224}Ra und ¹³³La

Nuklearmedizin 62, 149 (2023).

Blei, M. K.; Waurick, L.; Reissig, F.; Kopka, K.; Stumpf, T.;

Drobot, B.; Kretzschmar, J.; Mamat, C.

Equilibrium Thermodynamics of Macropa Complexes with Selected Metal Isotopes of Radiopharmaceutical Interest

Inorganic Chemistry 62, 20699–20709 (2023).

Doi: 10.1021/acs.inorgchem.3c01983.

Bok, F.

Formation constant of the double salt CsCl·2NaCl·2H₂O(cr)

THEREDA Journal 3, 1–6 (2023).

- Bok, F.; Moog, H. C.; Brendler, V.
The solubility of oxygen in water and saline solutions
Frontiers in Nuclear Engineering 2, 1–25 Article No. 1158109 (2023).
 Doi: 10.3389/fnuen.2023.1158109.
- Brandenburg, J. E.; Barrales-Mora, L. A.; Tsurekawa, S.; Molodov, D. A.
Dynamic behavior of grain boundaries with misorientations in the vicinity of $\Sigma 3$ coherent and incoherent twin boundaries in Al bicrystals.
Acta Materialia 259, Article No. 119272 (2023).
 Doi: 10.1016/j.actamat.2023.119272.
- Butorin, S. M.; Bauters, S.; Amidani, L.; Beck, A.; Rossberg, A.; Weiss, S.; Vitova, T.; Kvashnina, K. O.; Tougait, O.
Effect of carbon content on electronic structure of uranium carbides
Scientific Reports 13, Article No. 20434 (2023).
 Doi: 10.1038/s41598-023-47579-7.
- Caprani, R.; Martin, P.; Prieur, D.; Martinez, J.; Lebreton, F.; Desagulier, M. M.; Aloat, C.; Alibert, M.; Picard, L.; Gabriel, G.; Signoret, P.; Clavier, N.
Fission products speciation in spent mixed oxide nuclear fuel: synthesis and characterisation of Pu-bearing SIMfuel
Journal of Nuclear Materials 585, Article No. 154607 (2023).
 Doi: 10.1016/j.jnucmat.2023.154607.
- Chakraborty, S.; Banerjee, D.; Scheinost, A. C.; Grenèche, J. M.; Favre, F.; Géhin, A.; Charlet, L.
Assessing the reactivity of Fe(II) sorbed on smectite clays: U(VI) reduction
Journal of Materials Research 38, 2752–2763 (2023).
 Doi: 10.1557/s43578-023-00998-8.
- Chekhonin, P.; Das, A.; Bergner, F.; Altstadt, E.
Microstructural characterisation of brittle fracture initiation sites in reactor pressure vessel steels
Nuclear Materials and Energy 37, Article No. 101511 (2023).
 Doi: 10.1016/j.nme.2023.101511.
- Das, A.; Chekhonin, P.; Houska, M.; Obermeier, F.; Altstadt, E.
Master Curve Testing of RPV Steels using Mini-C(T) Specimens – Irradiation Effects and Censoring Statistics
Nuclear Materials and Energy 34, Article No. 101395 (2023).
 Doi: 10.1016/j.nme.2023.101395.
- Dettmann, S.; Huittinen, N. M.; Jahn, N.; Kretzschmar, J.; Kumke, M. U.; Kutyma, T.; Lohmann, J.; Reich, T.; Schmeide, K.; Shams Aldin Azzam, S.; Spittler, L.; Stietz, J.
Influence of gluconate on the retention of Eu(III), Am(III), Th(IV), Pu(IV), and U(VI) by C-S-H (C/S = 0.8)
Frontiers in Nuclear Engineering 2, 1124856 (2023).
 Doi: 10.3389/fnuen.2023.1124856.
- Dewaele, A.; Amadon, B.; Bosak, A.; Svitlyk, V.; Ocelli, F.
Synthesis of Single Crystals of ϵ -Iron and Direct Measurements of Its Elastic Constants
Physical Review Letters 131, 034101 (2023).
 Doi: 10.1103/PhysRevLett.131.034101.
- Dominic, A. M.; Wang, Z.; Kuc, A. B.; Petkov, P.; Ly, H. K.; Pham, T. L. H.; Kutzschbach, M.; Cao, Y.; Bachmann, J.; Feng, X.; Dong, R.; Weidinger, I. M.
Oxidation State Dependent Conjugation Controls Electrocatalytic Activity in a Two-Dimensional Di-Copper Metal–Organic Framework
Journal of Physical Chemistry C 127, 7299–7307 (2023).
 Doi: 10.1021/acs.jpcc.2c08819.
- Eren, I.; Yun, A.; Kuc, A. B.
Hydrogen Transport Between Layers of Transition Metal-Dichalcogenides
Advanced Functional Materials (2023).
 Doi: 10.1002/admi.202300798.
- Estevenon, P.; Amidani, L.; Bauters, S.; Tamain, C.; Bodensteiner, M.; Meuer, F.; Hennig, C.; Dumas, T.; Kvashnina, K. O.
From molecular oxo-hydroxo Ce clusters to crystalline CeO₂
Chemistry of Materials 35, 1723–1734 (2023).
 Doi: 10.1021/acs.chemmater.2c03456.
- Filimonova, O. N.; Wermelle, D.; Kvashnina, K. O.
The state of Ag in pyrrhotite: insights from X-ray absorption spectroscopy
ACS Earth and Space Chemistry 7, 1648–1660 (2023).
 Doi: 10.1021/acsearthspacechem.3c00002.
- Freville, R.; Dewaele, A.; Bruzy, N.; Svitlyk, V.; Garbarino, G.
Comparison between mechanisms and microstructures of $\alpha - \gamma$, $\gamma - \epsilon$ and $\alpha - \epsilon - \alpha$ phase transitions in iron
Physical Review B 107, 104105 (2023).
 Doi: 10.1103/PhysRevB.107.104105.
- Fridman, E.; Bilodid, Y.; Valtavirta, V.
Definition of the neutronics benchmark of the NuScale-like core
Nuclear Engineering and Technology 55, 3639–3647 (2023).
 Doi: 10.1016/j.net.2023.06.029.
- Friedrich, S.; Sieber, C.; Drobot, B.; Tsushima, S.; Barkleit, A.; Schmeide, K.; Stumpf, T.; Kretzschmar, J.
Eu(III) and Cm(III) Complexation by the Aminocarboxylates NTA, EDTA, and EGTA Studied with NMR, TRLFS, and ITC – An Improved Approach to More Robust Thermodynamics
Molecules 28, Article No. 4881 (2023).
 Doi: 10.3390/molecules28124881.
- Gericke, R.; Bennett, M. A.; Privér, S.; Bhargava, S.
Formation of Heterobimetallic Complexes by Addition of d¹⁰-Metal Ions to (Me₃P)_xM(2-C₆F₄PPh₂)₂ (x = 1, 2; M = Ni and Pt): A Synthetic and Computational Study of Metallophilic Interactions
Inorganic Chemistry 62, 8846–8862 (2023).
 Doi: 10.1021/acs.inorgchem.3c00311.

- Guadalupe Sánchez-Loredo, M.; Chekhonin, P.; Ebert, D.; Fischer, U.; Liu, X.; Möckel, R.; Judith Labrada-Delgado, G.; Passerini, S.; Kelly, N.
Precipitation Stripping of V(V) as a Novel Approach for the Preparation of Two-Dimensional Transition Metal Vanadates
Nanomaterials 14, 38 (2024).
 DOI: 10.3390/nano14010038.
- Guida, C.; Ramothe, V.; Chappaz, A.; Simonnin, P.; Rosso, K. M.; Gilbert, B.; Ding, R. R.; Prieur, D.; Scheinost, A. C.; Charlet, L.
Revisiting the selenium interactions with pyrite: from adsorption to coprecipitation
ACS Earth and Space Chemistry 8, 67–78 (2024).
 Doi: 10.1021/acsearthspacechem.3c00219.
- Han, S. C.; Chang, E.; Bok, F.; Zechel, S.; Zavarin, M.
Application of Community Data to Surface Complexation Modeling Framework Development: Iron Oxide Protolysis
Journal of Colloid and Interface Science 648, 1015–1024 (2023).
 Doi: 10.1016/j.jcis.2023.06.054.
- Hanke, M.; Dornbusch, D.; Tomm, E.; Grundmeier, G.; Fahmy, K.; Keller, A.
Superstructure-dependent stability of DNA origami nanostructures in the presence of chaotropic denaturants
Nanoscale 15, 16590–16600 (2023).
 Doi: 10.1039/d3nr02045b.
- Hao, H.; Adams, E.; Funke, S.; Schwaab, G.; Havenith, M.; Head-Gordon, T.
Highly Altered State of Proton Transport in Acid Pools in Charged Reverse Micelles
Journal of the American Chemical Society 145, 1826–1834 (2023).
 Doi: 10.1021/jacs.2c11331.
- Heim, P.; Gericke, R.; Spedalotto, G.; Lovisari, M.; Farquhar, E. R.; McDonald, A. R.
Aromatic and aliphatic hydrocarbon hydroxylation via a formally Ni^{IV}=O oxidant
Dalton Transactions 52, 2663–2671 (2023).
 Doi: 10.1039/D2DT03949D.
- Heim, P.; Spedalotto, G.; Lovisari, M.; Gericke, R.; O'Brien, J.; Farquhar, E. R.; McDonald, A. R.
Synthesis and Characterization of a Masked Terminal Nickel-Oxide Complex
Chemistry - A European Journal 29, Article No. e202203840 (2023).
 Doi: 10.1002/chem.202203840.
- Heller, A.; Senwitz, C.; Foerstendorf, H.; Tsushima, S.; Holtmann, L.; Drobot, B.; Kretzschmar, J.
Europium(III) Meets Etidronic Acid (HEDP): a Coordination Study Combining Spectroscopic, Spectrometric, and Quantum Chemical Methods
Molecules 28, Article No. 4469 (2023).
 Doi: 10.3390/molecules28114469.
- Hilpmann, S.; Moll, H.; Drobot, B.; Vogel, M.; Hübner, R.; Stumpf, T.; Cherkouk, A.
Europium(III) as luminescence probe for interactions of a sulfate-reducing microorganism with potentially toxic metals
Ecotoxicology and Environmental Safety 264, Article No. 115474 (2023).
 Doi: 10.1016/j.ecoenv.2023.115474.
- Hilpmann, S.; Roßberg, A.; Steudtner, R.; Drobot, B.; Hübner, R.; Bok, F.; Prieur, D.; Bauters, S.; Kvashnina, K. O.; Stumpf, T.; Cherkouk, A.
Presence of uranium(V) during uranium(VI) reduction by *Desulfosporosinus hippei* DSM 8344^T
Science of the Total Environment 875, Article No. 162593 (2023).
 Doi: 10.1016/j.scitotenv.2023.162593.
- Hintersatz, C.; Singh, S.; Rojas, L. A.; Kretzschmar, J.; Wei, T. S.; Khambhati, K.; Kutschke, S.; Lehmann, F.; Singh, V.; Jain, R.; Pollmann, K.
***Halomonas gemina* sp. nov. and *Halomonas llamarensis* sp. nov., two siderophore-producing organisms isolated from high-altitude salars of the Atacama Desert**
Frontiers in Microbiology 14, Article No. 1194916 (2023).
 Doi: 10.3389/fmicb.2023.1194916.
- Hózer, Z.; Adorni, M.; Arkoma, A.; Busser, V.; Bürger, B.; Dieschbourg, K.; Girault, N.; Herranz, L. E.; Iglesias, R.; Jobst, M.; Kecek, A.; Leclere, C.; Lishchuk, R.; Massone, M.; Müllner, N.; Sholomitsky, S.; Slonszki, E.; Szabó, P.; Taurines, T.; Zimmerl, R.
Review of Experimental Database to Support Nuclear Power Plant Safety Analyses in SGTR and LOCA Domains
Annals of Nuclear Energy 193, Article No. 110001 (2023).
 Doi: 10.1016/j.anucene.2023.110001.
- Iakunkov, A.; Nordenström, A.; Boulanger, N.; Li, G.; Hennig, C.; Jørgensen, M. R. V.; Kantor, I.; Talyzin, A. V.
Effect of Chain Length on Swelling Transitions of Brodie Graphite Oxide in Liquid 1-Alcohols
Advanced Materials Interfaces, 2300554 (2023).
 Doi: 10.1002/admi.202300554.
- Jastrzembski, K.; Zhang, Y.; Lu, Y.; Sporrer, L.; Pohl, D.; Rellinghaus, B.; Waentig, A. L.; Zhang, H.; Mücke, D.; Fu, S.; Polozij, M.; Li, X.; Zhang, J.; Wang, M.; Morag, A.; Yu, M.; Mateo-Alonso, A.; Wang, H. I.; Bonn, M.; Kaiser, U.; Heine, T.; Dong, R.; Feng, X.
Tunable Crystallinity and Electron Conduction in Wavy 2D Conjugated Metal-Organic Frameworks via Halogen Substitution
Small, Article No. e2306732 (2023).
 Doi: 10.1002/smll.202306732.

- Jessat, L.; Foerstendorf, H.; Roßberg, A.; Scheinost, A. C.; Lützenkirchen, J.; Heim, K.; Stumpf, T.; Jordan, N.
Unraveling the Np(V) Sorption on the Nuclear Fuel Cladding Corrosion Product ZrO₂: a Batch, Spectroscopic and Modeling Combined Approach
Journal of Hazardous Materials 461, Article No. 132168 (2024).
Doi: 10.1016/j.jhazmat.2023.132168.
- Jessat, J.; John, W. A.; Moll, H.; Vogel, M.; Steudtner, R.; Drobot, B.; Hübner, R.; Stumpf, T.; Sachs, S.
Localization and chemical speciation of europium(III) in *Brassica napus* plants
Ecotoxicology and Environmental Safety 254, Article No. 114741 (2023).
Doi: 10.1016/j.ecoenv.2023.114741.
- Jha, G.; Heine, T.
Spin-orbit coupling corrections for the GFN-xTB method
Journal of Chemical Physics 158, Article No. 044120 (2023).
Doi: 10.1063/5.0129071.
- Jiahui, Z.; Changti, P.; Yue, Z.; Xiyu, L.; Guozhen, Z.; Yang, L.
Proton penetration mechanism and selective hydrogen isotope separation through two-dimensional biphenylene
RSC Advances 13, 27590–27598 (2023).
Doi: 10.1039/d3ra02993j.
- Jin, J.; Wulf, T.; Jorewitz, M.; Heine, T.; Asmis, K. R.
Vibrational spectroscopy of Cu⁺(H₂)₄: about anharmonicity and fluxionality
Physical Chemistry Chemical Physics 25, 5262–5270 (2023).
Doi: 10.1039/d2cp05802b.
- Jo, Y.; Çevirim-Papaioannou, N.; Franke, K.; Fuss, M.; Pedersen, M.; Lothenbach, B.; Blochouse, B. d.; Altmaier, M.; Gaona, X.
Effect of ISA and chloride on the uptake of niobium(V) by hardened cement paste and C-S-H phases: quantitative description and mechanistic understanding
Cement and Concrete Research 172, Article No. 107233 (2023).
Doi: 10.1016/j.cemconres.2023.107233.
- Johnstone, E. V.; Mayordomo, N.; Mausolf, E. J.
Hybridised production of technetium-99m and technetium-101 with fluorine-18 on a low-energy biomedical cyclotron
EPJ Techniques and Instrumentation 10, 1 (2023).
Doi: 10.1140/epjti/s40485–023–00089–2.
- Kandhavivorn, W.; Glaß, H.; Herrmannsdörfer, T.; Böckers, T. M.; Uhlarz, M.; Gronemann, J.; Funk, R. H. W.; Pietzsch, J.; Pal, A.; Hermann, A.
Restoring Axonal Organelle Motility and Regeneration in Cultured FUS-ALS Motoneurons through Magnetic Field Stimulation Suggests an Alternative Therapeutic Approach
Cells 12, Article No. 1502 (2023).
Doi: 10.3390/cells12111502.
- Kasko, J.; Li, X.; Müller, K.; Ge, Y.; Vettese, G. F.; Law, G. T. W.; Siitari-Kauppi, M.; Huittinen, N. M.; Raff, J.; Bomberg, M.; Herzig, M.
Uranium(VI) interactions with *Pseudomonas* sp. PS-0-L, V4-5-SB and T5-6-I
Applied Geochemistry 159, Article No. 105829 (2023).
Doi: 10.1016/j.apgeochem.2023.105829.
- Katheras, A. S.; Karalis, K.; Krack, M.; Scheinost, A. C.; Churakov, S. V.
Stability and speciation of hydrated magnetite 111 surfaces from ab initio simulations with relevance for geochemical redox processes
Environmental Science & Technology 58, 935–946 (2024).
Doi: 10.1021/acs.est.3c07202.
- Kempt, R.; Kuc, A. B.; Brumme, T.; Heine, T.
Edge conductivity in PtSe₂ nanostructures
Small Structures, Article No. 2300222 (2023).
Doi: 10.1002/ssstr.202300222.
- Klotzsch, M.; Vogel, M.; Sachs, S.; Raff, J.; Stumpf, T.; Drobot, B.; Steudtner, R.
How tobacco (*Nicotiana tabacum*) BY-2 cells cope with Eu(III) – A microspectroscopic study
Analyst 148, 4668–4676 (2023).
Doi: 10.1039/D3AN00741C.
- Koch, T.; Fischer, C.; Schad, F.; Siegesmund, S.
Quantification of surface changes and volume losses of selected rock types due to different cleaning processes
Environmental Earth Sciences 82, 132 (2023).
Doi: 10.1007/s12665–023–10776–8.
- Kolluri, M.; Martin, O.; Naziris, F.; D'Agata, E.; Gillemot, F.; Brumovsky, M.; Ulbricht, A.; Autio, J. M.; Shugailo, O.; Horvath, A.
Structural MATerias research on parameters influencing the material properties of RPV steels for safe long-term operation of PWR NPPs
Nuclear Engineering and Design 406, Article No. 112236 (2023).
Doi: 10.1016/j.nucengdes.2023.112236.
- Koner, K.; Sadhukhan, A.; Karak, S.; Sasmal, H. S.; Ogaeri, Y.; Nishiyama, Y.; Zhao, S.; Polozij, M.; Kuc, A. B.; Heine, T.; Banerjee, R.
Bottom-Up Synthesis of Crystalline Covalent Organic Framework Nanosheets, Nanotubes, and Kippah Vesicles: An Odd–Even Effect Induction
Journal of the American Chemical Society 145, 14475–14483 (2023).
Doi: 10.1021/jacs.3c03831.
- Lai, L.; Chekhonin, P.; Akhmedaliev, S.; Brandenburg, J. E.; Bergner, F.
Microstructural characterization of reactor pressure vessel steels
Metals 13, Article No. 1339 (2023).
Doi: 10.3390/met13081339.

- Ledoux, E.; Krug, M.; Gay, J.; Chantel, J.; Hilairt, N.; Bykov, M.; Bykova, E.; Aprilis, G.; Svitlyk, V.; Garbarino, G.; Guignot, N.; Sanchez-Valle, C.; Speziale, S.; Merkel, S.
In-situ study of microstructures induced by the olivine to wadsleyite transformation at conditions of the 410 km depth discontinuity
American Mineralogist 108, 2283–2293 (2023).
Doi: 10.2138/am-2022–8731.
- Ledoux, E. E.; Saki, M.; Gay, J. P.; Krug, M.; Castelnau, O.; Zhou, W. Y.; Zhang, J. S.; Chantel, J.; Hilairt, N.; Bykov, M.; Bykova, E.; Aprilis, G.; Svitlyk, V.; Garbarino, G.; Sanchez-Valle, C.; Thomas, C.; Speziale, S.; Merkel, S.
Deformation Mechanisms, Microstructures, and Seismic Anisotropy of Wadsleyite in the Earth's Transition Zone
Geochemistry, Geophysics, Geosystems 24, Article No. e2023GC011026 (2023).
Doi: 10.1029/2023GC011026.
- Lindley, B.; Velarde, F. Á.; Baker, U.; Bodi, J.; Cosgrove, P.; Charles, A.; Fiorina, C.; Fridman, E.; Krepel, J.; Lavarenne, J.; Mikityuk, K.; Nikitin, E.; Ponomarev, A.; Radman, S.; Shwageraus, E.; Tollit, B.
Impact of Thermal-Hydraulic Feedback and Differential Thermal Expansion on European SFR Core Power Distribution
Journal of Nuclear Engineering and Radiation Science 9, Article No. 031301 (2023).
Doi: 10.1115/1.4056930.
- Liu, J.; Wang, L.; Lin, J.; Yuan, W.; Li, L.; Peng, Y. K.; Xiong, X.; Cao, H.; Wei, X.; Ouyang, Q.; Lippold, H.; Wang, J.; Lin, K.
Applying thallium isotopic compositions as novel and sensitive proxy for Tl(I)/Tl(III) transformation and source apportionment
Science of the Total Environment 913, Article No. 169542 (2024).
Doi: 10.1016/j.scitotenv.2023.169542.
- Longo, A.; Mirone, A.; Gallerande, E. d. C.; Sahle, C. J.; Casaletto, M. P.; Amidani, L.; Theofanidis, S.; Giannici, F.
Oxygen vacancy clusters in bulk cerium oxide and the impact of gold atoms
Cell Reports Physical Science 4, Article No. 101699 (2023).
Doi: 10.1016/j.xcrp.2023.101699.
- Lv, K.; Patzschke, M.; März, J.; Kvashnina, K. O.; Schmidt, M.
Selective crystallization of a highly radiation-resistant isonicotinic acid-based metal-organic framework as a primary actinide waste form
ACS Materials Letters 5, 536–542 (2023).
Doi: 10.1021/acsmaterialslett.2c01087.
- Manceau, A.; Mathon, O.; Lomachenko, K. A.; Rovezzi, M.; Kvashnina, K. O.; Boiron, M. C.; Brossier, R.; Steinmann, S. N.
Revealing the Incorporation of Cerium in Fluorapatite
ACS Earth and Space Chemistry (2023).
Doi: 10.1021/acsearthspacechem.3c00274.
- Massonnet, M.; Claparede, L.; Martinez, J.; Martin, P.; Hunault, M. O. J. Y.; Prieur, D.; Mesbah, A.; Dacheux, N.; Clavier, N.
Influence of sintering conditions on the structure and the redox speciation of homogenous (U,Ce)O_{2+δ} ceramics : a synchrotron study
Inorganic Chemistry 62, 7173–7185 (2023).
Doi: 10.1021/acs.inorgchem.2c03945.
- Matulis, D.; Wadsö, L.; Fahmy, K.
Special Issue “Advances in Monitoring Metabolic Activities of Microorganisms by Calorimetry”
Microorganisms 11, Article No. 1204 (2023).
Doi: 10.3390/microorganisms11051204.
- Mayordomo, N.; Missana, T.; Alonso, U.
Cadmium sorption on alumina nanoparticles, and mixtures of alumina and smectite: An experimental and modelling study
Minerals 13, Article No. 1534 (2023).
Doi: 10.3390/min13121534.
- Milašinović, V.; Vuković, V. V.; Krawczuk, A.; Molčanov, K. K.; Hennig, C.; Bodensteiner, M.
The nature of π-hole interaction between iodide anion and quinoid ring in the crystalline state
IUCr 23, 156–163 (2023).
Doi: 10.1107/S2052252523000052.
- Missana, T.; Alonso, U.; Mayordomo, N.; García-Gutiérrez, M.
Analysis of Cadmium Retention Mechanisms by a Smectite Clay in the Presence of Carbonates
Toxics 11, 130 (2023).
Doi: 10.3390/toxics11020130.
- Mitrofanov, A.; Berencén, Y.; Sadrollahi, E.; Boldt, R.; Bodesheim, D.; Weiske, H.; Paulus, F.; Geck, J.; Cuniberti, G.; Kuc, A. B.; Voit, B.
Molecular engineering of naphthalene spacers in low-dimensional perovskites
Journal of Materials Chemistry C 11, Article No. 5024 (2023).
Doi: 10.1039/D3TC00132F.
- Murphy, G. L.; Gericke, R.; Gilson, S.; Bazarkina, E.; Roßberg, A.; Kaden, P.; Thümmel, R.; Klinkenberg, M.; Henkes, M.; Kegler, P.; Svitlyk, V.; Marquardt, J.; Lender, T.; Hennig, C.; Kvashnina, K. O.; Huittinen, N. M.
Deconvoluting Cr States in Cr-Doped UO₂ Nuclear Fuels via Bulk and Single Crystal Spectroscopic Studies
Nature Communications 14, Article No. 2455 (2023).
Doi: 10.1038/s41467–023–38109–0.

- Newman Portela, A.; Krawczyk-Bärsch, E.; Lopez Fernandez, M.; Bok, F.; Kassahun, A.; Drobot, B.; Steudtner, R.; Stumpf, T.; Raff, J.; Merroun, M. L. **Biostimulation of Indigenous Microbes for Uranium Bioremediation in Former U Mine Water: Multidisciplinary approach assessment** *Environmental Science and Pollution Research* 31, 7227–7245 (2024).
DOI: 10.1007/s11356-023-31530-4.
- Nikitin, E.; Fridman, E.; Ponomarev, A. **Analysis of loss of flow without scram test in the FFTF reactor – Part I: preparation of neutronics data** *Progress in Nuclear Energy* 168, Article No. 105018 (2024).
DOI: 10.1016/j.pnucene.2023.105018.
- Oertel, J.; Sachs, S.; Flemming, K.; Obeid, M. H.; Fahmy, K. **Distinct Effects of Chemical Toxicity and Radioactivity on Metabolic Heat of Cultured Cells Revealed by “Isotope-Editing”** *Microorganisms* 11, Article No. 584 (2023).
DOI: 10.3390/microorganisms11030584.
- Opitz, L.; Hübner, R.; Shams Aldin Azzam, S.; Gilson, S.; Finkeldei, S. C.; Huittinen, N. M. **Investigations towards incorporation of Eu³⁺ and Cm³⁺ during ZrO₂ crystallization in aqueous solution** *Scientific Reports* 13, Article No. 12276 (2023).
DOI: 10.1038/s41598-023-39143-0.
- Panda, C.; Anny-Nzekwue, O.; Doyle, L. M.; Gericke, R.; McDonald, A. R. **Evidence for a High-Valent Iron-Fluoride That Mediates Oxidative C(sp³)-H Fluorination** *JACS Au* 3, 919 (2023).
DOI: 10.1021/jacsau.3c00021.
- Paulsen, C.; Gerdes, J. M.; Svitlyk, V.; Reimann, M. K.; Rabenbauer, A.; Nilges, T.; Hansen, M. R.; Pöttgen, R. **Trimorphic TaCrP – A diffraction and ³¹P solid state NMR spectroscopic study** *Zeitschrift für Kristallographie* 238, 105–117 (2023).
DOI: 10.1515/zkri-2022-0070.
- Pidchenko, I. N.; Christensen, J. N.; Kutzschbach, M.; Ignatyev, K.; Puigdomenech, I.; Tullborg, E. L.; Roberts, N. M. W.; Rasbury, E. T.; Northrup, P.; Tappero, R.; Kvashnina, K. O.; Schäfer, T.; Suzuki, Y.; Drake, H. **Deep anoxic aquifers could act as sinks for uranium through microbial-assisted mineral trapping** *Communications Earth & Environment* 4, Article No. 128 (2023).
DOI: 10.1038/s43247-023-00767-9.
- Pingel, J. L.; Kulenkampff, J.; Jara-Heredia, D.; Zhou, W.; Fischer, C.; Schäfer, T. **In-situ flow visualization with Geo-Positron-Emission-Tomography in a granite fracture from Soultz-sous-Forêts, France** *Geothermics* 111, Article No. 102705 (2023).
DOI: 10.1016/j.geothermics.2023.102705.
- Ponomarev, A.; Nikitin, E.; Fridman, E. **Coupled 3D neutronics/thermal-hydraulics analysis of Superphénix start-up tests with DYN3D/ATHLET code system** *Nuclear Engineering and Design* 412, Article No. 112456 (2023).
DOI: 10.1016/j.nucengdes.2023.112456.
- Prüßner, T.; Meinderink, D.; Zhu, S.; Orive, A. G.; Kielar, C.; Huck, M.; Steinrück, H. G.; Keller, A.; Grundmeier, G. **Molecular Adhesion of a Pilus-derived Peptide Involved in *Pseudomonas aeruginosa* Biofilm Formation on non-polar ZnO Surfaces** *Chemistry - A European Journal*, Article No. e202302464 (2023).
DOI: 10.1002/chem.202302464.
- Qian, Y.; Scheinost, A. C.; Grangeon, S.; Greneche, J. M.; Hoving, A.; Bourhis, E.; Maubec, N.; Churakov, S. V.; Fernandes, M. M. **Oxidation state and structure of Fe in nontronite: From oxidizing to reducing conditions** *ACS Earth and Space Chemistry* 7, 1868–1881 (2023).
DOI: 10.1021/acsearthspacechem.3c00136.
- Ramzan, M. S.; Goodwin, Z. A. H.; Mostofi, A. A.; Kuc, A. B.; Lischner, J. **Effect of Coulomb impurities on the electronic structure of magic angle twisted bilayer graphene** *npj 2D Materials and Applications* 7, Article No. 49 (2023).
DOI: 10.1038/s41699-023-00403-2.
- Riedel, S.; Gerwig, M.; Gerlach, D.; Brendler, E.; Gericke, R.; Kroke, E.; Wagler, J. **The Hexacoordinate Si Complex SiCl₄(4-Azidopyridine)₂ – Crystallographic Characterization of Two Conformers and Probing the Influence of SiCl₄-Complexation on a Click Reaction with Phenylacetylen** *Inorganics* 11, 473 (2023).
DOI: 10.3390/inorganics11120473.
- Ruiz-Fresneda, M. A.; Schaefer, S.; Hübner, R.; Fahmy, K.; Merroun, M. L. **Exploring Antibacterial Activity and Bacterial-Mediated Allotropic Transition of Differentially Coated Selenium Nanoparticles** *ACS Applied Materials and Interfaces* 15, 29958–29970 (2023).
DOI: 10.1021/acsami.3c05100.
- Sabaghi, D.; Wang, Z.; Bhauriyal, P.; Lu, Q.; Morag, A.; Mikhailovia, D.; Hashemi, P.; Li, D.; Neumann, C.; Liao, Z.; Dominic, A. M.; Nia, A. S.; Dong, R.; Zschech, E.; Turchanin, A.; Heine, T.; Yu, M.; Feng, X. **Ultrathin positively charged electrode skin for durable anion-intercalation battery chemistries** *Nature Communications* 14, 760 (2023).
DOI: 10.1038/s41467-023-36384-5.

- Sánchez-Loredo, M. G.; Palomares-Sánchez, S. A.; Labrada-Delgado, G. J.; Helbig, T.; Chekhonin, P.; Ebert, D.; Möckel, R.; Afriyie, J. O.; Kelly, N.
Preparation of Volborthite by a Facile Synthetic Chemical Solvent Extraction Method
Nanomaterials 13, 1977 (2023).
Doi: 10.3390/nano13131977.
- Sánchez, M.; Cicero, S.; Kirk, M.; Altstadt, E.; Server, W.; Yamamoto, M.
Using mini-CT specimens for the fracture characterization of ferritic steels within the ductile to brittle transition range: a review
Metals 13, Article No. 176 (2023).
Doi: 10.3390/met13010176.
- Schabernack, J.; Oliveira, A. F.; Heine, T.; Fischer, C.
Variability of radionuclide sorption efficiency on muscovite cleavage planes
Advanced Theory and Simulations 6, 1–15 Article No. 2300406 (2023).
Doi: 10.1002/adts.202300406.
- Seidel, A.; Gericke, R.; Kutzner, B.; Wagler, J.
Lewis Acid-Base Adducts of α -Amino Acid-Derived Silaheterocycles and N-Methylimidazole
Molecules 28, 7816 (2023).
Doi: 10.3390/molecules28237816.
- Severin, T.; Karabtsova, V.; Börner, M.; Weiske, H.; Kuc, A. B.; Kersting, B.
Synthesis, Structures and Photophysical Properties of Tetra- and Hexanuclear Zinc Complexes Supported by Tridentate Schiff Base Ligands
Chemistry 5, 1028–1045 (2023).
Doi: 10.3390/chemistry5020070.
- Shugailo, O.; Kolluri, M.; Gillemot, F.; Ulbricht, A.; Brumovsky, M.
The Main Results of Structural Materials Research for Safe Long-Term Operation of LWR NPPs from the Viewpoint of Dissemination Activities
Nuclear and Radiation Safety 1, 41–50 (2023).
Doi: 10.32918/NRS.2023.1(97).05.
- Singer, H.; Steudtner, R.; Klein, A. S.; Rulofs, C.; Zeymer, C.; Drobot, B.; Pol, A.; Martinez-Gomez, C.; Daumann, L. J.
Minor Actinides Can Replace Essential Lanthanides in Bacterial Life
Angewandte Chemie - International Edition 62 (2023).
Doi: 10.1002/anie.202303669.
- Singer, H.; Steudtner, R.; Sottorff, I.; Drobot, B.; Pol, A.; Camp, H. J. M. O. D.; Daumann, L. J.
Learning from nature: recovery of rare earth elements by the extremophilic bacterium *Methylococcus jannaschii*
Chemical Communications 59, 9066–9069 (2023).
Doi: 10.1039/d3cc01341c.
- Sporrer, L.; Zhou, G.; Wang, M.; Balos, V.; Revuelta, S.; Jastrzembki, K.; Löffler, M.; Petkov, P.; Heine, T.; Kuc, A. B.; Cánovas, E.; Huang, Z.; Feng, X.; Dong, R.
Near IR bandgap semiconducting 2D conjugated metal-organic framework with rhombic lattice and high mobility
Angewandte Chemie - International Edition 62, Article No. e202300186 (2023).
Doi: 10.1002/anie.202300186.
- Stietz, J.; Amayri, S.; Häußler, V.; Prieur, D.; Reich, T.
Uptake of Pu(IV) by hardened cement paste in the presence of gluconate at high and low ionic strengths
Frontiers in Nuclear Engineering 2, Article No. 1268767. (2023).
Doi: 10.3389/fnuen.2023.1268767.
- Stricker, A.; Hilpmann, S.; Mansel, A.; Franke, K.; Schymura, S.
Radiolabeling of Micro-/Nanoplastics via In-Diffusion
Nanomaterials 13, 1–19 Article No. 2687 (2023).
Doi: 10.3390/nano13192687.
- Sucena, S. F.; Demirel, T. I.; Baitullina, A.; Hagenbach, A.; Grewe, J.; Spreckelmeyer, S.; März, J.; Barkleit, A.; Maia, P. I. D. S.; Nguyen, H. H.; Abram, U.
Gold-based Coronands as Hosts for M^{3+} Metal ions: Ring Size Matters
Molecules 28, 5421 (2023).
Doi: 10.3390/molecules28145421.
- Svitlyk, V.; Kuz'Min, M. D.; Mozharivskiy, Y.; Isnard, O.
Investigation of the intrinsic magnetic properties of $GdCo_4B$ single crystal: determination of the magnetocrystalline anisotropy from the first-order magnetization processes
European Physical Journal Plus 138, Article No. 388 (2023).
Doi: 10.1140/epjp/s13360-023-03996-1.
- Takeyama, T.; März, J.; Ono, R.; Tsushima, S.; Takao, K.
Neptunyl(VI) Nitrate Coordination Polymer with Bis(2-pyrrolidone) Linkers Highlighting Crystallographic Analogy and Solubility Difference in Actinyl(VI) Nitrates
Inorganics 11, 104–113 (2023).
Doi: 10.3390/inorganics11030104.
- Takeyama, T.; Tsushima, S.; Gericke, R.; Kaden, P.; März, J.; Takao, K.
Fate of Oxidation States at Actinide Centers in Redox-Active Ligand Systems Governed by Energy Levels of 5f Orbitals
Chemistry - A European Journal 29, Article No. e202302702 (2023).
Doi: 10.1002/chem.202302702.
- Takeyama, T.; Tsushima, S.; Takao, K.
Utility of redox-active ligands for reversible multi-electron transfer in uranyl(VI) complexes
Inorganic Chemistry Frontiers 10, 4028–4044 (2023).
Doi: 10.1039/D3QI00189J.

- Tapio, K.; Kielar, C.; Parikka, J. M.; Keller, A.; Järvinen, H.; Fahmy, K.; Toppari, J. J.
Large-Scale Formation of DNA Origami Lattices on Silicon
Chemistry of Materials 35, 1961–1971 (2023).
Doi: 10.1021/acs.chemmater.2c03190.
- Torres, K.; Kuc, A. B.; Maschio, L.; Pham, T.; Reidy, K.; Dekanovsky, L.; Sofer, Z.; Ross, F. M.; Klein, J.
Probing Defects and Spin-Phonon Coupling in CrSBr via Resonant Raman Scattering
Advanced Functional Materials 33, Article No. 2211366 (2023).
Doi: 10.1002/adfm.202211366.
- Tran, T. Q.; Huo, X.; Fridman, E.; Lee, D.
CEFR control rod drop transient simulation using RAST-F code system
Nuclear Engineering and Technology (2023).
Doi: 10.1016/j.net.2023.08.017.
- Ulbricht, A.; Dykas, J.; Chekhonin, P.; Altstadt, E.; Bergner, F.
Small-angle neutron scattering study of neutron-irradiated and post-irradiation annealed VVER-1000 reactor pressure vessel weld material
Frontiers in Nuclear Engineering 2, Article No. 1176288 (2023).
Doi: 10.3389/fnuen.2023.1176288.
- Vivas, J.; De-Castro, D.; Poplawsky, J. D.; Altstadt, E.; Houska, M.; Urones-Garrote, E.; San Martín, D.; Caballero, F. G.; Serrano, M.; Capdevila, C.
Creep strength boosted by a high-density of stable nanoprecipitates in high-chromium steels
European Journal of Materials 3, 2118082 (2023).
DOI: 10.1080/26889277.2022.2118082.
- Wagler, J.; Gericke, R.
Ge–Cu–Complexes Ph(pyO)Ge(μ^2 -pyO)₂CuCl and PhGe(μ^2 -pyO)₄CuCl - Representatives of Cu(I) → Ge(IV) and Cu(II) → Ge(IV) Dative Bond Systems
Molecules 28, Article No. 5442 (2023).
Doi: 10.3390/molecules28145442.
- Wagler, J.; Gericke, R.
Pd–Si complexes of the type ClPd(μ^2 -pyO)₄SiR (R = Me, Ph, Bn, Allyl, κ O-(pyO)PdCl(η^3 -allyl); pyO = pyridine-2-olate): The influence of substituent R on the Pd–Si bond
Polyhedron 245, 116663 (2023).
Doi: 10.1016/j.poly.2023.116663.
- Wilkins, M. C. D.; Townsend, L. T.; Stennett, M. C.; Kvashnina, K. O.; Corkhill, C. L.; Hyatt, N. C.
A multimodal X-ray spectroscopy investigation of uranium speciation in ThTi₂O₆ compounds with the brannerite structure
Scientific Reports 13, Article No. 12776 (2023).
Doi: 10.1038/s41598-023-38912-1.
- Wozniak, T.; Asghar, U. E. H.; Paulo, E. F. J.; Ramzan, M. S.; Kuc, A. B.
Electronic and Excitonic Properties of MSi₂Z₄ Monolayers
Small 19, Article No. 2206444 (2023).
Doi: 10.1002/sml.202206444.
- Yadav, P.; Rachamin, R.; Konheiser, J.; Baier, S.
Estimation of weight window parameters based on recursive Monte Carlo approach for reactor shielding problems
Annals of Nuclear Energy 197, Article No. 110277 (2024).
Doi: 10.1016/j.anucene.2023.110277.
- Yadav, P.; Rachamin, R.; Konheiser, J.; Baier, S.
Generation of optimal weight values based on the Recursive Monte Carlo (RMC) method for using in MC deep penetrations calculations
Nuclear Engineering and Design (2023).
Doi: 10.1080/00295639.2023.2211199.
- Yang, L.; Zhang, Y.; Huang, Y.; Deng, L.; Luo, Q.; Li, X.; Jiang, J.
Promoting Oxygen Reduction Reaction on Carbon-based Materials by Selective Hydrogen Bonding
ChemSusChem 16, Article No. e202300082 (2023).
Doi: 10.1002/cssc.202300082.
- Yang, Y.; Korzhavyi, P.; Nikolaychuk, P.; Bazarkina, E.; Kvashnina, K. O.; Butorin, S.; Tarakina, N.; Soroka, I.
Tuning catalytic activity of Ni–Co nanoparticles synthesized by gamma-radiolytic reduction of acetate aqueous solutions
Advanced Materials Interfaces 10, Article No. 202300038 (2023).
Doi: 10.1002/admi.202300038.
- Yin, J. F.; Amidani, L.; Chen, J.; Li, M.; Xue, B.; Lai, Y.; Kvashnina, K.; Nyman, M.; Yin, P.
Spatiotemporal Studies of Soluble Inorganic Nanostructures with X-rays and Neutrons
Angewandte Chemie - International Edition 63, Article No. e202310953 (2024).
Doi: 10.1002/anie.202310953.
- Yuan, L.; Zheng, B.; Zhao, Q.; Kempt, R.; Brumme, T.; Kuc, A. B.; Ma, C.; Deng, S.; Pan, A.; Huang, L.
Strong Dipolar Repulsion of One-Dimensional Interfacial Excitons in Monolayer Lateral Heterojunctions
ACS Nano 17, 15379–15387 (2023).
Doi: 10.1021/acsnano.2c12903.
- Zupunski, L.; Street, R.; Ostroumova, E.; Winde, F.; Sachs, S.; Geipel, G.; Nkosi, V.; Bouaoun, L.; Haman, T.; Schütz, J.; Mathee, A.
Environmental exposure to uranium in a population living in close proximity to gold mine tailings in South Africa
Journal of Trace Elements in Medicine and Biology 77, Article No. 127141 (2023).
Doi: 10.1016/j.jtemb.2023.127141.

Zurita, C.; Tsushima, S.; Solari, P. L.; Menut, D.;
 Dourdain, S.; Jeanson, A.; Creff, G.; Auwer, C. D.
**Interaction between the transferrin protein and
 plutonium (and thorium), what's new?**
Chemistry - A European Journal 29, Article No.
 e202300636 (2023).
 Doi: 10.1002/chem.202300636.

○ FURTHER CONTRIBUTIONS

Das, A.; Altstadt, E.; Chekhonin, P.; Houska, M.
**Fracture mechanics investigation of reactor pressure
 vessel steels by means of sub-sized specimens
 (KLEINPROBEN)**
*Wissenschaftlich-Technische Berichte / Helmholtz-
 Zentrum Dresden-Rossendorf; HZDR-125* (2023).

Scheinost, A. C.; Singh, B.
Metal Oxides
*Encyclopedia of Soils in the Environment Vol. 4,
 2nd edition, Elsevier, New York, U.S.A., 135–148* (2023).
 Doi: 10.1016/B978-0-12-822974-3.00069-0.

○ ORAL PRESENTATIONS

INVITED LECTURES

Adams, E.
**Probing Protein Hydration with Terahertz
 Spectroscopy**
*9th Summer School Solvation Science, May 30–
 June 02, 2023, Bochum, Germany* (2023).

Adams, E.
**Role of Protein Solvation in Liquid-Liquid Phase
 Separation**
*CMWS Seminar, November 02, 2023, DESY, Germany
 (2023).*

Adams, E.
Solvation Properties in Biomolecular Condensates
*6th Conference on Frontiers in Water Biophysics, May 19–
 24, 2023, Erice, Italy* (2023).

Bok, F.
**Blind prediction of K_a values from NORM sites
 using the Smart- K_a approach**
*Workshop of the ALLIANCE Topical Roadmap WG
 NORM, 06.-7.6.2023, Granada, Spain* (2023).

Charlet, L.; Guida, C.; Poulain, A.; Ding, R.; Ramothe, V.;
 Maria Papaslioti, E.; Kirsch, R.; Fernandez-
 Martinez, A.; Scheinost, A. C.; Marc Greneche, J.;
 Menguy, N.; Rosso, K. M.
**Nanoscale mineral/contaminant redox reaction
 processes: impact on oxyanion contaminant fate in
 oscillating anoxic environments**
*Goldschmidt Conference 2023, July 09–14, 2023, Lyon,
 France* (2023).

Di Lorenzo, F.; Stotskyi, V.; Scheinost, A. C.; Lanson, M.;
 Lanson, B.; Churakov, S. V.; Marques Fernandes, M.
**Metal sorption on clay minerals aiming at the
 geological storage of nuclear wastes**
*ROBL-Workshop, January 25, 2023, Dresden, Germany
 (2023).*

März, J.
**Bonding trends in early actinide (Th-Pu) complex
 series**
Actinides 2023, June 05–08, 2023, Golden, U.S.A. (2023).

März, J.
The complex chemistry of light actinides
*Öffentlicher Vortrag Department Chemie, July 10, 2023,
 Mainz, Germany* (2023).

März, J.
Coordination chemistry of the early actinides
*AC-Kolloquium, January 18, 2023, Leipzig, Germany
 (2023).*

Qian, Y.; Grangeon, S.; Scheinost, A. C.; Hoving, A.;
 Greneche, J. M.; Marques Fernandes, M.
**Retention of redox-sensitive Tc(VII) and Se(IV) on
 Fe(II)/Fe(III) bearing clay minerals**
*EURAD Annual Meeting, March 14–16, 2023, Larnaca,
 Cyprus* (2023).

- Qian, Y.; Grangeon, S.; Scheinost, A. C.; Hoving, A.; Greneche, J. M.; Marques Fernandes, M.
Retention of redox-sensitive Tc(VII) and Se(IV) on Fe(II)/Fe(III) bearing clay minerals
ROBL-Workshop, January 25, 2023, Dresden, Germany (2023).
- Rachamin, R.; Konheiser, J.; Barkleit, A.; Seidl, M.
Activation calculations for decommissioning planning of NPPs
86th Annual Conference of the DPG and DPG Spring Meeting, March 20–24, 2023, Dresden, Germany (2023).
- Rachamin, R.; Konheiser, J.; Barkleit, A.; Seidl, M.
Dosimetry for Decommissioning of Nuclear Power Plants
ANS Annual Meeting, June 11–14, 2023, Indianapolis, U.S.A. (2023).
- Raff, J.
Fundamentals and concepts for the bioremediation of contaminated sites and water
Interregional Training Course on Environmental Remediation Design and Implementation, November 27–December 01, 2023, Nanchang, China (2023).
- Raff, J.; Krawczyk-Bärsch, E.; Hilpmann, S.; Wollenberg, A.; Günther, A.; Klotzsche, M.; Steudtner, R.; Drobot, B.
Selected case studies on the bioremediation of uranium-contaminated (mine) waters
Interregional Training Course on Environmental Remediation Design and Implementation, November 27–December 01, 2023, Nanchang, China (2023).
- Tsushima, S.
Fragment molecular orbital (FMO) method for studying actinide-protein interaction
Theory Frontiers in Actinide Science: Chemistry and Materials, February 26–March 01, 2023, Santa Fe, U.S.A. (2023).
- Tsushima, S.
Fragment molecular orbital method as a tool to study actinide / lanthanide-protein interaction
Faculty of Mathematics and Natural Sciences, Department of Chemistry, Theoretical Chemistry, University of Cologne, June 28, 2023, Cologne, Germany (2023).

CONFERENCE LECTURES

- Adams, E.; Ahlers, J.; Bader, V.; Pezzotti, S.; Winklhofer, K. F.; Tatzelt, J.; Havenith, M.
Key Role of the Solvent in Driving Liquid-Liquid Phase Separation
DPG Spring Meeting Condensed Matter Section, March 26–30, 2023, Dresden, Germany (2023).
- Amidani, L.; E. Silva, C. L.; Kvashnina, K. O.
Approaches to HERFD XANES calculations of U M₄ edge
2nd International Workshop on Theory Frontiers in Actinide Science: Chemistry & Materials, February 26–March 01, 2023, Santa Fe, California, U.S.A. (2023).
- Amidani, L.; Kvashnina, K. O.
Insight into ThO₂ electronic structure through the O K edge XANES
52nd Journée des Actinides, April 17–21, 2023, Dresden, Germany (2023).
- Balas, J.; Urbank, C.; Kaden, P.; März, J.; Gericke, R.
Actinide(IV) Complexes Containing 2-Mercaptopyrindyl
Actinides 2023, June 05–08, 2023, Golden, U.S.A. (2023).
- Barkleit, A.
RADEKOR - Speziation und Transfer von Radionukliden im Menschen unter besonderer Berücksichtigung von Dekorporationsmitteln
KERNthemen2023 - Impulse. Kompetenzen. Projekte, May 03–04, 2023, Dresden, Germany (2023).
- Barkleit, A.; Rachamin, R.; Pönitz, E.; Konheiser, J.
Experimentelle Bestimmung der Aktivierung von deutschen Druckwasserreaktoren zur Validierung der Aktivitätsberechnungen
10. RCA-Workshop, June 12–14, 2023, Dresden, Germany (2023).
- Barkleit, A.; Rachamin, R.; Pönitz, E.; Konheiser, J.
Experimentelle und rechnerische Bestimmung der Aktivierung für die Rückbauplanung von Kernkraftwerken
55. Kraftwerkstechnisches Kolloquium, October 10–11, 2023, Dresden, Germany (2023).
- Bilodid, Y.; Zilly, M.; Fischer, M.; Henry, R.; Kliem, S.; Alexander, A.; Kilger, R.
Impact of the Fuel Rod Modeling on the X2 Control Rod Cluster Ejection Results
International Conference on Mathematics and Computational Methods Applied to Nuclear Science and Engineering (M&C 2023), August 13–17, 2023, Niagara Falls, Canada (2023).
- Blei, M. K.; Drobot, B.; Kretschmar, J.; Pietzsch, H. J.; Kopka, K.; Mamat, C.
Bestimmung von log K-Werten macropa-basierter Chelatoren für die stabile Komplexbildung von ¹³¹Ba, ^{223/224}Ra und ¹³³La
61. DGN-Jahrestagung, April 19–22, 2023, Leipzig, Germany (2023).

- Bok, F.; Moog, H. C.; Voigt, W.
THEREDA: Polythermal extension of the Pitzer database for strontium
Actinide and Brine Chemistry in a Salt Repository Workshop VII (ABC Salt VII), June 15–16, 2023, Santa Fe, U.S.A. (2023).
- Braga Ferreira dos Santos, L.; Svitlyk, V.; Richter, S.; Hennig, C.; Huittinen, N. M.
Luminescence spectroscopy and diffraction studies of zirconia solid phases containing cerium
BMBF AcE Methods, March 20–22, 2023, Dresden, Germany (2023).
- Braga Ferreira dos Santos, L.; Svitlyk, V.; Richter, S.; Hennig, C.; Marquardt, J.; Nießen, J.; Tonnesen, T.; Huittinen, N. M.
Evaluation of Ce/U doped zirconia: similarities and differences between these solid solutions
Actinides 2023, June 05–08, 2023, Golden, U.S.A. (2023).
- Braga Ferreira dos Santos, L.; Svitlyk, V.; Richter, S.; Szabo, P.; Gaona, X.; Hennig, C.; Huittinen, N. M.
Spectroscopy and diffraction investigations of cerium/uranium doped zirconia solid solutions
47th Scientific Basis for Nuclear Waste Management (SBNWM), November 06–10, 2023, Cologne, Germany (2023).
- Butscher, D.; Senwitz, C.; Heller, A.; Stumpf, T.; Barkleit, A.
Influence of Eu(III) and U(VI) on rat and human kidney cells
7th International Conference on Environmental Radioactivity (ENVIRA), September 17–22, 2023, Sevilla, Spain (2023).
- Cardaio, I.; Mayordomo, N.; Cherkouk, A.; Stumpf, T.; Müller, K.
Microbial immobilization of technetium-99
HZDR Science Conference 2023, November 15–16, 2023, Helmholtz-Zentrum Dresden-Rossendorf e. V., Germany (2023).
- Cardaio, I.; Mayordomo, N.; Stumpf, T.; Cherkouk, A.; Müller, K.
Application of dissimilatory iron reduction by a novel Desulfotobacterium sp. isolate for Tc-99 immobilization
ChemTUgether 2023 & Alumni Meeting 2023, September 29, 2023, TU Dresden, Germany (2023).
- Das, A.; Chekhonin, P.; Houska, M.; Obermeier, F.; Altstadt, E.
Fractography of Neutron Irradiated RPV Steels – A Comparison of Shift in Reference Temperature and Net Hardening
Pressure Vessels & Piping Conference PVP2023, July 19, 2023, Atlanta, U.S.A. (2023).
- Diaz Pescador, E.; Jobst, M.; Grahn, A.; Kliem, S.
Steam Line Break Analysis in NuScale SMR with the Coupled System Code ATHLET-DYN3D in the Framework of the EU H2020 McSAFER
20th International Topical Meeting on Nuclear Reactor Thermal Hydraulics (NURETH-20), August 20–25, 2023, Washington DC, U.S.A. (2023).
- Fischer, C.; Kulenkampff, J.; Bollermann, T.
Flow field analysis towards improved predictability of diffusive flux in host rocks for radioactive waste
Interpore 2023, May 22–25, 2023, Edinburgh, U.K. (2023).
- Fischer, C.; Kulenkampff, J.; Cardenas Rivera, M. A.; Zhou, W.; Schöngart, J.
Tomographic analysis of advective flow and diffusive flux toward improved migration predictability in host rocks for radioactive waste
EGU General Assembly 2023, April 24–28, 2023, Vienna, Austria (2023).
- Franke, K.; Mansel, A.; Schöngart, J.
Production of ⁷⁶Br at the cyclotron Cyclone 18/9
15th Workshop of the European Cyclotron Network (CYCLEUR), June 22–23, 2023, Bucharest, Romania (2023).
- Friedrich, S.; Kretzschmar, J.; Drobot, B.; Stumpf, T.; Barkleit, A.
Influence of EDTA and EGTA on the Eu(III)/Cm(III) speciation in the human digestive system
7th International Conference on Environmental Radioactivity (ENVIRA), September 17–22, 2023, Sevilla, Spain (2023).
- Gaona, X.; Ait Mouheb, N.; Altmaier, M.; Bosbach, D.; Deissmann, G.; Geckeis, H.; Kretzschmar, J.; Schmeide, K.; Stumpf, T.
Cement-based materials in the multi-barrier system of nuclear waste repositories – impact on radionuclide retention
Helmholtz Energy Conference, June 12–13, 2023, Koblenz, Germany (2023).
- Grödler, D.; Gericke, R.; Kaden, P.; Patzschke, M.; Lichtenberg, A.; Sperling, J. M.; Rotermund, B. M.; Scheibe, B.; Beck, N. B.; Albrecht-Schönzart, T. E.; Mathur, S.
Mono- and Bimetallic Alkoxides of Neptunium(IV) and Iron(III)
Actinides 2023, June 05–08, 2023, Golden, U.S.A. (2023).
- Hilpmann, S.; Jeschke, I.; Deev, D.; Zügan, M.; Lapanje, A.; Rijavec, T.; Hübner, R.; Bok, F.; Schymura, S.; Cherkouk, A.
Uranium(VI) reduction by a Desulfotobacterium species in pure culture and in artificial multispecies bio-aggregates
18th International Conference on the Chemistry and Migration Behaviour of Actinides and Fission Products in the Geosphere - Migration 2023, September 24–29, 2023, Nantes, France (2023).

- Hilpmann, S.; Jeschke, I.; Deev, D.; Zupan, M.; Lapanje, A.; Rijavec, T.; Steudtner, R.; Hübner, R.; Schymura, S.; Cherkouk, A.
Uranium(VI) reduction by iron- and sulfate-reducing bacteria in pure culture and in artificial multispecies bio-constructs
ACS Spring 2023: Crossroads of Chemistry, March 26–30, 2023, Indianapolis, U.S.A. (2023).
- Hong, B.; Kaden, P.; Näder, A.; Gericke, R.; Patzschke, M.; Schmidt, M.; Stumpf, T.; März, J.
Coordination chemistry of the early actinides in various oxidation states (+III to +V) with benzamidinate ligand
The 11th International Conference on f Elements (ICFE-11), August 22–26, 2023, Strasbourg, France (2023).
- Huittinen, N. M.; Gilson, S.; Bukaemskiy, A.; Murphy, G. L.; Marquardt, J.; Lender, T.; Lippold, H.; Svitlyk, V.; Nießen, J.; Hennig, C.; Richter, S.; Akhmadaliev, S.; Poonosamy, J.; Trautmann, C.
Structural analyses of heavy-ion irradiated monazites
47th Scientific Basis for Nuclear Waste Management (SBNWM), November 06–10, 2023, Cologne, Germany (2023).
- Jobst, M.; Diaz Pescador, E.; Kliem, S.
Core Damage Extent Analysis of Large-Break LOCA for 4-Loop Pressurized Water Reactor with Detailed 3D Model of Reactor Pressure Vessel and Core
20th International Topical Meeting on Nuclear Reactor Thermal Hydraulics (NURETH-20), August 20–25, 2023, Washington DC, U.S.A. (2023).
- Katheras, A.; Karalis, K.; Bucher, A.; Krack, M.; Scheinost, A. C.; Churakov, S. V.
Ab initio modelling of magnetite surfaces for radionuclide retention
Goldschmidt Conference 2023, July 09–14, 2023, Lyon, France (2023).
- Katheras, A. S.; Karalis, K.; Krack, M.; Scheinost, A. C.; Churakov, S. V.
Ab initio modelling of magnetite surfaces for plutonium retention
BMBF AcE Methods, March 20–22, 2023, Dresden, Germany (2023).
- Katz, A.; Veilly, E.; Lévrier, L.; Pérez-Sánchez, D.; Arnold, T.; Bok, F.; Montavon, G.; Bertin, C.; Urso, L.; Chardon, P.; Sarramia, D.; Vaudelet, P.; Mallet, C.
Modelling water circulation and solute transport at a former french uranium mining site
18th International Conference on the Chemistry and Migration Behaviour of Actinides and Fission Products in the Geosphere - Migration 2023, September 24–29, 2023, Nantes, France (2023).
- Klotzsche, M.; Steudtner, R.; Drobot, B.; Vogel, M.
Where I am – Chemical microscopy of Eu(III) in plants
International Conference on the Biogeochemistry of Trace Elements & International Conference of Heavy Metals (ICOBTE & ICHMET 2023), September 06–10, 2023, Wuppertal, Germany (2023).
- Klotzsche, M.; Steudtner, R.; Vogel, M.; Drobot, B.
Exploring the Eu(III) translocation in hydroponically grown plants
Goldschmidt Conference 2023, July 09–13, 2023, Lyon, France (2023).
- Klotzsche, M.; Steudtner, R.; Vogel, M.; Drobot, B.; Schymura, S.; Raff, J.
Investigations on the Eu(III) translocation in hydroponically grown plants
21st Jena Remediation Symposium, October 05–06, 2023, Jena, Germany (2023).
- Lessing, J.; Neumann, J.; Bok, F.; Lützenkirchen, J.; Brendler, V.; Schmidt, M.; Stumpf, T.
Influence of the Competition of Al on the Retention of Trivalent Actinides and their Homologues in Feldspar
Goldschmidt Conference 2023, July 09–14, 2023, Lyon, France (2023).
- Mayordomo, N.; Rodríguez, D. M.; Brendler, V.; Roßberg, A.; Schild, D.; Müller, K.
Fundamental understanding of technetium interactions in the environment of nuclear waste repositories
Helmholtz Energy Conference, June 12–13, 2023, Koblenz, Germany (2023).
- Moll, H.; Jessat, J.; Stumpf, T.; Sachs, S.
Europium(III) as luminescence probe for radionuclide interactions with plant cells
11th International Conference on f Elements (ICFE-11), August 22–26, 2023, Strasbourg, France (2023).
- Moog, H. C.; Bok, F.; Gaona, X.; Freyer, D.; Miron, D.; Wissmeier, L.
THEREDA – Recent, present, and future developments
Actinide and Brine Chemistry in a Salt Repository Workshop VII (ABC Salt VII), June 15–16, 2023, Santa Fe, U.S.A. (2023).
- Müller, S.; Ferrari, A.; Knodel, O.; Rachamin, R.
The Stopping Target Monitor of the Mu2e experiment
DPG Meeting SMuK, March 20–24, 2023, Dresden, Germany (2023).
- Nikitin, E.; Fridman, E.
Dynamic modeling of the neutronic behavior of pressure wave propagation in the Phenix reactor core by using nodal diffusion code DYN3D
International Conference on Mathematics and Computational Methods Applied to Nuclear Science and Engineering (M&C 2023), August 13–17, 2023, Niagara Falls, Canada (2023).

- Nikitin, E.; Fridman, E.
Static modeling of core flowering scenarios in SFRs with nodal diffusion code DYN3D
International Congress on Advances in Nuclear Power Plants (ICAPP 2023), April 23–27, 2023, Gyeongju, Korea (2023).
- Nivesse, A. L.; Landesman, C.; Arnold, T.; Sachs, S.; Stumpf, T.; Scheinost, A. C.; Coppin, F.; Fevrier, L.; Den Auwer, C.; Gourgiotis, A.; Del Nero, M.; Montavon, G.
Understanding uranium fate in wetland soils: a speciation and labile behavior study in the former extraction mine of Rophin (France)
18th International Conference on the Chemistry and Migration Behaviour of Actinides and Fission Products in the Geosphere - Migration 2023, September 24–29, 2023, Nantes, France (2023).
- Pönitz, E.; Roode-Gutzmer, Q. I.; Barkleit, A.; Konheiser, J.
Activity measurement and calculation for gamma-emitting radionuclides in concrete drill cores of unit 2 of the Greifswald NPP
17th International Symposium on Reactor Dosimetry, May 21–26, 2023, Lausanne, Switzerland (2023).
- Pönitz, E.; Roode-Gutzmer, Q. I.; Barkleit, A.; Konheiser, J.
Ways for Efficient Decommissioning of Reactor Components and Concrete Shielding
Helmholtz Energy Conference, June 12–13, 2023, Koblenz, Germany (2023).
- Pospiech, S.; van den Boogaart, K. G.
Compositionally relevant post hoc tests of compositional linear models
22st Annual Conference of the International Association for Mathematical Geosciences, August 05–12, 2023, Trondheim, Norway (2023).
- Rachamin, R.; Barkleit, A.; Konheiser, J.; Seidl, M.
Activation calculations of selected German PWR components using the MCNP-FLUKA codes
AAA Workshop, May 10, 2023, Garching, Germany (2023).
- Rachamin, R.; Di Falco, S.; Ferrari, A.; Giusti, V.; Müller, S.; Pronskikh, V.
Background Studies and Normalization of Signal Events in the Mu2e Experiment
New Frontiers in Lepton Flavor, May 15–17, 2023, Pisa, Italy (2023).
- Rachamin, R.; Di Falco, S.; Ferrari, A.; Giusti, V.; Müller, S. E.; Pronskikh, V. S.
Monte Carlo simulation studies of background contributions in the Mu2e experiment
86th Annual Conference of the DPG and DPG Spring Meeting, March 20–24, 2023, Dresden, Germany (2023).
- Sanchez-Torrijos, J.; Redondo-Valero, E.; Queral, C.; Cabellos, O.; Meca, R.; Petrásek, O.; Diaz Pescador, E.; Kliem, S.; Palmans, N.; Sanchez-Espinoza, V.
On the application of advanced modeling tools to the SLB analysis in NuScale. Part I: TRACE/PARCS, TRACE/PANTHER and ATHLET/DYN3D
International Conference on Mathematics and Computational Methods Applied to Nuclear Science and Engineering (M&C 2023), August 13–17, 2023, Niagara Falls, Canada (2023).
- Schmeide, K.; Kretzschmar, J.; Huittinen, N. M.
Influence of selected organics on the retention of uranium(VI) by calcium-(aluminate)-silicate-hydrate phases
Joint 6th International Workshop on Mechanisms and Modelling of Waste / Cement Interactions, November 20–22, 2023, Prague, Czech Republic (2023).
- Schmeide, K.; Philipp, T.; Huittinen, N. M.; Shams Aldin Azzam, S.; Kretzschmar, J.
U(VI) retention on bentonite and cementitious materials: Effect of increased ionic strengths and presence of organics
18th International Conference on the Chemistry and Migration Behaviour of Actinides and Fission Products in the Geosphere - Migration 2023, September 24–29, 2023, Nantes, France (2023).
- Schmeide, K.; Philipp, T.; Huittinen, N. M.; Sieber, C.; Kretzschmar, J.
Bentonite and concrete: Efficient barrier materials for actinide retention under hyperalkaline conditions at increased ionic strengths and in presence of organics
EGU General Assembly 2023, April 23–28, 2023, Vienna, Austria (2023).
- Schmidt, M.; Lyu, K.; März, J.; Fichter, S.; Patzschke, M.; Kaden, P.
Actinide-MOF chemistry and applications
Actinides 2023, June 05–08, 2023, Golden, U.S.A. (2023).
- Schmidt, M.; Lyu, K.; März, J.; Fichter, S.; Patzschke, M.; Kaden, P.
Actinide-MOF chemistry and applications
Journées des Actinides, April 17–21, 2023, Dresden, Germany (2023).
- Schymura, S.; Zörner, L.; Rybkin, I.; Drev, S.; Podlipec, R.; Lapanje, A.; Mansel, A.; Strok, M.; Franke, K.
Characterizing environmental behavior of nanomaterials using radiolabeling approaches
NanoSAFE 2023 & NanoSafety Cluster, June 05–09, 2023, Grenoble, France (2023).
- Stotskiy, V.; Di Lorenzo, F.; Marques Fernandes, M.; Krack, M.; Scheinost, A. C.; Lanson, M.; Lanson, B.; Churakov, S. V.
Molecular scale understanding of Ni²⁺ adsorption on swelling clay minerals
Goldschmidt Conference 2023, July 09–14, 2023, Lyon, France (2023).

Wegner, L.; Peiffer, S.; Scheinost, A. C.; Hockmann, K.
Catch me if you can – understanding antimony geochemistry during Fe(II) oxidation
ICOBTE & ICHMET, 1st Joint International Conference, September 06–10, 2023, Wuppertal, Germany (2023).

Wegner, L.; Scheinost, A. C.; Peiffer, S.; Hockmann, K.
Thick as thieves: Antimony sequestration during ferrous iron oxidation
Goldschmidt Conference 2023, July 09–14, 2023, Lyon, France (2023).

Wei, T. S.; Sushko, V.; Matschiavelli, N.; Kluge, S.; Cherkouk, A.
Friend or Foe? Microbial impact of Calcigel bentonite on metal materials used for nuclear waste repository
2nd Joint Symposium of the International Societies for Environmental Biogeochemistry & Subsurface Microbiology 2023, October 22–28, 2023, Banff, Canada (2023).

Wollenberg, A.; Acker, M.; Kretzschmar, J.; Schmeide, K.; Tsushima, S.; Chiorescu, I.; Krüger, S.
Influence of the cement additive PBTC on aquatic uranium(VI) speciation and retention on cementitious material
Joint 6th International Workshop on Mechanisms and Modelling of Waste / Cement Interactions, November 20–22, 2023, Prague, Czech Republic (2023).

Wollenberg, A.; Kretzschmar, J.; Schmeide, K.; Acker, M.; Taut, S.; Stumpf, T.
Characterisation of highly soluble U(VI)-PBTC complexes
5th International Caparica Conference on Pollutant Toxic Ions and Molecules (PTIM) 2023, November 06–09, 2023, Caparica, Portugal (2023).

Wollenberg, A.; Kretzschmar, J.; Tsushima, S.; Krüger, S.; Acker, M.; Taut, S.; Stumpf, T.
Structural identification of aquatic U(VI)-PBTC complexes by spectroscopic investigations
18th International Conference on the Chemistry and Migration Behaviour of Actinides and Fission Products in the Geosphere - Migration 2023, September 24–29, 2023, Nantes, France (2023).

Zimmermann, T.; Faria Oliveira, A.; Mayordomo, N.; Scheinost, A. C.
Reduction of pertechnetate by magnetite - influence of pH and time
18th International Conference on the Chemistry and Migration Behaviour of Actinides and Fission Products in the Geosphere - Migration 2023, September 24–29, 2023, Nantes, France (2023).

FURTHER LECTURES

Jessat, I.
Uptake of Np(V) and U(VI) by zirconia (ZrO₂): a batch, spectroscopy and modeling study
Seminar für Kern- und Radiochemie, January 30, 2023, Mainz, Germany (2023).

Matschiavelli, N.; Zarschler, K.
Wissenschaftler*in im Bereich Biologie
Girls' and Boys' Day 2023, April 27, 2023, Helmholtz-Zentrum Dresden-Rossendorf, Germany (2023).

Raff, J.
(Radio)metal interaction with selected biosystems - from nuclear waste repositories to the food chain
Institutsseminar, Department of Nuclear Chemistry, Czech Technical University, October 05, 2023, Prague, Czechia (2023).

Richter, S.
Synthese und Charakterisierung von Lanthanoid- und Actinoid-Zirkonaten
Women in Nuclear Germany Preis 2023, September 29, 2023, Grafenrheinfeld, Germany (2023).

THESES

(Technische Universität Dresden, 2023, except where noted)

HABILITATION

Lippold, H.

**Radiotracerstudien mobilitätsbestimmender
Wechselwirkungsmechanismen in
Huminstoff-Schadstoff-Systemen**

*Fakultät für Chemie und Mineralogie, Universität Leipzig,
Leipzig, Germany (2023).*

DOCTORAL THESES

Caprani, Rafael

**Fission products behaviour in irradiated (U,Pu)O₂
fuel: manufacturing and analysis of SIMMOx**
Université de Montpellier, France (2023).

He, Yihua

Interaction of radioelements (Ra, U) with diatoms
IMT Atlantique Bretagne–Pays de la Loire, France (2023).

Hilpmann, Stephan

**Wechselwirkung eines tongesteinsrelevanten
Mikroorganismus mit Uran und Europium**

Di Nora, Vincenzo Anthony

**Extension, validation, and optimization of
Serpent/DYN3D/ATHLET code system for SFR
application**

EPFL Lausanne, Switzerland (2023).

MASTER THESES

Börner, Caroline

**Wechselwirkung von Technetium mit
Eisen(II)phosphaten**

Pulibandla, Likhitha Chakra Priya

**Characterization of FUS Condensate dissolution by
isothermal titration calorimetry**

Balas, Johannes

**Synthese und Charakterisierung von Actinid-
Komplexen mit (N,S)-Donorliganden**

Zilbermann, Maud

**Comparative structural and (radio-)chemical
investigations of activated cement and concrete
samples**

Guo, Jianfeng

**Investigating the Solvation Properties of ATP with
THz Spectroscopy and Simulation**

○ WORKSHOPS, SESSIONS

○ AWARDS

○ SEMINARS

○ TEACHING ACTIVITIES

○ ACE-METHODS WORKSHOP

March 20–22, 2023, HZDR, Dresden, Germany

As part of the German national project AcE (Actinide immobilization by incorporation into solid phases relevant for final disposal) funded by the German Federal Ministry of Education and Research (BMBF), IRE organized a methods workshop at the HZDR from Monday 20th to Wednesday 22nd of March 2023 in hybrid format.

The aim of the workshop was to revive and foster the education and connection of emerging scientists working in the field of actinide solid-state chemistry in Europe, with workshop topics addressing syntheses and important methods for the characterization of crystalline, inorganic, solid phases containing actinides.

For the workshop we welcomed 19 students and early career scientists from Aachen, Frankfurt, Jülich, and Karlsruhe in Germany and from Belgium, the Czech Republic, France, Switzerland, and the United Kingdom. In addition, 30 participants, with affiliations in seven different countries, followed the workshop online. This included six plenary speakers who introduced the six core topics of the workshop in their presentations.

Plenary speakers:

Bulgheroni, Antonio

Microscopy

Joint Research Center, Karlsruhe, Germany

Dacheux, Nicolas

Syntheses

ICSM/Université Montpellier, Marcoule, France

Gaona, Xavier

Thermodynamics

Karlsruhe Institute of Technology, Karlsruhe, Germany

Hennig, Christoph

Diffraction

Helmholtz-Zentrum Dresden-Rossendorf, European Synchrotron Radiation Facility, Grenoble, France

Mermoux, Michel

Vibrational spectroscopy

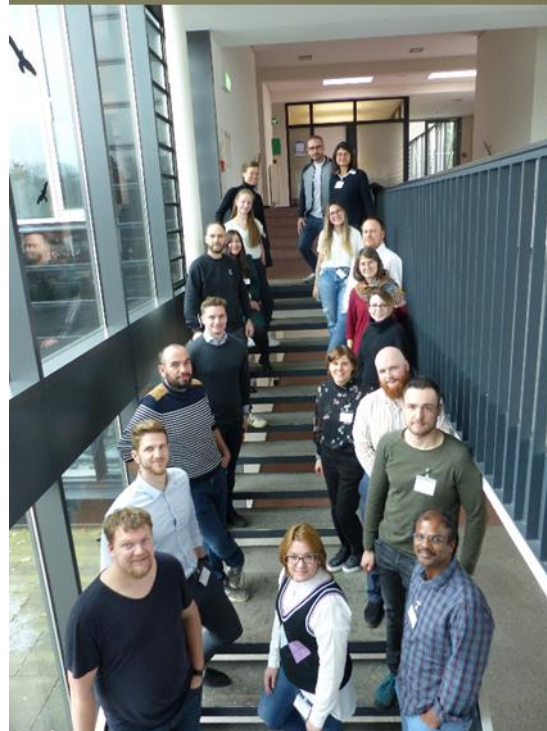
Université Grenoble Alpes, Université Savoie Mont Blanc, CNRS, Grenoble, France

Wiss, Thierry

Radiation damages

Joint Research Center, Karlsruhe, Germany

(contributed by: N. Huittinen)



WORKSHOP OF THE ALLIANCE TOPICAL ROADMAP WORKING GROUP NORM

June 6–7, 2023, Granada, Spain

The European Radioecological Alliance (ALLIANCE) promotes research in radioecology and acts as a European research platform. As one of five ALLIANCE working groups (WGs), WG Natural Occurring Radioactive Materials (NORM) is focusing on research related to science-based risk assessment, remediation and regulation of NORM-impacted sites and wastes. A workshop of WG NORM was organized in the Department of Microbiology at the University of Granada, Spain together with Mohamed Merroun. It focused on deepening the collaboration and cooperation within the WG and on the development of ideas for joint projects. 26 participants from 15 organizations from seven European countries were attending this workshop. The program was divided into six topical sessions.

Session 1: “Current activities of WG NORM members in national and international projects”

Session 2 “Stakeholder involvement”

Session 3 “Young researcher’s session – PhD and PostDocs working on NORM topics within the ALLIANCE WG NORM”

Session 4 “Web page”

Session 5 “Blind prediction of K_d values”

Session 6 “Funding opportunities within PIANOFORTE and other opportunities”

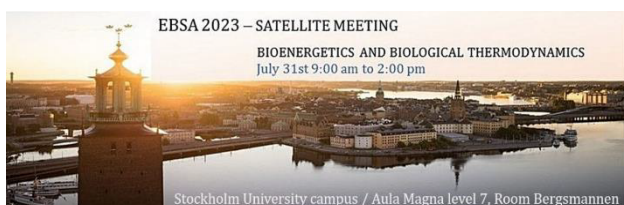
The workshop provided a very good opportunity to exchange information about ongoing NORM-related research activities of the attending members of WG NORM. Three PhD students and one PostDoc had the opportunity to present and discuss their NORM-related studies. A participant from the Wismut GmbH presented as a stakeholder work on dose assessment. As result of the previously organized blind prediction exercise for K_d values of uranium and radium, data gaps for the prediction of K_d values were identified and discussed. Several groups presented project ideas for new NORM-related projects.

We gratefully acknowledge the financial support of ALLIANCE for organizing the workshop, Mohamed Merroun and his team for organizing the workshop in Granada and the Faculty of Sciences for technical support.

(contributed by: S. Sachs)

EBSA 2023 – SATELLITE MEETING 14TH EUROPEAN BIOPHYSICS SOCIETIES ASSOCIATION (EBSA) CONGRESS 2023

July 31, 2023, Stockholm University Campus, Stockholm, Sweden



The EBSA-Satellite Meeting on „Bioenergetics and Biological Thermodynamics“ as well as the EBSA-2023 Congress Session under the same title were organized by the Biophysics Department of the Helmholtz-Zentrum Dresden-Rossendorf, led by Prof. Karim Fahmy. The events brought together researchers from European and other countries to exchange most recent results on the linkage of protein function to the entropic and enthalpic contributions of the underlying structural transitions. The presented systems ranged from the structural dynamics in enzymes and the conformational effects evoked by crowding to the thermodynamics of metabolic processes.

We acknowledge the support by our Co-Chair, Prof. Daumantas Matulis from Vilnius University and by Dr. Jana Oertel (HZDR), in organizing the Satellite Meeting.

Invited lecture were given by:

Åqvist, Johan

Uppsala University, Sweden

Structural Origin of Enzyme Cold-Adaptation

Harries, Daniel

The Hebrew University of Jerusalem, Israel

1. Macromolecular Crowding Beyond Hard-Core Repulsions

2. Thermodynamics of Proteins Vitrified in a Glassy Matrix

Kern, Dorothee

Brandeis University, U.S.A.

1. Aiming Higher - In Energy and Functional Understanding of Proteins

2. Evolution of Allosteric Activation and its Exploitation for Drug Design

Meyer-Almes, Franz-Josef

Darmstadt University of Applied Sciences, Germany

Chaperones and protein folding

(contributed by: K. Fahmy)

○ STRUMAT-LTO – WORKSHOP 2023

October 4–5, 2023, HZDR, Dresden, Germany

The running EU project STRUMAT-LTO (Structural Materials for Nuclear Safety and Longevity) is dedicated to structural materials research on parameters influencing the material properties of reactor pressure vessel (RPV) steels for safe long term operation of light-water reactor nuclear power plants. The first workshop of the project was held at HZDR as hybrid event with 53 participants (32 in person and 21 online) from 18 institutes in 10 nations. The division of Structural Materials of IRE stepped in as host because the meeting could not take place in Ukraine as originally planned in the project.

The event was supported by the EU under Grant Agreement No. 945272.

Lectures from leading experts were accompanied by presentations of young researchers about the topics of

- surveillance testing and high fluence embrittlement data for LTO > 60 years,
- miniature test methods for RPV integrity assessment: experiments and models,
- advanced microstructural characterization techniques including SEM/EBSD, TEM, APT, SANS, PAS,
- embrittlement trend curves for LTO: challenges and new developments,
- master curve versus Charpy testing for RPV integrity assessment, and
- remaining issues and advanced strategies for LTO.

(contributed by: A. Ulbricht)



○ AWARDS

Klotzsche, Max

First Poster Prize

10. RCA-Workshop, June 12-14, 2023, Dresden, Germany (2023).

Neumann, Julia

Doktorandenpreis des HZDR 2022

May 23, 2023, Dresden, Germany (2023).

Nikitin, Evgeny

Best Paper Award

International Congress on Advances in Nuclear Power Plants (ICAPP 2023), April 23–27, 2023, Gyeongju, Korea (2023).

Richter, Selina

IAEA Marie-Słodowska-Curie Fellowship Programme

International Atomic Energy Agency, Vienna, Austria (2023).

Schöngart, Jann

Second Poster Prize

10. RCA-Workshop, June 12-14, 2023, Dresden, Germany (2023).

E Silva, Clara Lisa

Best Lecture Award

52nd Journée des Actinides, April 17–21, 2023, Dresden, Germany (2023).

Wolf, Janis

Women in Nuclear (WiN) Germany Award 2023

Women in Nuclear (WiN) Germany e.V., Berlin, Germany, awarded at Faculty of Physics, Universität Wien, Vienna, Austria (2023).

○ SEMINARS (TALKS OF VISITORS)

Scheytt, Traugott

TU Bergakademie Freiberg, Germany

Micropollutants and microorganisms as groundwater indicators in karst catchments

January 11, 2023

Matyka, Maciej

Institute for Theoretical Physics, University of Wrocław, Poland

Pore scale fluid flow in complex porous media

February 06–07, 2023

Den Auwer, Christophe

Institut de Chimie de Nice, Université Côte d'Azur, Nice, France

The speciation of radionuclides in marine ecosystems, models and natural systems

February 16, 2023

Layfield, Richard

Department of Chemistry, University of Sussex, U.K.

Uranocenes Redux

March 15, 2023

Dacheux, Nicolas

ICSM, Université Montpellier, France.

Synthesis of zircon-type ceramic waste forms

March 20, 2023

Mermoux, Michel

Université Grenoble Alpes, France.

Some applications of Raman Spectroscopy in the Nuclear Field

March 21, 2023

Bulgheroni, Antonio

JRC, Germany.

When a micrograph is worth a 1Mx words

March 21, 2023

Gaona, Xavier

KIT, Germany.

Thermodynamics and dissolution

March 21, 2023

Wiss, Thierry

JRC, Germany.

Radiation damage studies: fuels and actinides compounds

March 22, 2023

Hedrich, Sabrina

Institute of Biosciences, TU Bergakademie Freiberg, Germany

Extremophilic microorganisms: Environmental impact and relevance in biohydrometallurgy

April 06, 2023

- Miron, George-Dan
Laboratory for Waste Management, Paul Scherrer Institut,
Villigen, Switzerland
**Behind the Scenes: The significance of
Thermodynamics in Assessing the long-term safety
of a deep geological radioactive waste repository**
April 12, 2023
- Natrajan, Louise
Department of Chemistry, The University of Manchester,
U.K.
**Luminescence Spectroscopy of the Actinides: From
First Principles to Applications within the Nuclear
Fuel Cycle**
May 08, 2023
- Scheck-Wenderoth, Magdalena
Department 4 Geosysteme, GeoForschungsZentrum
Potsdam, Germany
**Datengestützte Modellierung des Untergrunds -
Beispiele aus Deutschland**
May 10, 2023
- Walensky, Justin
College of Arts and Science, Radiochemistry Faculty,
University of Missouri, Columbia, MO, U.S.A.
**Small Molecule Activation and Reductive
Chemistry with Uranium(III) Complexes**
May 23, 2023
- Maurice, Rémi
ISCR – University of Rennes 1 – CNRS, France
**Exploring the chemistry of rare radioelements by
computational techniques**
June 19, 2023
- Reinhard, Sandra
Institute of Radioecology and Radiation Protection, Leibniz
University Hannover, Germany
**Characterization of colloidal Pu solutions by using
X-ray and UV-vis spectroscopy**
July 12, 2023
- Marquardt, Julien
Goethe Universität Frankfurt am Main, Germany
**Structural changes in lanthanide bearing monazite
under swift heavy ion irradiation**
July 26, 2023
- Powell, Brian A.
Department of Environmental Engineering and Earth
Sciences, Clemson University, U.S.A.
**Sorption of actinide ions to metal oxide surfaces:
Determination of surface complexation and
enthalpy values**
September 22, 2023
- Neumann, Julia
Argonne National Laboratory, U.S.A.
**Adsorption of uranyl on alumina (012) studied by
resonant anomalous X-ray reflectivity**
October 04, 2023

TEACHING ACTIVITIES

(Winter term: WT; summer term: ST)

Lectures

- Bok, F.
Friedrich-Schiller-Universität, Jena
ST 2023
**Geochemische und Reaktiver-Transport-
Modellierung**
- Brendler, V.
Dresden University of Applied Sciences
ST 2023
Radiochemistry
- Fahmy, K.
Technische Universität Dresden
WT 2022/2023, WT 2023/2024
Molecular Biophysics: Concepts and Methods
ST 2023
Biological Thermodynamics
- Fischer, C.
Universität Bremen
WT 2022/2023
Materials Analysis I - Radioanalytical Methods

Universität Leipzig
WT 2022/2023, WT 2023/2024
Mineralsystematik und Mikroskopie
WT 2022/2023, WT 2023/2024
Moderne Methoden in der Materialwissenschaft
ST 2023
Technische Mineralogie
- Heine, T.
Technische Universität Dresden
WT 2022/2023, WT 2023/2024
PC III (Einführung in die Computerchemie)
Methoden der Theoretischen Chemie
WT 2022/2023
Quantum Chemistry

Yonsei University Seoul, Korea
ST 2023
Digital Chemistry

Kuc, A. B.
Universität Leipzig
WT 2023/2024
Computational Spectroscopy

Lippold, H.
Universität Leipzig
ST 2023
Radioanalytik
Radiochemische Analysenmethoden
WT 2022/2023, WT 2023/2024
Radioanalytik

Mayordomo Herranz, N.
Technische Universität Dresden
WT 2022/2023, WT 2023/2024
Radioecology

Raff, J.
Dresden University of Applied Sciences
WT 2022/2023, WT 2023/2024
Mikrobiologie

Schmidt, M.
Technische Universität Dresden
WT 2022/2023, WT 2023/2024
Chemistry of the f-elements

Schymura, S.
Universität Leipzig
WT 2022/2023
Radioanalytik

Stumpf, T.
Technische Universität Dresden
WT 2022/2023, WT 2023/2024
Radiochemistry

Courses

☞ The laboratory course “Radiochemistry” was provided from August 21–September 01, 2023, as a part of a module of the chemistry master degree program at the Technische Universität Dresden.

Advisers:

Braga Ferreira dos Santos, L.	Mayordomo Herranz, N.
Cardaio, I.	Miladi, E.
Dück, V.	Näder, A.
Duckworth, T.	Nucke, L.
Grödler, D.	Patzschke, M.
Hong, B.	Sachs, S.
Klotzsche, M.	Saini, D.
Kaden, P.	Sawallisch, T.
Jordan, N.	Sieber, C.
Lessing, J.	Zimmermann, T.
Linares, R.	

☞ Biophysics course of the Dresden-International-Graduate School (WT 2022/2023 & WT 2023/2024).

Advisers:

Fahmy, K.	Oertel, J.	Philipp, J.
-----------	------------	-------------

☞ Courses and seminars were held referring to the following lectures:

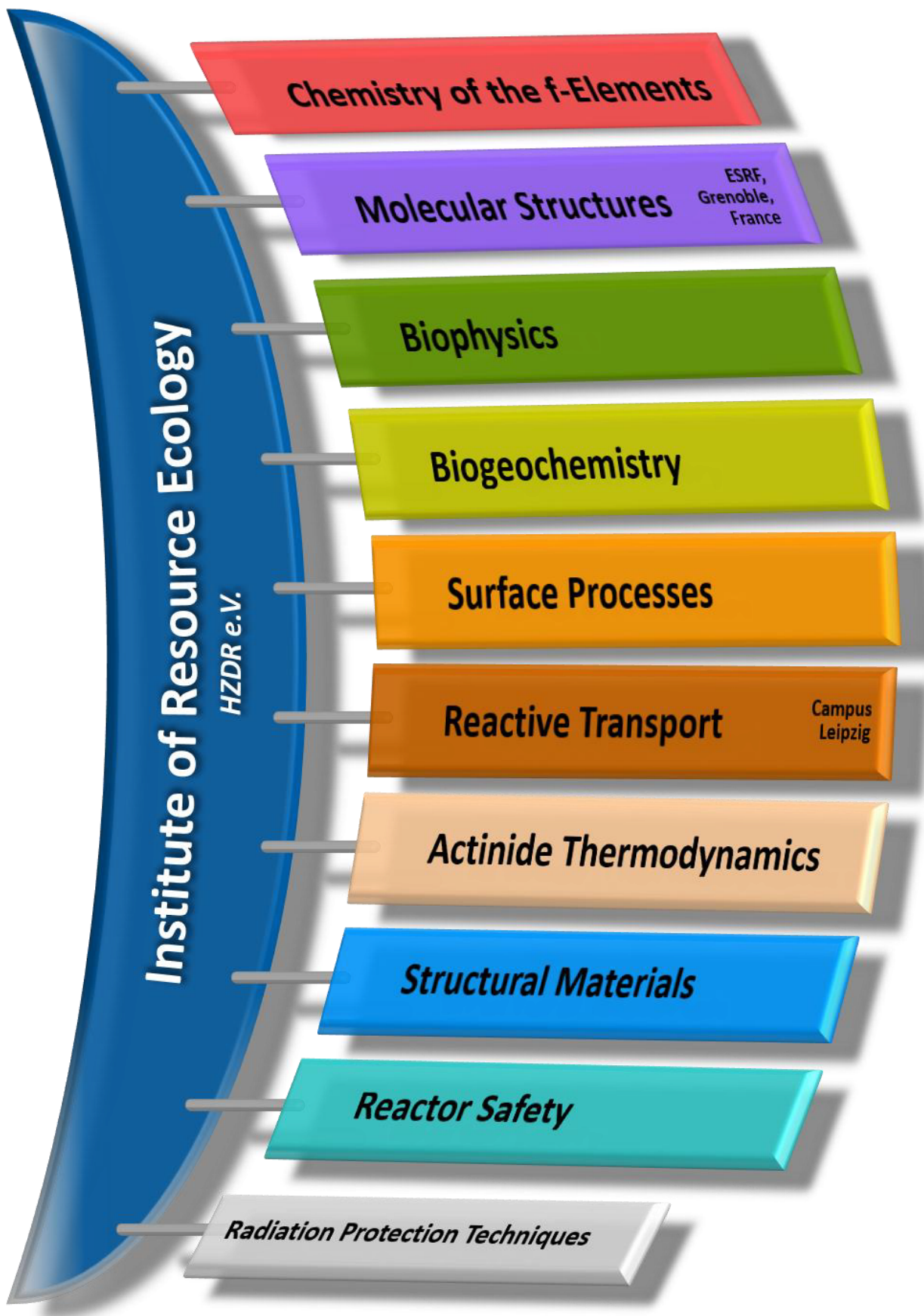
Fahmy, K.
Technische Universität Dresden,
WT 2022/2023, WT 2023/2024
Biophysics course of the Dresden-International-Graduate School

Fischer, C.
Universität Leipzig,
ST 2023
Technische Mineralogie
WT 2022/2023, WT 2023/2024
Mineralsystematik und Mikroskopie
Moderne Methoden in der Materialwissenschaft

Heine, T.
Technische Universität Dresden,
WT 2023/2024
Forschungsseminar Theoretische Chemie

Kuc, A. B.
Universität Leipzig,
WT 2023/2024
Computational Spectroscopy

PERSONNEL



HEAD OF INSTITUTE: Prof. Dr. Thorsten Stumpf

ADMINISTRATION:

Office Dresden: Gorzike, Jana; Kovacs, Jenny;
Kurde, Kerstin; Treuner, Bethina
Office Leipzig: Gerstner, Katrin; Pedrosa Gil, Nadja

RADIATION PROTECTION TECHNIQUES:
Bachmann, Stefanie; Eisold, Silke; Falkenberg, Dirk;
Jimenez Hernandez, Susana; Nebe, Kathrin; Täubrich, Eric
Sysad (IT): Berndt, Ronny

PROJECT COORDINATION:

Dr. Arnold, Thuro

ACTINIDE THERMODYNAMICS

PROF. DR. BRENDLER, VINZENZ

Dr. Abbasova, Dinara
Dr. Bok, Frank
Castro Biondo, Rodrigo*
Duckstein, Alexandra*
Diick, Viktor*
Dr. Kretzschmar, Jérôme
Dr. Pospiech, Solveig
Dr. Richter, Anke
Dr. Schmeide, Kathja
Shams Aldin Azzam, Salim
Sieber, Claudia*

Sushko, Vladyslav
Zechel, Susanne

ANALYTICS

Dr. Foerstendorf, Harald
Beutner, Sabrina
Gitzel, Tim
Goldbach, Dominik
Heim, Karsten
Schöne, Sylvia

SURFACE PROCESSES

DR. MÜLLER, KATHARINA

Butscher, Daniel*
Chlupka, Aline
Dietze, Alexandra
Friedrich, Sebastian*
Jessat, Isabelle*
Dr. Jordan, Norbert
Miliadi, Eya*
Müller, Christa
Saini, Diksha*
Weiss, Stephan

INCORP. INTO SOLID PHASES

Dr. Huttinen, Nina
Dr. Barkleit, Astrid
Braga Ferreira dos Santos, Luiza*
Dr. Gilson, Sara

TECRAD – YOUNG INV. GROUP

Dr. Mayordomo Heranz, Natalia
Bureika, Arkadz
Candao, Irene*
Saini, Vijay Kumar*

REACTIVE TRANSPORT

Campus Leipzig

PDD DR. FISCHER, CORNELIUS

Becker, Alexandra*
Candasa Rivera, Maria Alejandra*
Costa Guedes, Beatriz*
Dr. Franke, Karsten
Gouatiou Dongmo, Elivira*
Grubbe, Stefan
Dr. Hilppmann, Stephan
Dr. Kulenkampff, Johannes
PDD Dr. Lippold, Holger
Lösel, Dagmar

Dr. Mansel, Alexander
Schabernack, Jonas*
Schößler, Claudia
Schöngart, Jan*
Zhou, Wenyu*

NANOSAFETY

PROF. DR. HEINE, THOMAS, Chair Theor. Chem., TU Dresden/

PDD DR. KUC, AGNIESZKA BEATA
Bas, Ekin Esme*
Eren, Ismail*
Günzl, Johannes Jan*
Jha, Gautam*

Kempt, Roman*
Dr. Yang, Li
Umm-e-Hani, Umm-e-Hani*

Umm-e-Hani, Umm-e-Hani*

STRUCTURAL MATERIALS

DR. ALTSTADT, EBERHARD

Dr. Bergner, Frank
Dr. Brandenburg, Jann-Erik
Dr. Chekhonin, Paul
Dr. Das, Aniruddh
Dykas, Jakob
Houska, Mario
Dr. Kaden, Cornelia

Lai, Libang*
Pietzsch, Jens
Richter, Tony
Dr. Ulbricht, Andreas
Dr. Vogel, Karin
Webersinke, Wolfgang
Weiz, Tilo

BIOGEOCHEMISTRY

DR. RAFF, JOHANNES

Bertheau, Rahel
Dauwe, Julia*
Dr. Drobot, Björn
Flemming, Katrin
Dr. Günther, Alix
Dr. He, Yihua
Kirsch, Klemens*
Kronke, Tobias
Klotzsche, Max*
Dr. Krawczyk-Bärsch, Evelyn
Linares Jimenez, Raul Eduardo*
Dr. Moll, Henry

Newman Portela, Antonio*

Dr. Sachs, Susanne

Selbt, Jana

Dr. Stedtner, Robin

Waurick, Lukas*

Wolf, Janis*

Wolff, Janis*

Wolff, Janis*

Wolff, Janis*

Wolff, Janis*

Wolff, Janis*

Wolff, Janis*

Wolff, Janis*

Wolff, Janis*

Wolff, Janis*

Wolff, Janis*

Wolff, Janis*

Wolff, Janis*

Wolff, Janis*

Wolff, Janis*

Wolff, Janis*

Wolff, Janis*

Wolff, Janis*

Wolff, Janis*

Wolff, Janis*

MICRONUC
Dr. Krawczyk-Bärsch, Evelyn
Dr. Matschiavelli, Nicole
Dr. Wei, Ting-Shyang

Wolff, Janis*

Wolff, Janis*

Wolff, Janis*

Wolff, Janis*

Wolff, Janis*

Wolff, Janis*

Wolff, Janis*

Wolff, Janis*

Wolff, Janis*

Wolff, Janis*

Wolff, Janis*

Wolff, Janis*

Wolff, Janis*

Wolff, Janis*

Wolff, Janis*

Wolff, Janis*

Wolff, Janis*

Wolff, Janis*

Wolff, Janis*

Wolff, Janis*

Wolff, Janis*

Wolff, Janis*

Wolff, Janis*

Wolff, Janis*

Wolff, Janis*

Wolff, Janis*

Wolff, Janis*

Wolff, Janis*

Wolff, Janis*

Wolff, Janis*

Wolff, Janis*

Wolff, Janis*

Wolff, Janis*

Wolff, Janis*

Wolff, Janis*

Wolff, Janis*

Wolff, Janis*

Wolff, Janis*

Wolff, Janis*

Wolff, Janis*

Wolff, Janis*

Wolff, Janis*

Wolff, Janis*

Wolff, Janis*

Wolff, Janis*

Wolff, Janis*

Wolff, Janis*

Wolff, Janis*

Wolff, Janis*

Wolff, Janis*

Wolff, Janis*

Wolff, Janis*

Wolff, Janis*

Wolff, Janis*

Wolff, Janis*

Wolff, Janis*

Wolff, Janis*

Wolff, Janis*

Wolff, Janis*

Wolff, Janis*

Wolff, Janis*

Wolff, Janis*

Wolff, Janis*

*. Ph.D. student (as of 2023/12/31)

APPOINTMENT TO A PROFESSORSHIP

Institution

Université Grenoble Alpes, France

Kvashnina, Kristina O.

GUEST SCIENTISTS

Institution

Forschungszentrum Jülich GmbH, IEK-6, Germany

Potts, Shannon

Goethe Universität Frankfurt am Main, Germany

Marquardt, Julien

Heinrich-Heine-Universität Düsseldorf, Germany

De Bary, Philippe

Institute of Innovative Research, Tokyo Institute of Technology, Japan

Ono, Ryoma;
Takao, Koichiro

Ludwig-Maximilian-Universität München, Germany

Guthenhaler-Tietze, Sophie;
Singer, Helena

National Graduate School of Chemistry of Montpellier (ENSCM), France

Williot, Yann

RWTH Aachen, Germany

Lender, Theresa

School of Chemistry, Trinity College Dublin, Ireland

Baker, Robert J.

State Scientific and Technical Center for Nuclear and Radiation Safety (SSTC NRS), Ukraine

Iarmosh, Inna

Technische Universität Dresden, Germany

Baier, Silvio; Dykas, Jakub; Heller, Anne;
Kunigkeit, Jonas; Richter, Tony;
Schmidt, Quirin; Seliverstova, Kristina;
Thai, Quang Minh; Tippmann, Juliane;
Wollenberg, Anne; Stepanek, Laura

Universidad de Cantabria, Spain

Sánchez Matias, Marcos

University of Manchester, U.K.

Natrajan, Louise

University of Wrocław, Poland

Zehler, Justyna
Zych, Eugeniusz

CO-FUNDED PH.D. STUDENTS

Institution

Bundesanstalt für Materialforschung und -prüfung (BAM), Berlin, Germany

Kirsch, Klemens

Laboratoire de physique subatomique et des technologies associées (Subatech), Nantes, France

He, Yihua

Technische Universität Dresden, Germany

Czajkowski, Artur; Diaz Pescador, Eduard;
Kempt, Roman; Raj, Mantan

UGR Granada, Spain

Newman Portela, Antonio

Université de Lille, France

Miladi, Eya

Université Grenoble Alpes, France

Saini, Diksha

Université Nantes, France

Caprani, Rafael

MASTER/DIPLOMA/BACHELOR

Balas, Johannes
Börner, Caroline

Guo, Jianfeng
Pulibandla, Likhitha Ch. P.

Zilbermann, Maud

GRADUATE ASSISTANTS, STUDENT ASSISTANTS, TRAINEES

Bode, Tobias
Polishchuk, Yuliia

Richter, Selina
Seal, Ayush

Stepanek, Laura

ACKNOWLEDGEMENTS

The Institute of Resource Ecology is one of the ten institutes of the Helmholtz-Zentrum Dresden–Rossendorf e.V. (HZDR). As registered, non-profit institution, the HZDR is supported by the authorities of the Federal Government and the Free State of Saxony. In addition to the basic funding, the financial support of the projects listed below by the given organizations and companies is gratefully acknowledged.

FUNDING ORGANIZATION / COMPANY	PROJECT TITLE	CONTRACT NO. (if applicable)
Commission of the European Communities (EU)	COMET – Two dimensional lattices of covalent- and metal-organic frameworks for the Quantum Hall resistance standard	20FUN03
	ENTENTE – European Database for Multiscale Modelling of Radiation Damage	H2020-900018
	ESFR-SIMPLE - European Sodium Fast Reactor - Safety by Innovative Monitoring, Power Level flexibility and Experimental research	HEU-101059543
	EURAD – European Joint Programme on Radioactive Waste Management ConCorD, CORI, DONUT, FUTURE T2 + T3, MAGIC, SFC, UMAN, KMSoK	H2020-847593
	FRACTESUS – Fracture mechanics testing of irradiated RPV steels by means of sub-sized specimens	H2020-900014
	INNUMAT – Innovative Structural Materials for Fission and Fusion	HEU-101061241
	McSAFER – High-Performance Advanced Methods and Experimental Investigations for the Safety Evaluation of Generic Small Modular Reactors	H2020-945063
	PIANOFORTE – Partnership for European research in radiation protection and detection of ionising radiation : towards a safer use and improved protection of the environment and human health	HEU-101061037
	R2CA – Reduction of Radiological Consequences of Design Basis and Design Extension Accidents	H2020-847656
	RadoNorm – Towards effective radiation protection based on improved scientific evidence and social considerations – focus on radon and NORM + RadoNorm Open Call Grant	H2020-900009
	Sol2H2 – Computational Design of Materials for Photocatalytic Hydrogen Generation and Separation	H2020-101031846
	STRUMAT-LTO – STRUctural MATerials research for safe Long Term Operation of LWR NPPs	H2020-945272
	SurfBio – Innovation hub for surface and colloid biology research	H2020-952479
Federal Ministry of Education and Research (BMBF) & Federal Ministry for the Environment, Nature Conservation, Nuclear Safety and Consumer Protection (BMUV)	AcE – Grundlegende Untersuchungen zur Immobilisierung von Actiniden mittels Einbau in endlagerrelevante Festphasen	02NUK060A
	Am-BALL – Actinid-Metall Bindung auf atomarem Level	1501667
	EMPRADO – Entwicklung einer Methode zur Pre-Aktivitäts- und Dosisleistungsberechnung von reaktornahen Bauteilen auf Basis von Neutronenflussverteilungen Berechnung der Neutronenflussverteilung in reaktornahen Bauteilen und deren Validierung an Experimenten als Basis der Aktivitätsrechnungen	15S9409A

FUNDING ORGANIZATION / COMPANY	PROJECT TITLE	CONTRACT NO. (if applicable)
	FENABIUM-II – Untersuchungen zu den Wechselwirkungen von f-Elementen mit biologisch relevanten Strukturmotiven: Ableitung grundlegender Struktur-Wirkprinzipien für eine Mobilisierung in der Umwelt	02NUK077B
	f-Char – Verbundprojekt – Spektroskopische Charakterisierung von f-Element-Komplexen mit soft donor-Liganden	02NUK059B
	GRaZ II – Verbundvorhaben Geochemische Radionuklidrückhaltung an Zementalterationsphasen	02E11860B
	KRIMI Verbundprojekt Kinetik der Radionuklidimmobilisierung	02NUK056C
	KuRSiv – Konkurrenz und Reversibilität bei Sorptionsvorgängen	02E12052A
	MgO-C3 Verbundprojekt: MgO-Beton C3 als langzeitbeständiges und schnellwirksames Verschlusselement für Schachtverschlüsse zukünftiger HAW-Endlager im Salinar; Teilprojekt: Untersuchung der Kontakte innerhalb der Zuschlagskörnung	02E12072B
	PepTight – Lasst die Biologie ran – Peptide umgarnen entscheidende Rohstoffe: die „natürliche“ Trennung von Lanthaniden, Teilprojekt A	031B1122A
	RADEKOR – Verbundprojekt Speziation und Transfer von Radionukliden im Menschen unter besonderer Berücksichtigung von Dekorporationsmitteln	02NUK057A
	RENA – Biologische Radionuklidentfernung durch Nutzung natürlicher Assoziationsprozesse, Teilprojekt A	02NUK066A
	ResKin_Move – Geschwindigkeitsfeld-Analyse mit Positronen-Emissions-Tomografie (PET): Parametrisierung und Validierung von Transportmodellen (Plug-Skala)	03G0900A
	SANGUR – Systematic sensitivity analysis for mechanistic geochemical models using field data from crystalline rock	02E12112A
	TecRad – Wechselwirkung von Technetium mit Mikroorganismen, Metaboliten und an Mineral-Wasser Grenzflächen - Radioökologische Betrachtungen	02NUK072
	TRAVARIS Verbundvorhaben: Transfer langlebiger Radionuklide aus der vadosen Zone in die Rhizosphäre und deren Aufnahme in Pflanzen unter Berücksichtigung mikrobiologischer Prozesse - Teilprojekt C: Einfluss der Bodenmikrobiologie auf den RN-Transfer und Verifizierung von Aufnahmemechanismen für RN in Pflanzen	15S9437C
	TRANSIENT – Verständnis von Struktur, Stabilität und Redox in Hochabbrandregionen von abgebrannten Mischoxid-Kernbrennstoffen; Teilprojekt HZDR	02NUK088B
	UMB II – Umwandlungsmechanismen in Bentonitbarrieren II	02E11870B
	WTZ-Granit – Vorhersage der heterogenen Radionuklidsorption auf Kluft- und Störungsflächen in granitischen Gesteinen: Parametrisierung und Validierung verbesserter reaktiver Transportmodelle	02E11911A

FUNDING ORGANIZATION / COMPANY	PROJECT TITLE	CONTRACT NO. (if applicable)
Deutsche Forschungsgemeinschaft (DFG), German Research Foundation	DFG-Programmpauschalen ab 2014 – Verwaltung von 25 % der ab 2014 zu den DFG-Projekten bewilligten Programmpauschalen	
	DNA-Struktur Molekulare Mechanismen der Interaktion chaotroper Salze mit natürlichen und künstlichen DNA-Strukturen	FA 248/8-1
	Graduiertenkolleg „Wasserstoff-Isotope 1,2,3H“	GRK 2721/1
	SFB 1415 – Sonderforschungsbereich 1415 „Chemie der synthetischen zweidimensionalen Materialien“	SFB 1415/1 2020
ANDRA	REDOX – Redox reactivity of selenium in environmental geomeedia	n20087095HZDR
Framatome, SAS	DYN3D Support Service Framatome	
Bundesgesellschaft für Endlagerung mbH (BGE)	THEREDA IV Datenbank	
	SOREDA – Entwicklung von Oberflächenkomplexierungsmodellen und Erstellung einer Referenz-Datenbasis	VT2200102
GRS gGmbH	Gaslöslichkeiten TDB	
Helmholtz-Gemeinschaft Deutscher Forschungszentren e.V. (HGF, Helmholtz Association)	HEP CROSSING – Crossing borders and scales – an interdisciplinary approach	PIE-0007
	FACKEL – Pakt-Mittel - Rekrutierung Prof Kvashnina	
ITD	Berechnungen MCNP und FLUKA	
KIT & BGE	Parfrei	20823849
PreussenElektra GmbH	BRENK Benchmark	
	Monitoring – Rekursive Berechnung von Neutronenfeldern in Räumen außerhalb der biologischen Abschirmung	4500353697
South African Medical Research Council (SAMRC), Johannesburg, South Africa	Haarproben – Analyse von Uran in Haarproben von Kindern und Jugendlichen, die in der Nähe von Minenhalden in Südafrika leben	
TÜV NORD	Prüfung geologischer Fragen	M.ASS.06.015.01.F70
TÜV SÜD	DYN3D Wartung TÜV S 2020/2021 ff– FWOR	
	WWER AP03	500603389
ÚJV Řež, a.s., Czech Republic	DYN3D für UJV Wartung 2022/2023, 2023/2024	VT1100028
vgbe energy e. V.	Small Punch	FP448-2023-HZDR
VUJE, a. s.	DYN3D Support Service VUJE	4500080706
VW Stiftung	VW Stipendium Iarmosh	9C097

INDEX OF AUTHORS

AUTHOR..... PAGE

Adams, E. M.	21
Akhmadaliev, S.	67
Albrecht-Schönzart, T. E.	12
Alonso, U.	30
Altstadt, E.	64, 66
Amidani, L.	63
An, Y.	22
Balas, J.	11, 13
Barkleit, A.	17, 52, 53, 69, 70
Bauters, S.	49
Bazarkina, E. F.	18, 59, 62
Beck, N. B.	12
Bektas, U.	65
Bergner, F.	66, 67, 68
Blei, M. K.	55
Bodensteiner, M.	61
Bok, F.	28, 39, 40, 42, 49
Bourhis, E.	33
Brandenburg, J.-E.	67, 68
Brendler, V.	38
Bureika, A.	19
Butscher, D.	52
Caprani, R.	60
Cardaio, I.	51
Chekhonin, P.	65, 67
Cherkouk, A.	29, 49, 51
Churakov, S. V.	33
Clavier, N.	60
Das, A.	64
Daumann, L.	45
Dettmann, S.	25
Diaz-Pescador, E.	72
Dornbusch, D.	56
dos Santos, L. B. F.	31, 32
Drobot, B.	17, 20, 45, 46, 47, 49, 50, 53, 54, 55
Dück, V.	28
Duckstein, A.	38
Dumas, T.	63
Eren, I.	22
Estevenon, P.	63
Fahmy, K.	48, 56
Faria Oliveira, A.	35
Fischer, C.	34, 35
Foerstendorf, H.	26, 27, 54
Franke, K.	37
Fridman, E.	71
Friedrich, S.	17, 53
Funke, S.	21

AUTHOR.....PAGE

Gericke, R.	11, 12, 13, 14, 59
Gilson, S. E.	31, 32, 59
Grahn, A.	72
Grangeon, S.	33
Greneche, J.-M.	33
Grödler, D.	11, 12
Hao, H.	21
Havenith, M.	21
Head-Gordon, T.	21
Heim, K.	26, 27
Heine, T.	35
Heller, A.	52, 54
Henkes, M.	59
Hennig, C.	32, 59, 61
Hilpmann, S.	49
Hlawacek, G.	65
Holtmann, L.	54
Hong, B.	11, 12, 16
Hoving, A.	33
Hübner, R.	46, 49
Huittinen, N.	25, 31, 32, 59
Jahn, N.	25
Jessat, I.	26, 27
Jessat, J.	46
John, W. A.	46
Jordan, N.	26, 27, 28
Kaden, P.	11, 12, 13, 14, 59
Kassahun, A.	50
Kegler, P.	59
Keller, A.	56
Kirsch, K.	29
Klingner, N.	65
Klinkenberg, M.	59
Klotzsche, M.	47
Kluge, S.	51
Koerdt, A.	29
Konheiser, J.	69, 70
Krawczuk, A.	61
Krawczyk-Bärsch, E.	50
Kretzschmar, J.	17, 19, 25, 53, 54, 55
Kuc, A.	22
Kulenkampff, J.	34, 36
Kumke, M. U.	25
Kutyma, T.	25
Kvashnina, K. O.	18, 49, 59, 63
Lai, L.	67
Lender, T.	31, 59
Lohmann, J.	25
Lützenkirchen, J.	26
Lv, K.	18

AUTHOR.....	PAGE
Mamat, C.....	55
Marquardt, J.	32, 59
Marques Fernandes, M.	33
Martin, P.	60
Martínez, J.....	60
März, J.	13, 14, 18
Mathur, S.....	12
Matschiavelli, N.	29
Maubec, N.....	33
Mayordomo, N.....	19, 29, 30, 51
Merroun, M. L.	50
Milašinović, V.....	61
Missana, T.....	30
Molčanov, K.....	61
Moll, H.	46
Müller, K.	19, 51
Murphy, G. L.	59
Näder, A.....	11, 16
Newman-Portela, A. M.	50
Niessen, J.....	32
Nikitin, E.....	71
Oertel, J.....	48
Patzschke, M.....	11, 16, 18, 20
Poenitz, E.	70
Ponomarev, A.....	71
Pospiech, S.	38
Prieur, D.....	49, 60
Qian, Y.....	33
Rachamin, R.....	69
Raff, J.	47, 50
Reich, T.....	25
Reinhard, S.....	15
Reissig, F.	55
Richter, S.	31, 32

AUTHOR	PAGE
Rosberg, A.....	15, 26, 49, 59
Rotermund, B. M.....	12
Sachs, S.....	46, 47, 48
Sánchez, M.....	64
Schabernack, J.	35
Scheibe, B.....	12
Scheinost, A. C.	26, 33
Schild, D.....	29
Schmeide, K.....	17, 25, 53
Schmidt, M.	11, 18
Schwaab, G.....	21
Senwitz, C.....	52, 54
Shams Aldin Azzam, S.	25
Sieber, C.	17, 53
Singer, H.	45
Sperling, J. M.	12
Spittler, L.	25
Steuertner, R.....	45, 46, 47, 49, 50, 52
Stietz, J.....	25
Stumpf, T.	17, 26, 29, 46, 47, 49, 53
Svitlyk, V.	32, 59
Takao, K.	14
Takeyama, T.	14
Thümmler, R.	59
Tsushima, S.	14, 17, 53, 54
Ulbricht, A.	66
Urbank, C.	13
Vogel, M.....	46, 47
Vuković, V.....	61
Waurick, L.	20, 55
Zechel, S.	39, 40
Zhou, W.	34
Zilbermann, M.	70



Institute of Resource Ecology
Bautzner Landstrasse 400
01328 Dresden/Germany
Phone +49 351 260-3210
Fax +49 351 260-3553
Email contact.resourceecology@hzdr.de
<http://www.hzdr.de>

Member of the Helmholtz Association